AN INVESTIGATION OF THE REACTIONS OF SUPERCRITICAL CO_2 AND BRINE WITH THE BEREA SANDSTONE, MUSCOVITE, AND IRON BEARING MINERALS

by

Seth Alexander Mangini

A thesis submitted in partial fulfillment
of the requirements for the degree

of

Master of Science

in

Earth Sciences

MONTANA STATE UNIVERSITY
Bozeman, Montana

July 2015

©COPYRIGHT

By

Seth Alexander Mangini

2015

All Rights Reserved

DEDICATION

ἄνδρα μοι ἔννεπε, μοῦσα, πολύτροπον, ὃς μάλα πολλὰ
πλάγχθη, ἐπεὶ Τροίης ἱερὸν πτολίεθρον ἔπερσεν:
πολλῶν δ᾽ ἀνθρώπων ἴδεν ἄστεα καὶ νόον ἔγνω,
πολλὰ δ᾽ ὅ γ᾽ ἐν πόντῳ πάθεν ἄλγεα ὃν κατὰ θυμόν,
5ἀρνύμενος ἥν τε ψυχὴν καὶ νόστον ἑταίρων.
ἀλλ᾽ οὐδ᾽ ὣς ἑτάρους ἐρρύσατο, ἱέμενός περ:
αὐτῶν γὰρ σφετέρῃσιν ἀτασθαλίῃσιν ὄλοντο,
νήπιοι, οἳ κατὰ βοῦς Ὑπερίονος Ἠελίοιο
ἤσθιον: αὐτὰρ ὁ τοῖσιν ἀφείλετο νόστιμον ἦμαρ.
τῶν ἀμόθεν γε, θεά, θύγατερ Διός, εἰπὲ καὶ ἡμῖν.

Sing to me of the man, Muse, the man of twists and turns …
driven time and again off course, once he had plundered
the hallowed heights of Troy.
Many cities of men he saw and learned their minds,
many pains he suffered, heartsick on the open sea,
fighting to save his life and bring his comrades home.
But he could not save them from disaster, hard as he strove—
the recklessness of their own ways destroyed them all,
the blind fools, they devoured the cattle of the Sun
and the Sungod blotted out the day of their return.
Launch out on his story, Muse, daughter of Zeus,
start from where you will—sing for our time too.

-Homer (Translated by Robert Fagles)

This thesis is dedicated to my parents, Keith and Suzanne, and my sister Kristine, who have been there for me on course and off.

ACKNOWLEDGEMENTS

Many hands helped to make this thesis possible. I would like to acknowledge my family for their support through it all. I owe many thanks to my committee: Dr.'s Mark Skidmore, Colin Shaw, and David Mogk; my fellow rock and lab rats: Lauren Thomas, Chris Allen, Zoe Harrold, and Lori Babcock; my indomitable field assistant, Benjamin "Kentucky" Ballard; the programming wizard of New Zealand, Tim Brox; and the staff of ICAL, especially Laura Kellerman.

Last but certainly not least I would like to acknowledge my funding sources, who greased the wheels of science: the Big Sky Carbon Sequestration Partnership and the Department of Energy, the Geological Society of America, and the Clay Minerals Society.

VITA

The author was born on a dark and stormy night in a western Pennsylvania steel town to the union of a nurse and a geologist. He had dreams about the West and started to roam…

TABLE OF CONTENTS

1. INTRODUCTION 1

Background 1
CO_2 Sequestration, Basic Technical Information 2
CO_2 Phase Behavior 2
CO_2 in the Reservoir 3
Trapping Mechanisms 3
CO_2-Water Solubility 4
Implications for Experimental Work 5
Summary 5
Reactor Upgrades and Experimental Methods (Chapter 2) 6
Berea Experiments (Chapter 3) 6
Batch Experiments (Chapters 4 & 5) 7
Jefferson Formation Study (Chapter 6) 7

2. REACTOR DESIGN AND EXPERIMENTAL METHODS 12

Flow-Through Reactor Design and Capabilities 12
Reactor Upgrades (2012-2014) 13
Major Upgrades 13
New Accumulator 13
Two Syringe Pumps with Continuous Flow
Valve System 14
New CO_2 Injection Pump 14
Sample Collection Manifold 14
Heat Exchangers 15
CO_2-Brine Mixing Vessel 15
Influent Pressure Sensor 15
Pressure Gauges 16
Other Modifications 16
Methods 16
Berea Sandstone Flow-Through Experiments 16
Batch Experiments 16
Brine Theory and Preparation 17
Berea Experiment Brine Composition 19
Preparation Method 19
Analytical Methods 20
Gas 20
Brine 20
Cations and Anions 20
Silica 20

TABLE OF CONTENTS - CONTINUED

Iron 21

3. INVESTIGATION OF REACTIVE MINERAL PHASES OF THE BEREA SANDSTONE DURING THE INJECTION OF SUPERCRITICAL CO_2 UNDER SIMULATED SEQUESTRATION CONDITIONS 29

Introduction 29
Materials 29
Origin 30
Mineralogy 30
Phyllosilicate Cement 31
Elemental Composition 32
Hypotheses 32
Experimental Procedure 34
Results 36
pH 36
Conductivity 36
Ionic Composition 36
Changes to Elemental Composition 37
Changes to Mineralogy 37
Gas Concentrations 38
Discussion 38
Muscovite 39
Dolomite/Ankerite 39
Iron Oxides 39
Conclusions 40

4. INVESTIGATION OF THE REACTIONS OF IRON OXIDES AND IRON SULFIDE UNDER SIMULATED GEOLOGIC SEQUESTRATION CONDITIONS 65

Introduction 65
Hypothesis 67
Experimental 67
Materials 68
Pyrite 68
Magnetite 69
Substituted Hematite 69
Hematite 69
Iron(II) Chloride 70

TABLE OF CONTENTS - CONTINUED

Results....70
Control Experiment....70
Pyrite Experiments....71
Magnetite Experiment....72
Substituted Hematite Experiment....73
Iron(II) Chloride Experiment....73
Hematite Experiment....73
Hydrogen Gas Generation....74
Discussion....74
Enhanced CO_2 Dissolution....74
Dissolved Iron Deficit....75
Effects of pH and Eh on the Magnetite and Substituted Hematite Systems....76
A Model for the Magnetite-Brine-CO2 System....76
Effects of pH and Eh on the Pyrite System....78
A Model for the Pyrite-Brine-CO2 System....78
Summary....79
Conclusions....79

5. INVESTIGATION OF MUSCOVITE-scCO_2-BRINE REACTIONS....106

Introduction....106
Hypothesis....106
Experimental....107
Muscovite Sample....107
Results....108
Muscovite Batch Reaction #1....108
Muscovite Batch Reaction #2....108
Discussion....109
Conclusions....110

6. EVALUATION OF A JEFFERSON FORMATION OUTCROP INSUN CANYON AS AN ANALOG FOR THE JEFFERSON FORMATION IN THE SUBSURFACE OF THE KEVIN DOME....118

Introduction....118
Field Work....119
Field Area....119
Stratigraphy and Sedimentology....120
Stratigraphic Interpretation....121

TABLE OF CONTENTS – CONTINUED

Sampling 122
Rock Properties 123
Jefferson Facies #1 123
Jefferson Facies #2 124
Suitability as an Analog to the Kevin Dome 125
Conclusions 127

7. CONCLUSIONS 150

REFERENCES CITED 152

APPENDICES 158

APPENDIX A: Reactor Operational Procedures 159
APPENDIX B: Additional Reactor Modifications 170
APPENDIX C: 4-20mA Output Signal Reference 174
APPENDIX D: Brine Deoxygenation Experiments 177
APPENDIX E: Brine Deoxygenation Procedure 181
APPENDIX F: Gas and Brine Sample Retrieval Procedure 186
APPENDIX G: Sample Manifold Cleaning Procedure 191
APPENDIX H: Permeability Measurement Procedure 194
APPENDIX I: Parr Reactor Vessel Deoxygenation Procedure 199
APPENDIX J: Water Chemistry Data 201

LIST OF TABLES

Table Page

2.1 Berea Brine Recipe 21

3.1 Berea Pre-Reaction Elemental Analysis 41

3.2 Berea Pre- and Post-Reaction Elemental Analysis 42

3.3 Berea Gas Analysis Data 43

4.1 Hydrogen Gas Data from Iron Bearing Mineral Experiments 81

4.2 CO_2 Data from CO_2-Brine-Iron Bearing Mineral Batch Experiments 82

H1 Table of Values Necessary for Calculation of Permeability Using Flow-Through Reactor 197

J.1 Water Chemistry of Batch Reaction Experiments 202

J.2 Water Chemistry of Flow-Through Control Experiment 203

J.3 Water Chemistry of Berea Flow-Through Experiment Using Oxygenated Brine (8-29-13) 204

J.4 Water Chemistry of Berea Flow-Through Experiment Using Deoxygenated Brine (10-5-13) 205

J.5 Water Chemistry of Berea Flow-Through Experiment Using Deoxygenated Brine + $NaSO_3$ (11-5-13) 206

LIST OF FIGURES

Figure Page

1.1 Map of D.O.E. Regional Carbon Sequestration Partnerships....8

1.2 Location of Kevin Dome Large Scale Storage Project....9

1.3 Stratigraphic Cross Section of Kevin Dome Storage Horizon....10

1.4 CO_2 Phase Diagram....11

2.1 Flow-Through Reactor Design....22

2.2 Five Gallon Diaphragm Accumulator....23

2.3 Dual Syringe Pumps with Continuous Flow System....24

2.4 Photograph and Schematic of Brine Sampling Manifold....25

2.5 Heat Exchanger Schematic....26

2.6 Fluid Pre-Heating System Schematic....27

2.7 Photograph and Schematic of CO_2-Brine Mixing Vessel....28

3.1 Photomicrographs of Berea Sandstone....44

3.2 FEM Image of Iron Oxide Grains....45

3.3a Whole Rock XRD Profile of Berea Sandstone....46

3.3b Whole Rock XRD Profile of Berea Sandstone....47

LIST OF FIGURES – CONTINUED

Figure Page

3.4 FEM Image and Elemental Map Showing Carbonate Cement and Elemental Composition 48

3.5 XRD Profiles of Oriented Mounts from Berea 49

3.6 SEM SEI Image and EDS Elemental Analysis of Phyllosilicate Cement in Berea Sandstone 50

3.7 FEM Image and Elemental Map Showing Muscovite and Kaolinite Cement in Berea Sandstone 51

3.8 Photograph of Typical Core Used in Flow-Through Experiments 52

3.9 Photograph of Core 8-29 Divided For Post Reaction Analysis 53

3.10a Water Chemistry Data for Experiment with Oxygenated Brine (8-29-13) 54

3.10b Explanation of Water Chemistry Data for Experiment Using Oxygenated Brine (8-29-13) 55

3.11a Water Chemistry Data for Experiment Using Deoxygenated Brine (10-5-13) 56

3.11b Explanation of Water Chemistry Data for Experiment Using Deoxygenated Brine (10-5-13) 57

3.12a Water Chemistry Data for Experiment with Deoxygenated Brine + $NaSO_3$ (11-5-13) 58

3.12b Explanation of Water Chemistry Data for Experiment With Deoxygenated Brine + NaSO3 (11-5-13) 59

3.13a Water Chemistry Data for Control Experiment 60

LIST OF FIGURES – CONTINUED

Figure Page

3.13b Explanation of Water Chemistry Data Control Experiment 61

3.14 Potassium-Silica-Aluminum Phase Diagram 62

3.15 Core Showing Post-Reaction Oxidation 63

3.16 Iron-Sulfur-CO_2 pH-Eh Diagram 64

4.1 Photographs of Parr Reactor Vessels 83

4.2 Photographs of Iron Bearing Minerals Used In Experiments 84

4.3 EDS Analysis of Pyrite 85

4.4 XRD and XRF Analyses of Magnetite 86

4.5 XRD and XRF Analyses of Substituted Hematite 87

4.6 FEM Analysis of Substituted Hematite 88

4.7 XRD and XRF Analysis of Micaceous Hematite 89

4.8 Control Batch Reaction Experimental Data 90

4.9 Pyrite Batch Reaction 1 Experimental Data 91

4.10 Pyrite Batch Reaction 2 Experimental Data 92

4.11 FEM Images of Pyrite Pre- and Post-Reaction 93

4.12a FEM Images of Post-Reaction Precipitate on Pyrite 94

4.12b EDS Analyses of Post-Reaction Precipitate on Pyrite 95

4.13 Magnetite Batch Reaction Experimental Data 96

LIST OF FIGURES – CONTINUED

Figure Page

4.14a FEM Image of Magnetite Post Reaction Precipitate 97

4.14b EDS Analyses of Magnetite Post-Reaction Precipitate 98

4.15 Substituted Hematite Batch Reaction Experimental Data 99

4.16a FEM Image of Post-Reaction Precipitate on Substituted Hematite 100

4.16b EDS Analyses of Post-Reaction Precipitate on Substituted Hematite 101

4.17 Iron(II) Chloride Batch Reaction Experimental Data 102

4.18 Hematite Batch Reaction Experimental Data 103

4.19 pH-Eh Diagram of Iron-Sulfur-CO_2 System 104

4.20 Model of Magnetite-Brine-CO_2 System 105

5.1 Photograph of Muscovite Sample 112

5.2 SEM Photo and EDS Analysis of Muscovite 113

5.3 Muscovite Batch Reaction 1 Experimental Data 114

5.4 Muscovite Batch Reaction 2 Experimental Data 115

5.5 FEM Images of Muscovite Pre- and Post-Reaction 116

5.6 Potassium-Silica-Aluminum Phase Diagram 117

6.1 Regional Geology Map 128

LIST OF FIGURES – CONTINUED

Figure Page

6.2 Map of Montana Showing Field Area and Kevin Dome....129

6.3 Topographic and Geologic Maps of Home Gulch....130

6.4 Google Earth Image of Home Gulch Sampling Showing Sampling Locations and Location of Measured Section....131

6.5 Stratigraphic Column of Sun Canyon....132

6.6 Stratigraphic Column of Kevin Dome....133

6.7 Picture of Outcrop with Labels....134

6.8 Measured Section of Jefferson Formation (Oversized Figure)....135

6.9 Stromatoporoid Boundstone at Gibson Dam....136

6.10 Duperow Facies Model....137

6.11 Idealized Sedimentary Cycle....138

6.12 Interpreted Depositional Environments in Jefferson Outcrop (Oversized Figure)....139

6.13 Stratigraphic Interpretation of Jefferson (Oversized Figure)....140

6.14 Jefferson Facies #1 in the Field and Lab....141

6.15 Picture of Cores Retrieved from Facies #1 Block....142

6.16 Facies #1 Mineralogy and Diffraction Pattern....143

6.17 Facies #1 Elemental Composition....144

6.18 Facies #1 Photomicrographs....145

LIST OF FIGURES – CONTINUED

Figure Page

6.19 Facies #2 in the Field and Lab 146

6.20 Facies #2 Mineralogy and Diffraction Pattern 147

6.21 Facies #2 Elemental Composition 148

6.22 Facies #2 Photomicrographs 149

D1 Graphs of Brine Deoxygenation Times 180

E1 Picture of Carboy Used for Brine Deoxygenation 184

E2 Picture of Gas Impermeable Media Bag Used For Holding Deoxygenated Brine 185

F1 Picture of Apparatus for Capture of Gas Samples From Reactor Manifold 189

F2 Pictures Illustrating Procedure for Capture of Brine Samples from Sample Manifold 190

H1 Example Graph of Time vs. Permeability Using Flow-Through Reactor 198

ABSTRACT

The reduction of anthropogenic CO_2 emissions while still generating energy is a challenge that society faces. Most current energy production comes from fossil fuels that increase atmospheric CO_2 concentrations. Pending a breakthrough in clean energy production, technological solutions that increase efficiency and sequester CO_2 are required. Carbon Capture and Storage (CCS) or carbon sequestration technology can provide part of the solution by providing disposal of point source CO_2 emissions. The research described in this thesis aims to aid development of CCS technology. There are three parts to the thesis. First, is an experimental study of the Berea sandstone to determine the reactivity of its minerals, as these could impact its potential as a reservoir for CO_2 storage. Cores of Berea were placed in a "flow-through reactor" that pumped a continuous stream of supercritical CO_2 ($scCO_2$) mixed with simulated groundwater through the rock. Chemical and physical changes to the solid, liquid and gas phases were monitored. Second, batch experiments were conducted to study the behavior of pyrite, magnetite, hematite, and muscovite when subjected to simulated groundwater and $scCO_2$. Third, is an outcrop study of the Devonian Jefferson Formation, a carbonate formation to serve as an analog to the same formation in the subsurface where it is the target of a Department of Energy CCS pilot project. The field study provided analysis of the mineralogy, sedimentology, and stratigraphy so as to better understand its potential as a reservoir for CO_2 storage. The flow-through experiments on the Berea sandstone demonstrated that carbonate cement and iron oxides were reactive phases. It was equivocal as to whether muscovite was reactive. The batch experiments quantified the reactivity of iron oxides and pyrite and demonstrated significant dissolution of the $scCO_2$, such that supercritical conditions were not maintained for the duration of the experiment. The batch experiments also showed that muscovite was not reactive within the time frame of the Berea flow-through experiments (72 hours), but was reactive over longer time periods (500+ hours). The field study indicated that the best potential reservoir zones of the Jefferson Formation are altered reef complexes composed mostly of dolomite.

CHAPTER 1 – INTRODUCTION

Background

A major challenge that society is currently facing is how to produce electricity and industrial products while reducing emissions of the greenhouse gas carbon dioxide (CO_2). The capture and sequestration of CO_2 in geologic reservoirs (also known as Carbon Capture and Storage or CCS) can be part of the solution. In order to facilitate the development of CCS technology the Department of Energy began the partnership program in 2003, "to help develop the technology, infrastructure, and regulations to implement large-scale CO_2 storage in different regions and geologic formations within the Nation." (D.O.E., 2015). The country was divided into seven regions, and within each, a Regional Sequestration Partnership (RCSP) was formed (Fig. 1.1) to inventory potential geologic storage sites, validate CCS technology by developing pilot injection programs of greater than 1 million tons of CO_2, and perform basic science related to understanding CO_2 behavior in the subsurface.

The Big Sky Carbon Sequestration Partnership (BSCSP) is the regional partnership that covers eastern Idaho and Washington, western Montana, South Dakota, and Wyoming. The BSCSP is currently developing a megaton scale underground CO_2 storage project in Toole County, MT in a structure known as the Kevin-Sunburst Dome (Fig. 1.2) (BSCSP, 2015). The Jefferson Formation (also known as the Duperow), a Devonian carbonate unit, is the target CO_2 storage reservoir (Fig. 1.3). The BSCSP and partners at Montana State University are conducting scientific research to support the

Kevin Dome project and better understand of the effects of CO_2 injection on other potential reservoir types.

CO_2 Sequestration, Basic Technical Information

There are some basic physical factors in CO_2 sequestration that need to be understood in order to constrain the way experiments are performed. These include the 1) physical behavior of CO_2 with respect to temperature and pressure, and 2) the way it interacts with the brine in the reservoir.

CO_2 Phase Behavior

With increasing depth in the Earth, temperature increases along a geothermal gradient of approximately 25ºC/km. Pressure increases lithostatically, equation 1.1:

$$p=\rho gh \qquad (1.1)$$

where p= pressure, ρ= the density of the rock, g= the gravitational constant, and h= the depth of burial. The pressures and temperatures in reservoirs suitable for CCS are generally above the critical point of CO_2 (7.38MPa, 31.1ºC) and so CO_2 exists as a supercritical fluid ($scCO_2$) (Fig. 1.4). These potential CO_2 reservoirs generally lie >1,000m depth. In the supercritical form the boundary between the liquid and gas phases disappears and the fluid has unique properties such as the expandability of a gas and a density closer to that of a liquid (~2/3 that of water) (DePaolo and Cole, 2013).

CO_2 in the Reservoir

Trapping Mechanisms. There are several "trapping mechanisms" for CO_2 in a subsurface reservoir. These include 1) structural trapping, 2) residual trapping, 3) solubility trapping, and 4) mineral trapping (Kaldi et al., 2009). The types of trapping from 1-4 represent increased storage stability and decreased possibilities of leakage (Kaldi et al., 2009). Structural trapping, results from buoyant CO_2 being trapped underneath a caprock. Once emplaced under a caprock, the CO_2 will displace any water present in the formation because $scCO_2$ is less dense than water. As the $scCO_2$ migrates upward through the reservoir small bubbles of CO_2 will be left behind and trapped in the pore space of the rock surrounded by brine. These bubbles will be inhibited from further movement due to differences in the wetting properties of CO_2 and the surrounding water (Kim et al., 2012). This is residual trapping. Through time, CO_2 will dissolve into the formation water until it reaches saturation (typically 0.5%-1.5% of the molar volume of the $scCO_2$) (DePaolo and Cole, 2013). This is solubility trapping. Above the brine-$scCO_2$ interface the $scCO_2$ will become saturated with water vapor. The solubility of water in $scCO_2$ is much lower than that of $scCO_2$ in water (a few tenths of a percent) (King et al., 1992).

Below the $scCO_2$-brine interface dissolved CO_2 forms carbonic acid which lowers the pH of the brine to ~3.5-4.0 (Kaszuba and Janecky, 2009). The acidified brine dissolves minerals, which begins the process of buffering the pH to higher values. If the pH reaches high enough values, carbonate minerals will precipitate, trapping CO_2 in solid form (mineral trapping). Even if the pH does not reach values high enough to cause

precipitation, CO_2 can still be bound in the aqueous phase as bicarbonate or a cation-bicarbonate complex. This enhanced solubility trapping can cause a significant increase in the amount of CO_2 that can be dissolved over conventional solubility trapping and may represent a previously underappreciated form of CO_2 trapping (see Chapter 4).

CO_2-Water Solubility. Supercritical CO_2 dissolves in brine according to a modified version of Henry's Law (equation 1.2):

$$p = K_H c \quad (1.2)$$

Where p= the partial pressure of the gas of interest, K= the Henry's Law constant, and c= the concentration of the dissolved gas. Equation 1.3, shows a modification of Henry's Law for supercritical CO_2 in brine (Duan et al., 2006):

$$\ln m_{CO2} = \ln \gamma_{CO2}\, \Phi_{CO2}\, P - \frac{\mu_{CO2}^{1(0)}}{RT} - 2\lambda_{CO2-Na}\left(m_{Na} + m_K + 2m_{Ca} + 2m_{Mg}\right) - \zeta_{CO2-Na-Cl} m_{Cl}\left(m_{Na} + m_K + m_{Mg} + m_{Ca}\right) + 0.07 m_{SO4} \quad (1.3)$$

T is absolute temperature in Kelvin, P represents the total pressure of the system in bar, R is universal gas constant, *m* is the molality of components dissolved in water, γCO_2 is the mole fraction of CO_2 in vapor phase, Φ_{CO2} is the fugacity coefficient of CO_2, $\mu_{CO2}^{1(0)}$ is the standard chemical potential of CO_2 in liquid phase, $2\lambda_{CO2-Na}$ is the interaction parameter between CO_2 and Na^+, and $\zeta_{CO2-Na-Cl} m_{Cl}$ is the interaction parameter between CO_2 and Na^+, Cl^-. The main factors that influence the solubility of CO_2 are temperature, pressure, and total dissolved solids. CO_2 solubility increases with pressure and decreases as a function of temperature and total dissolved solids (Langmuir, 1997).

Implications for Experimental Work

Various experimental apparati can be used to simulate different components of the CO_2-brine reservoir system. For example, experiments using the flow-through reactor are two phase, (brine and pure phase $scCO_2$). The amount of free phase $scCO_2$ can be minimized by keeping the CO_2 injection level as close to saturation as possible. Flow-through experiments cannot be used to model equilibrium as fresh, acidified brine is always flowing through the sample, favoring dissolution over precipitation.

Batch reactions can be used to simulate systems that are allowed to approach equilibrium. In a batch reactor, pH may reach levels that favor the precipitation of secondary mineral phases. Samples in batch reactors can be kept below or above the brine-$scCO_2$ interface and so can be used to study either the CO_2 saturated brine phase, or the H_2O saturated $scCO_2$ phase. The experiments described in this thesis are intended to focus on the CO_2 saturated brine phase. Flow-through experiments were designed to minimize the amount of free phase $scCO_2$. Samples in the batch reactors were submerged below the brine-$scCO_2$ interface (with the exception of one experiment where evaporation led to the unintended exposure of the top of a sample).

Summary

The research presented in this thesis aims to improve understanding of CO_2-brine-reservoir rock interactions. This work is divided into four sections 1) A description of upgrades made to a flow-through reactor located in the Skidmore Lab at Montana State University, and its operational scheme, 2) Experiments conducted on the Berea sandstone

using the flow-through reactor, 3) Batch experiments conducted on certain mineral phases of the Berea sandstone that were considered to be reactive based on the experiments in 2). 4) A field study with mineralogical and stratigraphic analysis of an outcrop of the Jefferson Formation, the BSCSP's target formation for its megaton scale CO_2 injection project.

Reactor Upgrades and Experimental Methods (Chapter 2)

A flow-through reactor is a device that holds a sample of rock core at pressures and temperatures relevant to a subsurface reservoir. It is designed to allow fluids to be pumped through it to simulate subsurface fluid flow. The reactor in the Skidmore Lab at Montana State had previously been configured with a single syringe pump that allowed a brine-CO_2 solution to be pumped through a core. Upgrades included two additional pumps that allowed for the continuous injection of brine and separate injection of CO_2. Other improvements included a sample manifold that allowed fluid samples to be collected at experimental pressures and temperatures, an additional pressure sensor to allow measurement of sample permeability, and a mixing vessel to better facilitate the dissolution of CO_2 into the brine stream. In addition to the physical upgrades, a corresponding experimental procedure was developed.

Berea Experiments (Chapter 3)

Three 72-hour flow-through experiments were conducted on samples of the Berea sandstone. A fourth was conducted without a core to serve as a control. The Berea is a subarkosic sandstone from northeast Ohio commonly used in laboratory experiments due

to its high porosity and permeability, and homogeneous chemical composition. These experiments indicated several potential reactive minerals, including dolomite, muscovite, iron oxides, and pyrite. Results from these experiments can be used to better understand the behavior of CO_2 in other CCS reservoirs.

Batch Experiments (Chapters 4 & 5)

The depletion and possible oxidation of iron was observed during flow-through experiments on the Berea sandstone. Therefore, batch experiments on individual iron bearing minerals (magnetite, hematite, and pyrite) were designed to improve understanding of their behavior in the context of CO_2 sequestration. It has been recognized that experimental work on the reactions of these minerals with CO_2 is lacking (Kaszuba et al., 2013). In the Berea experiments, there was data to suggest that muscovite may dissolve or alter to kaolinite during CO_2 brine exposure but evidence for these processes was equivocal. Therefore, batch experiments with muscovite were conducted to determine if its dissolution or alteration could be expected in the Berea sandstone during the timeframe of the flow-through experiments.

Jefferson Formation Study (Chapter 6)

The Jefferson Formation is the target formation for the BSCSP's large scale injection project. A field study of the Jefferson Formation was conducted on an outcrop in Sun Canyon, west of Augusta, MT to characterize its mineralogy, sedimentology, and stratigraphy and assess how these factors affect its ability to serve as a CCS reservoir. Samples of the Jefferson Formation were obtained from the outcrop and analyzed for their porosity and permeability, mineralogy, texture, and chemical composition. The next

stage of the project was to conduct flow-through experiments on these samples, but technical difficulties with the flow-through reactor prevented this. This study provides information that can be used for future laboratory or field studies.

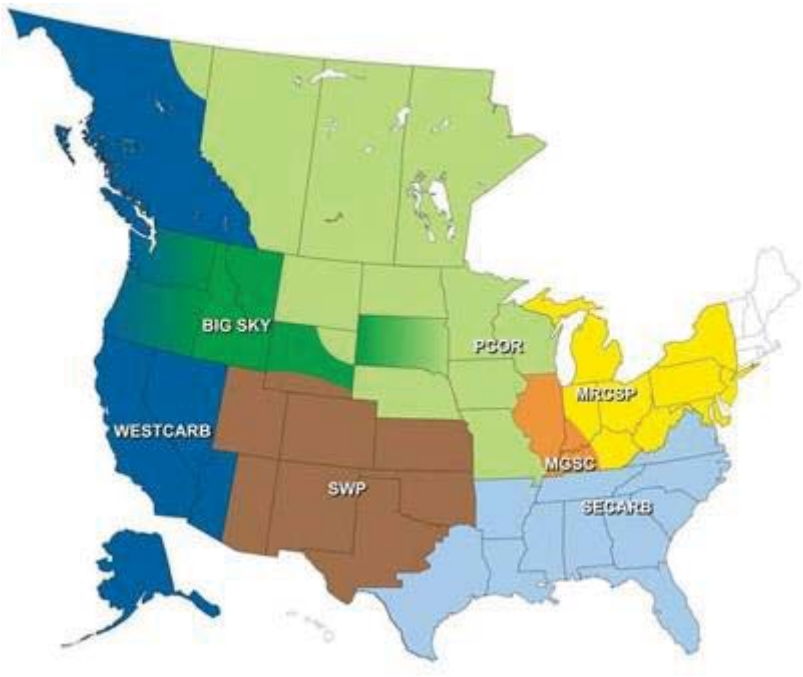

Fig. 1.1 – Department of Energy Regional Carbon Sequestration Partnerships. (D.O.E., 2015)

Fig. 1.2 – Location of Kevin Dome Large Scale Storage Project. (BSCSP, 2015)

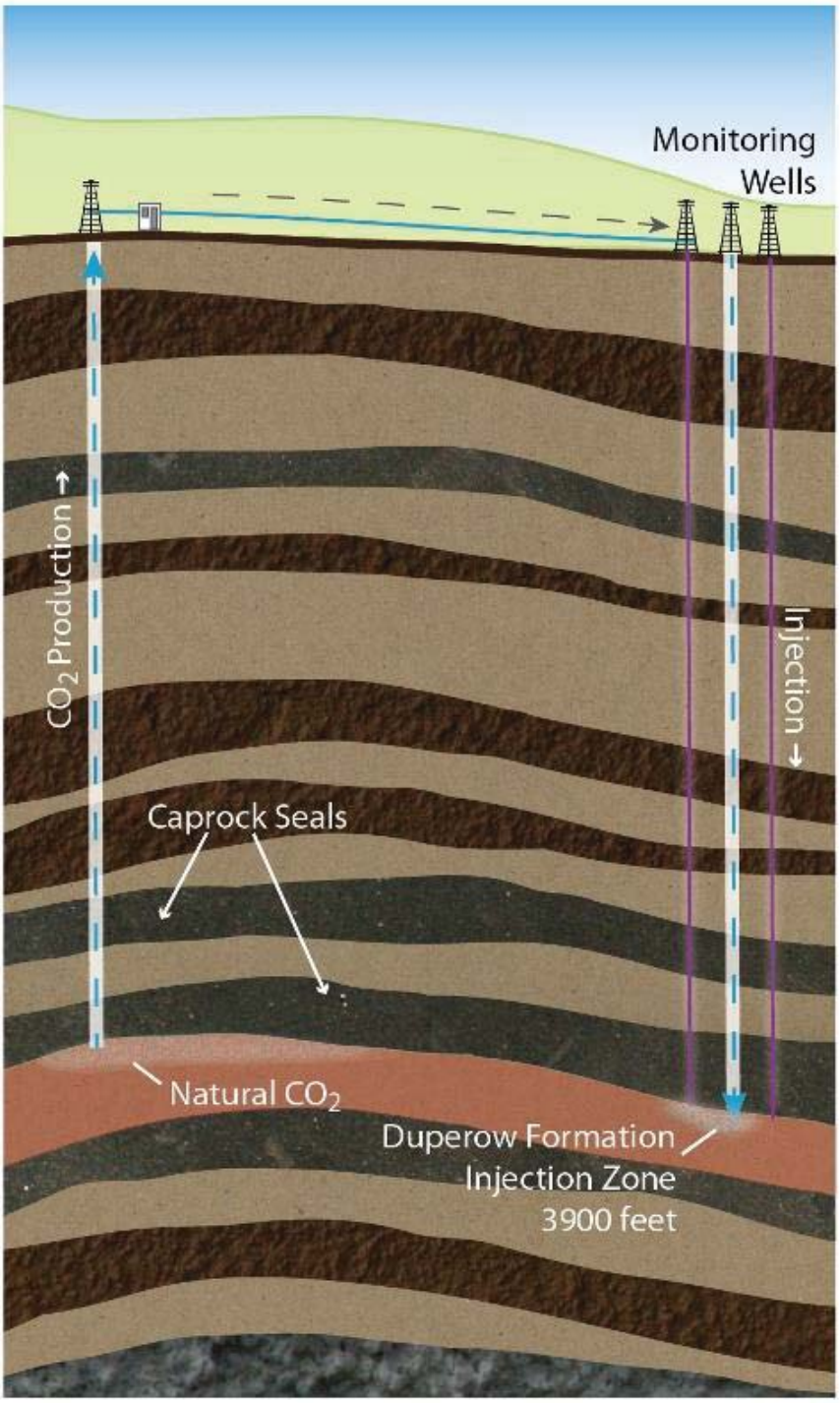

Fig. 1.3 – Stratigraphic cross section of Kevin Dome storage horizon. The terms Jefferson Formation and Duperow Formation are interchangeable. (BSCSP, 2015)

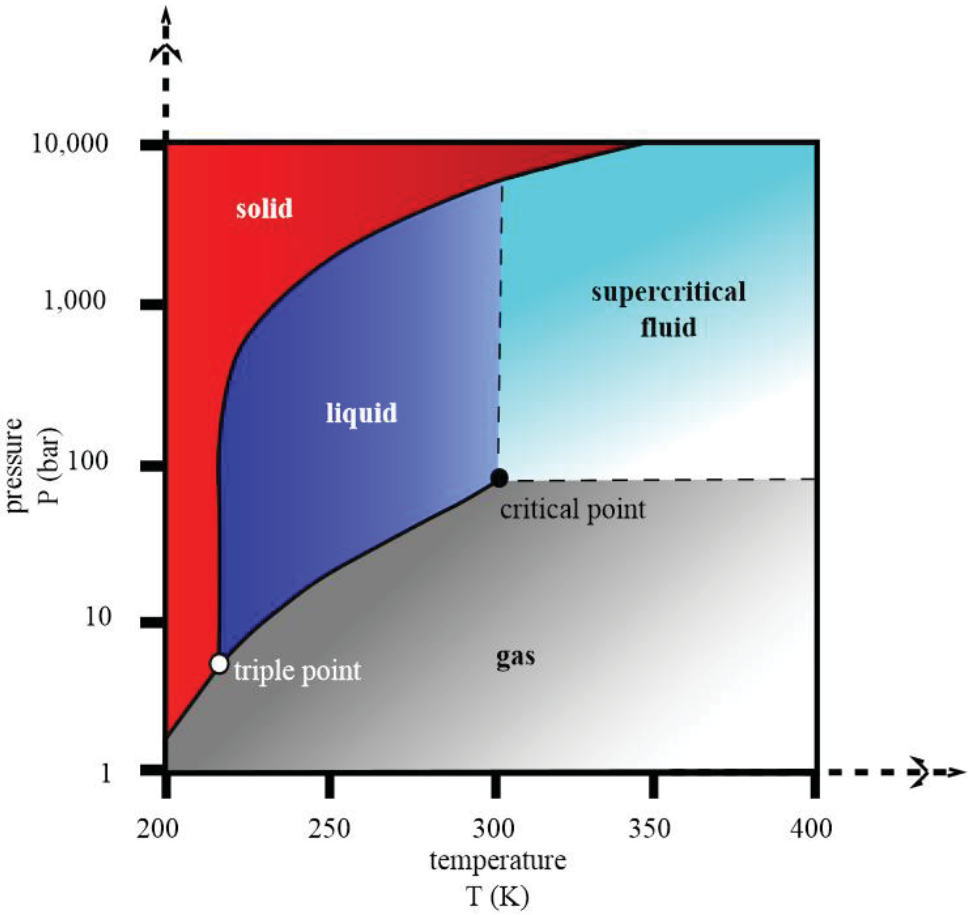

Fig. 1.4 – CO_2 phase diagram (Finney and Jacobs, 2010)

CHAPTER 2 – REACTOR DESIGN AND EXPERIMENTAL METHODS

Flow-through Reactor Design and Capabilities

This chapter describes the design and upgrade of a unique flow-through reactor capable of pumping a mixture of brine and supercritical CO_2 through a core sample with real time monitoring of pH, conductivity, and differential pressure (Fig. 2.1). Experiments conducted with this reactor are used to simulate the effects that CO_2-saturated brine has on reservoir rock below the CO_2-brine boundary.

The system constantly injects fresh CO_2-brine solution through the rock and therefore this experimental method is not ideal for looking at chemical equilibrium processes (such as carbonate precipitation), but it is a good tool for studying the processes that occur during the early phases of injection, such as:

- Initial dissolution of silicate and carbonate minerals
- Changes to water chemistry
- Precipitation of secondary silicate minerals (which can happen at low pH)
- Changes to rock porosity and permeability

Construction on the reactor began in 2007 and has evolved through several iterations. Current capabilities include:

- the ability to conduct experiments at up to 100ºC and 17MPa (2500psi)
- Independent control of brine and CO_2 flows (each fluid having its own pump(s)). This allows the creation of experimental conditions in which the brine is under-

saturated, saturated, or oversaturated with respect to CO_2. Brine only or CO_2 only experiments can be conducted if desired.

- real time measurement of pH, electrical conductivity (EC), pressure, differential pressure, and temperature
- the ability to capture fluid samples without perturbing the system's pressure

Reactor Upgrades (2012-2014)

The system in 2012 had one syringe pump that delivered both CO_2 and brine simultaneously (maximum capacity of 508mL for both CO_2 and brine). Fluid samples were obtained by opening a valve in the reactor downstream of the core. This caused the pressure to drop below the threshold required to maintain CO_2 as a supercritical fluid inside the reactor. A series of upgrades over the past two years, has added new operational capabilities to the reactor, improved existing capabilities, and replaced various components as they have worn out.

Major Upgrades

1.) New Accumulator (Fig. 2.2). The original piston accumulator (1 gallon) was replaced with a larger (5 gallon) diaphragm type model. The increased capacity allows longer periods between emptying. The internal diaphragm design (a balloon inside the steel cylinder with N_2 backpressure on one side, and accumulated fluids on the other) helps to maintain constant pressure during experiments. The piston type accumulator was prone to "stick slip" type events in which the pressure built up and then suddenly

released. The backpressure of the accumulator sets the pressure of the reactor, thus its smooth operation is important.

2.) Two Syringe Pumps with Continuous Flow Valve System (Fig. 2.3). Two additional Teledyne Isco 500D series syringe pumps with a continuous flow valve system were added to serve as the dedicated brine delivery system for the reactor. This allowed the third pump to be dedicated solely to the delivery of supercritical CO_2. All three pumps are controlled from a common control unit. A series of 4-20mA output cards were added to the analog output circuit board to allow pressure, flow rate, and volume remaining functions for the two additional pumps to be logged by the data logger. The wiring schedule of the 4-20mA output card is located in Appendix C.

3.) A New Pump for CO_2 Injection. In summer 2014 a fourth 500D syringe pump was received and used to replace the original pump. The original pump was then dedicated to servicing the lab's new Parr reactor vessels.

4.) Sample Collection Manifold. A sample collection system was designed and constructed by Swagelok, USA (Fig. 2.4). The design allows the collection of up to six water-gas samples without perturbing the pressure inside the reactor. Samples are collected by diverting the flow of effluent from the reactor into a series of 25mL sample cylinders sealed with valves on both ends. The system was further modified in the laboratory to include a bypass that allows the cylinders to be removed, emptied, and replaced during an experiment. Its components were either coated with nickel or

replaced with Monel (copper-nickel alloy) when it became apparent that corrosion was an issue.

5.) Heat Exchangers. Two heat exchangers were constructed to keep the fluids at a constant temperature before they enter the incubator (Fig. 2.5). Heat loss resulting in a temperature drop below the supercritical threshold has the potential to reduce the solubility of the CO_2. The heat exchangers are plumbed in line with the heating jackets that surround each of the three syringe pumps. Heating fluid is delivered by a constant temperature bath (Fig. 2.6). Originally ethylene glycol was used as the heating fluid, but its noxious odor prompted a search for a replacement. Propylene glycol is currently used.

6.) CO_2-Brine Mixing Vessel. In order to ensure that brine was saturated with CO_2, a vessel to mix the two fluids was built (Fig. 2.7). The vessel is a 150mL stainless steel cylinder filled with 1mm borosilicate glass beads. The beads are held inside the cylinder by stainless steel mesh cemented with Bob Smith Industries Maxi-Cure™ superglue. The vessel is positioned vertically. The brine-CO_2 stream enters in the bottom and percolates upwards. The surface area of the beads encourages dispersive forces to aid CO_2 dissolution.

7.) Influent Pressure Sensor. A dedicated influent pressure sensor was added upstream of the core holder in order to measure core permeability. The new sensor (PX411T0-3.5KGI) provides more precise measurement than the previous one (PX41T0-3.5KGI) (0.3% vs. 3.0%).

8.) Pressure Gauges. Two 0 - 5,000psi (34.4MPa) pressure gauges (for influent and effluent) replaced units that only measured up to 1500psi (10.3MPa). This was deemed necessary for safe operation.

9.) Other Modifications. A number of more minor upgrades and modifications are described in Appendix B.

Methods

Berea Sandstone Flow-Through Experiments

The flow-through reactor was used to conduct four 72-hour flow through experiments to determine the effects of CO_2-injection on the Berea sandstone (three with cores, one without a core to serve as a control). The operational procedure for the flow-through reactor is located in Appendix A. Water and brine samples were analyzed as described below in "Analytical Methods." A full description of the experiments is located in Chapter 3.

Batch Experiments

Eight batch reaction experiments were conducted to determine the effects of CO_2 on samples of individual minerals. Experiments were conducted in Parr Reaction vessels at 96°C and 12-13 MPa (1750 – 2000psi). The brine used in these batch experiments was of the same composition as in the Berea flow-through experiments. Brine samples were analyzed as described below in "Analytical Methods." A full description of these experiments is located in Chapters 4 & 5.

Brine Theory and Preparation

All experiments were conducted using brines that were designed to replicate those found in deep saline aquifers. These tend to have high levels of total dissolved solids (TDS) (>50,000ppm) (Langmuir, 1997). In these systems, there is little to no exchange of aquifer water with meteoric water. The result is a *rock dominated system* (Kaszuba and Janecky, 2009). In a rock dominated system, the rock and water have been exposed to each other for a long enough period of time that they have achieved chemical equilibrium. An aquifer with recharge does not achieve equilibrium. It is referred to as a *water dominated system* (Kaszuba and Janecky, 2009).

Equilibrium is the chemical condition in which the forward rate of a reaction equals the reverse rate, resulting in no net change to the composition of the chemical system. When a solid such as a mineral is placed into a solvent such as water, the natural result is for the two to engage in dissolution-precipitation reactions until equilibrium is reached. In the case of mineral-water reactions this means that the rate of formation of a given mineral is equal to its rate of dissolution. Thus, the concentrations of dissolved elements in the water are saturated (or close to saturated) with respect to the mineral phases present. If the elements present in the rock are undersaturated in the water, then additional rock will, over time, dissolve until its chemical species reach aqueous levels high enough for that mineral to precipitate. Thus, saturation is achieved. The ratio of reactants to products in a reaction at equilibrium is defined by an equilibrium constant (K_{eq}). For a given reaction:

$$aA + bB \rightarrow cC + dD$$

K is defined by the ratio of the concentration of products to the concentration of reactants:

$$K_{eq} = \frac{[C]^c[D]^d}{[A]^a[B]^b}$$

The equilibrium constant of a given reaction is related to the thermodynamic property of Gibbs free energy at a given temperature and pressure:

$$\Delta G^\circ_{(T,P)} = -RTln(K_{eq})$$

Equilibrium can be considered an accurate way of describing water-rock equilibria for minerals that are truly stable at the temperature of the aquifer. These include minerals such as calcite, dolomite, quartz, and kaolinite. The situation is complicated in the aquifer setting, by the fact that many minerals present in a rock (for instance potassium feldspar) were formed under high temperature conditions and thus they are only truly stable at these high temperatures. When they enter into a lower temperature environment, they are actually meta-stable (and thus theoretically over time their atoms should rearrange into a mineral form that is stable at the new pressure-temperature conditions). However, mineral grains that are meta-stable can remain intact indefinitely because even though their rearrangement is thermodynamically favorable, it is kinetically inhibited. It must be aided by factors such as water, heat, acidity, fluid movement and catalyzing species (Winter, 2010).

There are several databases of equilibrium constants available that have been determined through previous research (Robie and Waldbaum, 1968). Constants for these experiments were derived from the MINTEQ databases that are included in Geochemist's Workbench and Visual MINTEQ. Not all aqueous species are controlled by minerals

physically present in the aquifer. The water in the aquifer was derived from other sources (ocean, lake, or river water that was buried with the sediment or one or more ancient groundwater sources). Thus a multitude of dissolved elements may be present. Sodium and chloride generally constitute a high fraction of the total dissolved solids in deep saline aquifers (Langmuir, 1997). They are so highly soluble that they rarely exist in the presence of their natural solid phase, halite and concentrations can be highly variable.

Berea Experiment Brine Composition

The brine composition used in the Berea experiments was similar to that used in (Hansen, 2009; Vogt et al., 2014). The brine recipe was simplified relative to the actual formation waters, with these assumptions. Minor and trace elements were not added to the brines either because they are either not critical to the mineral reactions being studied (strontium, phosphate), or if they are, their equilibrium concentration is extremely low (aluminum). High concentrations of sodium chloride reduce the solubility of carbon dioxide via the "salting out effect" (Langmuir, 1997). Therefore sodium and chloride concentrations were deliberately kept low.

Preparation Method

Brine was prepared by adding the appropriate mass of each salt into a Class A 6L volumetric flask (tolerance +/- 0.1mL) and mixed with a stir bar for one half hour. Since subsurface aquifers have low dissolved oxygen (DO) concentrations (Langmuir, 1997), the brine was deoxygenated prior to use in the experiments (Appendix D).

Analytical Methods

Gas

Gas samples were analyzed using a SRI8610C gas chromatograph. Methane, carbon monoxide, and carbon dioxide were measured using a Flame Ionization Detector (FID). Hydrogen was measured using a Pulsed Discharge Helium Ionization Detector (PDHID).

Brine

Brine samples were analyzed, with special attention paid to elements that indicate changes to the minerals present in the core samples. For the Berea this was potassium and calcium.

Cations and Anions. Brine samples from the first three experiments on the Berea Sandstone (8-29-13, 10-04-13, 11-04-13) were analyzed for major cations (Na^+, K^+, Ca^{2+}, Mg^{2+}) using a Metrohm 800 series ion chromatograph. Dilutions of 1:100 and 1:10 were prepared in 0.01M trace metal grade HCl. Brine samples were analyzed for anions (F^-, Br^-, Cl^-, NO_3^-, PO_4^{3-}, and SO_4^{2-}) by ion chromatography. Samples were diluted to 1:10 and 1:100 concentrations with Nano-pure water.

Silica. Silica concentrations were measured with a Perkin-Elmer Lambda 35 spectrophotometer using the molybdate blue method (ASTM D859-10, Standard Test Method for Silica in Water). Silica concentrations were not measured for the first three experiments because the laboratory had not yet obtained the instrument, but silica was

measured for the control experiment in the flow-through reactor and the batch experiments.

Iron. Iron(II) concentrations in samples from the first three Berea experiments were measured using a Hach Iron IR-24 test kit (using Ferrozine colorimetry). Samples underwent a 1:25 dilution. Later testing of the method showed that it did not always deliver repeatable results and hence, the measurements should be taken with caution. In later experiments Iron(II) and Iron(III) were measured with spectrophotometry, Iron(II) via the Ferrozine method (Viollier et al., 2000) and Iron(III) via the thiocyanate method (Baily, 1957).

Berea Brine Recipe (6L) **(tolerance +/-0.0005g)**	
NaCl	4.6090 g
$CaCl_2$	6.0960 g
$MgSO_4$	13.7080 g
$MgCl_2$	9.4960 g
Na_2CO_3	0.3010 g

Table 2.1 Brine recipe used in Berea sandstone flow-through experiments

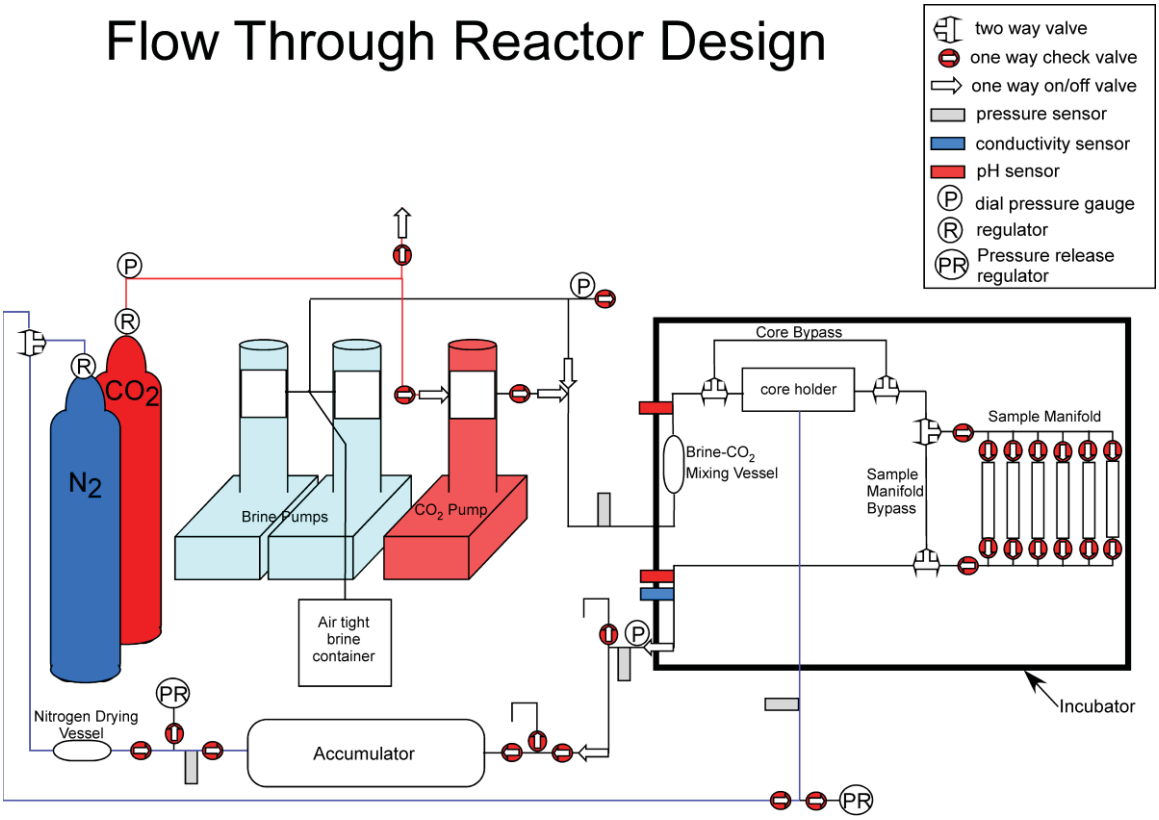

Fig. 2.1 – Flow-through reactor design

Fig. 2.2 – 5 gallon diaphragm accumulator

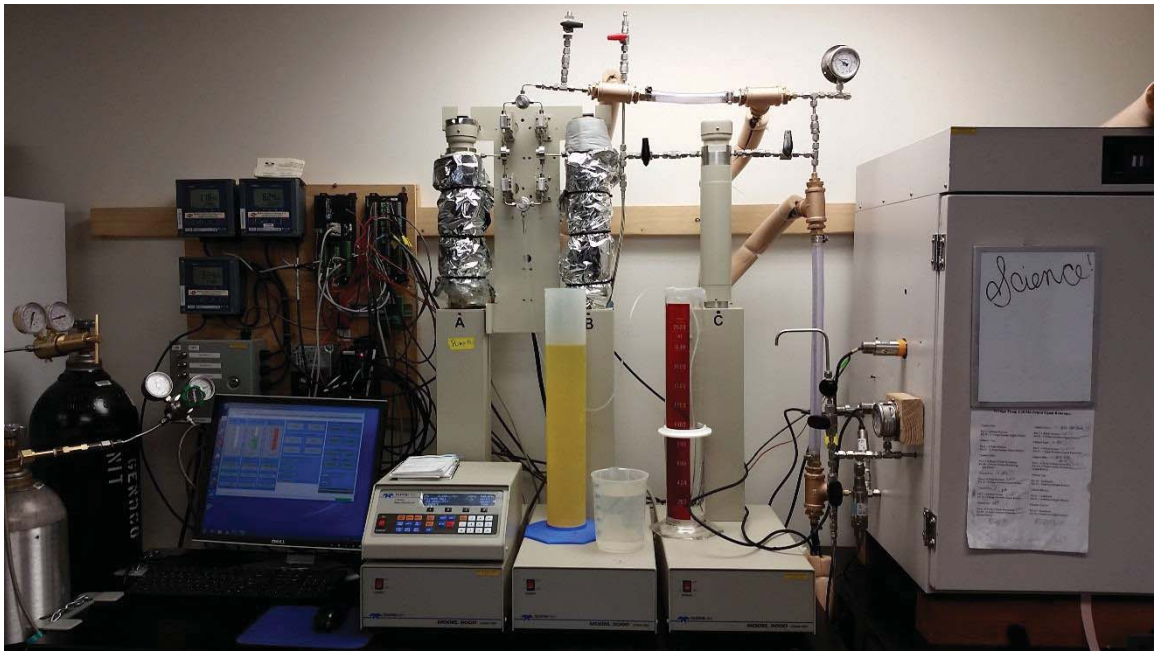

Fig. 2.3 – Dual syringe pumps with continuous flow system. Incubator at right contains core holder, mixing vessel, sampling manifold, and pH and conductivity sensors. Computer and electronics package on left monitor system and record data.

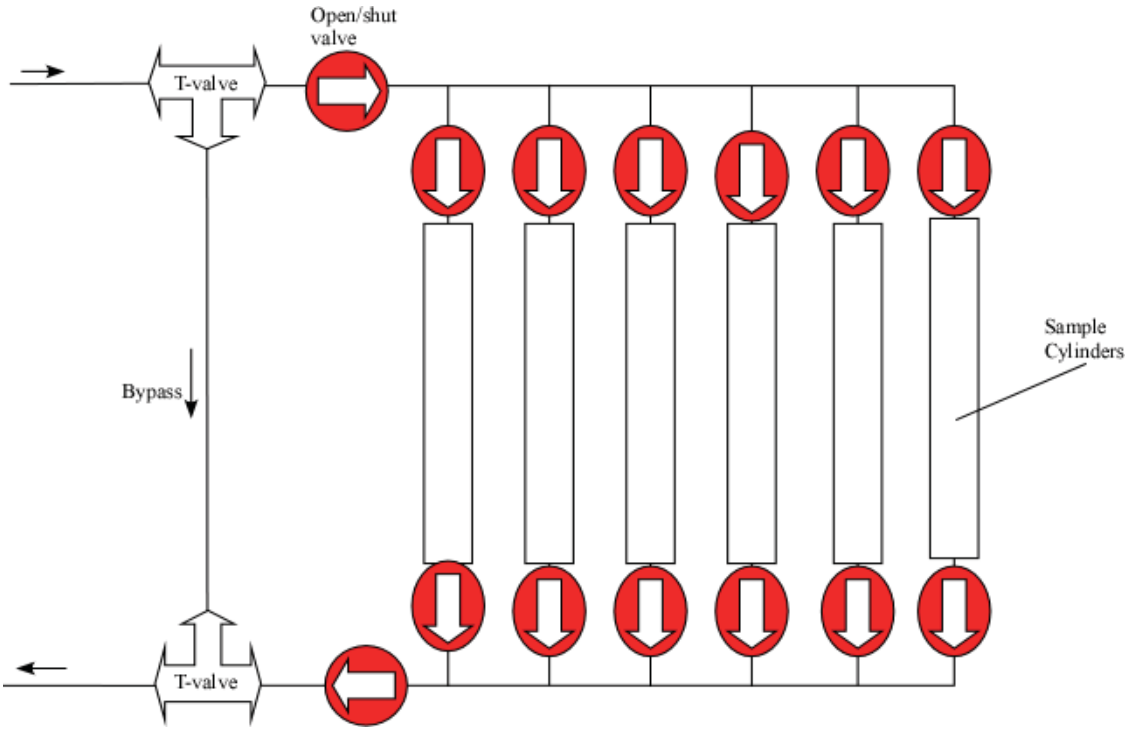

Fig. 2.4 – Photograph and schematic of sampling manifold.

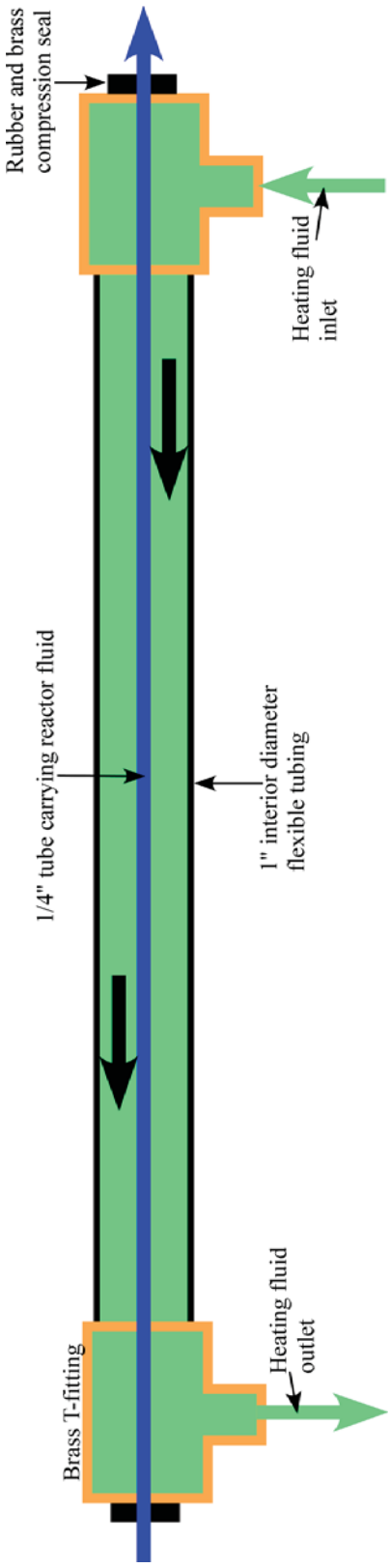

Fig. 2.5 – Heat exchanger design

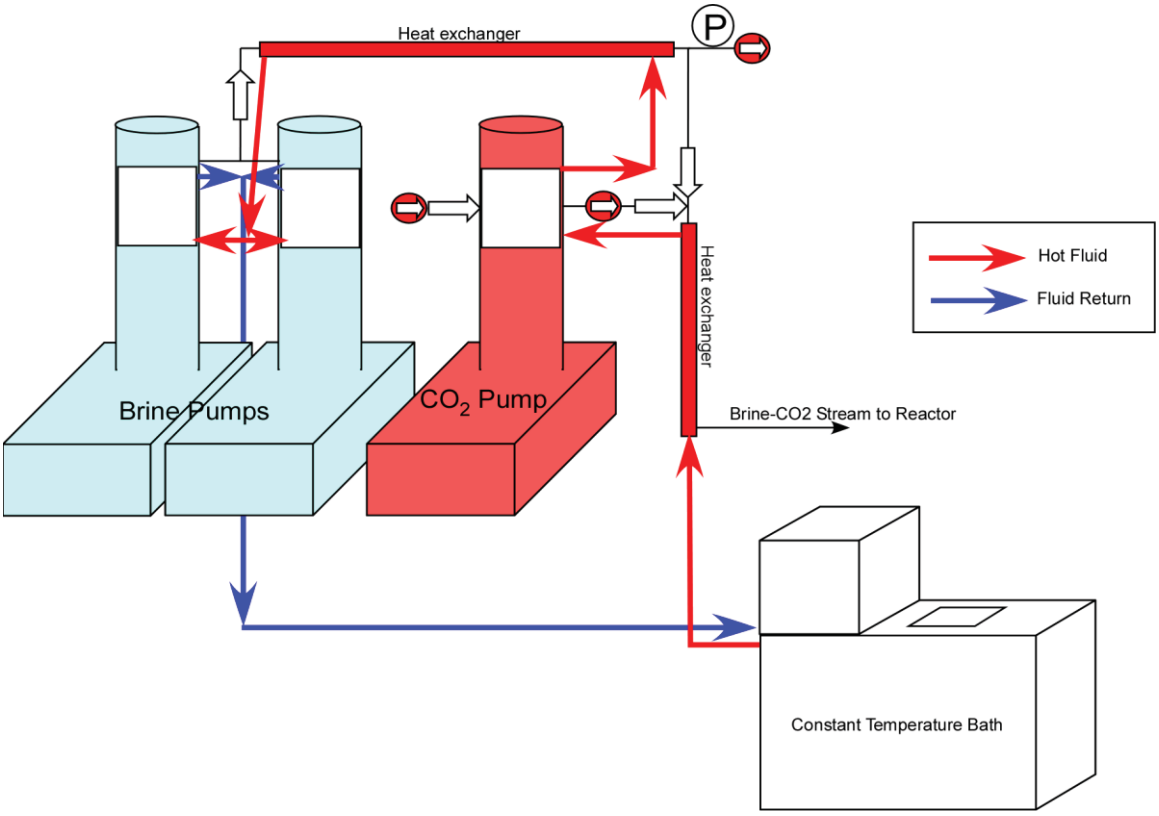

Fig. 2.6 – Fluid pre-heating system.

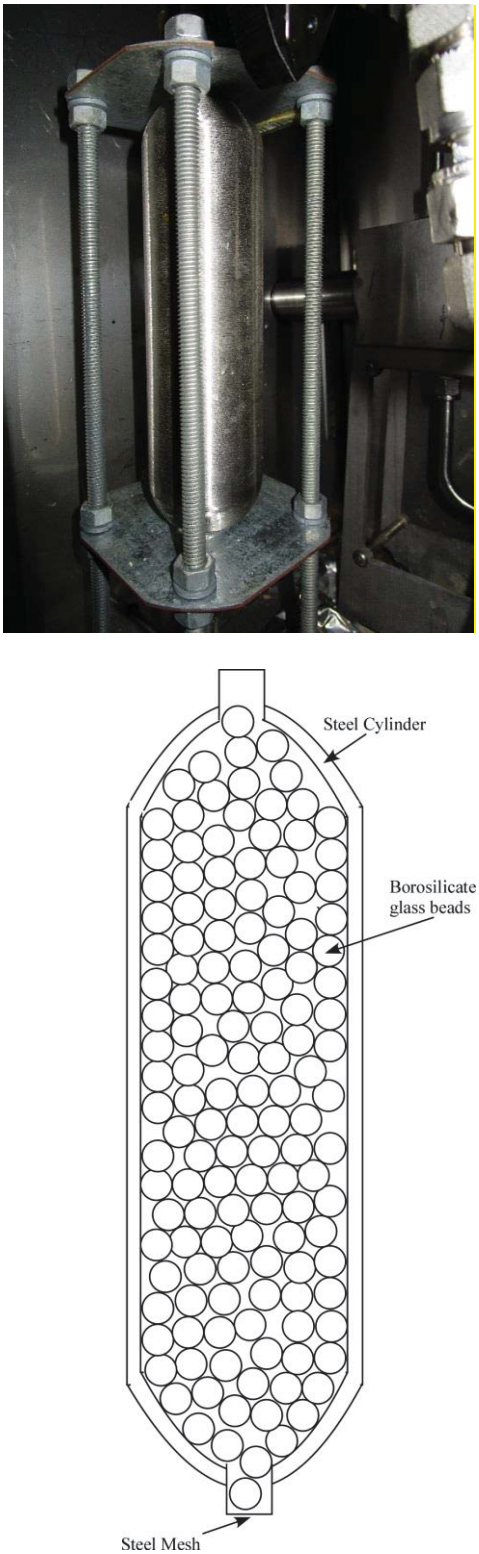

Fig. 2.7 - Brine-CO_2 mixing vessel

CHAPTER 3 – INVESTIGATION OF REACTIVE MINERAL PHASES OF THE BEREA SANDSTONE DURING SIMULATED GEOLOGIC SUPERCRITICAL CO_2 SEQUESTRATION

Introduction

Sandstones with sufficient porosity and permeability to enable fluid storage and movement make excellent subsurface reservoirs. This study identifies the reactive effects of a brine-CO_2 mixture with the Berea sandstone. The Berea is a plagioclase bearing sub-arkosic sandstone. It is prized in the building industry for its appearance, strength, and durability. It has high porosity and permeability, homogeneous composition, and ready availability. It is commonly used as a model sandstone in scientific studies involving reservoir rock (Dawson et al., 2015; Gunde et al., 2010; Halevy, 2013; Peng et al., 2014; Romero et al., 2013; Shi et al., 2011; Vogt et al., 2014).

The experiments described here were designed to study the effects of CO_2 saturated brine injection on the Berea sandstone. Four 72 hour flow-through experiments were conducted: three with cores of Berea, and a control.

Materials

A block of Berea (approximately 12” x 12” x 8”) was obtained from Cleveland Quarries of Vermillion, Ohio for these experiments. Porosity was approximately 17%[1]

[1] Measured by author using mass difference between water saturated and dry core. It was verified by measuring the area of blue epoxy relative to the area of the thin section using the background tool in JMicrovision.

and permeability was ~150mD[2]. It was analyzed by thin section petrography, whole rock XRD, oriented mount XRD, SEM/EDS, and FEM-EDS. Elemental composition was measured by X-Ray fluorescence.

Origin

The Berea sandstone was deposited in a deltaic setting (DeWitt, 1951; Pepper et al., 1954) in the Appalachian Basin during early Mississippian times (DeWitt, 1970; Pepper et al., 1954).

Mineralogy

Thin section petrography of the Berea shows framework grains of quartz, plagioclase feldspar, and muscovite (Fig. 3.1). Quartz (~80%)[3] and plagioclase (11-20% by volume)[3] are the primary detrital grains. Clasts are angular to sub-angular and range in size from 75 - 200µm. Accessory minerals include chert fragments, zircon, and sphene (titanite). Many plagioclase grains and what appear to be detrital biotite grains have been partially dissolved and replaced with clay minerals during diagenesis, creating secondary porosity. Opaque grains are common (3-5% by volume)[4]. They are predominantly iron oxides (Fig. 3.2). It could not be determined whether the iron oxides are magnetite or hematite.

Most quartz grains are cemented with quartz overgrowths. The clay minerals formed by the dissolution of plagioclase act as a second mineral phase of cement.

[2] Value given by Cleveland Quarries.
[3] A point count of 5 images of the Berea taken at 5x was conducted using JMicrovision.
[4] This was determined using the background calculation tool in JMicrovision to identify opaque grains.

Dolomite/ankerite is an important cement component that is prevalent in thin section. Whole rock XRD analysis identified dolomite as composing 3% of the Berea by mass (patterns from two samples shown in Fig. 3.3a &b). FEM elemental mapping showed the carbonate grains as having varying ratios of calcium, magnesium, and iron (Fig. 3.4).

Phyllosilicate Cement

Analysis of the phyllosilicate fraction of the Berea sandstone by XRD and SEM-EDS indicates that kaolinite and muscovite are the main minerals present (Fig. 3.5). Muscovite occurs both as detrital grains and as cement. Kaolinite occurs as cement and is often (but not always) in close proximity to the relict plagioclase grains from which it formed. Samples were prepared as oriented mounts using the Millipore filter transfer method (Moore and Reynolds, 1997). Four oriented mounts were prepared for each sample (per USGS Open-File Report 01-041 procedure). Analysis was conducted using a SCINTAG X1 Diffraction System in Montana State University's Imaging and Chemical Analysis Laboratory (ICAL). Oriented mounts were scanned from 3.00° – 17.00° at 1°/minute. The peak at 7Å is kaolinite and the 10Å peak is muscovite (Fig. 3.5). The lack of shift in peak positions when glycolated or heated indicates that the phyllosilicates are non-expandable. The 7Å peak disappears when heated to 550ºC, which is diagnostic of kaolinite. In XRD, peak intensity is proportional to a minerals abundance, though the method is only semi-quantitative. The ratio of kaolinite to muscovite indicates that kaolinite is dominant.

Analysis of a fragment of the Berea sandstone using a scanning electron microscope (SEM) shows the framework grains cemented together by microscopic

phyllosilicate crystals (Fig. 3.6a). Energy Dispersive Spectroscopy (EDS) (3.6b) of the cement shows that the crystals are composed of silicon, potassium, and aluminum, which is consistent with the mixture of muscovite and kaolinite indicated by XRD. Some of the muscovite crystals are still visible as individual crystals, but are smaller (~10-20μm) than the detrital muscovite grains (100-200μm). These crystals occur in clusters. Their boundaries with other muscovite grains assume euhedral forms, but their boundaries with the larger detrital grains truncate them, indicating that the detrital grains were there when the muscovite crystals grew. These properties indicate that these muscovite grains are authogenic (Fig. 3.7).

Elemental Composition

The whole rock chemical composition of samples of the Berea sandstone was measured using a Thermo Scientific Niton XL3t GOLDD portable X-Ray Fluorescence spectrometer (XRF). The instrument is capable of quantifying elements of atomic mass 14 (magnesium) and heavier. Notably, sodium (an important element in plagioclase) cannot be measured. Six samples (1cm x 2.54cm diameter) were taken at random from the block of Berea sandstone from which the cores were cut. They were powdered using a shatter box and analyzed via XRF. The elemental averages with standard deviations are displayed in Table 3.1.

Hypotheses

Several minerals in the Berea are hypothesized to be reactive to $scCO_2$ saturated brine. Reaction of these minerals should provide predictable chemical and mineralogical

signatures such as: 1.) dissolved ions in the brine; 2.) depletion of elements from solid core material (detectable by XRF); 3.) depletion of reactant minerals and increases to product minerals (may be detectable by XRD if changes are large enough to overcome XRD's uncertainty (+/-10%); 4.) textural evidence may be evident in thin section as analyzed by petrographic microscope and SEM.

The following reactions have the potential to occur in the presence of the acidity that is generated by the dissolution of CO_2 via the reaction:

$$H_2O_{(l)} + CO_{2\,(aq)} \leftrightarrow H^+_{(aq)} + HCO_3^-{}_{(aq)} \quad (1)$$

- Muscovite to kaolinite

$$2\,KAl_2(AlSi_3O_{10})(OH)_{2\,(muscovite)} + 3H_2O_{(l)} + 2H^+_{(aq)} \rightarrow 3Al_2Si_2O_5(OH)_{4\,(kaolinite)} + 2K^+_{(aq)} \quad (2)$$

Methods of detection: This reaction could be detected by measuring dissolved K^+, depletion of K from solid phase, or an increase in XRD peak size of kaolinite and decrease in peak size of muscovite.

- Plagioclase feldspar (as albite) to kaolinite

$$NaAlSi_3O_{8\,(albite)} + 0.5\,H_2O_{(l)} + H^+_{(aq)} \rightarrow Na^+_{(aq)} + 0.5\,Al_2Si_2O_5(OH)_{4\,(kaolinite)} + 2\,SiO_{2(aq)} \quad (3)$$

Methods of detection: This reaction could be detected by measuring dissolved Na^+ and silica, measuring an increase in XRD peak size of kaolinite and decrease in peak size of plagioclase, or by textural evidence in thin section.

- Dissolution of dolomite/ankerite

$$Ca(Mg,Fe)(CO_3)_{2\ (ankerite)} + H^+_{(aq)} \rightarrow Ca^{2+}_{(aq)} + (Fe^{2+}\ Mg^{2+})_{(aq)} + HCO_3^-{}_{(aq)} \quad (4)$$

Methods of detection: This reaction could be detected by measuring increases in levels of dissolved Ca^{2+}, Mg^{2+}, and Fe^{2+} or by measuring the depletion of Ca/Mg/Fe from the solid phase. Textural evidence may also be visible in thin section.

- Magnetite to hematite or goethite

$$Fe(II)Fe(III)_2O_{4\ (magnetite)} + H_2CO_3^0{}_{(aq)} \rightarrow FeHCO_3^-{}_{(aq)} + Fe_2O_{3\ (hematite)} + OH^-_{(aq)} \quad (5)$$

$$Fe(II)Fe(III)_2O_{4\ (magnetite)} + 2H_2CO_3^0{}_{(aq)} \rightarrow FeHCO_3^+{}_{(aq)} + HCO_3^-{}_{(aq)} + 2FeO(OH)_{(goethite)} \quad (6)$$

Methods of detection: These reactions may be detected by measuring increases in levels of dissolved Fe^{2+}/Fe^{3+} or depletion of Fe from solid phase. Textural evidence may be visible under SEM. Macroscopic iron staining may also be visible.

- Resistant Minerals

Several of the mineral phases present in the Berea sandstone are hypothesized to be resistant to reaction with $scCO_2$ saturated brine. These include quartz, and zircon.

Experimental Procedure

Four 72 hour experiments at 94°C and ~10MPa were performed in the flow-through reactor using the procedure described in Appendix A. Three used 100mm cores

of Berea (Fig. 3.8) and the fourth was a control with no core. The Berea brine recipe (Table 2.1) was used. The amount of oxygen present in the brine was varied in the three experiments to see if the oxidation of iron bearing minerals observed by Vogt et al. (2014) was a result of atmospheric contamination or dissolved oxygen in the brine. The first experiment (BER 8-29-13) was conducted with brine exposed to atmospheric gasses (the brine solution in a flask open to the air). In the second experiment (BER 10-5-13), the brine was deoxygenated as described in Appendix B. In the third experiment (BER 11-5-13), brine prepared as described in Appendix B and then injected (via a septum in the gas bag) with a small amount of sodium sulfite, to act as an oxygen scavenger. The brine used in the control experiment was prepared according to Appendix B. An unintended consequence of the use of sodium sulfite as an oxygen scavenger is that it contributed to the corrosion of the stainless steel fittings and tubing. This caused some valves on the reactor to seize. Future experiments should not use sodium sulfite.

After the experiment the cores were cut into pieces (Fig. 3.9). The four end pieces (A, B, D, E) were analyzed by XRF and XRD[5]. The center section was cut into thin sections for microscopic analysis. Water and gas samples were analyzed as described in Chapter 2.

[5] Only the tab closest to where flow first entered the core was analyzed by XRD due to the time consuming nature and high uncertainties of the method. This tab experienced the greatest exposure to scCO2-brine mixture and therefore had the highest probability of chemical alteration.

Results

Conductivity and pH were continuously monitored throughout the experiments. Discrete water samples were taken every 12 hours (Table J.2 - J.4).

pH

The pH decreased from 6.5 - 5.5 before CO_2 injection to 3.0 - 4.5 after injection (+12 hours) (Figs 3.10 – 3.13). Problems with the injection of CO_2 began to develop during the second experiment due to the buildup of corrosion at the brine-CO_2 junction. By the time of the control experiment all of the stainless steel plumbing in the reactor had been replaced with monel (a copper nickel alloy).

Conductivity

During the three Berea experiments, the measurement of conductivity was not found to provide quantifiable results and was of questionable accuracy. Conductivity measurements were not obtained during the control experiment due to a malfunction of the sensor. Therefore, this data has not been included.

Ionic Composition

The concentrations of most species remained constant during the course of the experiments (Fig. 3.10- 3.13). Two exceptions were K^+ and Ca^{2+}. Potassium was also measured in the control, indicating that it was likely a contaminant. Experiment 8-29-13 showed an initial calcium spike after the injection of CO_2 (Fig. 3.10) which most likely resulted from the dissolution of carbonate cement. This was not observed in the latter two experiments.

During the three Berea experiments dissolved iron was measured using a Hach Iron IR-24 test kit. Iron concentrations for the control experiment were determined by spectrophotometry (see Chapter 2). The dissolved iron measured in the three experiments was probably partially derived from the cores, but this signal was overwhelmed by iron dissolved from the reactor tubing. Corrosion of the tubing was so intense that flakes of rust were observed in water samples prior to filtering. Due to this contamination issue the data was not included here. The problem was largely solved when the steel tubing was replaced with monel. The tubing had been replaced at the time of the control experiment.

Changes to Elemental Composition

After each core was removed from the reactor, two 1cm tabs were cut from each end of the cores, powdered, and their elemental composition analyzed. Variations in elemental composition greater than the standard deviation of the unreacted average are interpreted to indicate chemical changes that resulted from the experiment (Table 3.2). Calcium and iron were depleted following the experiments relative to the initial values. This supports the observations in the aqueous phase that showed enrichment of calcium and iron in some water samples. Notably, potassium was not measurably depleted in the reacted samples.

Changes to Mineralogy

Changes in the ratio of muscovite and kaolinite peaks was not observed in any of the three experiments (Fig. 3.5). However, the accuracy of XRD for quantitative

purposes is, at best, +/-10% (Moore and Reynolds, 1997). Therefore, substantial changes to the mineralogy would have to occur in order to be measurable by XRD.

Gas Concentrations

Methane, carbon monoxide, and hydrogen were measured (Tables 3.3a-c) in the headspace of the water samples. Low concentrations of methane and carbon monoxide were present in the CO_2 tank. These may have been subsequently concentrated in the headspace of the sampling cylinders, as they are less soluble than carbon dioxide in water.

The hydrogen was most likely generated by the anaerobic oxidation of the iron in the reactor under acidic conditions.

$$Fe^0_{(s)} \rightarrow Fe^{2+}_{(aq)} + 2e^-$$

$$2H^+_{(aq)} + 2e^- \rightarrow H_2\,(g)$$

$$Fe^0(s) + 2H^+_{(aq)} \rightarrow Fe^{2+} + H_2$$

Hydrogen and methane were also measured in the control experiment, indicating that these gasses are a likely product of the reactor and not the reactions involving the rock.

Discussion

The discussion will focus on how the experimental data supported or refuted the hypotheses that muscovite, ankerite, and iron oxides would be reactive phases during these experiments.

Muscovite

At first, the presence of potassium in the water samples of the three Berea experiments seemed to indicate the dissolution of muscovite. However, the presence of dissolved potassium in the control experiment called this into question. The lack of measured potassium depletion in the post-reaction core samples supports the conclusion that if any muscovite was dissolved, the amount was small. XRD data also showed no change, although as noted, XRD has a large uncertainty when used quantitatively.

The phase diagram for the potassium-aluminum-silicate system (Fig. 3.14) shows equilibrium mineral phases as a function of dissolved silica, potassium, and pH. Future experiments should measure dissolved silica and attempt to obtain potassium measurements that are free from contamination. This will better constrain the effects of CO_2 injection on muscovite.

Dolomite/Ankerite

The spike in dissolved calcium at +24 hours in experiment 8-29-13 is most likely a result of carbonate dissolution. Although such calcium peaks were not observed in the other two experiments, the XRF data shows a depletion of calcium and to a lesser extent magnesium from the solid phase, indicating that carbonate minerals were being dissolved. It is also likely that a portion of the iron that was dissolved from the cores came from the carbonate cement.

Iron Oxides

"Leisegang" hematite banding and iron depletion was observed in the core in the oxic experiment (BER 8-29-13) (Fig. 3.10 and 3.15, Table 3.3). Iron depletion (as

measured by XRF) was noteworthy even in the deoxygenated experiments indicating that dissolution was still occurring, under deoxygenated conditions (Table 3.3).

A pH-Eh diagram of the iron-sulfur-CO_2 system (Fig. 3.16) can be used to aid data interpretation. The ratio of iron(II) to iron(III) measured in the control experiment was used to calculate the Eh value in Geochemist's Workbench. It was around 0.5V. At this Eh value and the pH values present in this experiment (~3.5-4.5) the system is in equilibrium with $FeHCO_3^+$ at lower pH values and hematite at higher pH values and so ferrous iron bearing minerals should either be bound as the iron bicarbonate complex or oxidize to hematite.

Conclusions

The injection of scCO_2-brine solution dissolved carbonate cement and reacted with iron oxides in the Berea sandstone. No measureable change was detected in the phyllosilicate minerals. The flow-through reactor is effective at examining overall changes to a rock during scCO_2-brine injection, but is not the best tool for examining the reactions of individual minerals, especially less abundant phases. Batch experiments using pure mineral phases will help further elucidate the effects of CO_2-brine interaction with individual minerals in Chapters 4 and 5.

Elemental Composition of Samples of Berea Sandstone (% mass) based on six random samples																		
Sample	Mg	+/-	Ca	+/-	Si	+/-	Al	+/-	K	+/-	Fe	+/-	S	+/-	Ti	+/-	Zr	+/-
1	0.594	0.317	1.038	0.033	42.865	0.211	2.443	0.116	0.978	0.022	1.187	0.018	0.024	0.007	0.176	0.005	0.019	0.001
2	0.489	0.294	0.902	0.031	42.754	0.206	2.251	0.108	0.942	0.021	1.007	0.016	0.056	0.007	0.155	0.005	0.015	0.001
3	0.802	0.312	1.139	0.036	42.249	0.203	2.299	0.108	0.961	0.022	1.229	0.018	0.046	0.007	0.181	0.005	0.018	0.001
4	1.109	0.329	1.391	0.038	42.314	0.203	2.402	0.11	0.948	0.021	1.299	0.019	0.029	0.006	0.166	0.005	0.016	0.001
5	< LOD	0.6	0.719	0.027	42.516	0.198	2.305	0.105	0.941	0.02	0.948	0.015	0.015	0.006	0.154	0.005	0.014	0.001
6	0.526	0.284	1.153	0.035	40.971	0.199	2.554	0.107	1.004	0.022	1.206	0.018	0.034	0.006	0.183	0.005	0.017	0.001
Avg. % Composition	0.704	0.257	1.057	0.231	42.278	0.684	2.376	0.113	0.962	0.025	1.146	0.137	0.034	0.015	0.169	0.013	0.017	0.002

Table 3.1 – Average elemental composition of the Berea sandstone block used in flow-through experiments. Measurements were taken with XRF. The +/- values on the individual measurements are the uncertainties computed by the XRF software. The +/- values of the average values are the standard deviations of the six individual measurements. This data demonstrates that the Berea is a relatively homogeneous rock.

Comparison of Pre- and Post- Reaction Average Elemental Compositions of Berea Sandstone																		
	Mg	+/-	Ca	+/-	Si	+/-	Al	+/-	K	+/-	Fe	+/-	S	+/-	Ti	+/-	Zr	+/-
Avg. 8-29 (n=5)	0.554	0.087	0.579	0.384	42.917	0.965	2.354	0.129	0.937	0.023	0.881	0.245	0.034	0.001	0.158	0.015	0.015	0.002
Avg. 10-5 (n=5)	0.528	0.135	0.253	0.180	44.154	1.022	2.459	0.298	0.902	0.115	0.749	0.102	0.025	0.012	0.165	0.029	0.019	0.009
Avg. 11-5 (n=7)	0.731	0.185	0.540	0.264	42.984	0.941	2.365	0.179	0.954	0.058	0.869	0.161	0.022	0.009	0.161	0.011	0.015	0.001
Avg. % Composition (n=6)	0.704	0.257	1.057	0.231	42.278	0.684	2.376	0.113	0.962	0.025	1.146	0.137	0.034	0.015	0.169	0.013	0.017	0.002

Table 3.4 – Comparison of average composition of pre- and post-reaction Berea sandstone as measured by XRF. Note the measurable depletion of calcium and iron from the samples. The +/- values are the standard deviations of the individual measurements for each core.

Table 3.3a - Gas Concentrations (ppm) - Experiment BER 10-5-14			
Sample Number	**CO**	**CH_4**	**H_2**
1	27.3		320.5
2	-	-	-
3	24.1	10.3	430.7
4	-	-	-
5	24.1	6.5	578.5
6	-	-	-
CO_2 tank	pbq	2.6	0
pbq – analyte present below quantification limit			

Table 3.3b - Gas Concentrations (ppm) - Experiment BER 11-5-14			
Sample Number	**CO**	**CH_4**	**H_2**
1	2.5	0.0	56.3
2	37.9	1.1	104.9
3	3.1	0.0	32.5
4	3.1	0.0	102.8
5	2.5	0.0	27.7
6	pbq	1.1	0.0
CO_2 tank	pbq	2.6	0.0
pbq – analyte present below quantification limit			

Table 3.3c - Gas Concentrations (ppm) – Control Experiment			
Sample Number	**CO**	**CH_4**	**H_2**
1	-	-	-
2	-	-	-
3	-	5.4	pbq
4	-	5.3	pbq
5	-	5.8	pbq
6	-	5.2	991
CO_2 tank	-	2.6	0.0
pbq – analyte below quantification limit			

Tables 3.3a-c – Concentrations of gasses measured in the headspaces of sample cylinders. Hydrogen concentrations declined following the replacement of the tubing with monel and the coating of the cylinders in nickel. CO was measured in the 10-05-13 and 11-05-13 experiments, but could not be quantified in the control because the GC had been reconfigured. Quantification limits are around 1ppm.

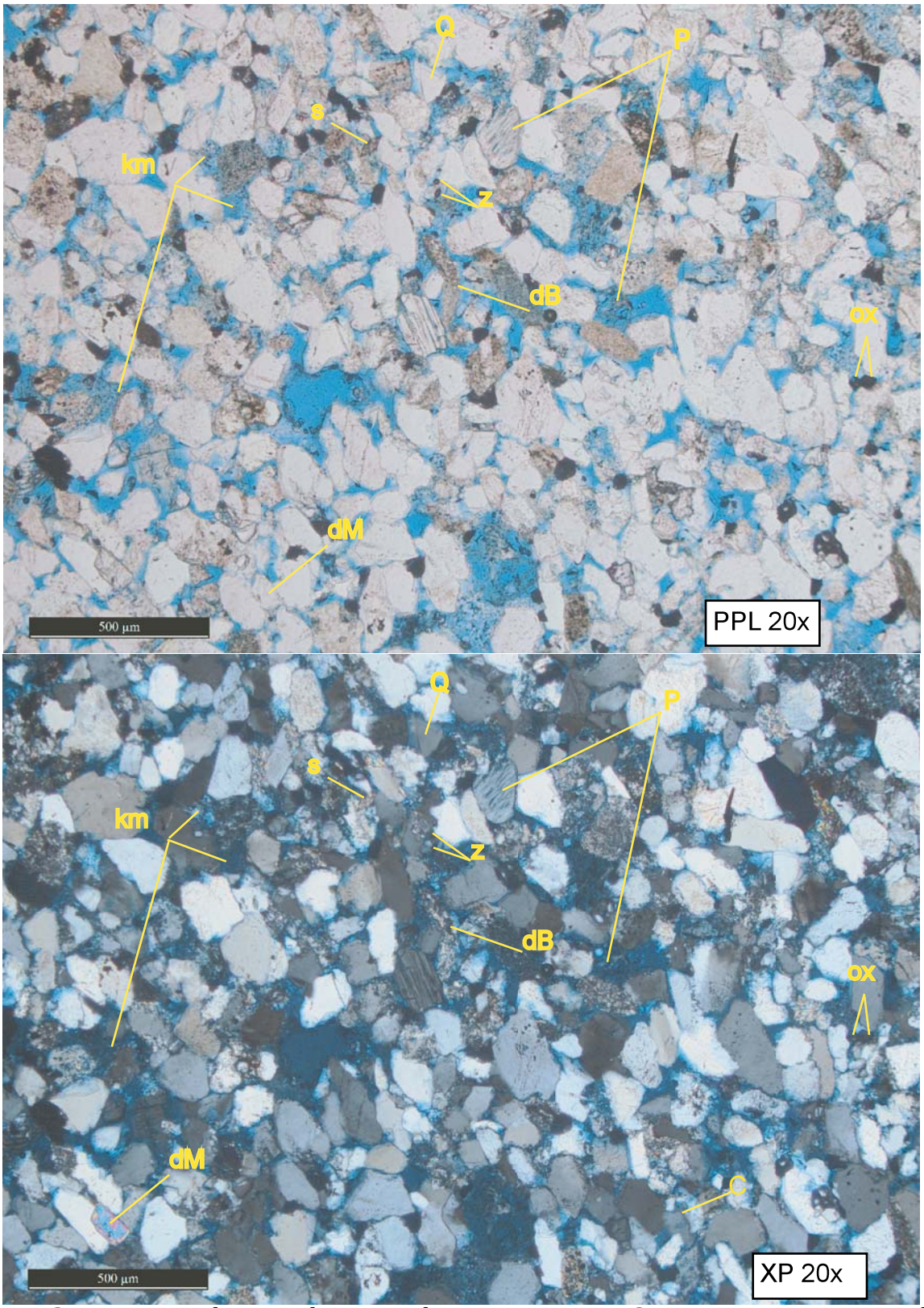

Fig. 3.1 - Berea sandstone. Blue epoxy denotes pore space. Q = quartz. Note overgrowth on grain. P = plagioclase. Note dissolution and replacement by clay minerals. dM = detrital muscovite. dB = detrital biotite with replacement by clay minerals. s = sphene. z = zircon. ox = iron oxide. km = phyllosilicate cement. C=carbonate cement.

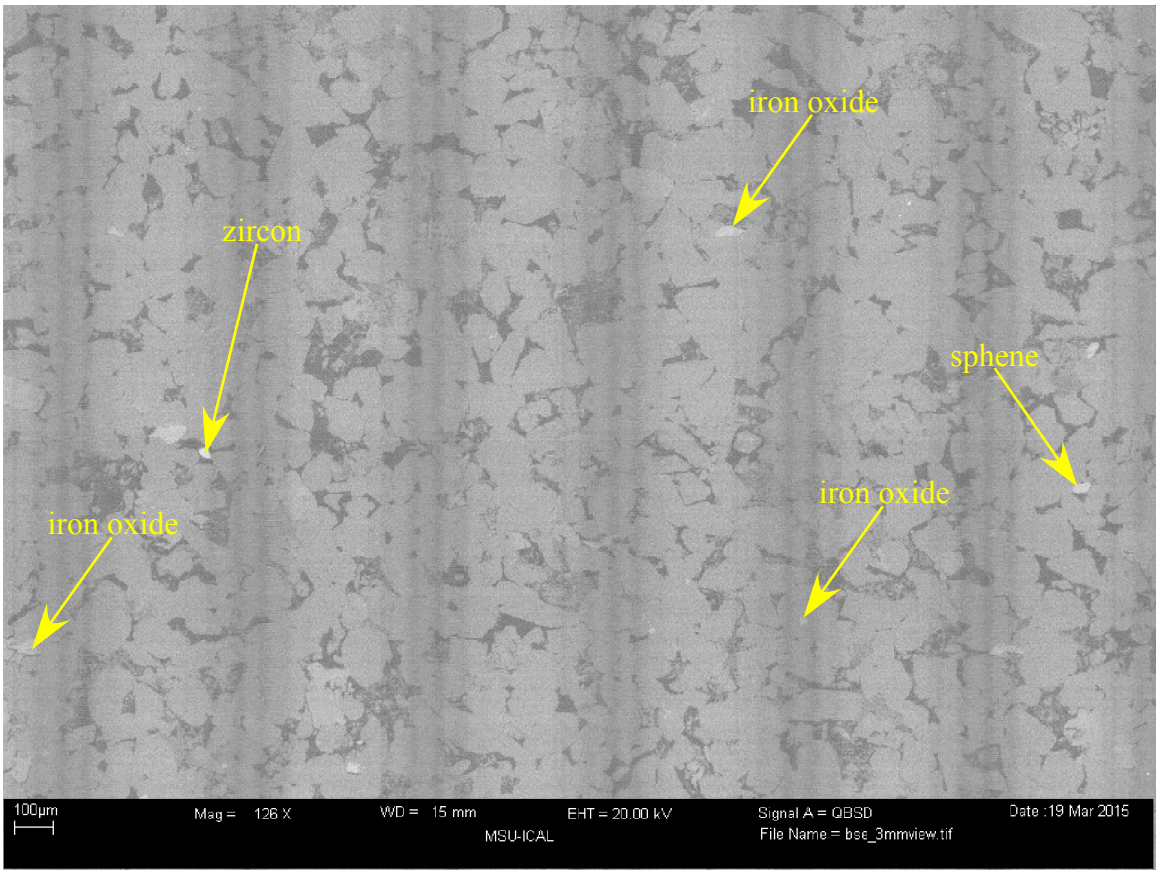

Fig. 3.2 - Backscattered image of Berea sandstone showing iron oxides and other heavy minerals.

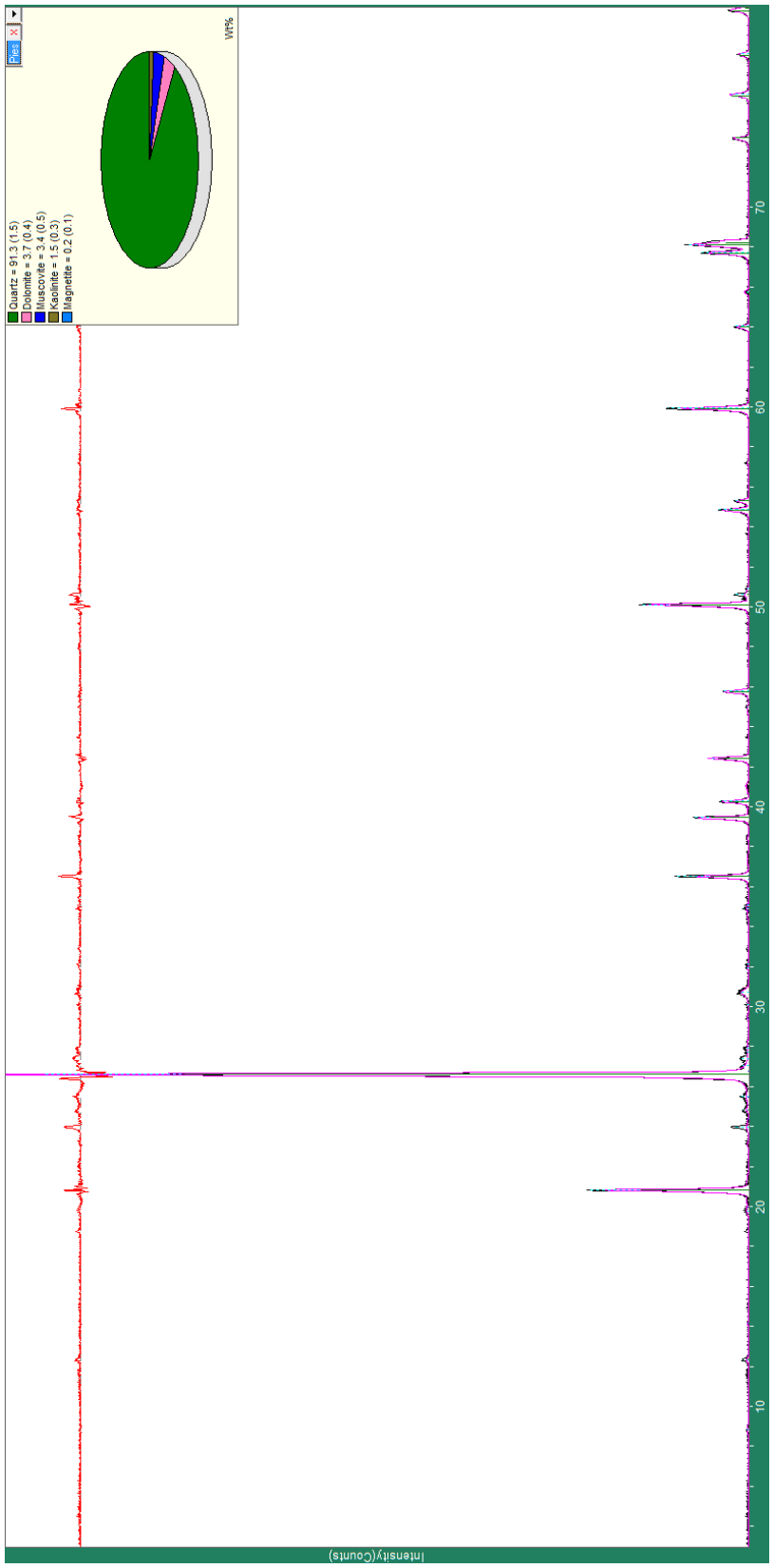

Fig. 3.3(a) – Whole rock XRD profile of Berea sandstone. Identified phases include quartz, dolomite, muscovite, kaolinite and magnetite. Magnetite might not be an accurate identification.

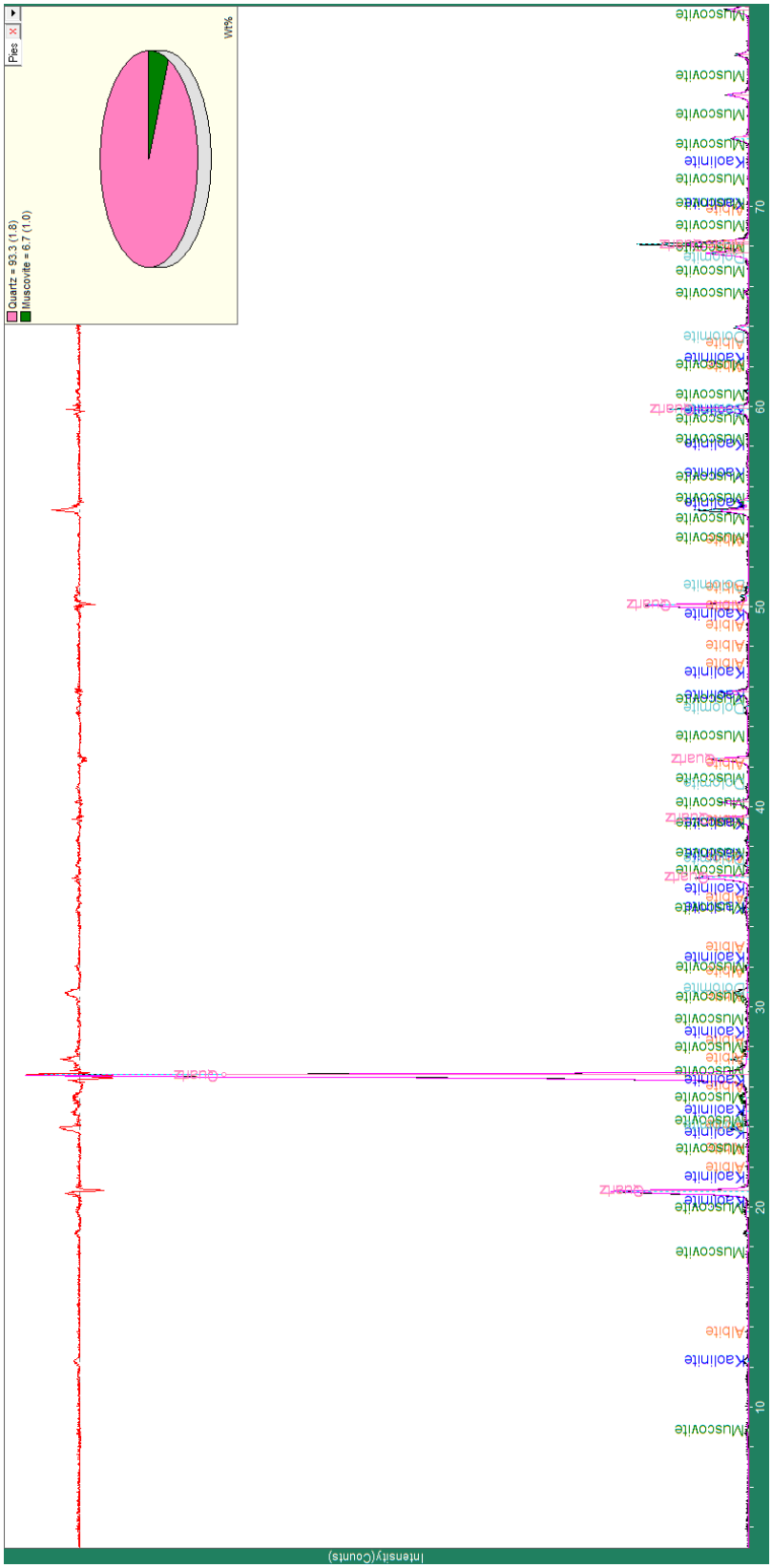

Fig. 3.3(b) – Whole rock XRD profile of Berea sandstone. Identified phases include quartz, albite, muscovite, and kaolinite.

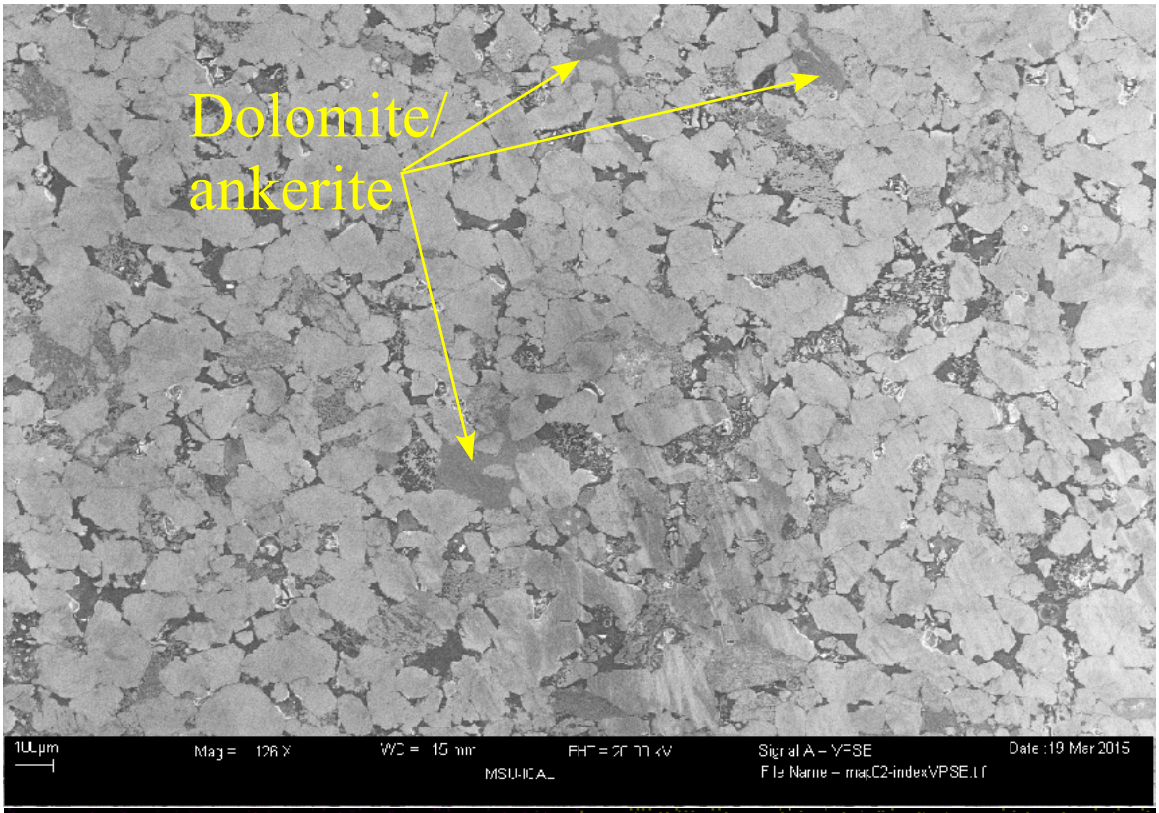

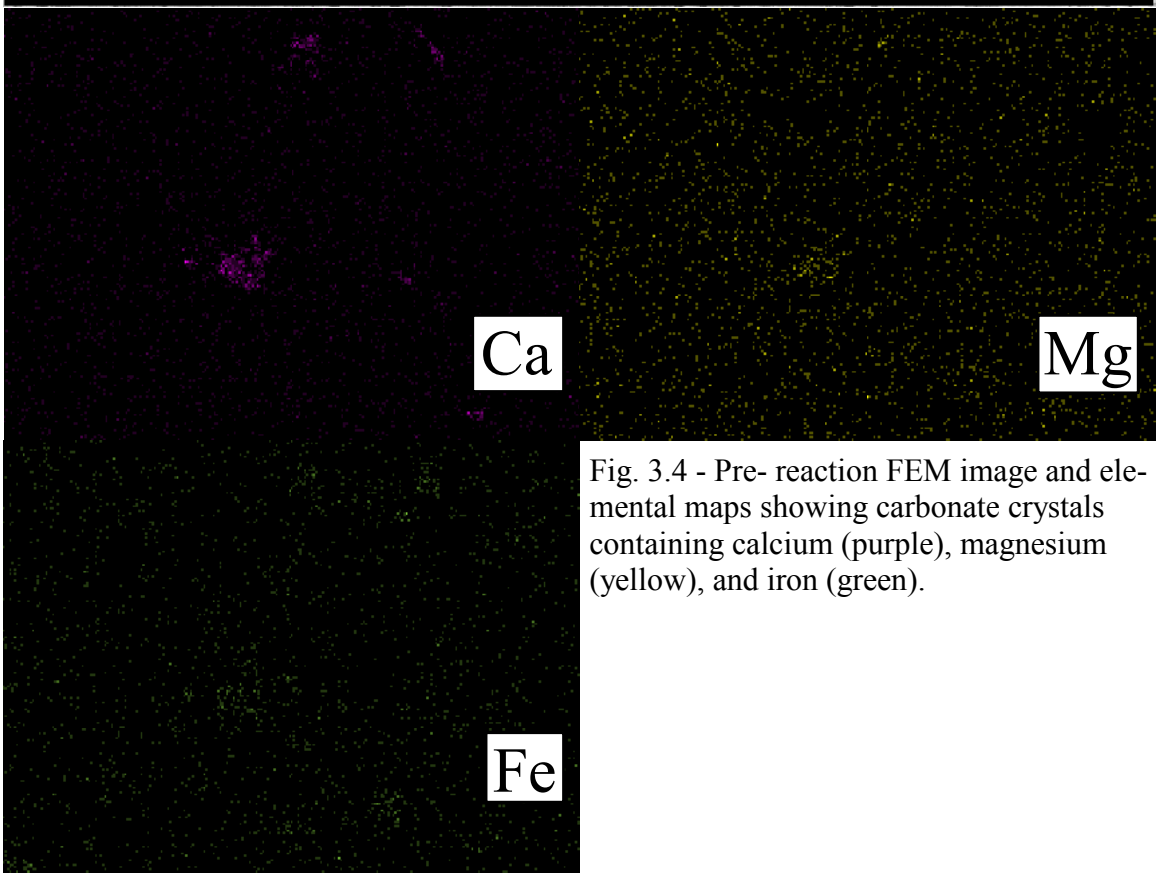

Fig. 3.4 - Pre- reaction FEM image and elemental maps showing carbonate crystals containing calcium (purple), magnesium (yellow), and iron (green).

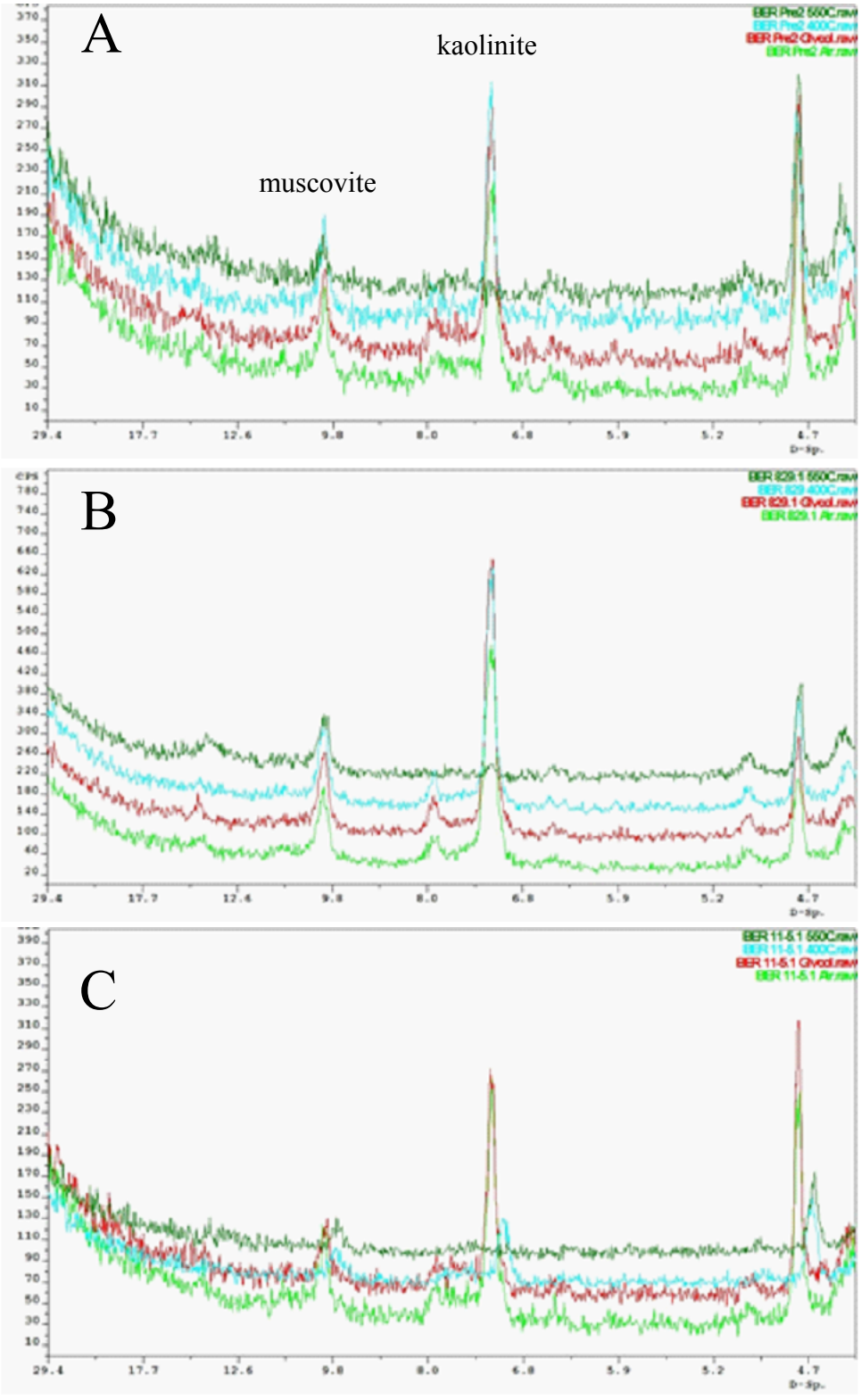

Fig. 3.5 - Diffraction patterns of oriented mounts for analysis of phyllosilicates. A is the pattern of an unreacted sample. B and C are post reaction samples from experiments 8-29 and 11-5 respectively. Note there is no significant difference between the three.

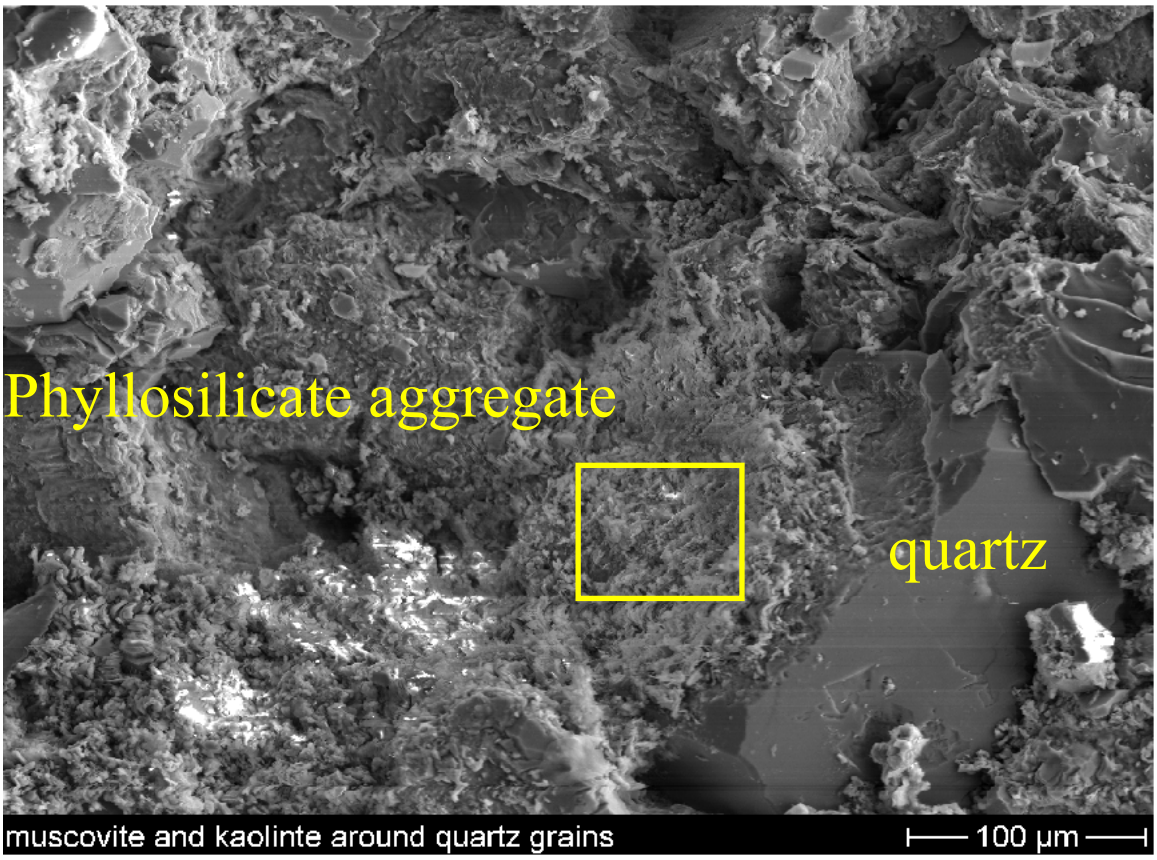

EDS Quantification (in %molar abundance)

elem/line	P/B	B	F	c	c(atom)	confid.	h	
C	K-ser	@Coat?	1.00000	1.00000	2.29	4.95	+- 1.17	n
Ca	K-alpha	@ 0.0	1.01874	1.02194	0.00	0.00	+- 0.01	<
Cr	K-alpha	@ 0.0	1.02369	1.07486	0.00	0.00	+- 0.01	<
O	K-ser	@	1.00000	1.00000	42.40	68.90	+- 6.91	n
Ba	L-ser	@ 0.0	1.02120	1.08393	0.00	0.00	+- 0.01	<
Fe	K-alpha	9.2	1.02585	1.10188	0.63	0.29	+- 0.07	
Ni	K-alpha	0.5	1.02785	1.15496	0.03	0.01	+- 0.05	<
Na	K-ser	@ 9.4	1.00240	1.00655	1.24	1.40	+- 0.56	*
Mg	K-ser	@ 2.0	1.00480	1.01235	0.22	0.24	+- 0.23	<
Al	K-ser	@ 60.1	1.00700	1.01558	6.06	5.84	+- 0.62	*
Si	K-ser	@177.6	1.00903	1.00543	15.76	14.59	+- 1.21	*
P	K-ser	@ 9.5	1.01092	1.00798	0.79	0.67	+- 0.15	
S	K-ser	@ 0.0	1.01268	1.01233	0.00	0.00	+- 0.01	<
Cl	K-ser	@ 0.0	1.01433	1.01937	0.00	0.00	+- 0.00	<
K	K-alpha	@ 65.0	1.01735	1.01629	4.68	3.11	+- 0.25	
standardless					74.11	100.00	[1s]	

Fig. 3.6 - a) SEM secondary electron image (SEI) of the Berea sandstone. Note phyllosilicates encrusting euhedral quartz crystals and guarding pore throats. b) EDS analysis for area in box. Elemental composition suggests muscovite and kaolinite. Sodium and magnesium could indicate small amounts of other clay minerals as well.

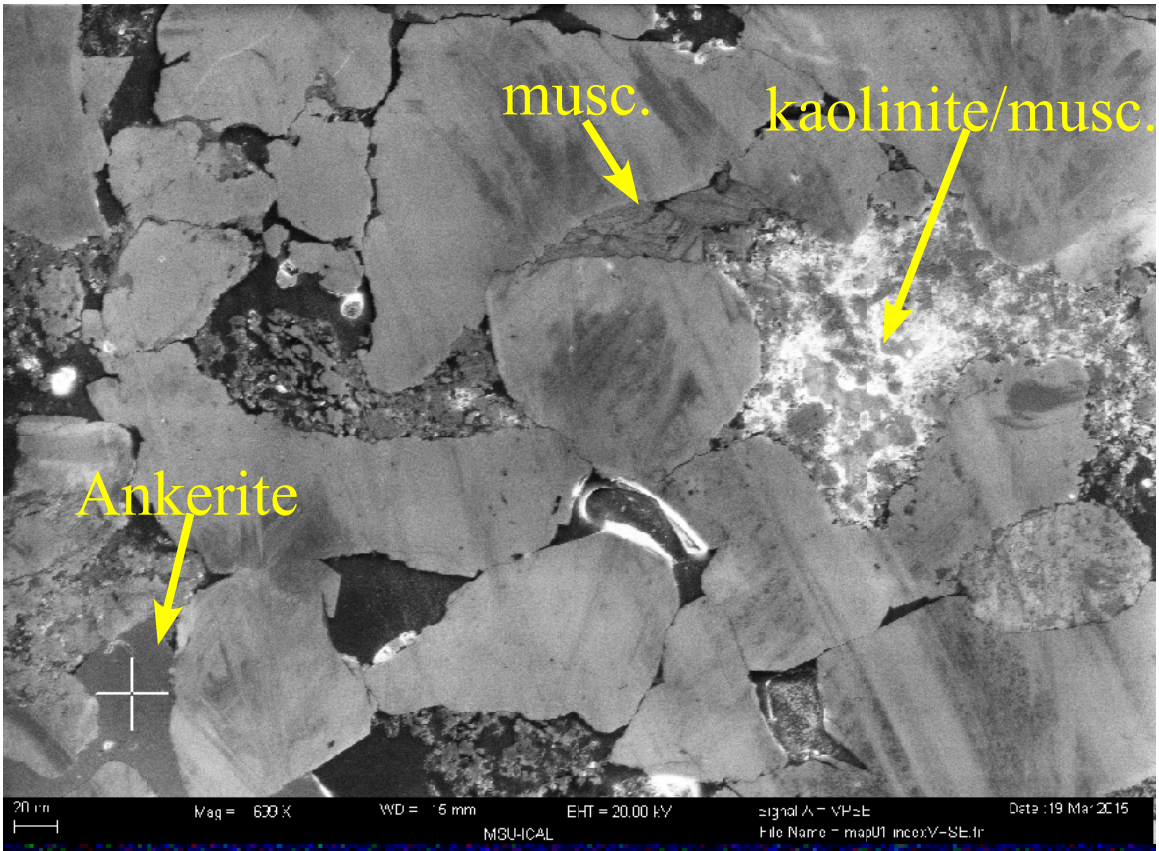

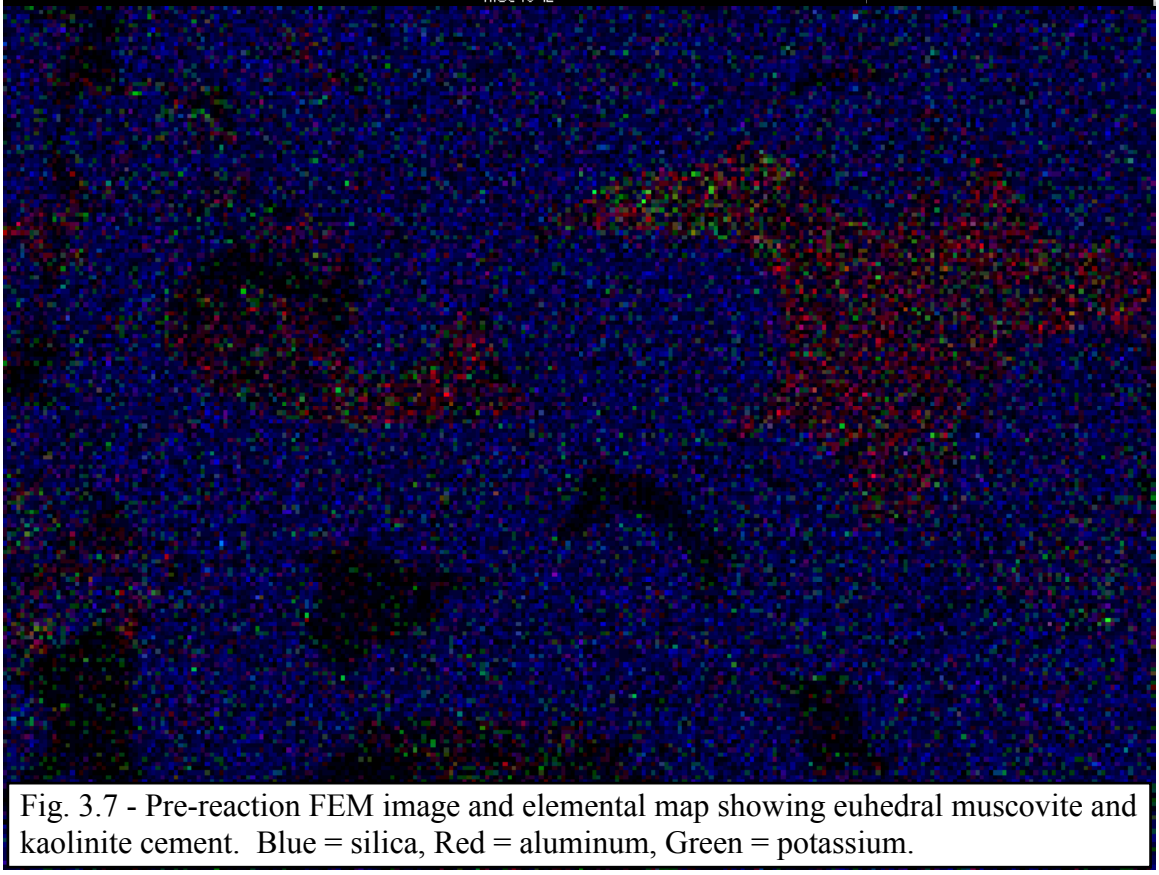

Fig. 3.7 - Pre-reaction FEM image and elemental map showing euhedral muscovite and kaolinite cement. Blue = silica, Red = aluminum, Green = potassium.

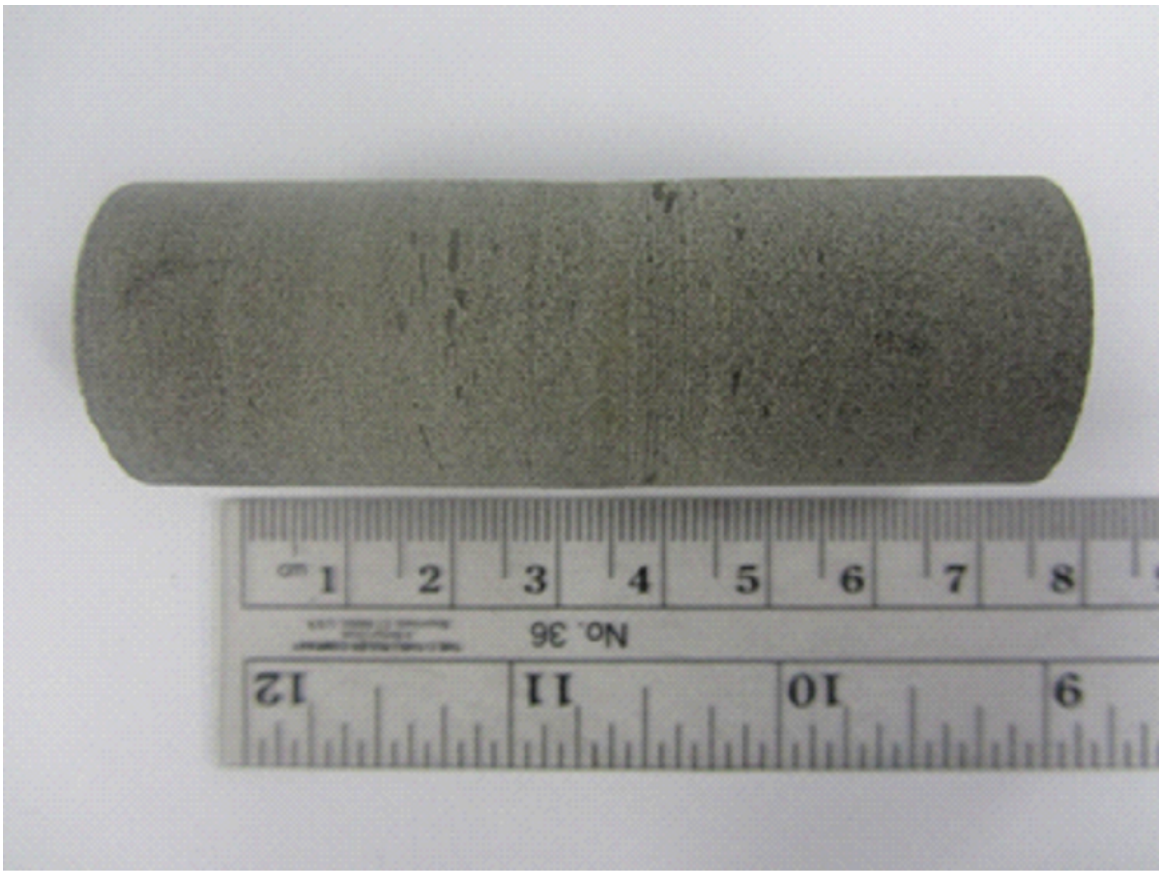

Fig. 3.8 - A typical core used in flow through reactor.

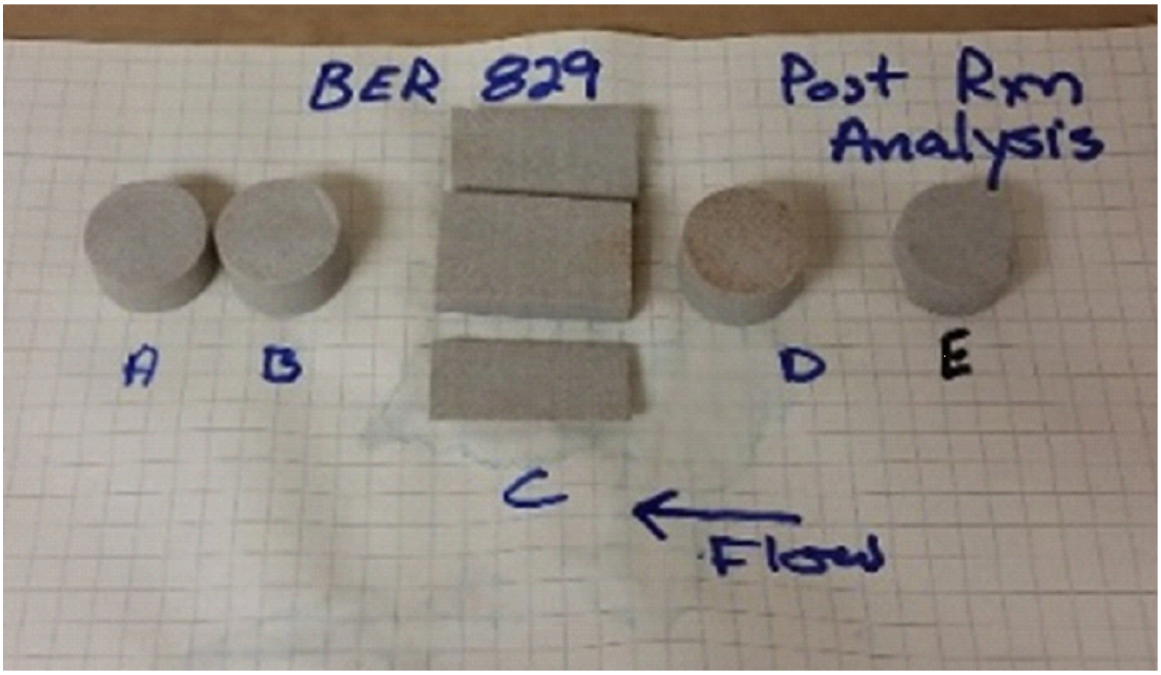

Fig. 3.9 - Core 8-29 cut into pieces following experiment. A, B, C, D, and E were ground for XRF analysis. The rectangular billet was made into a thin section.

Oxygenated Brine

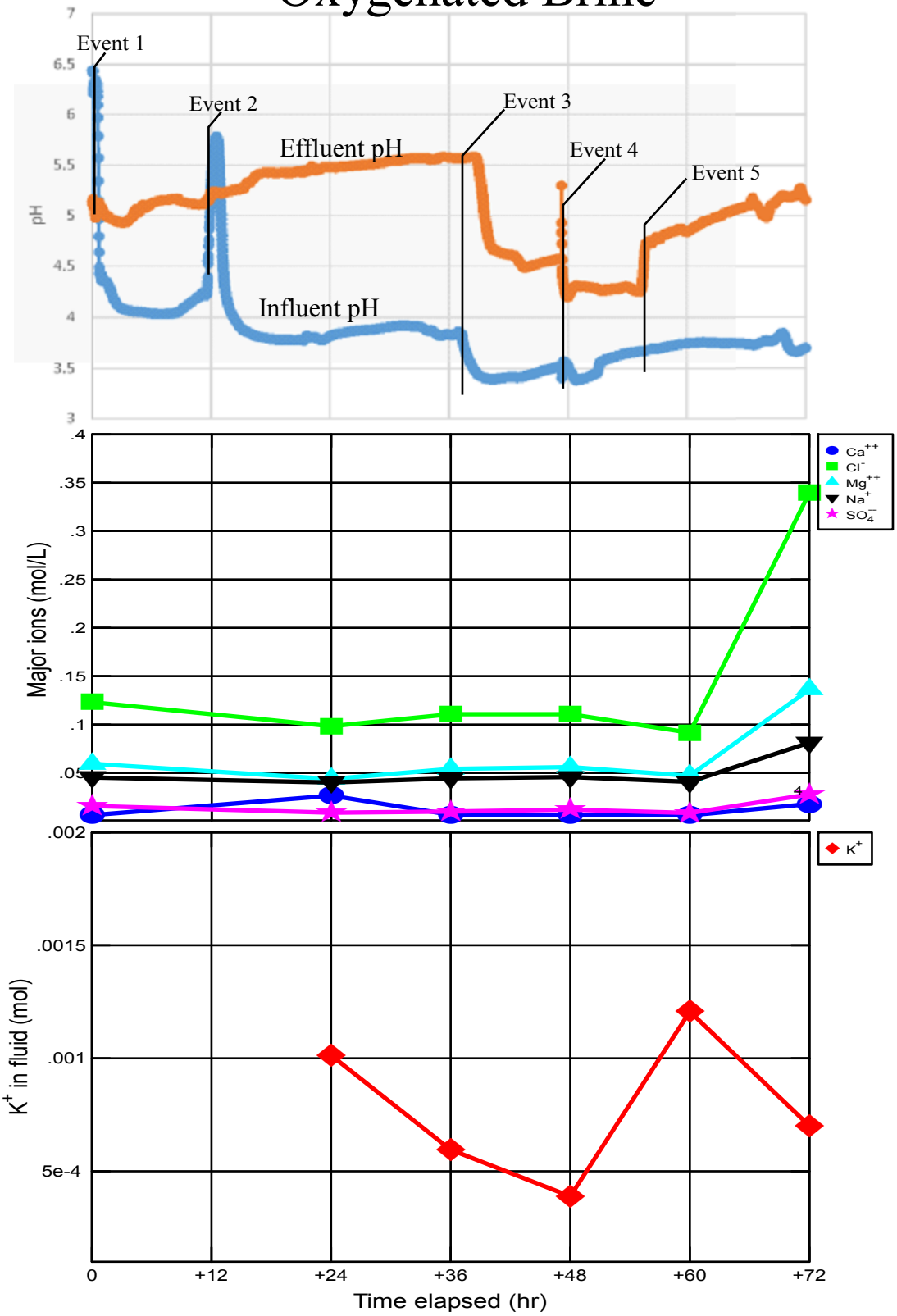

Fig. 3.10a - Water chemistry data for experiment 8-29-13. See log for descriptions of events.

Fig. 3.10b - Description of Events for Experiment 8-29-13

Event 1 – Brine introduced to core

Event 2 – CO_2 reaches sensors and core

Event 3 – CO_2 injection rate increased in order to see if pH would decline

Event 4 – CO_2 injection rate increased again

Event 5 – CO_2 injection ceased

Notes on Water Chemistry

Iron was not measured in this experiment. The water sample at +12 hours was lost due to opening the sample container too quickly.

Deoxygenated Brine

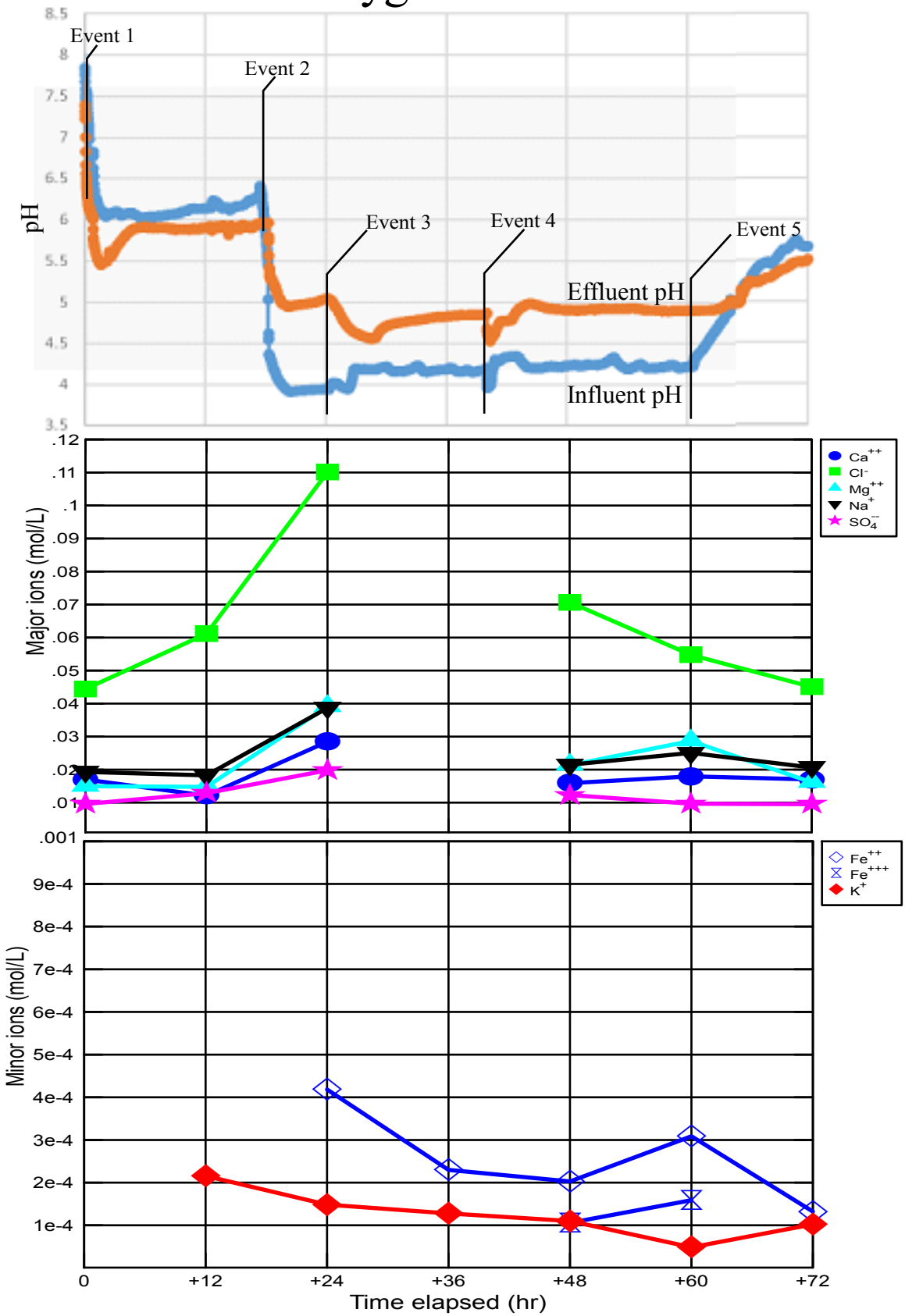

Fig. 3.12a - Experiment 10-5-13 water chemistry. See log for event descriptions.

Fig. 3.11b - Description of Events for Experiment 10-5-13

Event 1 – Brine introduced to core

Event 2 – CO_2 reaches sensors and core

Event 3 – CO_2 injection rate increased

Event 4 – CO_2 injection rate increased and then decreased

Event 5 – CO_2 injection ceased

Notes on Water Chemistry

The iron measurement for +12 hours was lost. Iron(III) samples were contaminated during the reduction process for all samples other than +48 and +60 hours. The water sample at +36 hours was lost due to opening the sample container too quickly.

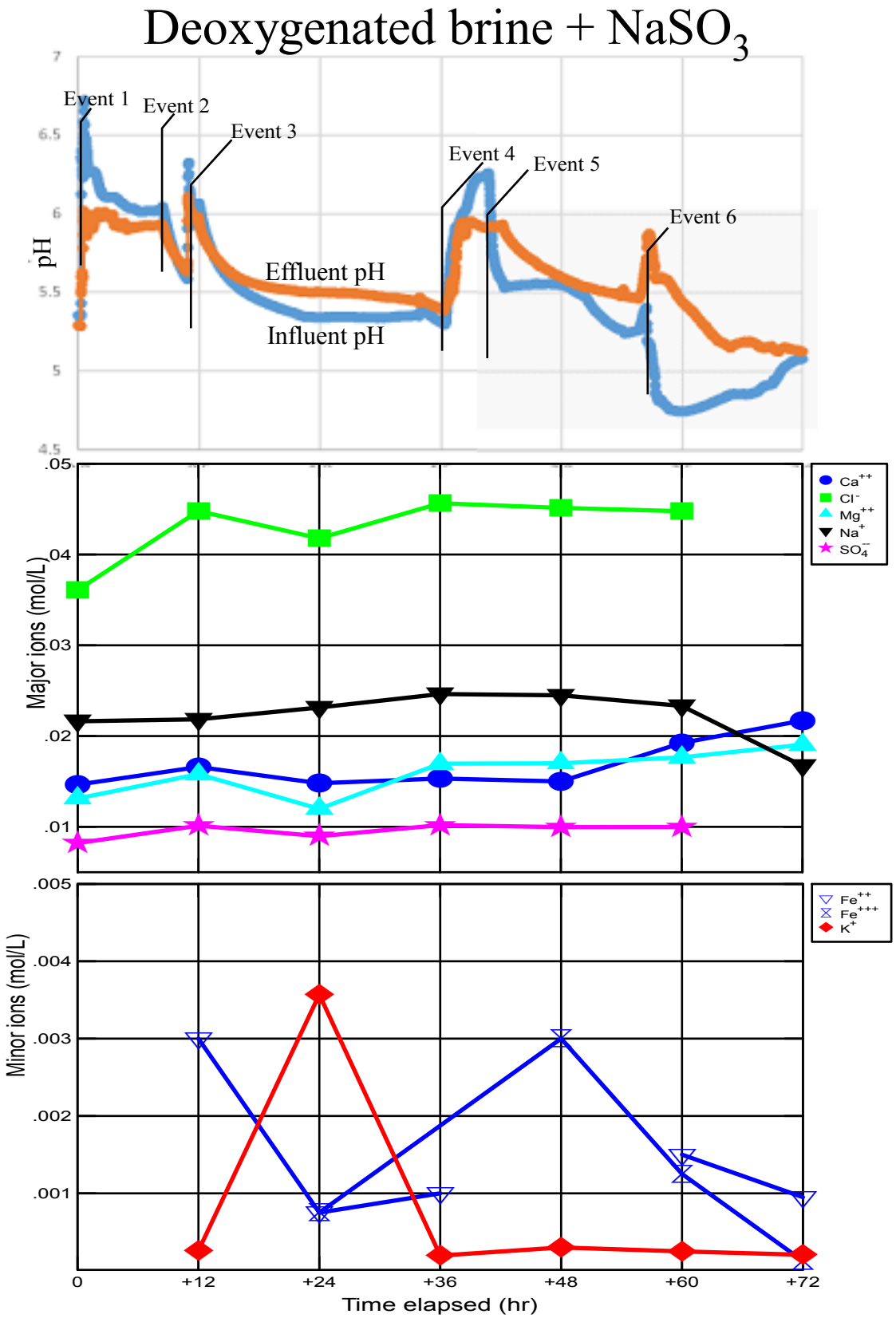

Fig. 3.13a - Experiment 11-5-13 water chemistry. See log for descriptions of events.

Fig. 3.12b - Description of Events for Experiment 11-5-13

Event 1 – Brine introduced to core

Event 2 – CO_2 reaches sensors and core

Event 3 – Problem with CO_2 injection, CO_2 flow stopped and restarted.

Event 4 – Problem with CO_2 injection, CO_2 flow stopped.

Event 5 – CO_2 pump pressure (and therefore flow) increased in order to overcome corrosion forming on CO_2-brine mixing junction.

Notes on Water Chemistry

Chloride and sulfate measurements for +72 hours suspect and therefore not included.

Iron(III) sample for +48 hours lost during reduction process.

Control Experiment

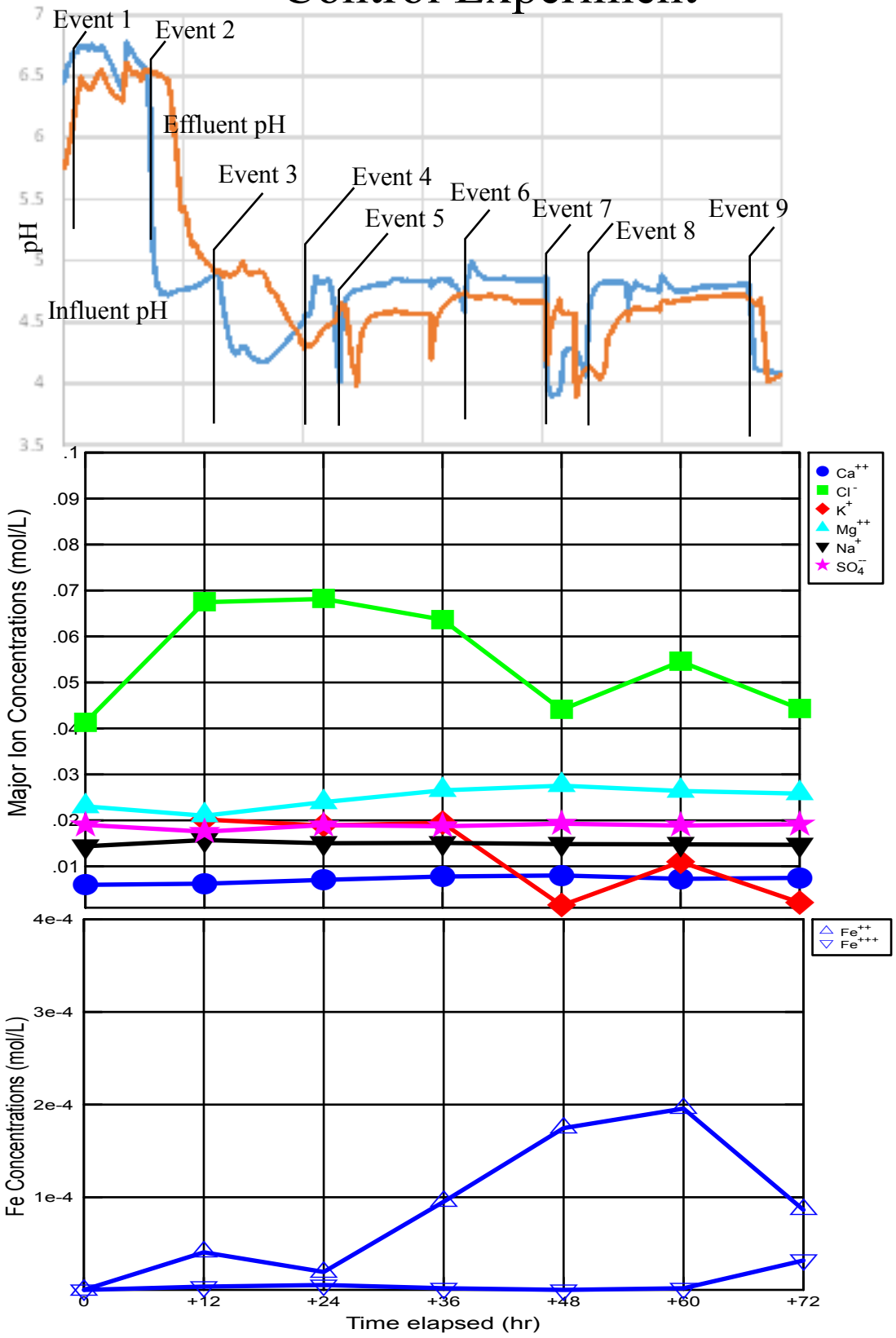

Fig. 3.13a - Water chemistry data for control experiment. See log for event descriptions.

Fig. 3.13b - Description of Events for Control Experiment

Event 1 – Brine introduced to core

Event 2 – CO_2 reaches sensors and core holder

Event 3 – CO_2 injection rate increased

Event 4 – CO_2 injection rate increased

Event 5 – CO_2 injection rate decreased

Event 6 – Pressure perturbation due to emptying accumulator

Event 7 – CO_2 injection rate increased

Event 8 – CO_2 injection rate decreased

Event 9 – CO_2 injection rate increased

The reason that the CO_2 flow rate was increased and decreased so many times was to try and get a lower pH. However, there were issues with the pump that prevented the flow rate from being kept high.

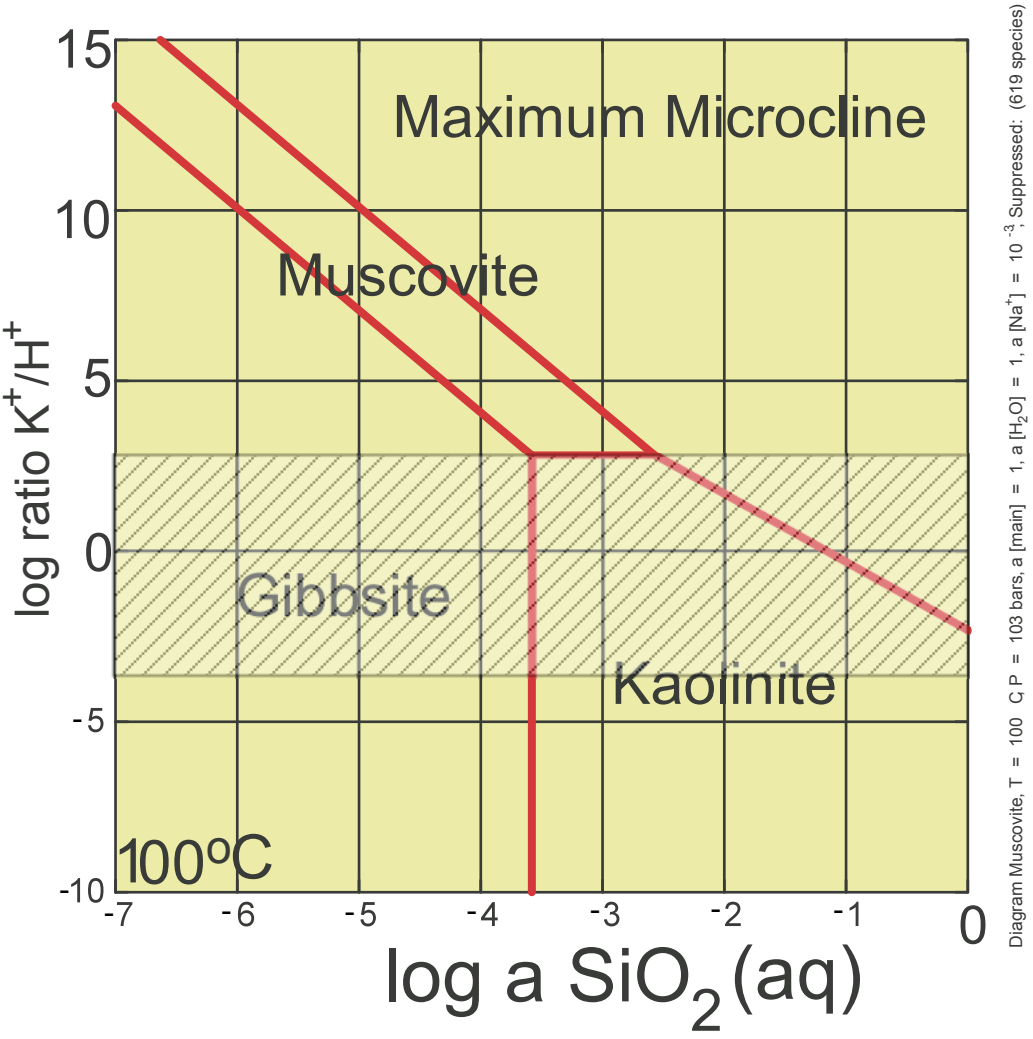

Fig. 3.14 - Potassium-silica-aluminum phase diagram. The striped box represents the range of log[K^+/H^+] values in the flow-through experiments. Since silica concentrations were not measured the vertical range cannot be ascertained. The formation of kaolinite or gibbsite would seem to be favorable, but this does not necessarily mean that the dissolution of muscovite or the formation of gibbsite or kaolinte would occur during a flow-through experiment. The phase diagram was constructed in Geochemist's Workbench for a system at 100°C and 103bars. It assumes the activity of water is 1 and the activity of Na^+ is 10^{-3} mol/L. All species other than those labeled were suppressed.

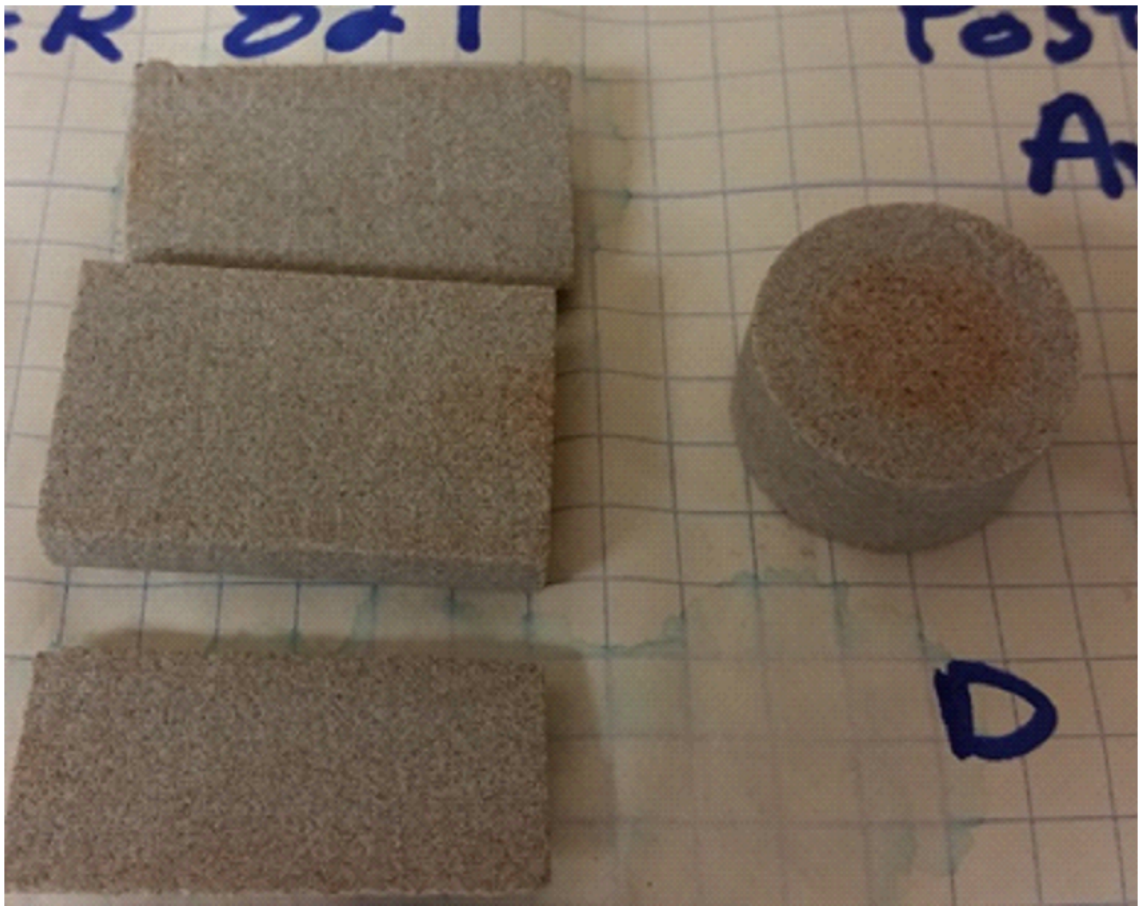

Fig. 3.15 - Core showing oxidation post reaction.

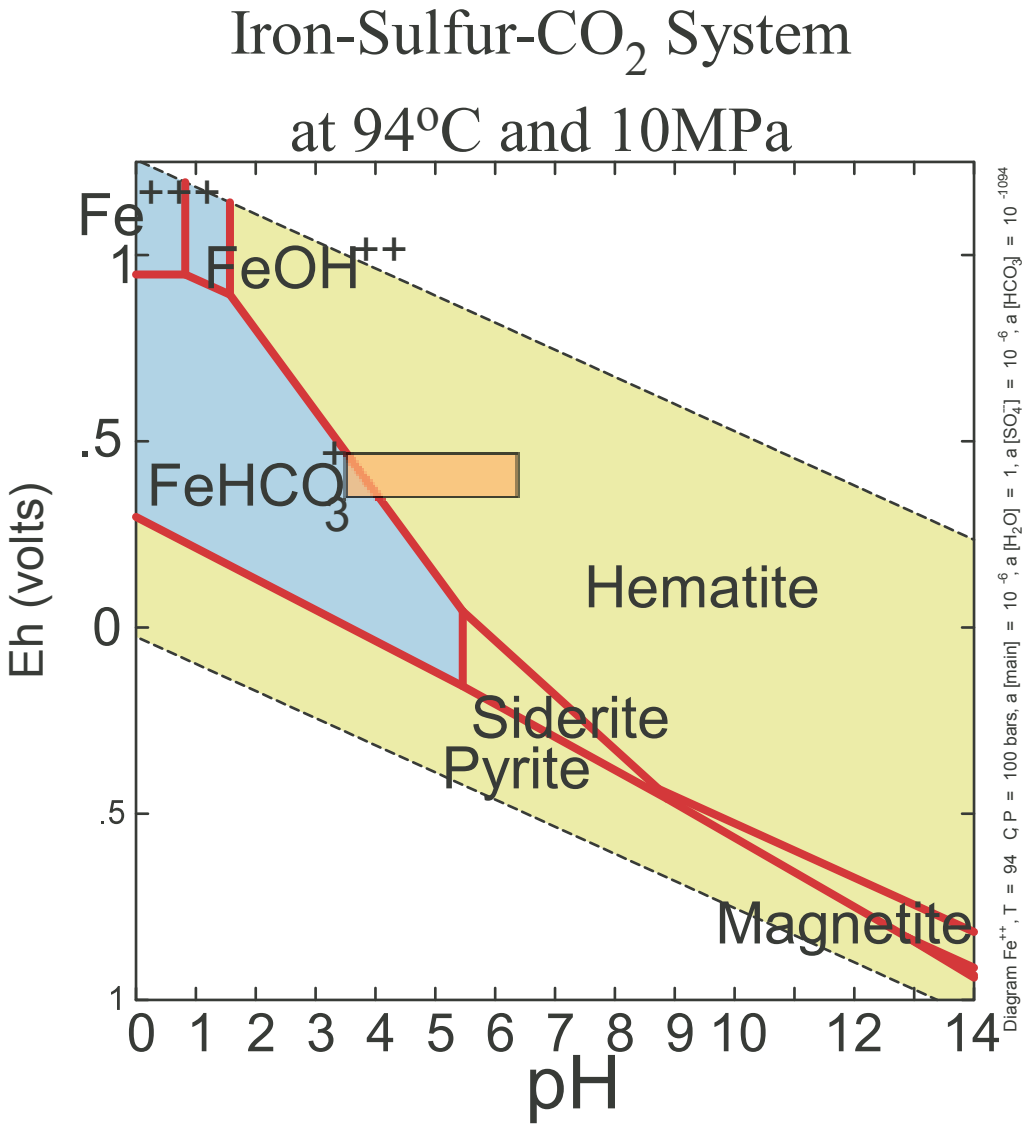

Fig. 3.16 - pH Eh diagram for the iron-carbon dioxide-sulfur system. The box outlines the probable pH-Eh range of the flow-through experiments. Eh was calculated inGeochemist's Workbench using the ratio of iron(II) to iron(III) in the control experiment. Diagram constructed in Geochemist's Workbenchfor 94ºC and 100bars. The activity of water is 1, the activity of HCO_3^- is $10^{-.1094}$, the activity of all other species is 10^{-6}.

CHAPTER 4 - INVESTIGATION OF THE REACTION OF IRON OXIDES AND IRON SULFIDE UNDER SIMULATED GEOLOGIC SEQUESTRATION CONDITIONS

Introduction

This chapter describes experiments that explore the reactions that take place between $scCO_2$-brine solution and iron oxides (magnetite, hematite, and "substituted hematite"), and pyrite. The impetus for these experiments was the observation of iron oxide staining on cores of the Berea sandstone noted by this author and others (Vogt et al., 2014). Pyrite and iron oxides (magnetite and hematite) are minor, but chemically important components of sandstone reservoirs (Kaszuba et al., 2013).

Pyrite was found to display minor dissolution textures following batch experiments with $scCO_2$-SO_2 and the Madison Limestone (Chopping and Kaszuba, 2012). However, pyrite was only a small component (1% wt.) of the mineral assemblage used in these experiments. This study was examining CO_2-SO_2 co-sequestration and did not isolate the CO_2-brine-pyrite system. Furthermore, (Kaszuba et al., 2013) notes that there are few experimental studies that report results for pyrite precipitation or dissolution during $scCO_2$ experiments.

Previous experiments between CO_2 and iron oxides has focused on hematite and iron oxyhydroxides. It has been demonstrated that dry gaseous CO_2 will form carbonate and bicarbonate surface complexes with iron oxyhydroxides. These complexes are stable as long as they are in the presence of gaseous CO_2 and break down upon its removal (Hausner et al., 2009; Pierre-Louis, 2014). A solution of $scCO_2$-brine has been shown to

cause iron(III) bearing montmorillonite to react to form hematite (Montes-Hernandez and Pironon, 2009).

There has been a great deal of research on the interaction between iron(III) bearing minerals and CO_2-SO_2/H_2S-brine. Modeling work showed that it was theoretically possible for reduced sulfur species to reduce iron(III) to iron(II) in the presence of CO_2 to form solid siderite and pyrite (Palandri and Kharaka, 2005). This reaction has been experimentally demonstrated between hematite and SO_2-CO_2-brine (Garcia et al., 2011; Palandri and Kharaka, 2005) and between hematite and sulfide-brine (Murphy et al., 2011). Iron oxyhydroxides have been experimentally determined to behave in a similar fashion. Goethite has been shown to react with CO_2-SO_2-brine to form siderite (Garcia et al., 2012). Other oxyhydroxides have been shown to react to form siderite when reacted with CO_2-sulfide-brine solutions (Lammers et al., 2011; Murphy et al., 2010).

The reaction of $scCO_2$ and reduced iron oxides, such as magnetite, has been underrepresented in the literature. Magnetite decorated carbon nano-particles have been shown to adsorb to CO_2 at high pressure non-aqueously (Mishra and Ramaprabhu, 2011) and Ti-magnetite was present in batch reactions looking at $scCO_2$-brine-basalt reactions (Sissmann et al., 2014) but it does not seem that there has been published work on $scCO_2$-brine batch reactions with magnetite. However, since the dissolution of magnetite produces iron(II) it was hypothesized that a reaction may take place. Magnetite could prove important in the context of sequestration in serpentinites and ultramafic rocks where it is an important alteration product of the reaction between water and olivine (Winter, 2010).

Hypothesis

It was hypothesized that pyrite and magnetite, which both contain ferrous iron, would dissolve and react with $scCO_2$-brine to form siderite. It was hypothesized that hematite would not react with $scCO_2$-brine because iron(III) has a low solubility at pH values above 3, such as those that would be generated in these experiments (Kaszuba and Janecky, 2009) and there would be no reductants present to convert it to iron(II).

Experimental

Five experiments were conducted to determine the effects of the CO_2-brine system on iron bearing minerals. They were: 1) Pyrite (two experiments); 2) Magnetite (one experiment); 3) "Substituted hematite" (one experiment) [this mineral was sold as hematite, but analysis showed it to be a mixture of magnetite and an iron oxide with abundant strontium and aluminum substitution]; 4) hematite (one experiment); and 5) control (one experiment).

Mineral samples of two sizes were utilized for these experiments. Half to three-quarters of the sample mass was crushed to finer than 35 mesh (0.5mm), one or more crystals larger than 10 mesh (2mm) (comprising the balance of the sample mass) were placed on top in order to provide a sample that could be easily examined microscopically. The mass of each mineral was measured to contain approximately 0.14mol of Fe(II) [6]. The exception to this was the experiments utilizing hematite (iron(III)), and substituted

[6] This assumed 100% purity, which subsequent analysis showed to not be the case, but in all experiments the amount placed in the reaction vessel was greatly in excess of the amount that could be dissolved.

hematite (initially thought to be iron(III)). In these experiments a mass of mineral containing 0.14mol of total iron was used.

The mineral samples were placed inside a Teflon liner inside a 35mL Parr Reaction Vessel (PRV), also referred to as a batch reactor (Fig. 4.1). Samples were submerged in 20mL of brine (Berea recipe, Table 2.1). The vessel and brine were deoxygenated with ultra-high purity N_2 (Appendix I) to ensure oxygen contamination would not lead to oxidation of the mineral samples. The vessel was then filled with ultra-high purity CO_2 to a starting pressure of 120 bar and placed in an incubator at 96°C. The length of the experiments varied from 72-600 hours. The first experiment (Pyrite 1), was conducted for 72 hours. The unexpected reactivity of the pyrite was the impetus for lengthening the subsequent experiments. The main sign of reactivity was depressurization of the vessel, indicating the consumption of CO_2. The other experiments were allowed to continue until the internal pressure stopped declining (300-600 hours). The vessels were opened at the end of the experiment, the mineral samples were dried under a vacuum to prevent oxidation, and the brine composition was analyzed (see Chapter 2 for methods). The solid mineral samples were examined by FEM for evidence of dissolution or precipitation.

Materials

Samples of pyrite, magnetite, "substituted hematite", hematite, and iron(II) chloride were obtained and characterized for use in these batch reaction experiments.

Pyrite. Pyrite crystals were obtained from Earth's Treasures in Bozeman, Montana. Single euhedral crystals ~1cm x 1cm in size were selected for these

experiments (Fig. 4.2d). All crystals were from the same locality (though the store was unsure of where precisely this location was). EDS analysis showed the crystals to be ~93% pure FeS_2 (by atomic percent) (Fig. 4.3).

Magnetite. Magnetite was obtained as "lodestone" from Amazon.com (Fig. 4.2b). XRD analysis showed it to be composed of 80% magnetite and 20% hematite (Fig. 4.4a). Iron is the major cation present (Fig. 4.4b). Silicon and calcium are also present, probably as silicate impurities. A variety of minor elements are also present.

Substituted Hematite. This was labeled as hematite from Earth's Treasures (Fig. 4.2a). XRD analysis showed that it was not hematite at all, but actually a combination of magnetite and another mineral or minerals that had no definite match in the ICAL diffraction database (Fig. 4.5a). The closest match was strontium chromium iron oxide. Elemental analysis showed that iron was the predominant cation, but strontium, aluminum and a variety of other elements were present (Fig. 4.5b). Additional characterization with FEM-EDS showed that the sample had iron oxide zones where aluminum was more abundant than strontium and zones of iron oxide where strontium was more abundant than aluminum (Fig. 4.6). The sample seems to be a combination of magnetite and one, perhaps two other varieties of iron oxide that have abundant strontium and aluminum substitution. The sample proved to be reactive with the $scCO_2$-brine, and produced abundant dissolved ferrous iron.

Hematite. Hematite in the form of micaceous hematite, was obtained from Ward's Science (Republic Mine, Michigan) (Fig. 4.2c). XRD showed that the sample was ~25%

hematite and ~75% muscovite (Fig. 4.7a). The elemental composition reflects this. Iron, aluminum, silica, and potassium are the most abundance elements (Fig. 4.7b).

Iron(II) Chloride. The iron(II) chloride tetrahydrate used in this experiment was from Acros Organics, CAS No. 13478-10-9. Purity was >99% as certified by the manufacturer.

Results

Control Experiment

The control experiment was run with brine and CO_2 only. It provided a baseline to differentiate between changes resulting from mineral-CO_2 reactions, and artifacts of the experiment (Fig. 4.8). The CO_2 pressure was constant (140 bars) throughout the experiment. Observed changes included the formation of small amounts of hydrogen gas (~100ppm or less) and the appearance of several ions that were not measured in the brine prior to the experiment. These included ferrous iron (4.7ppm), phosphate (21ppm), fluoride (2ppm), potassium (22ppm) and unexpectedly high concentrations of nitrogen species (ammonium (21ppm), nitrate (93ppm), nitrite (2.9ppm)). The ferrous iron and hydrogen likely resulted from the anaerobic corrosion of the stainless steel Parr vessel in the presence of CO_2 (see Chapter 3). The nitrogen species may have resulted from the reduction/oxidation of N_2 that was left over from the de-oxygenation procedure. The origin of the phosphate, fluoride, and potassium is not clear but it could have resulted from contamination of the vessel or liner. The final brine pH was 5.1.

Pyrite Experiments

Two experiments were conducted with pyrite. The first was 72 hours, (Fig. 4.9) and the second was 588 hours (Fig 4.10). The first pyrite experiment was designed to run for the same amount of time as a Berea sandstone flow-through experiment. The pressure drop that resulted (120 bars to 70 bars) was unexpected and initially thought to be a leak. More CO_2 was added to bring the pressure back up and again the pressure dropped (from 103 bars to 76 bars). This represented reaction of 63% of the total moles of CO_2 injected into the vessel during the experiment[8] (Span and Wagner, 1996).

The second experiment was conducted to see if the pressure drop was repeatable. The experimental time was lengthened to 588 hours. The rate of CO_2 reaction was not measured, but a large pressure drop from 119 to 34 bars was observed during this second experiment. This represents dissolution of 82% of the moles of CO_2 that were initially present. There was a substantial increase in bicarbonate concentration (calculated from charge imbalance) in the first experiment, but a decrease in bicarbonate concentration in the second experiment. The final brine pH in both experiments was around 5.5 – 6.0 dropping from an initial brine pH of 7.5. Dissolved ferrous iron concentrations were greater than the control in both experiments (44ppm and 17ppm vs. 4.7ppm in the control), indicating mineral dissolution. Sulfate concentrations increased (from 1823ppm to 2053ppm in experiment 1 and from 1823ppm to 2184ppm in experiment 2), which is consistent with the dissolution of pyrite and the oxidation of some of the sulfur.

[8] The calculation was made by converting pressure data into density using the Equations of State (EOS) for CO_2 published by Span and Wagner (1996). Density and head space volume were then converted into moles.

The pyrite crystals displayed dissolution textures when viewed both in hand sample and under FEM (Fig. 4.11). FEM imaging also showed the formation of a white crust on the mineral surface (Fig. 4.11 & 4.12 a&b). The identity of the white crust was difficult to determine because it was very thin and the EDS beam also returned signal from the underlying pyrite. The beam detected a variety of elements including carbon, oxygen, iron, sulfur, magnesium, calcium, and silicon. The crystals in the pre- and post-reaction photos have similar compositions, but as mentioned are far more abundant in the post reaction photos.

Magnetite Experiment

The magnetite batch reaction ran for 518 hours (Fig. 4.13). The pressure dropped from 120 bar to 29 bar over the course of the experiment, levelling off after around 270 hours. This represents dissolution of 82% (molar) of the CO_2 initially present. Bicarbonate concentrations increased from 2.8ppm to around 2800ppm (calculated). Dissolved ferrous iron increased to 8.8ppm, indicating magnetite dissolution. Calcium concentrations anomalously increased (from 540ppm to 880ppm). The final pH was around 6.

FEM examination of pre-and post-reaction surfaces of the magnetite showed that small (~5μm), euhedral, cubic to rhombohedral crystals had formed on the magnetite's surface during the experiment (Fig. 4.14a). EDS analysis showed them to be composed predominantly of iron and oxygen (Fig. 4.14b). They may be hematite.

Substituted Hematite Experiment

The substituted hematite batch reaction ran for 344 hours (Fig. 4.15). The pressure in the vessel dropped from 140 bars to 50 bars, representing dissolution of 73% of the moles of CO_2 initially present. Bicarbonate concentrations increased from 2.8ppm to 2500ppm (calculated). Dissolved ferrous iron rose to 17.5ppm. The final brine pH was 6.2.

FEM examination of pre- and post-reaction surfaces revealed the formation of similar crystals to those found on the surface of the magnetite (Fig. 4.16a & b). This indicates a similar reaction pathway may have been occurring, which is not surprising considering that magnetite is one of the components of this mineral.

Iron(II) Chloride Experiment

The iron(II) chloride experiment ran for 518 hours (Fig. 4.17). No detectable reaction occurred. The pressure held steady and there were no significant changes in the major ion chemistry except that the pH decreased to 1.5. The low pH probably inhibited the dissolution of CO_2 because bicarbonate cannot form at low pH (Langmuir, 1997).

Hematite Experiment

The batch experiment with hematite did not show any noticeable reactions as detected by monitoring the pressure, which held steady at 115 bars for the duration of the 300 hour experiment (Fig. 4.18).

Hydrogen Gas Generation

The concentration of hydrogen gas in the headspace of the reaction vessels was measured after both pyrite experiments, the control, and the substituted hematite experiment (Table 4.1). It was not measured after the magnetite experiment because the author did not realize its significance. The concentration of hydrogen gas in the control experiment was 101ppm. The concentration in the headspace of substituted hematite was 2429ppm. The concentration was 205ppm for Pyrite #1. Hydrogen was present in Pyrite #2, but it was less than the amount required for quantification (~1ppm). Thus, there was a source of hydrogen gas generation in the substituted hematite experiment that was not present in the other experiments.

Discussion

Enhanced CO_2 Dissolution

The dissolution of CO_2 is enhanced by the presence of minerals containing iron(II), but not iron(III) (with the exception of iron(II) chloride which will be discussed below). During the pyrite, magnetite, and the substituted hematite experiments, between 63% and 82% of the total moles of CO_2 present in the headspace of the reaction vessels was dissolved into the brine (Table 4.2). No measurable CO_2 was dissolved in the control experiment or the experiment with hematite. The amount of CO_2 dissolved into solution in the pyrite, magnetite, and substituted hematite experiments was around 5x greater than would be predicted for brine alone under the same conditions (120bar, 96ºC). About 4.5mole/L of CO_2 was dissolved during the experiments. Only, around 0.9mol/L

would have been dissolved in brine alone[9]. The amount of CO_2 dissolved is even more impressive when the drop in pressure is taken into account. As the pressure becomes lower, the solubility of CO_2 decreases. Just below the critical point it is 0.6mol/L, and at 40bar is 0.4bar. Therefore, when the pressure decrease is taken into account the amount of CO_2 dissolved at the end of the experiment is actually ~10x the amount that would have been dissolved (calculation made at 40bar and 96ºC).

Dissolved Iron Deficit

The concentrations of dissolved iron measured following the pyrite, magnetite, and substituted hematite experiments are substantially lower than the dissolution reactions predict.

Pyrite dissolution in the presence of carbonic acid:

$$FeS_{2(pyrite)} + H_2CO_3^0{}_{(aq)} \rightarrow Fe^{2+}{}_{(aq)} + HCO_3^-{}_{(aq)} + HS_2^-{}_{(aq)} \quad (4.1)$$

Magnetite Dissolution in the presence of carbonic acid:

$$Fe(II)Fe(III)_2O_4{}_{(magnetite)} + H_2CO_3^0{}_{(aq)} \rightarrow Fe^{2+}{}_{(aq)} + HCO_3^-{}_{(aq)} + OH^-{}_{(aq)} + Fe_2O_3{}_{(hematite)} \quad (4.2)$$

In the case of pyrite, in order to dissolve, via reaction 4.1 the amount of CO_2 dissolved in in Pyrite Experiment 2 (0.13 moles), the same amount of iron(II) would be required to be in solution. This would mean a dissolved iron concentration of 363ppm. However, the dissolved iron concentration was only 17.2ppm[10].

During the magnetite experiment, 0.07 moles of CO_2 was dissolved. Equation 4.2 predicts that for this amount of CO_2 0.035 moles of Fe(II) would be dissolved. This

[9] Calculated using Duan et al., 2006 CO_2 dissolution model.
[10] Calculation made by dividing the necessary 0.13 moles of Fe^{2+} by the 20mL of brine in the reaction vessel and then converting to mg/L.

corresponds to 97.7ppm dissolved iron(II). Only 8.8ppm was measured. Thus, there must be an iron removal mechanism present in the pyrite, magnetite, and substituted hematite experiments.

Effects of pH and Eh on the Magnetite and Substituted Hematite Systems

A pH-Eh model of the iron-sulfur-CO_2 system (Fig. 4.19) was used to elucidate the fate of the iron. The pH-Eh range found in the magnetite and substituted hematite systems[11] lies within the stability fields of $FeHCO_3^+$ at the lower end of the pH range and the hematite stability field in the upper pH range. Thus the model predicts that dissolved iron would be found as $FeHCO_3^+$ early in the experiment and then converted to hematite as the experiment progressed and the pH rose. This is consistent with the experimental observation of iron oxide crystals on the post-reaction magnetite and substituted hematite samples.

A Model for the Magnetite-Brine-CO_2 System

Magnetite and substituted hematite are theorized to have reacted via the following pathway (see Fig. 20 for a graphical representation):

$$2CO_{2(supercritical)} + 2H_2O_{(l)} \rightarrow 2H_2CO_3^0{}_{(aq)} \quad (4.3)$$

$$2H_2CO_3^0{}_{(aq)} \rightarrow 2HCO_3^-{}_{(aq)} + 2H^+_{(aq)} \quad (4.4)$$

$$2Fe(II)Fe(III)_2O_{4\ (magnetite)} + 2H^+_{(aq)} \rightarrow 2Fe^{2+}_{(aq)} + 2OH^-_{(aq)} + 2Fe_2O_{3\ (hematite)} \quad (4.5)$$

$$2Fe^{2+}_{(aq)} + 2OH^- \rightarrow 2Fe^{3+}_{(aq)} + H_{2(g)} + 2O^{2-} \quad (4.6)$$

$$2Fe^{3+}_{(aq)} + 2O^{2-} + H_2O_{(l)} \rightarrow Fe_2O_{3\ (hematite)} + 2H^+_{\ (aq)} \quad (4.7)$$

[11] Eh estimates made in Geochemist's Workbench using ration of iron(II) to iron(III) and nitrate to nitrite.

Net Reaction:

$2Fe(II)Fe(III)O_{4(magnetite)} + 2H_2CO_{3(aq)} + H_2O_{(l)} \rightarrow 2HCO_3^- + 3Fe_2O_{3hematite} + H_{2(g)} + 2H^+_{(aq)}$ (4.8)

This pathway is summarized as follows:

- CO_2 dissolves and forms carbonic acid and bicarbonate (Reaction 4.3).
- The carbonic acid dissociates into protons and bicarbonate (Reaction 4.4).
- The protons attack the magnetite, dissolving the iron(II) and leaving behind Fe_2O_3. Hydroxide ions are generated (Reaction 4.5).
- The iron(II) is oxidized by the hydrogen in the hydroxide generating hydrogen gas and oxide ions (Reaction 4.6).
- The iron(III) bonds to the oxide ions an oxygen from a water molecule and precipitates as hematite, or another similar oxide. Protons are generated. (Reaction 4.7).
- Reaction 4.8 is the net reaction.

Hydrogen is the most likely electron acceptor in this system. The quantity of H_2 measured after the substituted hematite experiment accounted for ~2/3 of the "missing" dissolved iron[12] (Reaction 4.6).

Unfortunately, H_2 was not measured after the magnetite experiment and so it cannot be definitely asserted that the same reaction pathway occurred. However, since magnetite was a component of substituted hematite, and both displayed similar post reaction precipitates, it is likely that both followed similar reaction pathways.

[12] $2.6x10^{-2}$ moles of H_2 was calculated to be inside the substituted hematite reaction vessel. The amount of missing iron needed to account for the calculated dissolved CO_2 levels is around 0.1moles, assuming the dissolution of the mineral proceeded according to reaction (2).

The only unexplained part of the system is the mechanism that was responsible for raising the pH. The net reaction (Reaction 4.8) generates as many protons as it consumes and therefore the pH should have remained the same.

The Effects of pH-Eh on the Pyrite System

The calculated Eh range for the pyrite experiments[13] lies in the same field as those found in the magnetite and substituted hematite experiments. However, these values may be higher than the actual Eh that existed inside the reaction vessels during the experiments. The Eh in these experiments would probably have been controlled by the dissolution of pyrite which would generate reduced sulfur species, such as HS_2^- (Reaction 1). Reduced sulfur is difficult to measure and was not quantified during these experiments. The actual Eh value may have lay along the boundary line between pyrite and siderite/$FeHCO_3^+$ (Fig. 4.19). This assumption is corroborated by the lack of precipitated iron oxide and the low levels H_2 gas generation (which indicate that iron was not oxidizing in large amounts). Iron(II) that was dissolved from the pyrite likely remained iron(II).

A Model for the Pyrite-Brine-CO_2 System

The chemical pathway of the pyrite-brine-CO_2 system is not clear. The texture of the samples after the experiments indicated that dissolution occurred, and the pressure drop indicates that a large amount of CO_2 was consumed. Reaction 1 is a likely first step in the reaction process:

$$FeS_{2(pyrite)} + H_2CO_3^0{}_{(aq)} \rightarrow Fe^{2+}{}_{(aq)} + HCO_3^-{}_{(aq)} + HS_2^-{}_{(aq)} \quad (4.1)$$

[13] Calculated in Geochemist's Workbench from iron(II)/(III) ratios.

The fate of the dissolved sulfur is not known. Some was probably oxidized to sulfate, but the measured increases in dissolved sulfate during the pyrite experiments is not sufficient to account for what is predicted to have dissolved.

The identity of the white crystals observed on the surfaces of the pyrite after the reactions cannot be positively identified. As mentioned the crust contained a variety of elements. It may be a carbonate of some sort, it may be a salt, or it may be an agglomeration of several compounds.

Summary

These experiments validated the hypothesis that iron(II) bearing minerals would react with CO_2 and iron(III) bearing minerals would not. In the case of pyrite the hypothesis that siderite would form could not be validated. In the case of magnetite, the results were unexpected. The production of hematite and the storage of CO_2 as bicarbonate was unexpected. The reaction rates of CO_2 with pyrite, magnetite, and substituted hematite were faster than expected.

Conclusions

From these experiments the following conclusions can be drawn:

1) CO_2–brine solution is reactive with minerals that contain iron(II), but not iron(III). Reactions proceed quickly at first and then slow as equilibrium is approached.

2) The presence of iron(II) bearing minerals facilitated the dissolution of ~5x the CO_2 (by moles) that would have been dissolved in only a brine-CO_2 system.

3) Dissolved iron levels are much lower than predicted by stoichiometry, indicating that the presence of an iron removal mechanism.

4) The removal of iron seems to follow a different pathway in the magnetite/substituted hematite-brine-CO_2 system than in the pyrite-brine-CO_2 system.

In the magnetite/substituted hematite systems the iron is removed as an iron oxide, probably hematite. In the pyrite system the removal mechanism is not clear, but there is no evidence of iron oxidation.

Hydrogen Production in Experimental Vessels		
Experiment	[H_2] In Headspace (ppm)	Total H_2 in Reaction Vessel (moles)
Control	101	$1.2x10^{-3}$
Substituted Hematite	2429	$2.6x10^{-2}$
Pyrite #1	205	$8.7x10^{-4}$
Pyrite #2	pbq*	-
pbq – gas present in quantities below quantification		

Table 4.1 – Hydrogen was detected in the headspace of the above experiments. The column in the right was the measured concentrations of the H_2 in the headspace gasses. The column on the left is the calculated total quantities of H_2 present in the reaction vessels. Hydrogen was not measured for the magnetite experiment or the iron(II) chloride experiment. The results seem to support the assertion that no significant oxidation of iron (with hydrogen as an electron acceptor) took place in the pyrite or control experiments, while significant oxidation of iron (with hydrogen as the electron acceptor) took place in the substituted hematite experiment.

Moles of CO_2 Reacted in Iron Batch Experiments						
	Pyrite 1	Pyrite 2	Magnetite	Substituted Hematite	Iron(II) chloride	Hematite
Initial moles of CO_2	0.15	0.14	0.09	0.15	0.11	0.12
Final moles CO_2	0.06	0.02	0.02	0.04	0.11	0.12
Moles consumed	0.09	0.12	0.07	0.11	0	0
Moles consumed as % of total	63%	82%	82%	73%	0%	0%
Equation of best fit line for molar dissolution	Not recorded	Not recorded	$y= 0.017ln(x) +0.0311$	$y= 0.0202ln(x) -0.0036$	NA	NA

Table 4.2 – CO_2 reaction data for iron-CO_2-brine experiments. The initial moles of CO_2 in the magnetite experiment are lower than in the others because a larger volume of magnetite is required than the others to deliver the same moles of Fe^{2+} to the system, reducing headspace volume. Hematite, having no iron(II) was measured for moles of total iron, as was substituted hematite because it was initially thought to be hematite.

Fig. 4.1 - Parr reactor vessels (batch reactors) disassembled (top left), assembled and pressurized (top right). Bottom photo shows Teflon Liner and pyrite crystals.

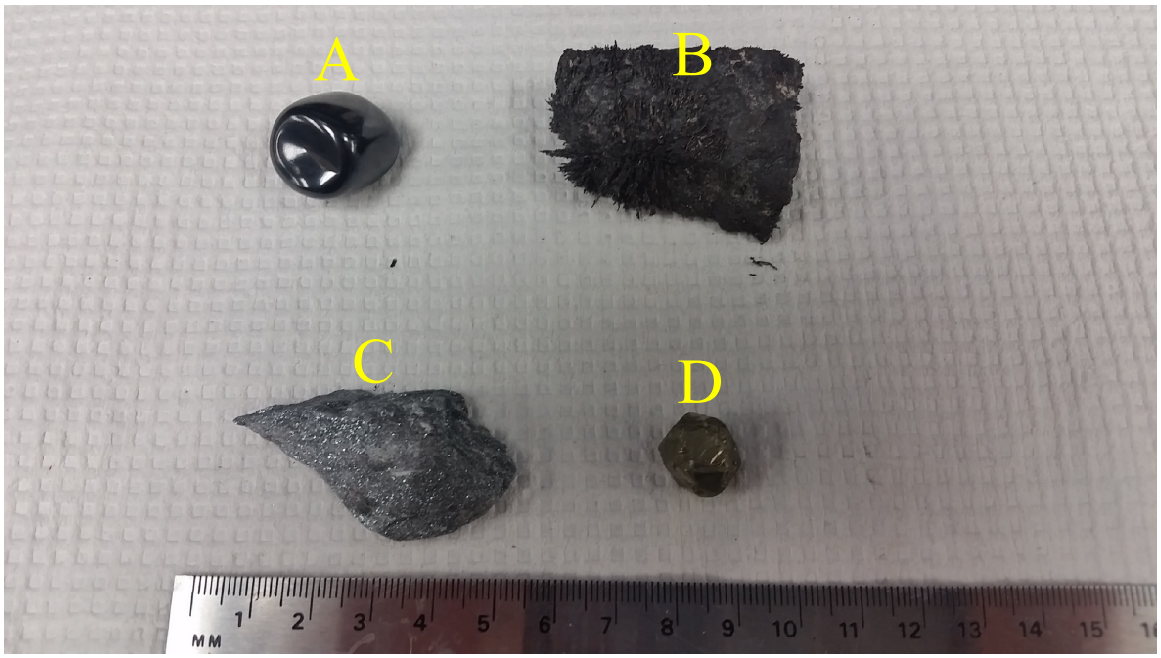

Fig. 4.2 - Mineral samples used in experiments. A) substituted hematite, B) lodestone (magnetite), note rock fragments being held to stone by magnetic force, C) micaceous hematite, D) pyrite

ICAL MSU
Spectrum Report
Tuesday, April 28, 2015

File: z:\Lupine Medical\M-8-15\xpg12-33F_S001.pgt
Collected: April 28, 2015 11:14:33

Live Time:	80.00	Count Rate:	1895	Dead Time:	34.02 %
Beam Voltage:	19.70	Beam Current:	2.00	Takeoff Angle:	32.78

4-6-15rxpg12-33F_S001.pgt

FS: 3200

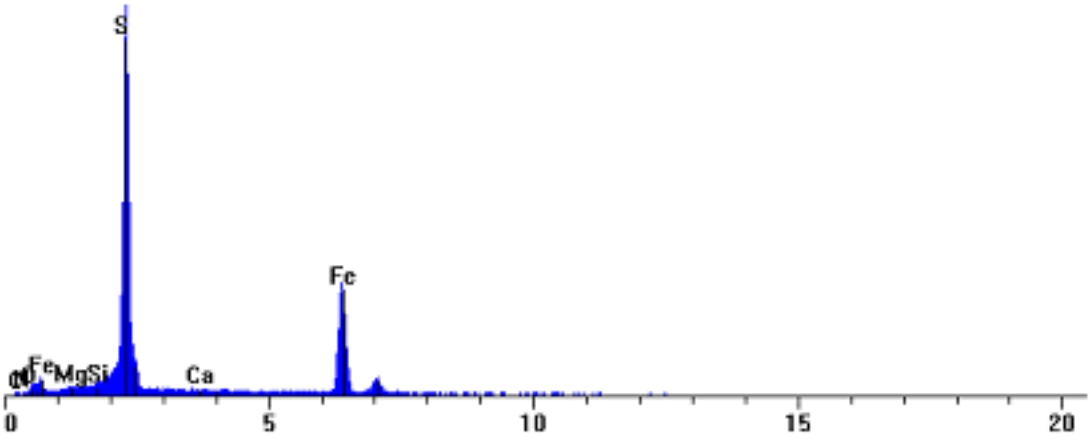

Element	KRatio	Wt%	At%	ChiSquared	Z Corr	A Corr	F Corr
C	0.0089	1.99	6.38	1.16	0.868	13.870	1.000
N	0.0000	0.00	0.00	6.55	0.870	8.052	0.999
O	0.0000	0.00	0.00	17.06	0.880	5.273	0.998
Mg	0.0005	0.12	0.19	2.97	0.940	2.832	0.994
Si	0.0001	0.01	0.01	2.35	0.947	1.619	0.978
Ca	0.0000	0.00	0.00	1.64	0.972	1.211	0.985
Fe	0.4940	46.92	32.30	1.54	1.068	1.026	1.000
S	0.5086	50.96	61.11	2.73	0.957	1.223	0.998
Total	1.0000	100.00	100.00	0.87			

Residual peak detected at 2.108 keV.

Fig. 4.3 - EDS analysis of pyrite crystal used in batch reaction experiments. Analysis shows that the sample is of high purity.

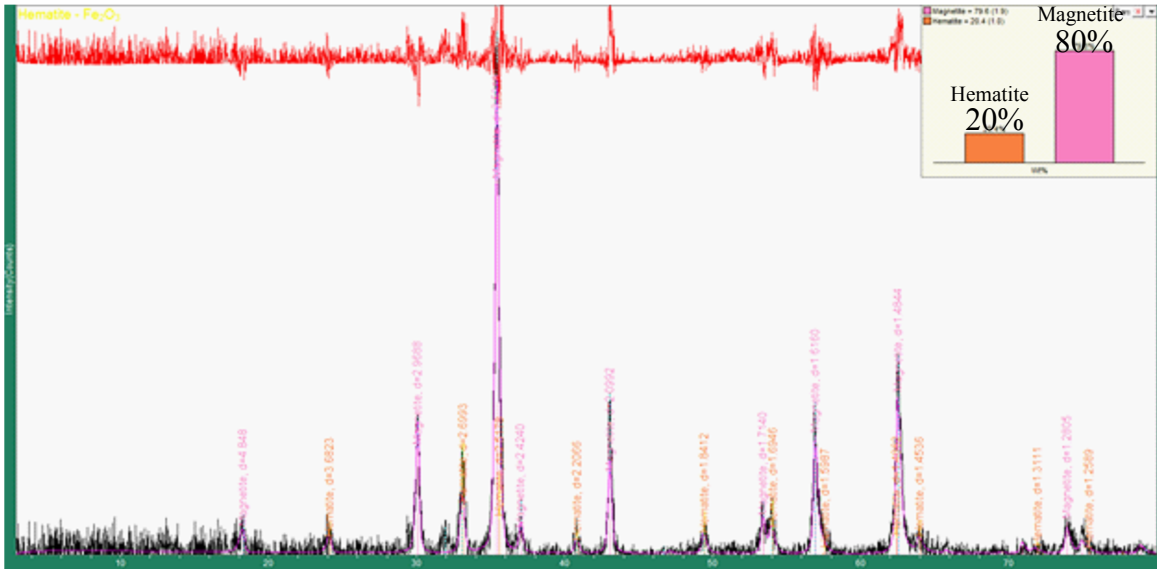

Fig. 4.4a - Diffraction pattern of lodestone from Amazon.com. Composed of ~80% magnetite and ~20% hematite.

Lodestone Elemental Analysis									
Major Elements (>1%)									
Bal	**Bal Error**	**Fe**	**Fe Error**	**Ca**	**Ca Error**	**Si**	**Si Error**		
26.8	0.9	68.5	0.9	1.3	0.1	1.4	0.1		
Minor Elements (<1%)									
Al	**Al Error**	**P**	**P Error**	**V**	**V Error**	**K**	**K Error**	**Cl**	**Cl Error**
0.7	0.1	0.59	0.02	0.13	0.01	0.12	0.02	0.16	0.01
Co	**Co Error**	**Mn**	**Mn Error**	**Cr**	**Cr Error**	**Ba**	**Ba Error**	**Zn**	**Zn Error**
0.12	0.05	0.09	0.02	0.05	0.01	0.02	0.01	0.009	0.004
Ag	**Ag Error**	**Pd Error**	**Pd Error**	**Nb**	**Nb Error**	**Sr**	**Sr Error**		
0.002	0.001	0.003	0.002	0.002	0.001	0.002	0.001		

Fig. 4.4b - Elemental analysis of Lodestone. The major divalent cation is iron. Note variety of other elements. The "Bal" is the balance of elements that are too light for XRF to quantify, primarily oxygen.

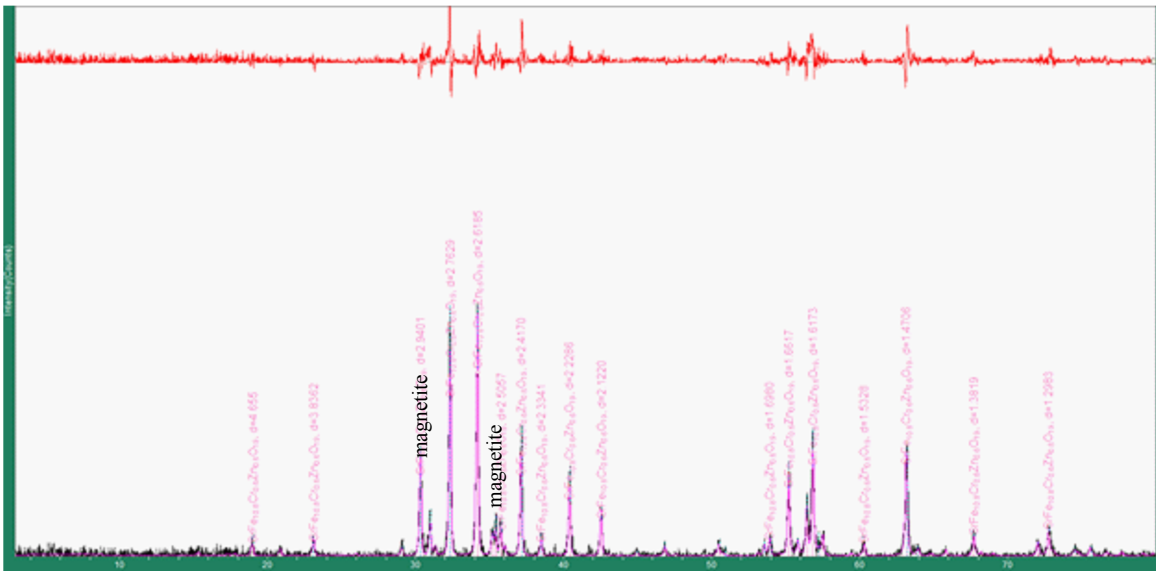

Fig. 4.5a - Diffraction pattern for "substituted hematite". Magnetite is an identifiable component. The other peaks are a closest match for a highly substituted (with chromium and zinc) form of iron oxide, but no exact match or matches could be found. It is thought that the crystal structure of substituted hematite is similar to this chromium zinc iron oxide, but the substituting elements are strontium and aluminum.

Substituted Hematite Elemental Analysis									
Major Elements (>1%)									
Bal	**Bal Error**	**Fe**	**Fe Error**	**Sr**	**Sr Error**	**Si**	**Si Error**	**P**	**P Error**
27.3	1.0	60.9	0.8	4.4	0.1	3.9	0.1	1.25	0.03
Minor Elements (<1%)									
Al	**Al Error**	**Mn**	**Mn Error**	**Ca**	**Ca Error**	**Ba**	**Ba Error**	**K**	**K Error**
0.93	0.14	0.51	0.03	0.42	0.06	0.13	0.01	0.11	0.02
As	**As Error**	**Cr**	**Cr Error**	**Cl**	**Cl Error**	**W**	**W Error**	**V**	**V Error**
0.03	0.01	0.058	0.007	0.053	0.004	0.04	0.02	0.02	0.01
S	**S Error**	**Zr**	**Zr Error**	**Sn**	**Sn Error**	**Pd**	**Pd Error**	**Ag**	**Ag Error**
0.02	0.01	0.02	0.01	0.01	0.003	0.004	0.001	0.003	0.001

Fig. 4.5b - Elemental composition of substituted hematite. Note the abundance of strontium and high amounts of aluminum and silica. EDS analysis shows that the strontium and aluminum occur in the same minerals as the iron. The silica occurs as small silicate inclusions. The "Bal" is the balance of elements too light for XRF to quantify, primarily oxygen.

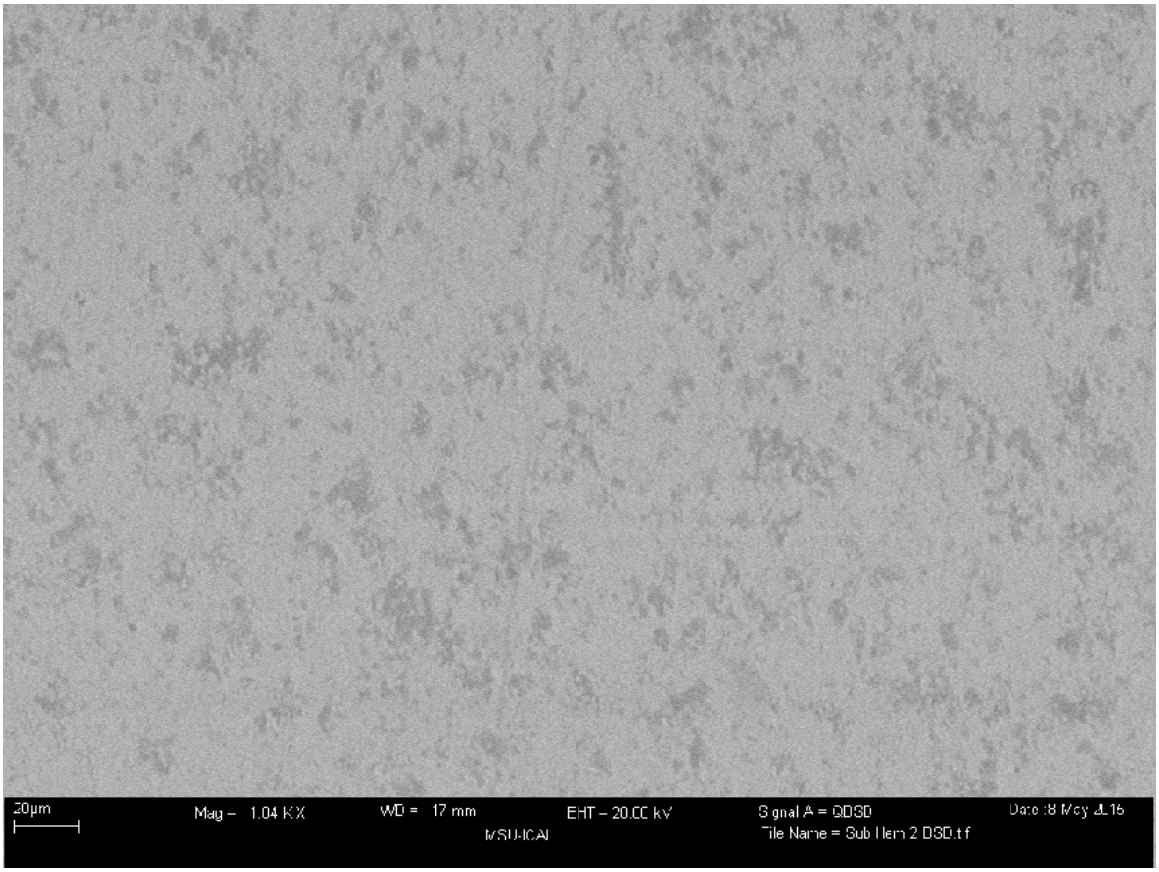

Element	KRatio	Wt%	At%	ChiSquared	Z Corr	A Corr	F Corr
Mg	0.0008	0.21	0.27	1.34	0.931	3.532	0.998
Si	0.0000	0.00	0.00	1.46	0.937	1.945	0.999
Ca	0.0016	0.12	0.10	1.09	0.963	1.083	0.972
Ti	0.0000	0.00	0.00	1.23	1.054	1.039	0.927
Fe	0.7309	58.24	33.20	6.72	1.058	0.999	1.000
O	0.1817	29.43	58.56	1.84	0.872	2.469	0.998
C	0.0000	0.00	0.00	3.22	0.861	6.019	0.999
S	0.0006	0.06	0.06	1.16	0.947	1.482	0.997
Cl	0.0000	0.00	0.00	1.11	0.990	1.329	0.995
Al	0.0200	3.67	4.33	3.52	0.962	2.531	0.998
Ir	0.0000	0.00	0.00		1.446	1.000	0.998
Na	0.0003	0.11	0.15	0.02	0.950	5.590	0.999
K	0.0000	0.00	0.00	0.68	0.985	1.136	0.983
P	0.0043	0.55	0.57	2.46	0.971	1.752	0.998
V	0.0000	0.00	0.00	0.80	1.076	1.024	0.888
Sr	0.0598	7.62	2.77	1.69	1.137	1.487	1.000
Total	1.0000	100.00	100.00	0.65			

Fig. 4.6 - Backscattered image of substituted iron oxide with EDS analysis of entire field of view. The EDS analysis corroborates the XRF data showing high concentrations of strontium and aluminum. Spot analyses showed that the darker areas are iron oxide more enriched in aluminum than strontium, and the lighter areas are iron oxide more enriched in strontium than aluminum.

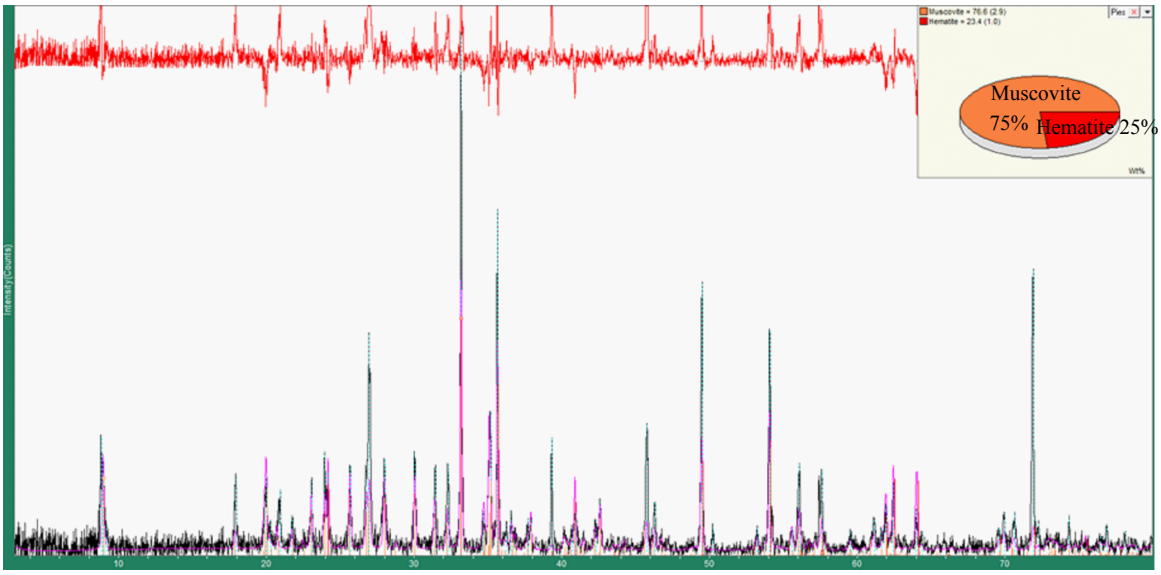

Fig. 4.7a - Diffraction pattern for micaceous hematite. It is composed of ~25% hematite and 75% muscovite.

Micaceous Hematite Elemental Analysis									
Major Elements (>1%)									
Bal	**Bal Error**	**Fe**	**Fe Error**	**Al**	**Al Error**				
19.8	0.9	47.5	0.5	16.2	0.5				
Si	**Si Error**	**K**	**K Error**	**Mg**	**Mg Error**				
12.6	0.2	2.4	0.1	1.7	0.9				
Minor Elements (<1%)									
Ti	**Ti Error**	**Ca**	**Ca Error**	**Ba**	**Ba Error**	**P**	**P Error**	**Co**	**Co Error**
0.96	0.03	0.12	0.05	0.11	0.01	0.098	0.022	0.08	0.04
Mn	**Mn Error**	**Zr**	**Zr Error**	**Cr**	**Cr Error**	**V**	**V Error**	**Sr**	**Sr Error**
0.07	0.01	0.039	0.001	0.03	0.01	0.03	0.01	0.01	0.001
Nb	**Nb Error**	**Sn**	**Sn Error**	**Rb**	**Rb Error**				
0.006	0.001	0.003	0.002	0.004	0.001				

Fig. 4.7b - Elemental composition of micaceous hematite. The "Bal" is the balance of elements too light for the XRF to quantify, primarily oxygen.

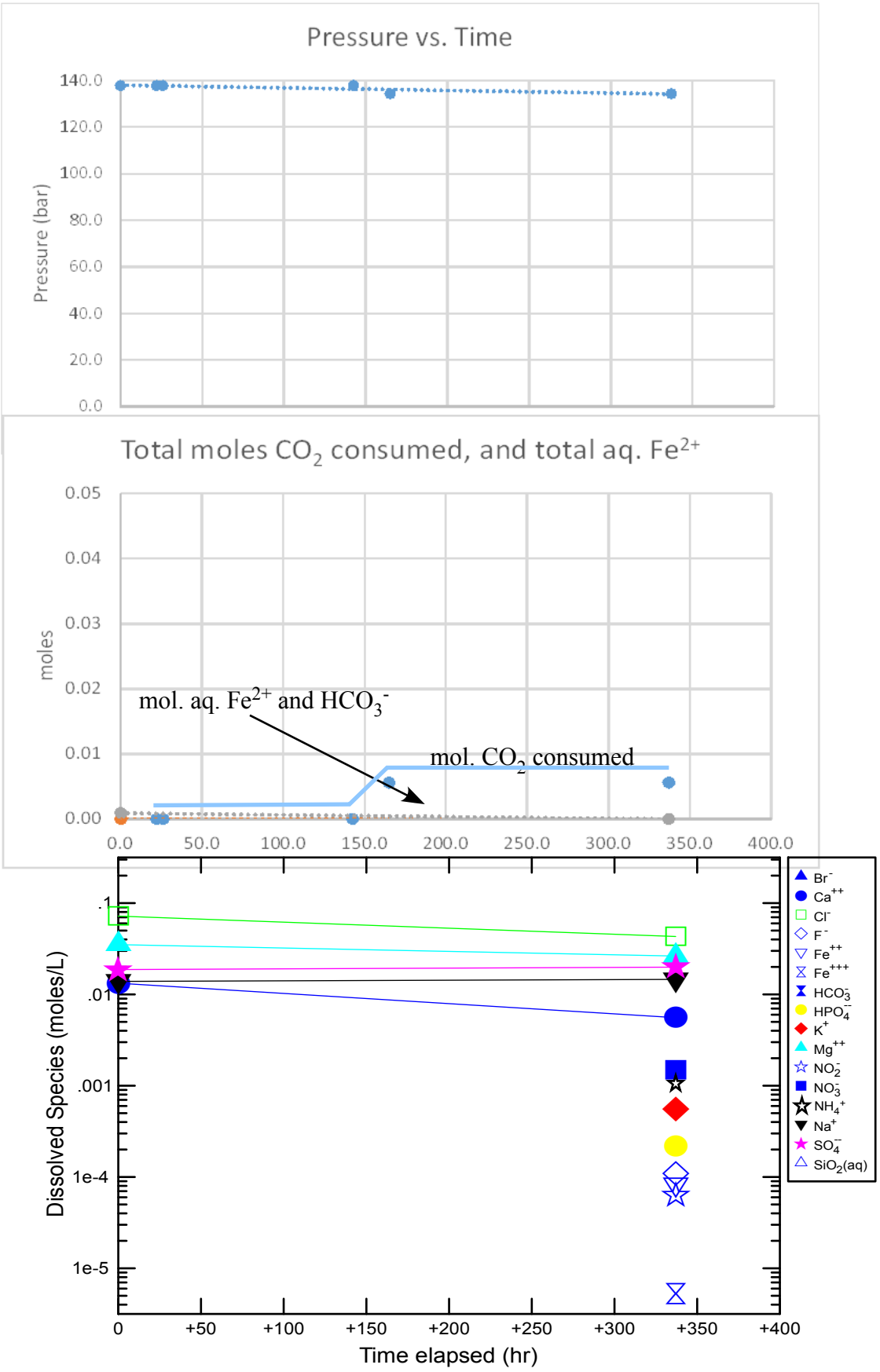

Fig. 4.8 - Control batch reaction experimental data. Note lack of CO_2 dissolution.

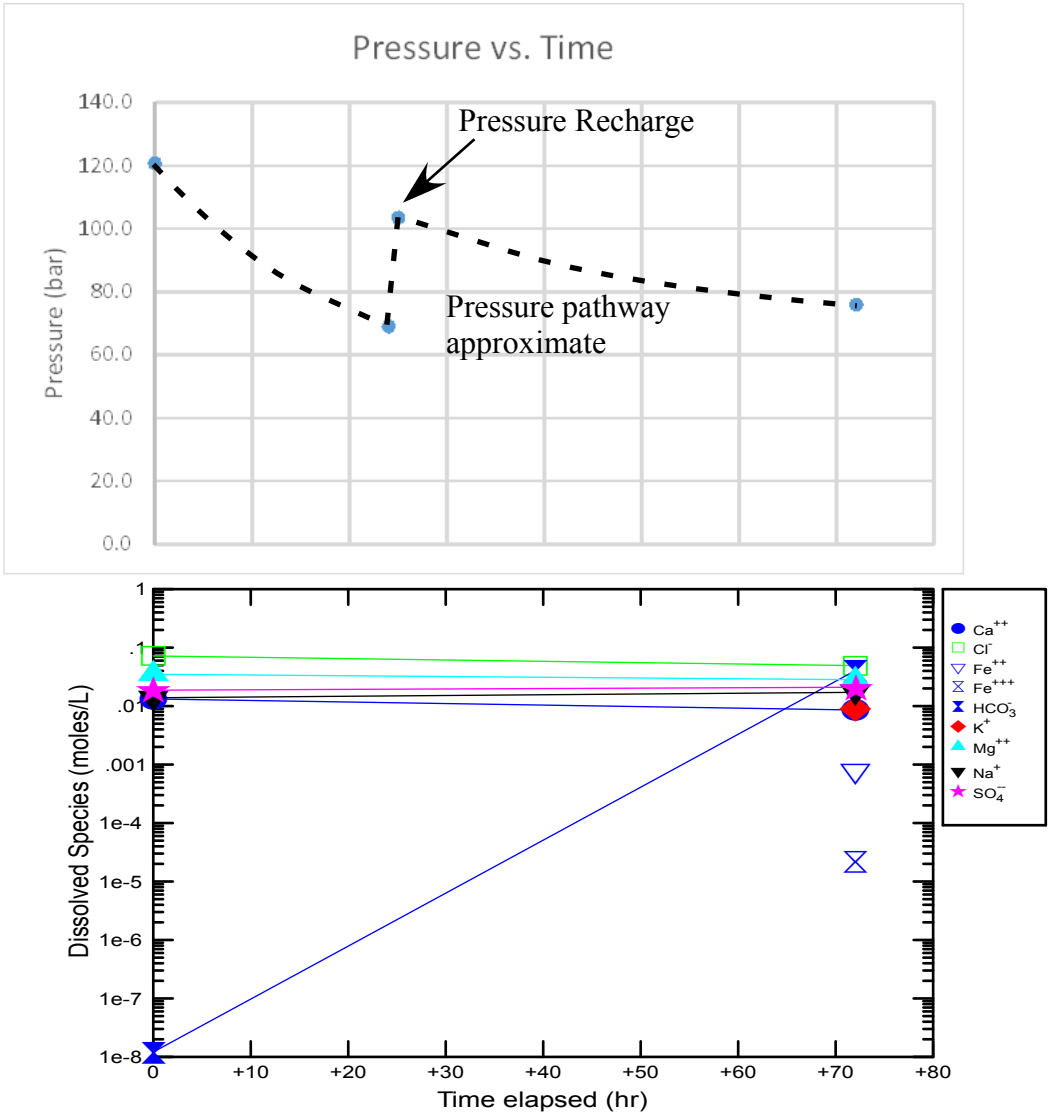

Fig. 4.9 - Pyrite batch reaction 1 experimental data.

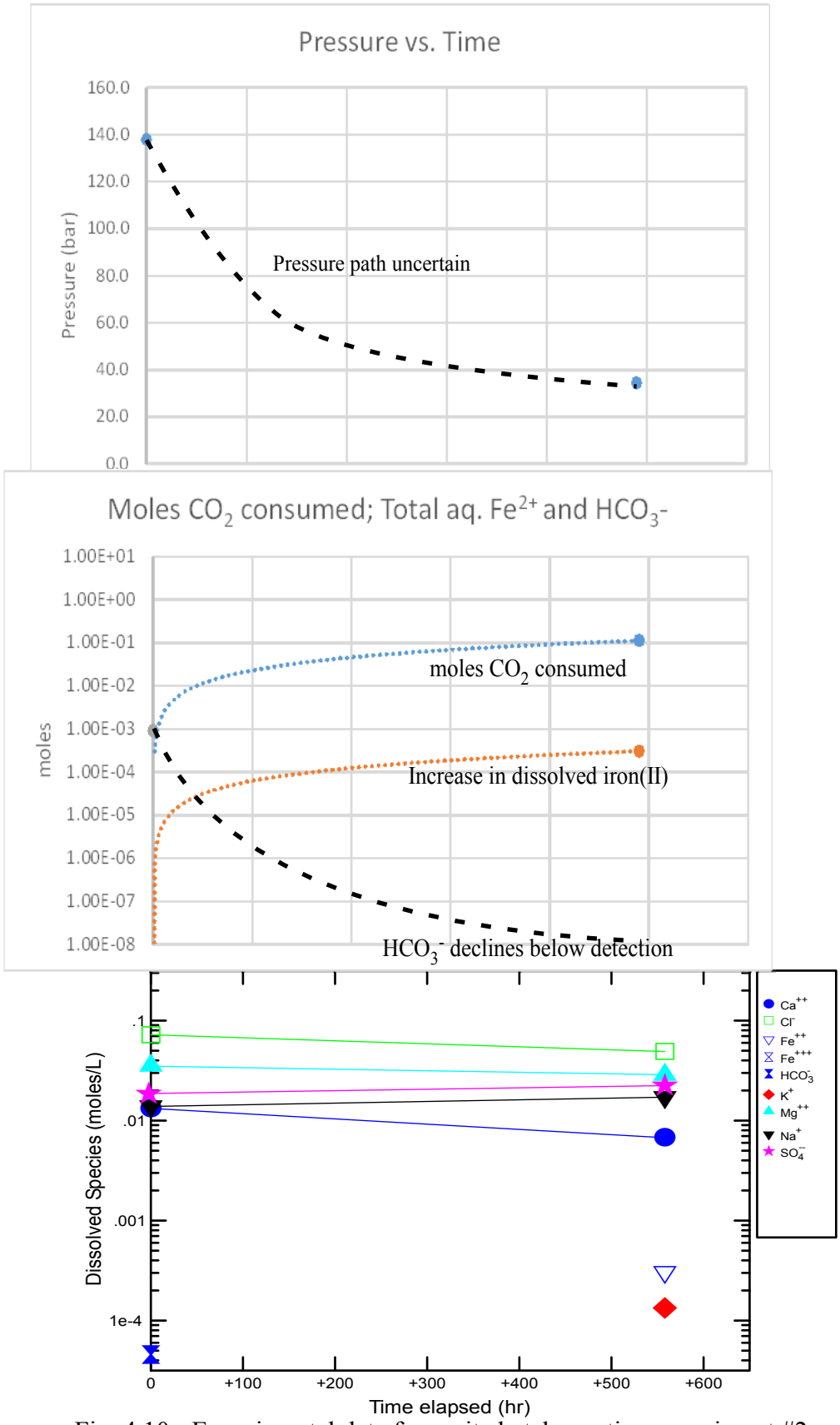

Fig. 4.10 - Experimental data for pyrite batch reaction experiment #2.

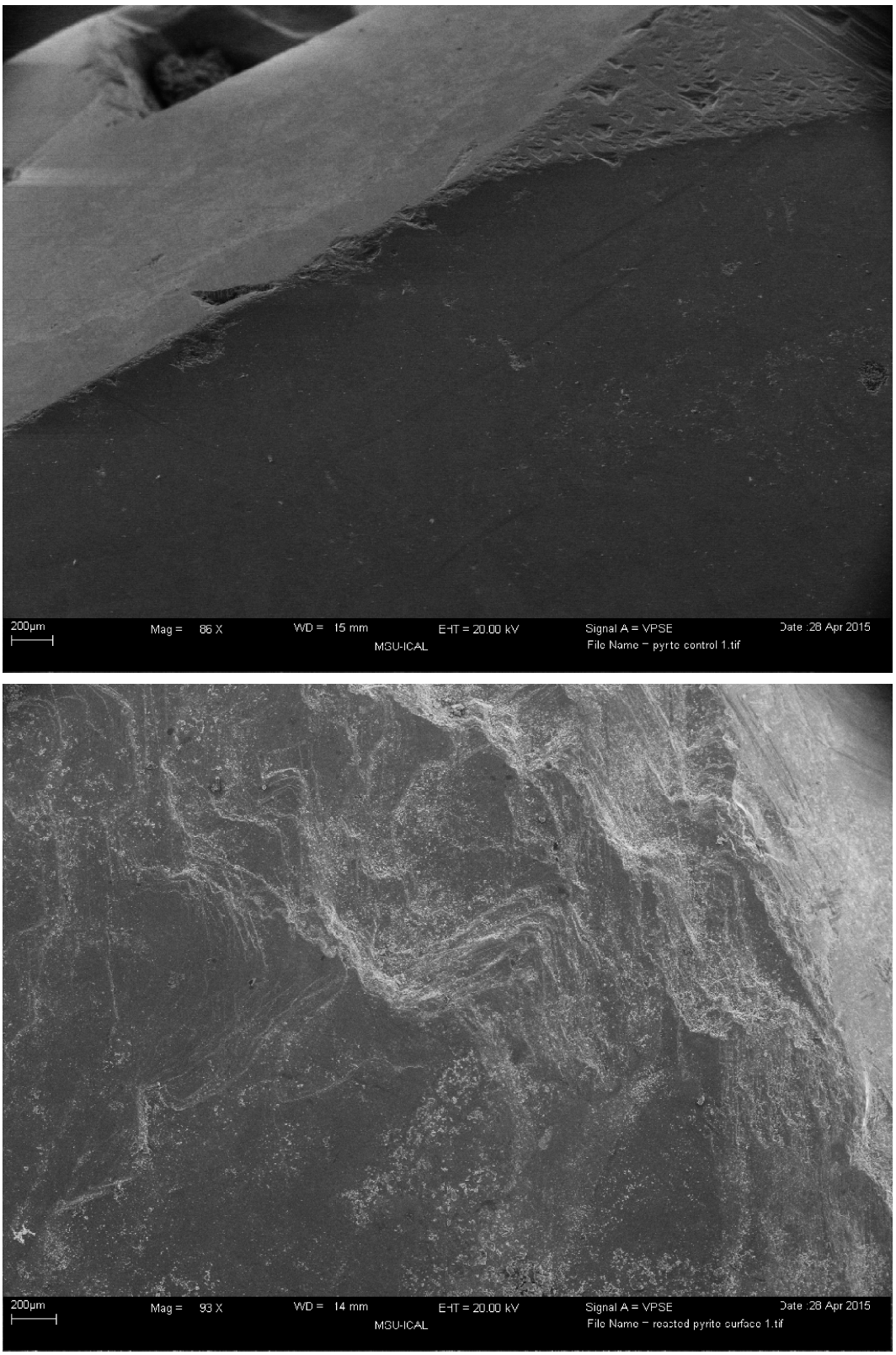

Fig. 4.11 - The top photo shows unreacted pyrite. The bottom photo shows pyrite that was reacted for 588 hours. Note the extensive dissolution texture and the white precipitate on the mineral surface.

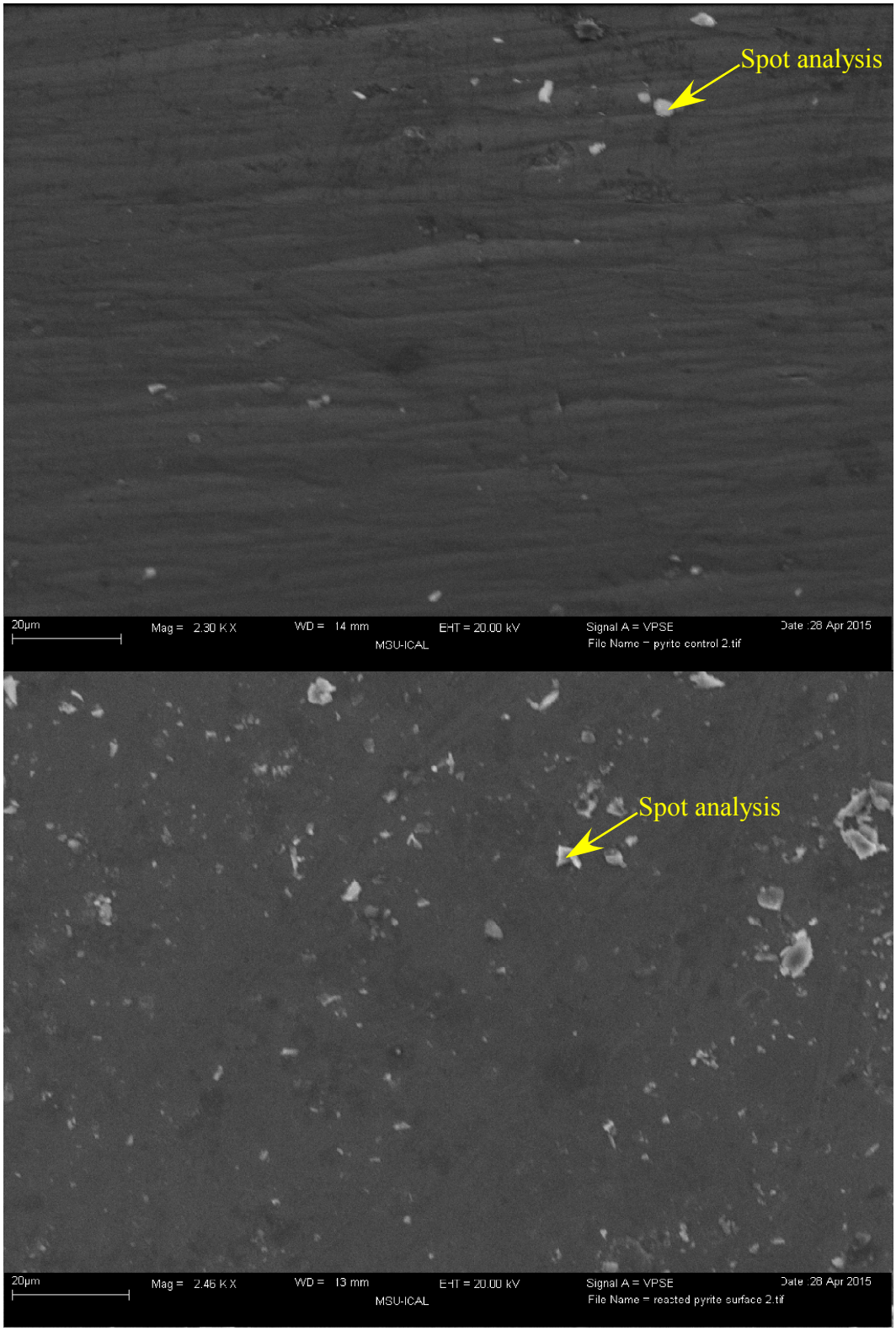

Fig. 4.12a - Image of pyrite crystal before reaction (top) and after reaction (bottom). Note that small white crystals are present in both photographs, but are far more abundant in the bottom photograph. EDS spot analyses are shown on the following page (Fig. 4.12b).

Element	KRatio	Wt%	At%	ChiSquared	Z Corr	A Corr	F Corr
C	0.0062	5.53	15.04		0.882	12.755	1.000
N	0.0000	0.00	0.00	0.18	0.884	8.674	0.999
O	0.0190	6.82	13.93	1.00	0.893	5.100	0.998
Mg	0.0000	0.00	0.00	1.32	0.951	2.800	0.995
Si	0.0024	0.28	0.33	1.12	0.958	1.600	0.980
Ca	0.0005	0.04	0.03	1.15	0.984	1.188	0.986
Fe	0.4836	42.13	24.64	1.18	1.083	1.021	1.000
S	0.4883	45.19	46.03	1.66	0.968	1.216	0.998
Total	1.0000	100.00	100.00	0.32			

EDS spot analysis of white crystal in pre-reaction photo.

Element	KRatio	Wt%	At%	ChiSquared	Z Corr	A Corr	F Corr
C	0.0058	2.07	14.62	5.54	0.673	5.748	1.000
N	0.0000	0.00	0.00	5.42	0.664	6.751	1.000
O	0.0146	5.63	29.88	1.22	0.674	6.215	1.000
Mg	0.0008	0.18	0.63	0.87	0.759	3.236	1.000
Si	0.0009	0.12	0.36	2.09	0.778	1.912	1.000
Ca	0.0000	0.00	0.00	0.51	0.797	1.593	0.998
Fe	0.1751	15.08	22.95	2.76	0.841	1.128	0.987
S	0.8028	76.93	31.55	49.02	1.052	0.989	1.000
Total	1.0000	100.00	100.00	2.82			

EDS spot analysis of white crystal in post-reaction photo.

Fig. 4.12b - EDS spot analyses for photographs in 4.12a. Crystals in both photos have carbon, iron, oxygen, and magnesium, and silicon. It is possible that both are iron carbonate crystals, although definite identification is difficult because of the signal returned from the underlying pyrite. The other elements detected could be impurities in the crystal structure (Mg, Ca) or it could be that these crystals nucleated on pieces of foreign material that were already on the crystal surface (Si). If the crystals in the pre-reaction photo are $FeCO_3$, they may have formed by the reaction of iron from the pyrite and carbonic acid that was present in their place of formation.

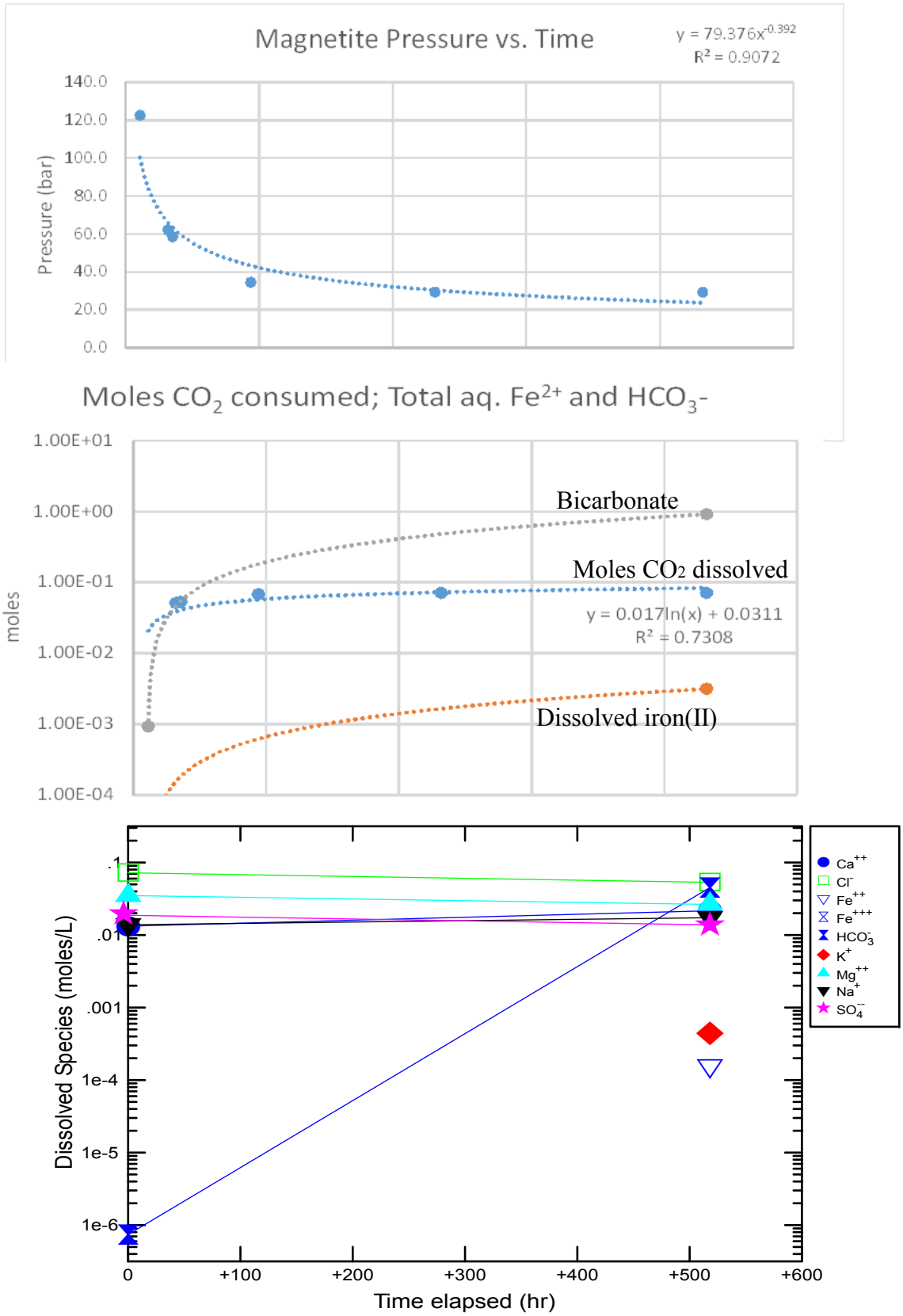

Fig. 4.13 - Results of magnetite batch reaction experiment.

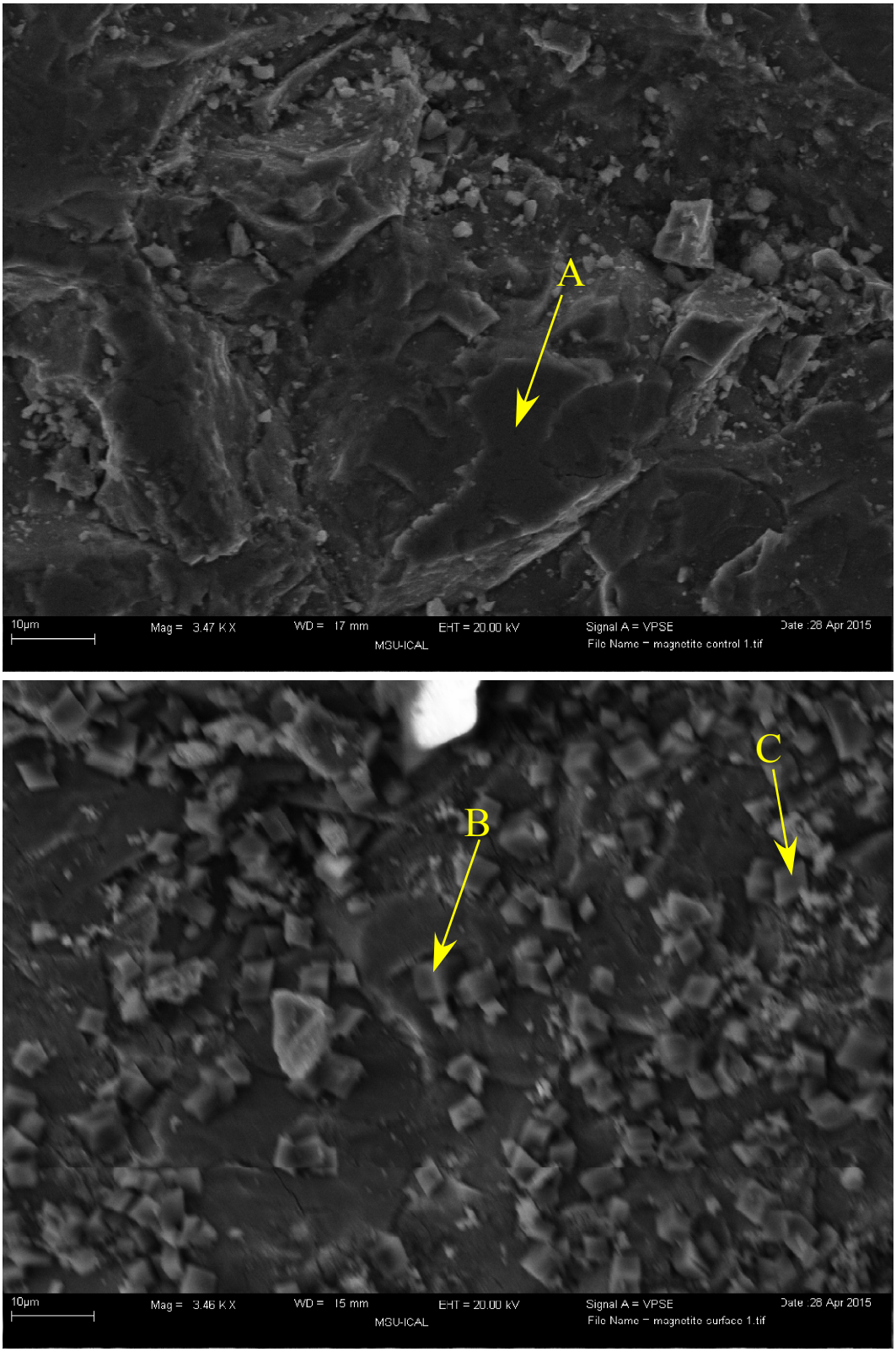

Fig. 4.14a - The top picture is magnetite pre-reaction, the bottom is magnetite post-reaction. Note the abundance of euhedral crystals encrusting the surface in the bottom photo. Spot analyses show the crystals to be composed of predominantly iron and oxygen. Analyses A, B, and C are shown in the following figure (4.14b).

Element	KRatio	Wt%	At%	ChiSquared	Z Corr	A Corr	F Corr
C	0.0013	0.45	1.06	0.83	0.880	4.918	0.999
N	0.0000	0.00	0.00	1.64	0.882	3.042	0.996
O	0.2768	37.65	66.47	1.77	0.892	1.943	0.998
Mg	0.0033	0.91	1.06	0.47	0.949	3.728	1.000
Si	0.0070	1.02	1.03	0.96	0.955	1.945	0.999
Ca	0.0026	0.21	0.15	0.84	0.981	1.051	0.964
Fe	0.7085	59.72	30.20	2.30	1.080	0.992	1.000
S	0.0004	0.04	0.03	1.61	0.964	1.364	0.996
Total	**1.0000**	**100.00**	**100.00**	**0.35**			

EDS spot analysis of "A" in top image (Fig. 4.14a). This is a pre-reaction analysis.

Element	KRatio	Wt%	At%	ChiSquared	Z Corr	A Corr	F Corr
N	0.0104	1.78	2.86	8.24	0.918	2.705	0.994
O	0.4598	56.82	79.80	3.24	0.928	1.909	0.999
Mg	0.0027	0.61	0.56	0.68	0.983	3.243	1.000
Si	0.0014	0.17	0.13	1.15	0.987	1.750	0.999
Cl	0.0013	0.11	0.07	0.67	1.042	1.175	0.994
Ca	0.0242	1.72	0.96	0.45	1.015	1.027	0.973
Fe	0.5002	38.79	15.61	3.80	1.123	0.989	1.000
Total	**1.0000**	**100.00**	**100.00**	**0.41**			

EDS spot analysis of "B" in bottom image (Fig. 4.14a). This is a crystal that appears to have grown during the reaction.

Element	KRatio	Wt%	At%	ChiSquared	Z Corr	A Corr	F Corr
N	0.0174	3.02	5.28	6.76	0.904	2.681	0.995
O	0.3595	47.19	72.12	1.32	0.914	1.999	0.998
Mg	0.0032	0.77	0.78	2.20	0.969	3.430	1.000
Si	0.0052	0.67	0.58	0.41	0.974	1.826	0.999
Cl	0.0004	0.03	0.02	0.80	1.029	1.202	0.994
Ca	0.0051	0.37	0.23	0.73	1.002	1.037	0.968
Fe	0.6091	47.95	21.00	5.68	1.106	0.989	1.000
Total	**1.0000**	**100.00**	**100.00**	**0.62**			

EDS spot analysis of "C" in bottom image (Fig. 4.14a). This is a crystal that appears to have grown during the reaction.

Fig. 4.14b - EDS spot analyses of areas labeled in images in Fig. 4.14b.

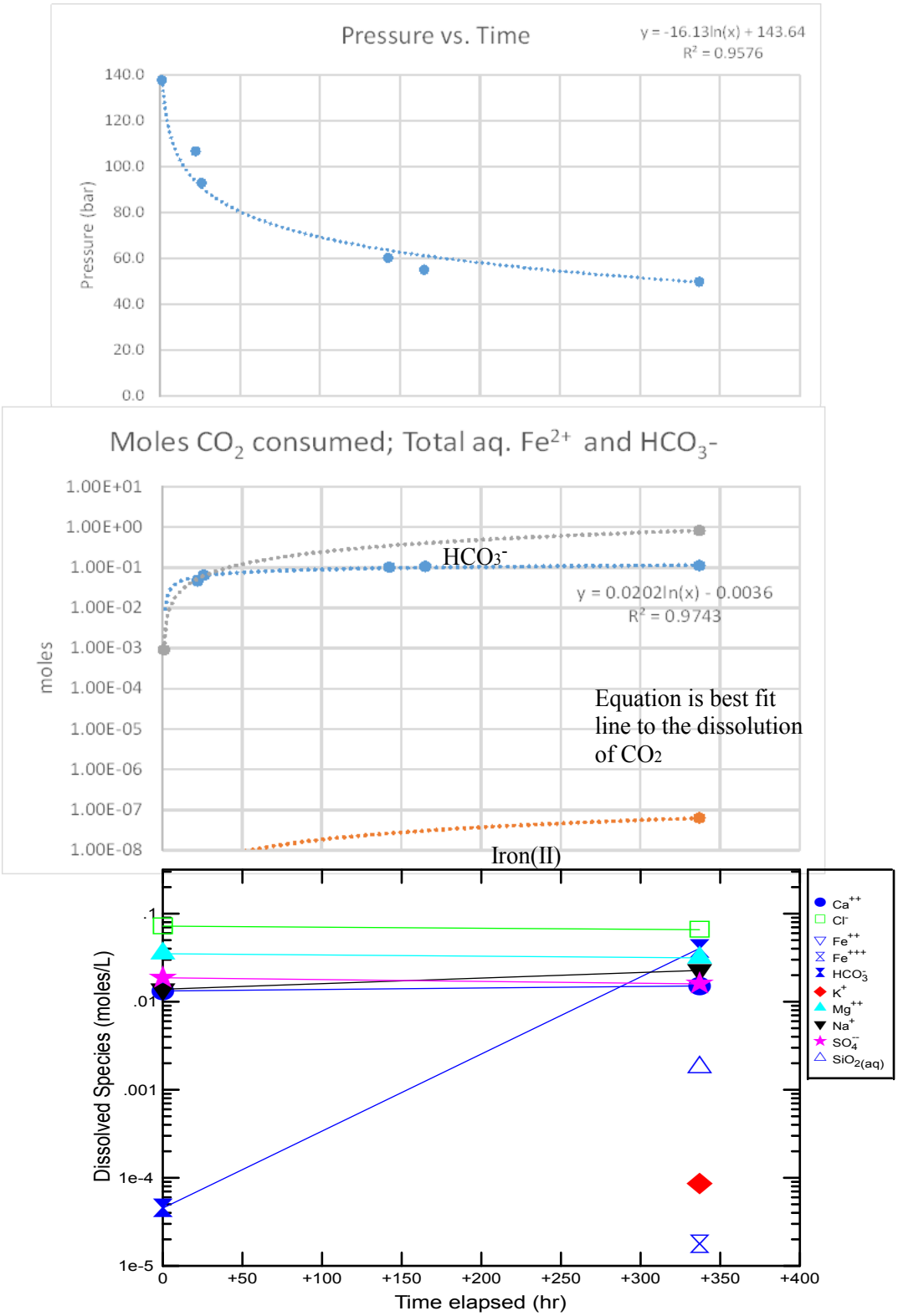

Fig. 4.15 - Experimental data for batch reaction of "substituted hematite." In center graph the line for the dissolution rate of CO_2 into solution is measured. The lines for bicarbonate and iron(II) are inferred based on beginning and end points.

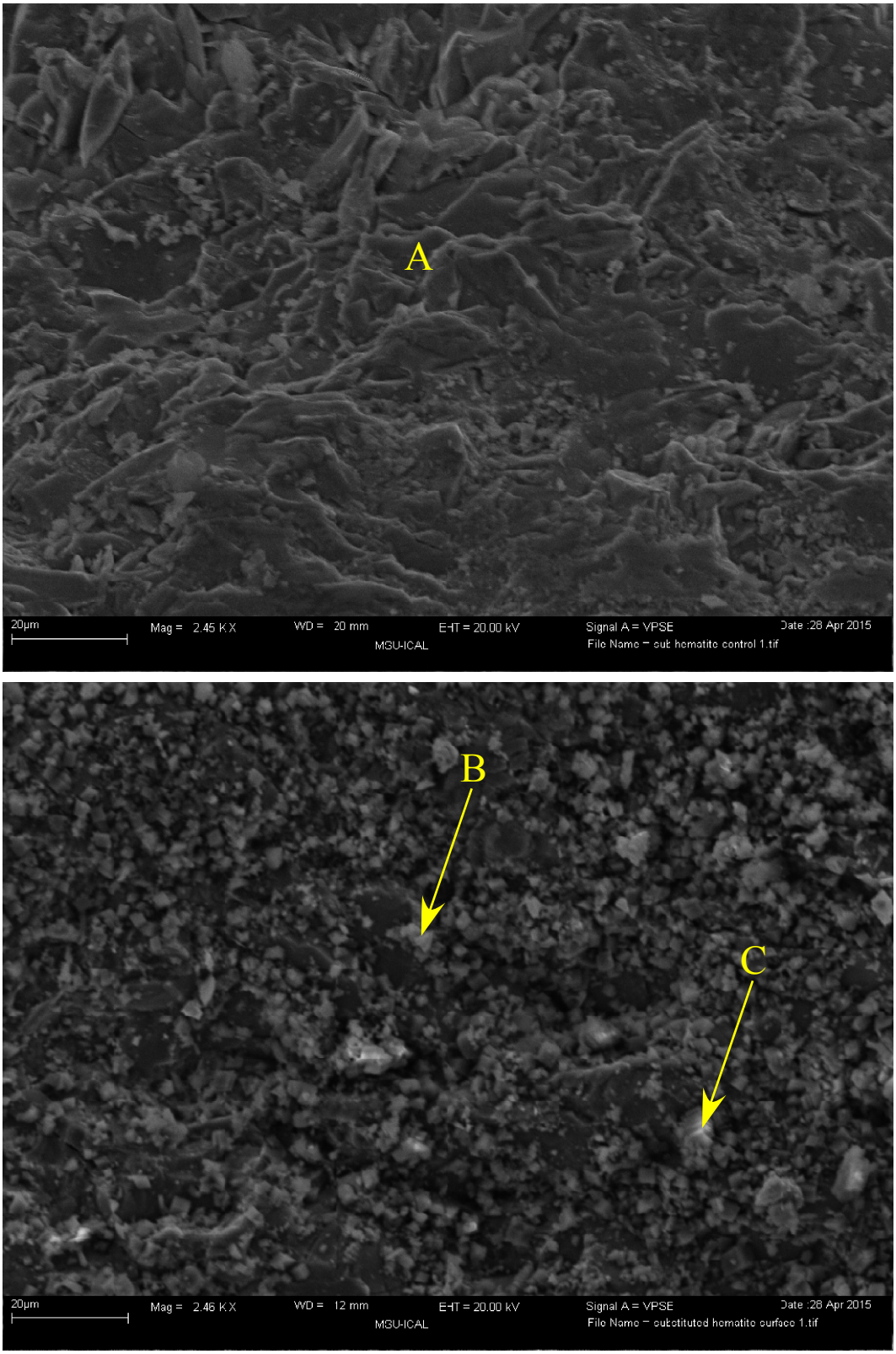

Fig. 4.16a - The top photo shows the surface of substituted hematite before reaction with brine-CO_2. The bottom photo shows after. Note the extensive crystal formation present in the bottom photo. EDS analysis shows the crystals to be predominantly composed of iron and oxygen.

Element	KRatio	Wt%	At%	ChiSquared	Z Corr	A Corr	F Corr
C	0.0109	3.04	6.34	0.10	0.895	4.399	0.999
N	0.0158	3.03	5.40	0.50	0.899	3.015	0.996
O	0.2938	41.31	64.55	1.18	0.908	2.182	0.998
Mg	0.0002	0.06	0.06		0.964	3.511	1.000
Si	0.0017	0.21	0.19		0.969	1.845	0.999
Ca	0.0013	0.09	0.06		0.996	1.038	0.966
Fe	0.6763	52.26	23.40	0.68	1.099	0.989	1.000
S	0.0000	0.00	0.00		0.979	1.312	0.997
Total	**1.0000**	**100.00**	**100.00**	**0.04**			

EDS analysis for entire area of photo around A

Element	KRatio	Wt%	At%	ChiSquared	Z Corr	A Corr	F Corr
N	0.0101	1.99	3.84	0.94	0.889	2.966	0.996
O	0.2814	39.77	67.18	1.68	0.898	2.089	0.998
Mg	0.0019	0.50	0.56	1.16	0.955	3.645	1.000
Si	0.0049	0.68	0.66	1.30	0.961	1.904	0.999
Cl	0.0000	0.00	0.00	1.38	1.014	1.227	0.993
Ca	0.0113	0.85	0.57	1.38	0.987	1.045	0.965
Fe	0.6904	56.20	27.19	3.76	1.088	0.992	1.000
Sr	0.0000	0.00	0.00	1.18	1.165	1.444	1.000
Total	**1.0000**	**100.00**	**100.00**	**0.47**			

EDS spot analysis for B

Element	KRatio	Wt%	At%	ChiSquared	Z Corr	A Corr	F Corr
C	0.0005	0.11	0.48		0.777	3.147	0.999
N	0.0012	0.19	0.67	0.41	0.798	2.004	0.998
O	0.0309	3.63	11.47	1.92	0.817	1.473	0.995
Mg	0.0002	0.03	0.07		0.878	1.851	1.000
Si	0.0001	0.01	0.02		0.882	1.307	1.000
Ca	0.0095	0.85	1.07	0.21	0.908	1.020	0.987
Fe	0.9577	95.18	86.23	0.69	1.014	1.000	1.000
Total	**1.0000**	**100.00**	**100.00**	**0.10**			

EDS spot analysis for C

Fig. 4.16b - EDS data for labeled areas in Fig. 4.16a.

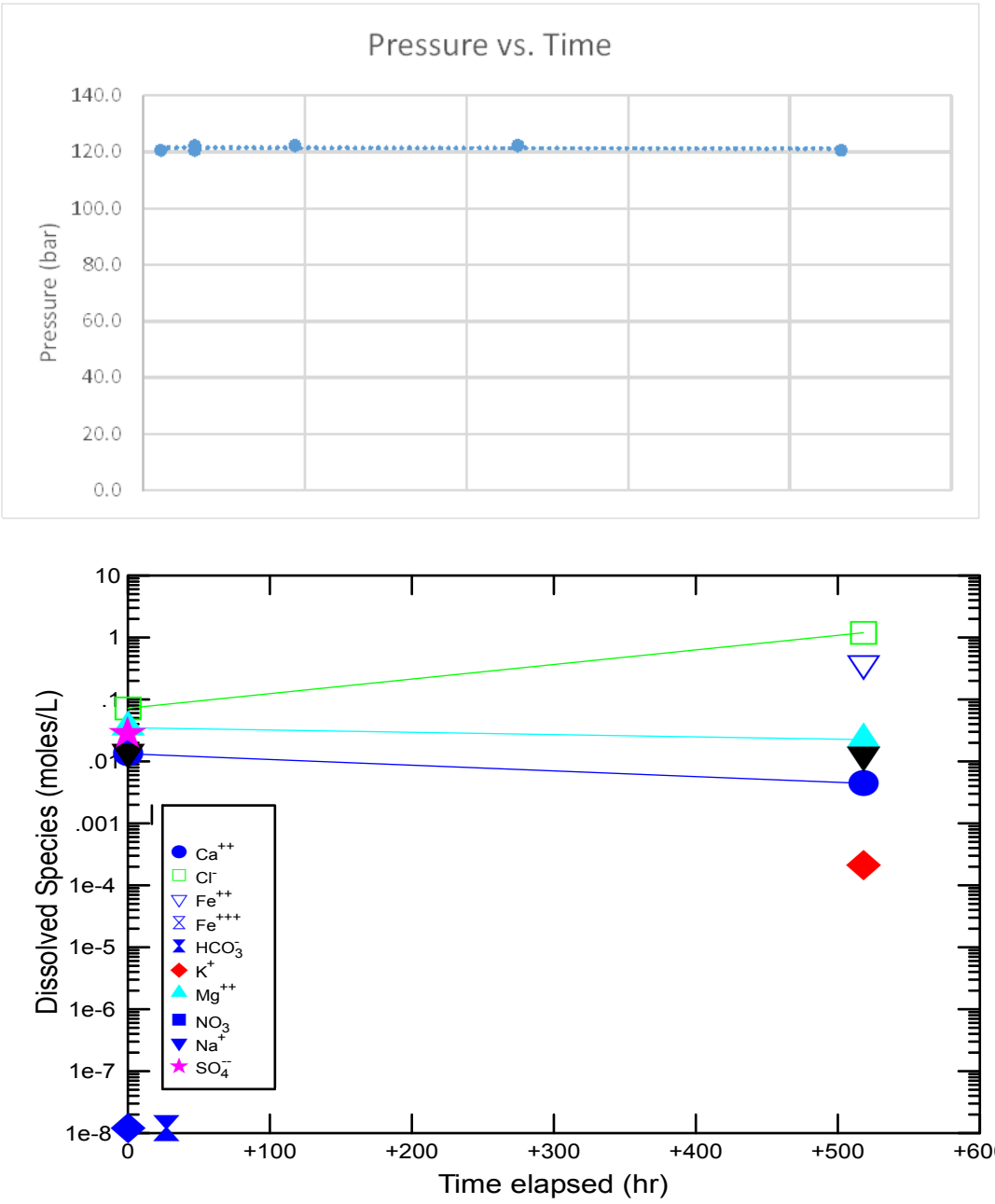

Fig. 4.17 - Iron(II) chloride batch reaction. No detectable reactions occurred during this experiment.

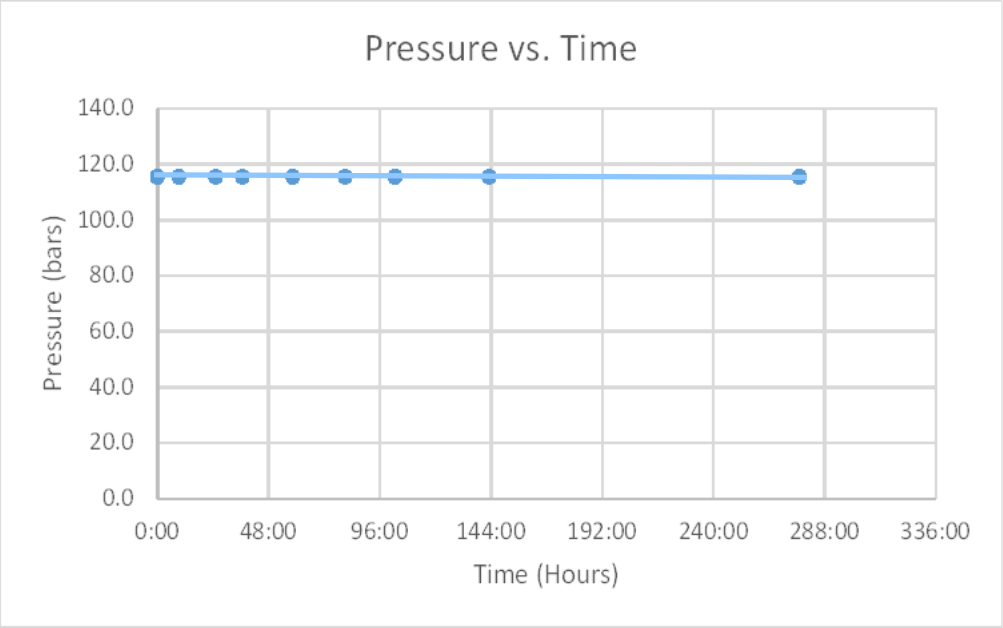

Fig. 4.18 - Hematite experiment pressure vs. time.

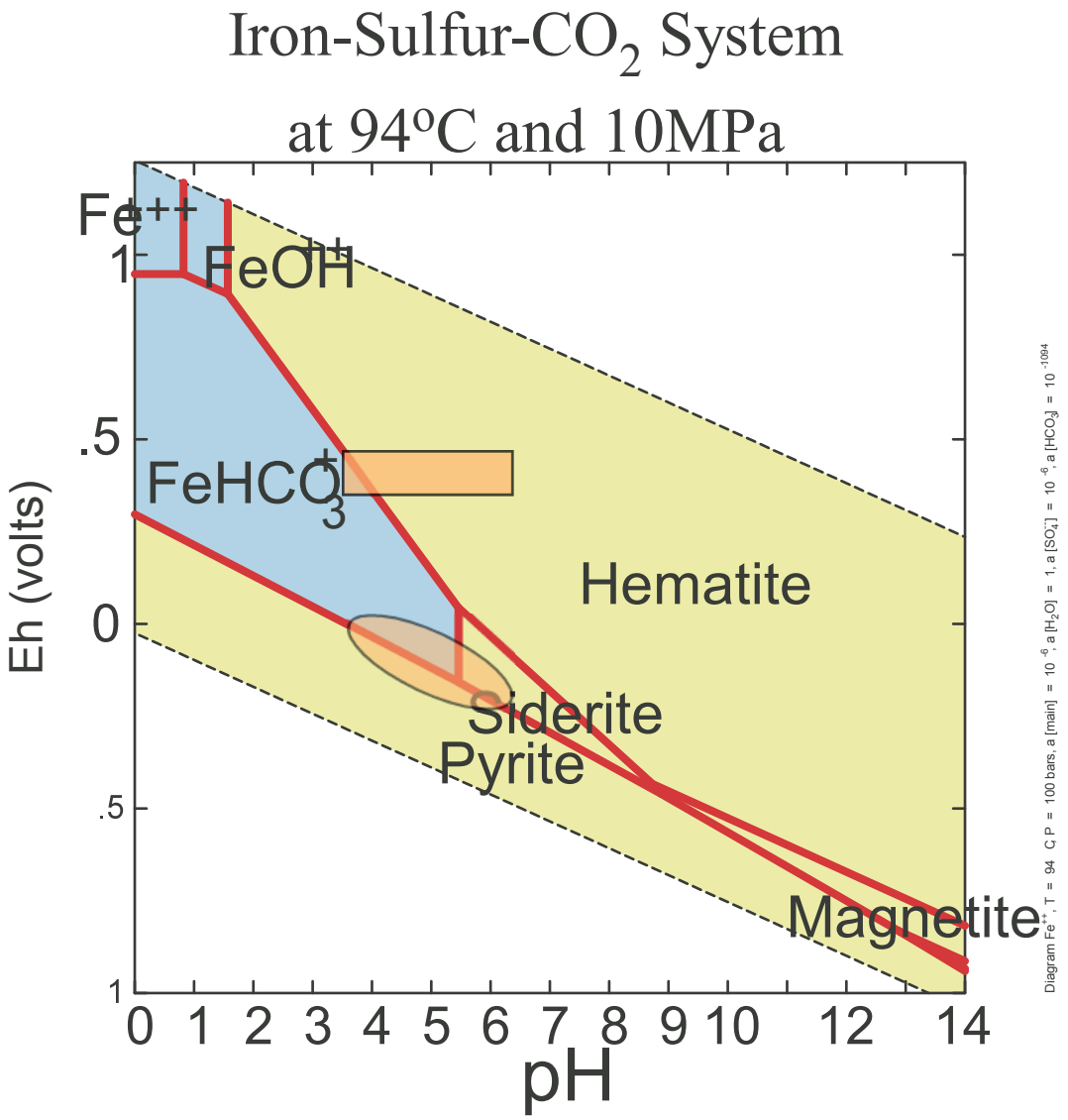

Fig. 4.19 - pH Eh diagram for the iron-carbon dioxide-sulfur system. The box outlines the pH-Eh range of the experiments. Eh was calculated in Geochemist's Workbench using the ratio of iron(II) to iron(III) in the water samples. The ellipse represents the possible Eh of the pyrite experiments prior to the possible oxidation of any dissolved sulfide that would have occurred prior to opening the reaction vessel. Diagram constructed in Geochemist's Workbench for 94°C and 100bars. The activity of water is 1, the activity of HCO_3^- is $10^{-.1094}$, the activity of all other species is 10^{-6}.

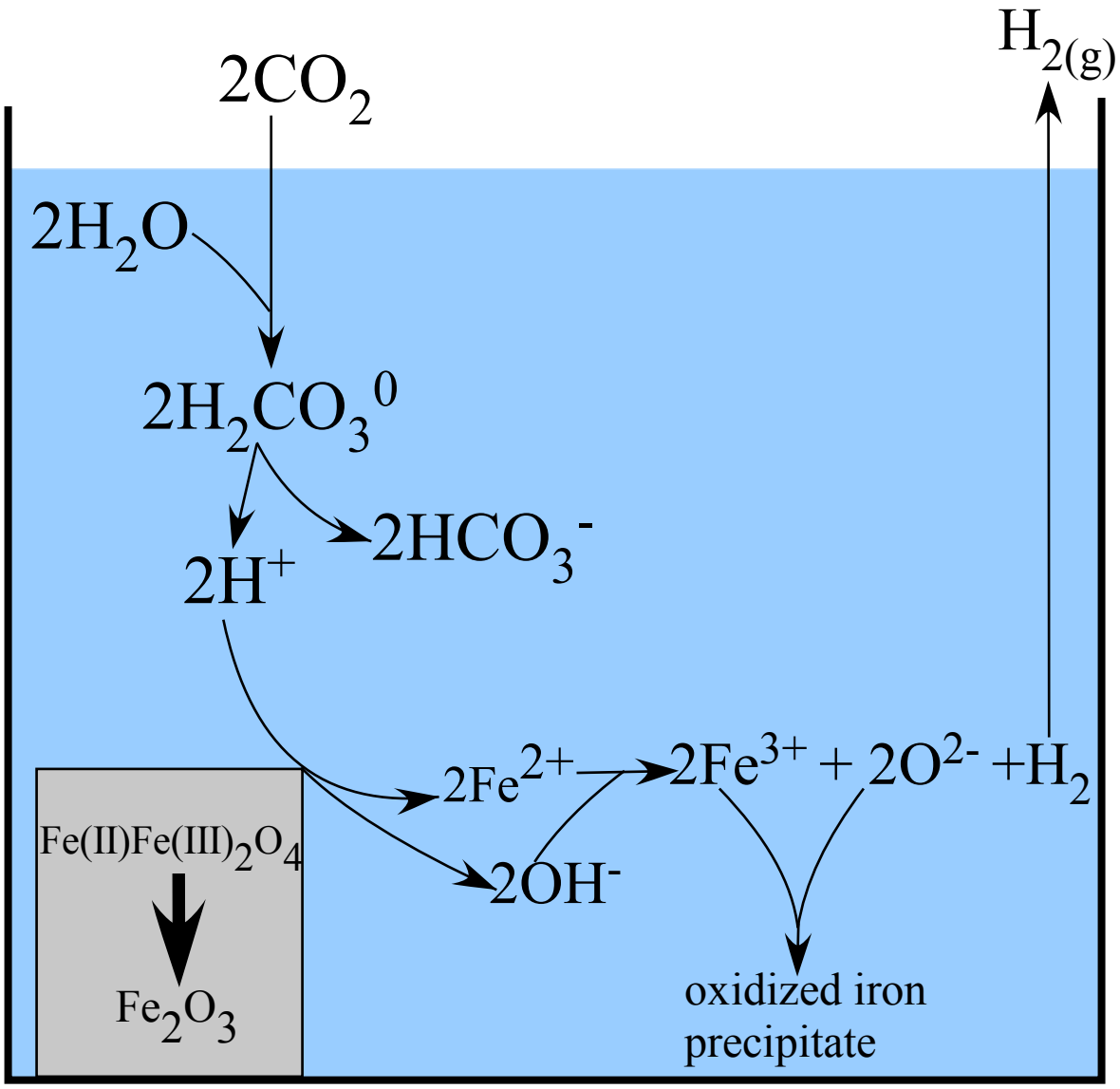

Fig. 4.20 - A model showing potential chemical pathways for the reaction of $scCO_2$ with magnetite. Carbonic acid is formed by the dissolution of CO_2. The protons react with the magnetite and preferentially dissolve iron(II) from the mineral. The iron(II) is then oxidized to yield iron(III) and hydrogen gas. Iron(III) then precipitates as an oxide. The removal of iron from the system by precipitation either has the possibility of driving the CO_2 dissolution reaction forward or hindering it by covering the magnetite with insoluble precipitate.

CHAPTER 5 – INVESTIGATION OF THE REACTION OF MUSCOVITE AND CO_2 UNDER SIMULATED GEOLOGIC SEQUESTRATION CONDITIONS

Introduction

The results of the experiments on the Berea sandstone in Chapter 3 suggested that muscovite (as both authigenic cement and detrital grains) could be a reactive phase. However, it proved difficult to distinguish any signal from muscovite relative to the other minerals in flow-through experiments. Therefore, two experiments were conducted with samples of muscovite in a Parr reaction vessel at (95°C, 120 bars) to better understand the behavior of the muscovite-brine-scCO_2 system.

Hypothesis

It was hypothesized that the carbonic acid generated by the dissolution of scCO_2 into the brine would result in the dissolution of muscovite and the formation of kaolinite via the reactions:

$$2KAl_2(AlSi_3O_{10})(OH)_{2(muscovite)} + 16H^+_{(aq)} \rightarrow 2K^+_{(aq)} + 6Al^{3+} + 6SiO_{2(aq)} + 8H_2O_{(l)} + 4OH_{(aq)} \quad (5.1)$$

$$6Al^{3+}_{(aq)} + 6SiO_{2(aq)} + 3H_2O(l) + 4OH^-(aq) \rightarrow 3Al_2Si_2O_5(OH)_{4\ (kaolinite)} + 6H^+(aq) \quad (5.2)$$

Evidence of these reactions would include dissolution textures on the muscovite, dissolved potassium, silica, and aluminum and potentially the growth of kaolinite crystals.

Experimental

Two experiments of 72 hours and 588 hours were conducted to determine the extent of the reaction of muscovite. These were compared to a control experiment (described in Chapter 4). The experimental procedure followed is described in Chapter 4 with the exception of the solid phase sample preparation. The muscovite was in the form of a large crystal 4cm x 4cm x 0.25cm (Fig. 5.1). The sheets of the crystal were separated and clipped into tabs approximately 1cm x 2cm. A 6g sample was weighed for each experiment and 3 grams was crushed to finer than 10 mesh. These were placed in the Teflon cup in the Parr reaction vessel (Fig. 5.1) with 20mL of brine (Berea recipe, Table 2.1). The vessel was deoxygenated (see Appendix I) and charged with ultra-pure CO_2. The vessels were placed in an incubator at 96°C for the respective times (72 hours and 588 hours). After the experiments the solid sample was dried under vacuum and the brine chemistry was analyzed (see Chapter 2).

Muscovite Sample

The muscovite sample used in these experiments was obtained from Earth's Treasures in Bozeman, MT. It was characterized by SEM-EDS analysis and determined to be of high purity (Fig. 5.2). The only impurities were traces of sodium and iron (0.7% and 0.3% by atomic % respectively).

Results

These experiments were compared to the control experiment described in Chapter 4.

Muscovite Batch Reaction 1 (72 hours)

The 72 hour experiment showed little evidence of reaction as no CO_2 depletion was measured (Fig. 5.3). Dissolved potassium concentrations were lower than those present in the control (5ppm vs. 22ppm) and dissolved silica was below detection. The mineral showed no evidence of dissolution under SEM. The only notable chemical changes were a slight increase in dissolved Na^+ (from 279ppm to 324ppm), and a decrease in Ca^{2+}, Mg^{2+}, and Cl^-. The sodium may have been leached from the muscovite, or may have been concentrated by evaporation, with the other ions being depleted by preferentially precipitating as salt around the edge of the Teflon liner. The final pH was 5.5.

Muscovite Batch Reaction 2 (588 hours)

There was evidence of muscovite dissolution in this experiment (Fig. 5.4). While the K^+ concentration (14ppm) was still lower than in the control (22ppm), there was measurable dissolved silica (39ppm). No dissolved silica was measured in the control. Dissolved iron(II) was around 8ppm, which is higher than the control (5ppm) and may reflect a contribution from the muscovite. Extensive dissolution textures were visible under FEM (Fig. 5.5). The sodium concentration increased from 324ppm to 388ppm, which may indicated leaching of Na^+ from the muscovite or may indicate concentration

via evaporation. Other species (e.g. calcium and chloride) were substantially depleted (540ppm to 84ppm and 2598ppm to 1745ppm), by precipitation as salt. The tops of the muscovite crystals stuck out slightly from the top of the brine and provided a surface for the precipitation of salt. The salt was green-white due to nickel oxide contamination from the corrosion of the Parr vessel's corrosion proof nickel coating. There does not seem to be evidence of kaolinite precipitation based on examination by FEM. The final pH was ~6.

Discussion

The dissolution of muscovite was slow, and did not proceed quickly enough to be measured during the course of a 72 hour experiment. Therefore, it is unlikely that the chemical signature of muscovite dissolution would be measurable in a 72 hour flow through experiment on the Berea sandstone. The amount of aqueous silica measured in the 588 hour experiment corresponds to the dissolution of 35mg of muscovite or around 0.5% of the mass of the muscovite used in the experiment. This amount of dissolved silica theoretically corresponds to an equivalent molar amount of dissolved aluminum (this was not measured). Since no new aluminum containing precipitates were found, the assumption is made that the aluminum was probably dissolved.

The saturation indices of various minerals were calculated in MinTEQ using the experimentally determined water chemistry data and the calculated aluminum concentration (at pH 6, 96°C). The solution was oversaturated with respect to kaolinite, but also oversaturated with respect to gibbsite and amorphous solid $Al(OH)_3$. At pH 6, aluminum preferentially speciates as $Al(OH)_3^{0}{}_{(aq)}$ (46%) and $Al(OH)^{4-}$ (51%). Only a

small amount (0.04%) speciates as $AlH_3SiO_4^{2+}$, a precursor to kaolinite precipitation. Thus gibbsite or $Al(OH)_{3(am)}$ would probably be the dominant aluminum precipitate, at least initially. A phase diagram of the silica-potassium-aluminum system shows that the water chemistry in the second muscovite batch experiment was in equilibrium with muscovite at the end of the experiment (Fig. 5.6). This equilibrium may inhibit the formation of kaolinite or gibbsite even though the water is saturated with respect to both phases. The diagram suggests that a decrease in pH and/or K^+ may be required to facilitate the precipitation of one of these two phases. Interestingly, the conditions created in a flow-through experiment do remove K^+ and maintain a lower pH than the batch experiment, which theoretically could create conditions favorable for the formation of kaolinite or gibbsite, but the slow muscovite dissolution rate observed in the batch experiment would still apply in the flow-through environment which means that muscovite dissolution and kaolinite or gibbsite formation is unlikely during the course of a 72 hour flow-through experiment.

Conclusions

The dissolution of muscovite was not measurable on the time scale of a 72 hour experiment but was observable under FEM, and chemically measurable in the 588 hour experiment. No new precipitates were formed in either experiment, although the water was saturated with respect to kaolinite, gibbsite, and amorphous $Al(OH)_3$ as modeled in MinTEQ. A modeled phase diagram of the silica-potassium-aluminum system showed that the water in second muscovite batch experiment was in equilibrium with muscovite.

This suggests that unfavorable pH and K^+ levels possibly had an inhibitory effect on the precipitation of phases such as kaolinite or gibbsite.

Fig. 5.1 - Muscovite sample from Earth's Treasures. The whole sample is at the bottom and the trimmed pieces used for one of the experiments are in the cup at top.

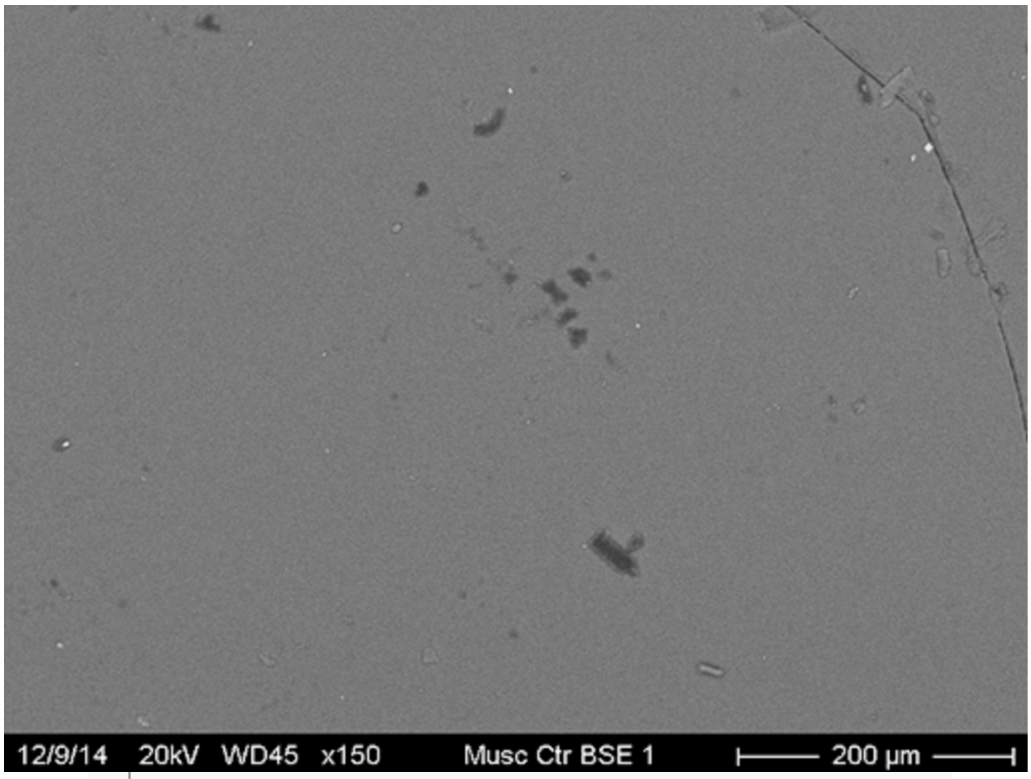

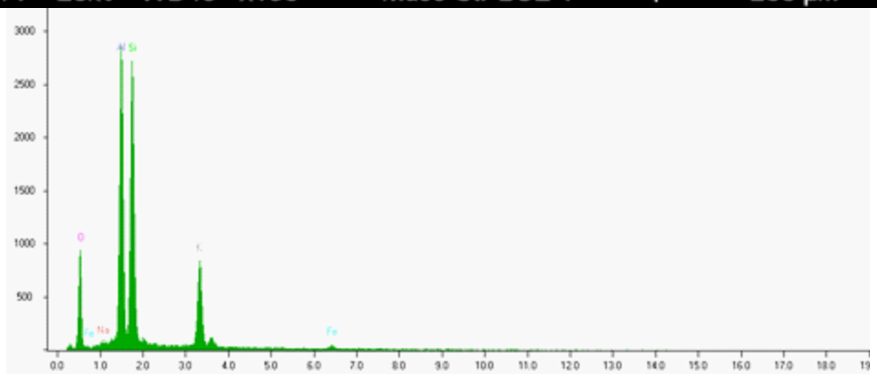

RONTEC EDWIN WinTools MUSCCTR1 09.12.2014 (16:26)

NT vers: 3.2 eng Eo:20.0 keV (TO:40.0 TI:-4.0)

*** PUzaf results ***

elem/line	P/B	B	F	c	c(atom)	confid.	h
O K-ser @	1.00000	1.00000	48.61	60.88	+- 5.77	n	
Fe K-alpha 10.1	1.02740	1.09129	0.75	0.27	+- 0.09		
Na K-ser @ 5.7	1.00255	1.00884	0.81	0.70	+- 0.21		
Al K-ser 195.1	1.00742	1.01325	21.09	15.66	+- 1.24		
Si K-ser 260.9	1.00958	1.00492	24.77	17.67	+- 1.31		
K K-alpha 121.6	1.01839	1.01407	9.39	4.81	+- 0.40		
standardless		105.43	100.00	[1s]			

Atomic %

Fig. 5.2 - Muscovite crystal under SEM (150x) along with EDS elemental analysis of entire picture area.

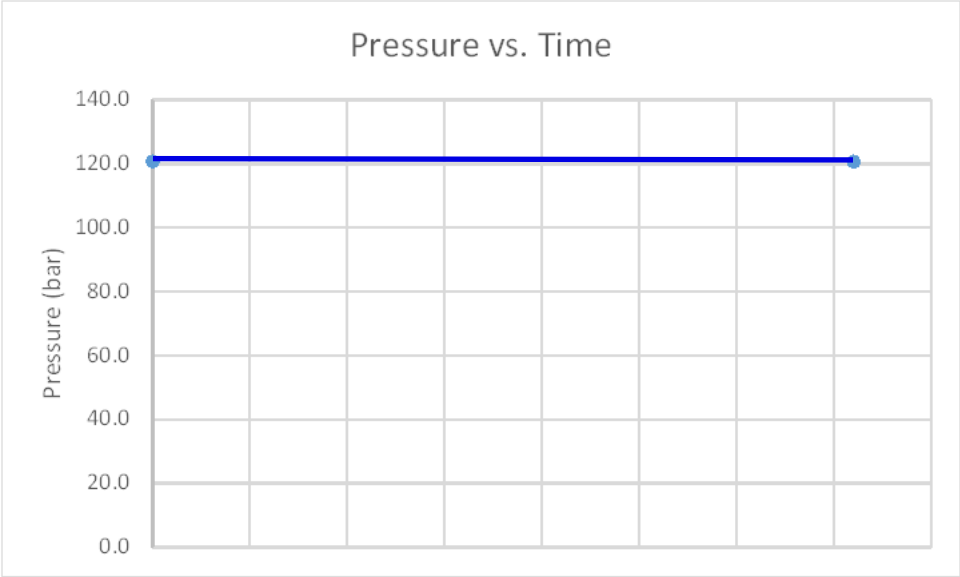

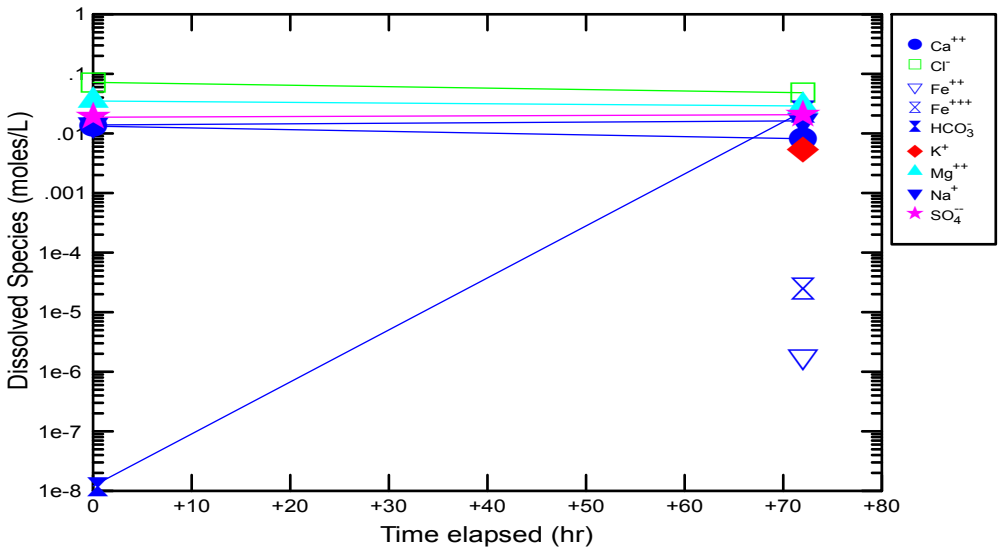

Fig. 5.3 - Experimental data for muscovite experiment 1.

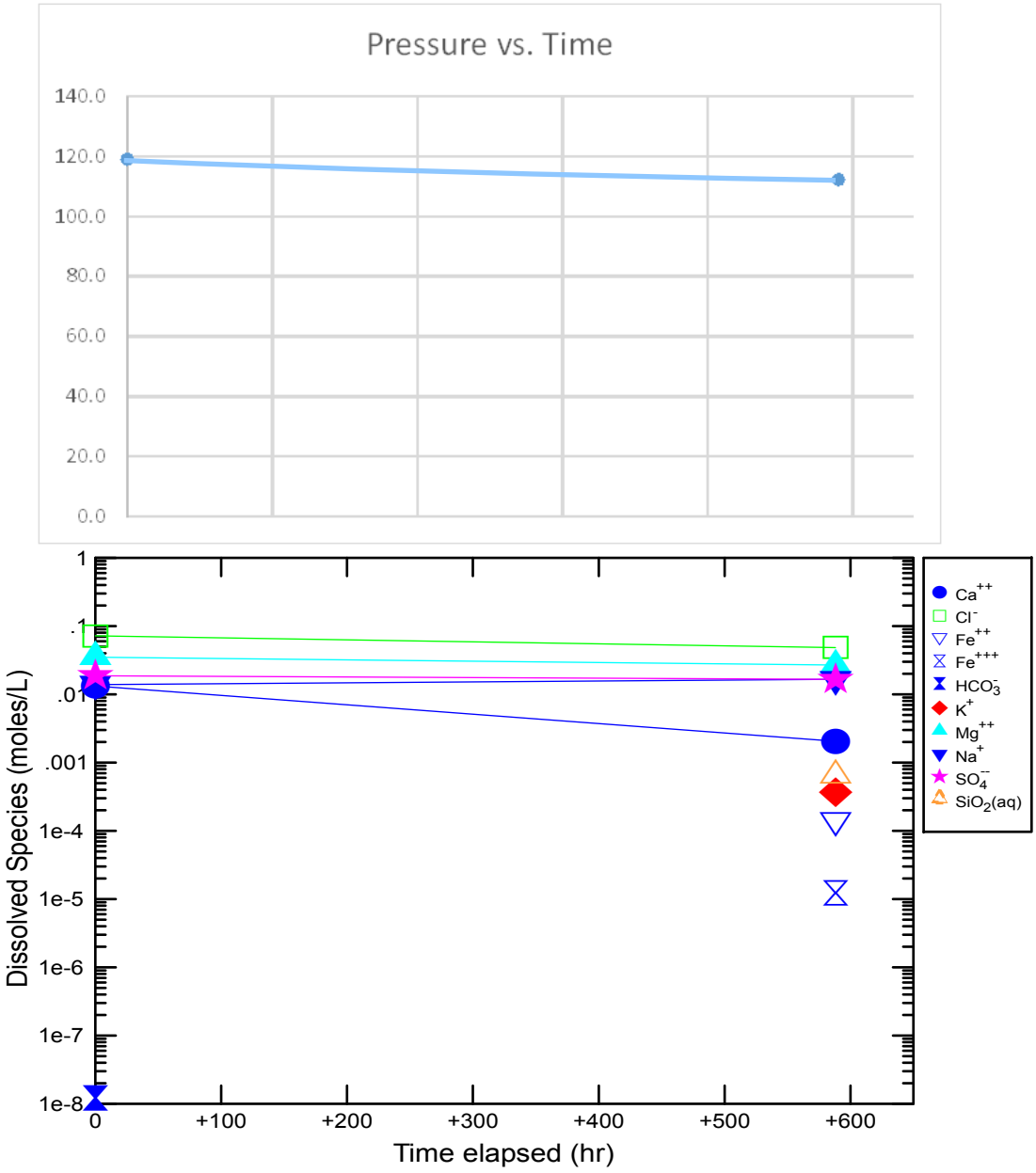

Fig. 5.4 - Experimental data for muscovite experiment 2.

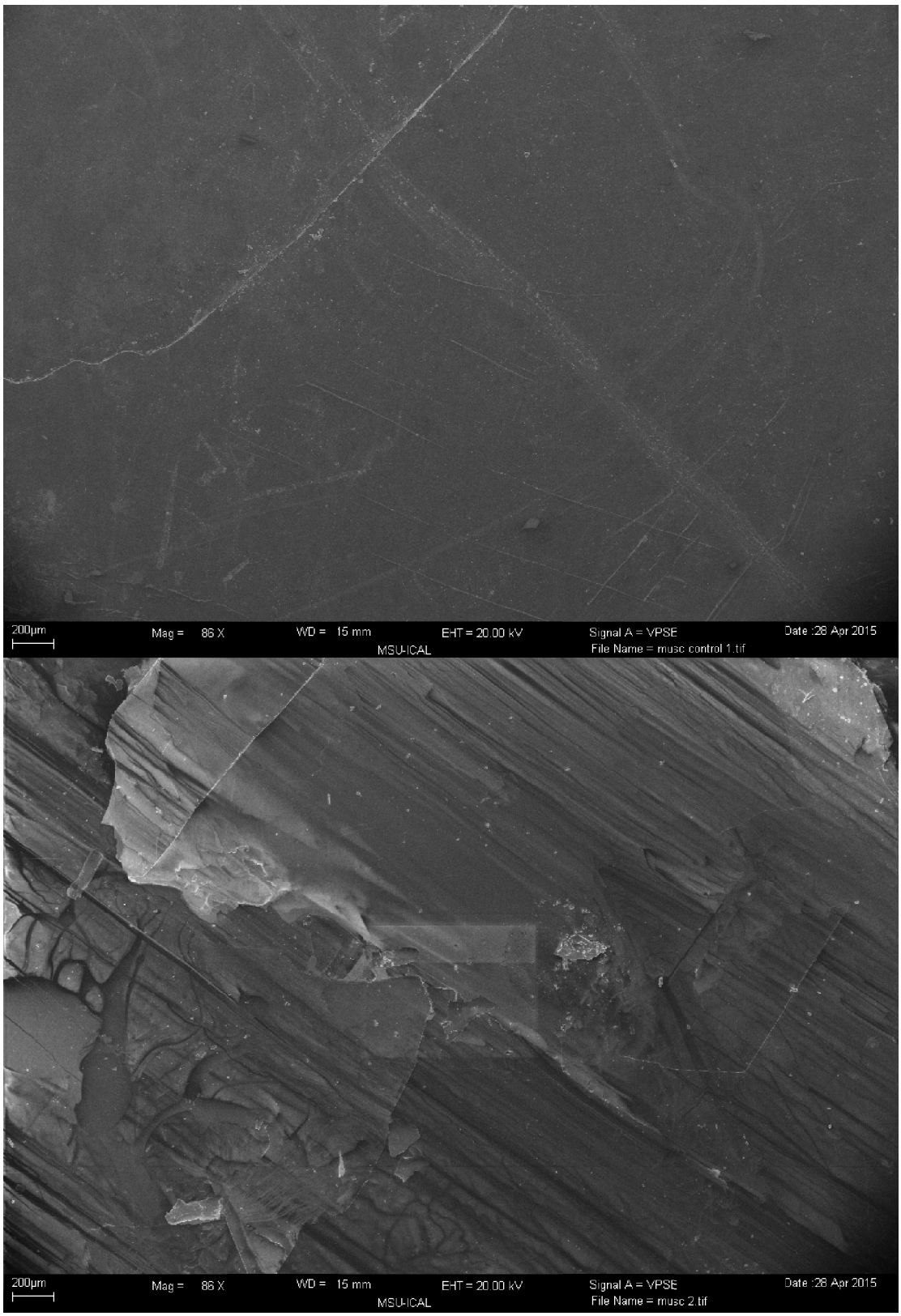

Fig. 5.5 - FEM images of a muscovite crystal before (top) and after (bottom) the 588 hour batch reaction experiment. Note the extensive dissolution textures in the bottom photo.

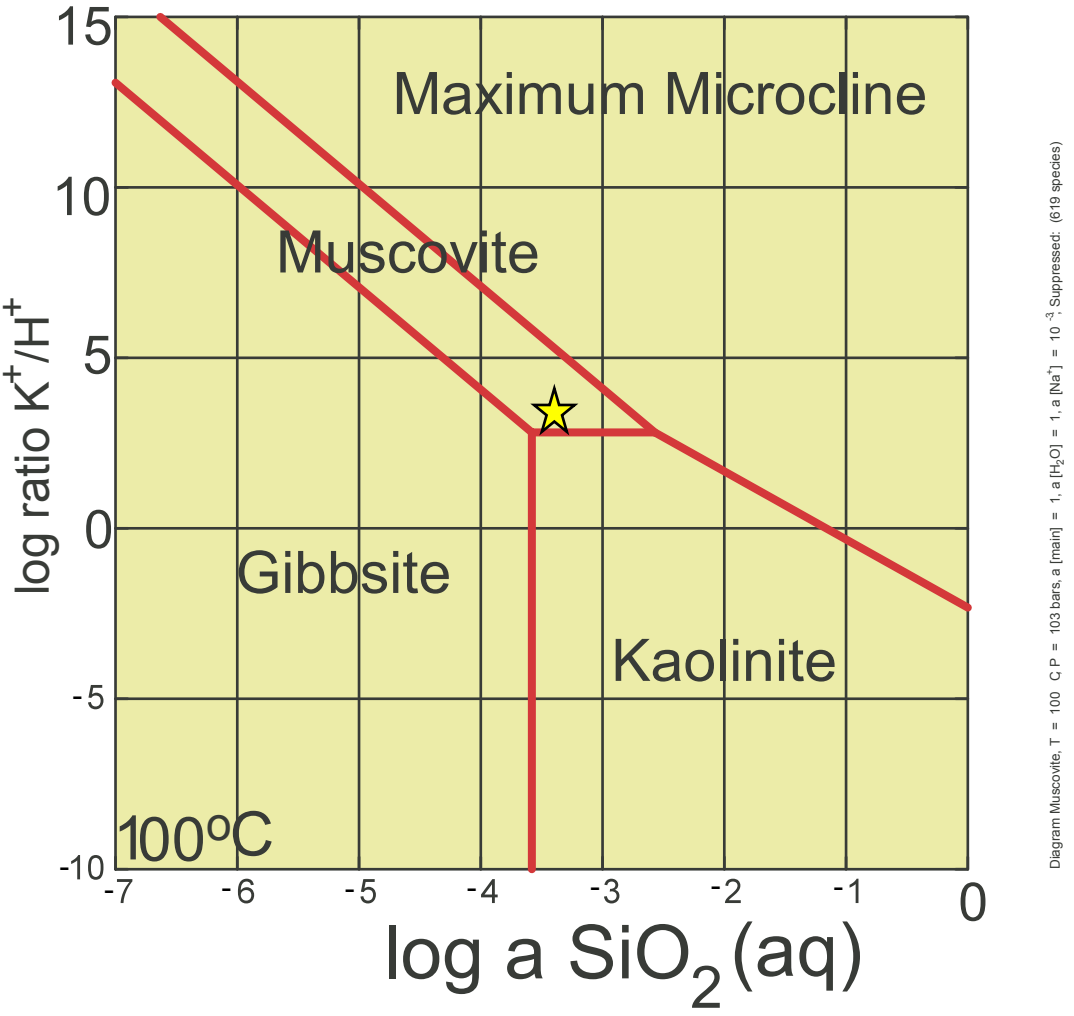

Fig. 5.6 - Potassium silica aluminum phase diagram. The star represents the chemical composition of the sample from muscovite Exp. 2. The phase diagram was constructed in Geochemist's Workbench for a system at 100°C and 103bars. It assumes the activity of water is 1 and the activity of Na^+ is 10^{-3}. All species other than those labeled were suppressed.

CHAPTER 6 – EVALUATION OF A JEFFERSON FORMATION OUTCROP IN SUN CANYON AS AN ANALOG FOR THE JEFFERSON IN THE KEVIN DOME

Introduction

To aid preparation of Big Sky Carbon Sequestration Partnership's megaton scale injection project in the Kevin Dome a study of an outcrop analog of the Jefferson Formation was conducted. The goals of the study were to identify reservoir zones and retrieve samples for analysis and experiments.

The Jefferson Formation lies in the subsurface in the Kevin Dome vicinity, but outcrops in several areas around Montana including the Rocky Mountain Front, the Little Belt Mountains, and Tobacco Root Mountains (Fig. 6.1). Candidate sections in all three locations were reconnoitered, and an outcrop in the Rocky Mountain Front in Sun Canyon, was chosen.

Locations in the Tobacco Roots were deemed far enough away from the Kevin Dome that they might have sedimentological differences. They were also thinner than at the Kevin Dome. An outcrop in the Little Belts, while otherwise suitable, proved difficult to describe and quarry because it outcropped as a vertical cliff. The outcrop in Sun Canyon was chosen because of its proximity to the Kevin Dome (Fig. 6.2), ease of access, and suitability for quarrying blocks.

The Jefferson Formation was brought to the surface of the fold and thrust belt (also known as "the disturbed belt") of the Rocky Mountains during the extensive folding the thrusting which took place during the late Cretaceous and early Paleocene, (Mudge, 1972) (Fig. 6.1). Faulting created a topography of north-south trending ridges and

valleys. The erosion resistant Madison Group forms the ridges which tower over valleys occupied by recessive Cretaceous and Jurassic mudstones and sandstones (Mudge, 1972). Rocks along the eastern edge of the belt are typically younger Cretaceous and Mississippian rocks. Older Devonian, Cambrian, and Paleozoic strata are more common to the west. The "Home Thrust" emplaced the Jefferson and the Madison Group on top of the Cretaceous Blackleaf and Kootenai Formations (Mudge, 1972).

The Sun River dissects a succession of eastward verging imbricate thrust sheets that dip to the west at around 40º (Mudge, 1972). Access to the west, where exposures of the Jefferson are more common is difficult, as it is located in the remote and roadless Bob Marshall Wilderness.

The outcrop was measured and described. Two beds were selected for block/core sampling. The first was a dolomite bed with abundant macroscale porosity and the second was an argillaceous dolomite bed. Both facies were analyzed for porosity, permeability, mineralogy, chemical composition, and texture. The goal was to conduct laboratory experiments to determine the rocks' reaction to CO_2 injection, but technical delays made this unfeasible. This analysis can instead provide the foundation for future laboratory experiments or field studies.

Field Work

Field Area

The area selected for analysis and sampling is located along Sun Canyon Road, 20 miles west of Augusta, MT (Fig. 6.2). The Jefferson Formation is exposed on both sides of Diversion Lake and in Home Gulch (Fig. 6.3 & 6.4). Rocks in the area range in age

from Cretaceous to Devonian (Fig. 6.5). The Jefferson Formation is stratigraphically overlain by the Devonian Three Forks Formation, the Mississippian Madison Group, and Jurassic and Cretaceous rocks (Mudge, 1972). It is underlain by the Devonian Maywood Formation and Cambrian strata (Mudge, 1972) (neither of which are exposed in the field area). The Lower Jefferson is the equivalent of the Duperow in the Kevin Dome and the Birdbear is the equivalent of the Nisku (Fig. 6.6).

Stratigraphy and Sedimentology

The Jefferson is of Frasnian age (Alcorn, 2012) it is composed of two members, the Lower Jefferson and the overlying Birdbear. The Lower Jefferson is composed predominantly of dolomite. The Birdbear is interbedded dolomite and argillaceous dolomite. The Jefferson was measured and described on the north side of Diversion Lake, where it is exposed in its entirety (Fig. 6.7). The goal was to locate the best reservoir zones and sample them. The Jefferson in this location is 120m thick (Lower Jefferson is 90m thick, the Birdbear is 41m) (Fig. 6.8).

There are several reservoir zones in the Lower Jefferson (6-7m, 27-35m, 71-75m, 80-90m) and two thinner ones in the Birdbear (117-118m and 121-124m) (Fig. 6.8). All are dolomite beds marked by a vuggy texture and little recognizable depositional fabric. Thin section examination shows them to be “crystalline carbonates” composed of euhedral dolomite crystals with little evidence of primary texture (Fig. 6.18).

It is theorized by the author that these beds are highly altered stromatoporoid boundstone (reef) facies. Three pieces of evidence support this assertion:

1.) The beds must have had high primary porosity and permeability in order to conduct sufficient fluids to allow for full, or nearly full recrystallization. Beds immediately above and below the vuggy beds were not altered in this fashion. Reef boundstones would have the required primary porosity and permeability to facilitate the movement of dolomitizing fluids.
2.) There are beds in nearby outcrops that have both a vuggy texture and features identified as stromatoporoid fossils (47°36'1.34"N; 112°46'36.13"W) (Fig. 6.9).
3.) Cores retrieved from the Kevin Dome showed selective dolomitization of reef facies. The primary depositional texture was preserved in these cores (Bowen and Eby, 2014). Since reef facies were selectively dolomitized in the Kevin Dome it is plausable that the same process operated in the Sun Canyon area.

Stratigraphic Interpretation

The Jefferson Formation is composed of packages of conformable, upward shallowing facies (Van Waggoner et al., 1990) representing successions of adjacent environments on a carbonate platform (Fig. 6.10) (Bowen and Eby, 2014). These packages are also defined as “cycles (or “parasequences” in the sequence stratigraphic nomenclature (Van Waggoner et al., 1990)). These cycles are the rock record of cyclic changes in relative water depth. These stacks of “cycles” can be grouped together into larger “sequences”. A sequence is defined as “a relatively conformable succession of genetically related strata bounded at its top and base by their unconformities or correlative conformities” (Mitchum et al., 1977). A full sequence records a succession of

sediments (or non-deposition) that progresses from a low stand of relative sea level to a high stand, and back to a low stand.

A typical cycle has facies deposited in environments farthest from shore at the bottom and closest to shore at the top (Fig. 6.11). Partial cycles are common, as a particular location does not always undergo complete succession from offshore to nearshore. The transition to the next depositional cycle is signaled by a flooding surface and an unconformable shift to deeper water facies.

There is a hierarchy to these sedimentary cycles. Large scale changes that occur at less frequent intervals are referred to as “low order cycles”. Smaller magnitude, changes that occur more frequently are “higher order” cycles. The Lower Jefferson and Birdbear are composed of two low order cycles separated by flooding surfaces that deposit sediments that are interpreted to be fore reef on top of tidal flat deposits (Fig. 6.12 & 6.13). The bottom low order cycle has at least two higher order cycles within it, separated by a flooding surface that represents a smaller shift in water depth. The overlying low order cycle has at least thirteen higher order flooding surfaces within it. The Birdbear member has been hypothesized to lie conformably upon the Lower Jefferson (Mudge, 1972). The bottom of the Birdbear does mark a period of clastic influx, indicating a change in depositional conditions.

Sampling

Sampling was conducted in three locations. Blocks of a reservoir zone of the Lower Jefferson (Facies #1) were quarried from a location on the north side of the lake (47°36'59.73"N; 112°43'15.09"W) and at the base of the small round knoll in Home

Gulch (47°36'45.85"N; 112°43'10.77"W). A block of the argillaceous zone of the Birdbear Member (Facies #2) was quarried on the south side of the reservoir (47°36'58.97"N; 112°43'18.52"W) (Fig. 6.3).

Rock Properties

The Jefferson Formation samples were analyzed for porosity and permeability, mineralogy (XRD), chemical composition (XRF), and texture (thin section microscopy). X-Ray diffraction was conducted using the SCINTAG X1 Diffraction System. Results were quantified using the JADE software package. XRF analyses were conducted using a Thermo Scientific Niton XL3t GOLDD portable X-Ray Fluorescence spectrometer.

Jefferson Facies #1 (Measured Section 83-90m)

This facies was chosen for sampling because of its relatively high macroscale porosity relative to other facies. The block used for these analyses came from sampling location #2. It was trimmed to measure 48cm x 48cm x 10cm (Fig. 6.14). The block had abundant vugs ranging in size from 0.25cm to 1cm. Filled bedding parallel fractures are present. No depositional textures were readily visible.

Two cores were cut for flow through experiments. They were partitioned as shown (Fig. 6.15). Core A had a porosity of 7.03% and a permeability of 1.37+/-0.05mD. Core B had a porosity of 7.55%. The permeability of core B was not measured due to technical difficulties with the flow through reactor. Cores were drilled in such a way that vugs and open fractures were avoided. Therefore, measurements reflect the

microscale porosity and permeability of the rock. If the vugs and fractures are included the porosity and permeability values would be higher.

Facies #1 is composed predominantly of dolomite, calcite, and quartz (averaging 91.7%, 7.7%, and 0.6% on respectively) (Fig. 6.16). The elemental composition of the rock reflects the mineralogy (Fig. 6.17). Major elements (>1% by mass) are magnesium (8.2%) and calcium (average 29.3%). Minor elements (<1% by mass) include silica, aluminum, iron, sulfur, strontium, and chlorine. The presence of aluminum and potassium indicates that an aluminosilicate such as potassium feldspar or muscovite may be present in quantities below the detection limit of XRD. Little to no depositional texture is recognizable in thin section (Fig. 6.18). Pores range in size from vugs (1cm diameter) to small pores of <5 μm. Calcite lines most of the vugs and fractures. Dolomite and calcite crystals range in size from 25-100μm, with most being on the upper end of the size range. No silicate minerals are visible in thin section. This rock is interpreted to be a highly altered stromatoporoid reef boundstone.

Jefferson Facies #2 (Measured Section 116-117m)

This facies was sampled because of its high phyllosilicate content. This provides a contrasting sample to facies #1 as the effect that phyllosilicate minerals have on properties of carbonate rocks during $scCO_2$ injection is unknown. The sample of Facies #2 was difficult to handle in the lab due to its fissile nature and cores such as those obtained from Facies #1 could not be obtained. The block was 10cm x 10cm x 5cm in size after trimming. Polishing the block revealed depositional textures including fine laminations, ripple marks, and fossils (Fig. 6.19).

The porosity and permeability of this facies were below detection. However, the fissile nature of this rock could mean that it has fracture porosity that could not be measured on the scale of the samples used in these experiments. Facies #2 has a diverse mineralogical composition (Fig. 6.20). As measured by whole rock XRD, it was composed of 74.1% dolomite, 9.6% quartz, 9.6% muscovite, and 6.7% orthoclase. Peaks indicating kaolinite and albite were also visible. The elemental composition of Facies #2 reflects its greater silicate abundance (Fig. 6.21). Major elements are Mg (5.73%), Ca (14.93%), Si (14.33%), Al (4.35%), K (2.36%), and Fe (1.89%). Minor elements (<1%) include Ti, S, Xr, Ba, Sr, and Rb. In thin section the sample was fine grained (crystals typically <10μm in size). Laminations are readily visible. Silicate minerals cannot be seen, but may be included in the dusky "caps" on the laminations (Fig. 6.22). This rock is interpreted to be a tidal flat deposit, as evidenced by the wavy laminations, fine grained nature, and place in the stratigraphic succession.

Suitability as an Analog to the Kevin Dome

The suitability of the Jefferson Formation outcrop at Sun Canyon as an analog for the Jefferson Formation in the Kevin Dome was determined once cores from the Kevin Dome were retrieved. In 2014 the Big Sky Carbon Sequestration Partnership cored sections of the Jefferson Formation from two wells in the Kevin Dome (Wallewein 22-1 and Danielson 33-17 (Fig. 1.3). The Jefferson Formation in the cores exhibited similarities and differences to the rocks seen in outcrop (Bowen and Eby, 2014).

The sedimentology is similar in both the Kevin Dome cores and the Sun Canyon outcrops but there are also some differences between the two locations, due primarily to

differences in diagenesis. The rocks in the Kevin Dome cores retained much of their primary depositional fabric. In contrast, the rocks in Sun Canyon exhibited erasure of primary depositional fabrics in stromatoporoid boundstone beds and increased frequency of brecciation.

Stromatoporoid boundstone facies are the beds with the highest porosity and permeability in both locations. At Sun Canyon these facies have had most of their original depositional texture erased by diagenesis, but in the Kevin Dome cores they retain their depositional fabric. Features only observed in Sun Canyon outcrops, such as the calcite infilling of pores and fractures, and possibly some vug formation, are likely attributable to groundwater circulation during periods of erosion of the overlying Madison Group (Blount, 1986).

The Jefferson Formation at Sun Canyon had a higher frequency of intraformational breccias than the cores from the Kevin Dome. The breccias in Sun Canyon may have been generated by multiple processes. Some may be evaporate solution breccias, while others were formed by groundwater circulation during orogeny (Blount, 1986). The brecciation at Sun Canyon may also have had a hydrothermal component, as low-grade mineralization was observed in several locations. Brecciation was not limited to specific facies.

It is not clear how extensive brecciation is in the dome. The core from the Wallewein well at Kevin Dome showed some brecciation, but the core from the Danielson only several kilometers away had none. Proximity to volcanic intrusions could have induced brecciation by hydrothermal fluid flow, or the breccia could predate the intrusions and have another cause, such as evaporite solution brecciation.

There are both positive and negative qualities when comparing the Sun Canyon outcrop samples as analogs for the core samples of the Kevin Dome. The mineralogy of the Jefferson Formation is similar in both locations, but the reservoir facies at Sun Canyon are more homogeneous due to recrystallization, while porosity and permeability in the Kevin reservoir facies are more heterogeneous due to the distribution of stromatoporoid fossils.

Conclusions

This study provides a framework for future work on the Jefferson Formation, whether it be carbon sequestration related or sedimentological research.

1. The rocks at Sun Canyon have value as an analog for the Jefferson Formation in the Kevin Dome, but there are caveats.
2. The best reservoirs in the Jefferson Formation are dolomitized stromatoporoid reef facies which are heavily affected by diagenesis.
3. The location of these reef facies is stratigraphically controlled. They cluster towards the tops of low order depositional cycles.

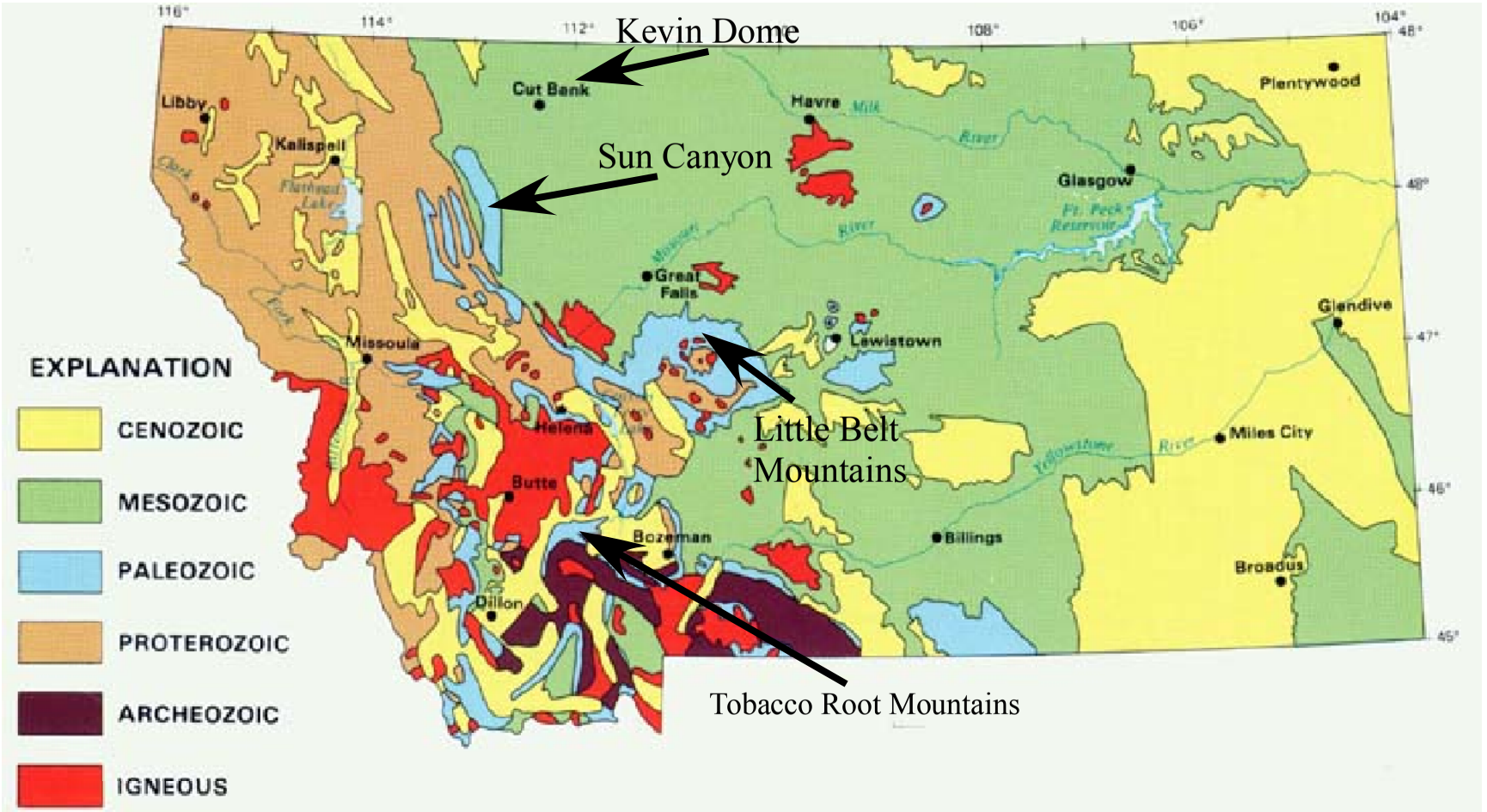

Fig. 6.1 - Geologic map of Montana showing locations of outcrops of various ages. The Jefferson Formation outcrops in the Paleozoic areas. Kevin Dome is the location of the BSCSP's large scale CO_2 injection project. Sun Canyon, the Little Belts, and the Tobacco Root Mountains were all evaluated as potential sites of outcrop analogs for the Jefferson Formation in the Kevin Dome. Map from Montana Bureau of Mines and Geology.

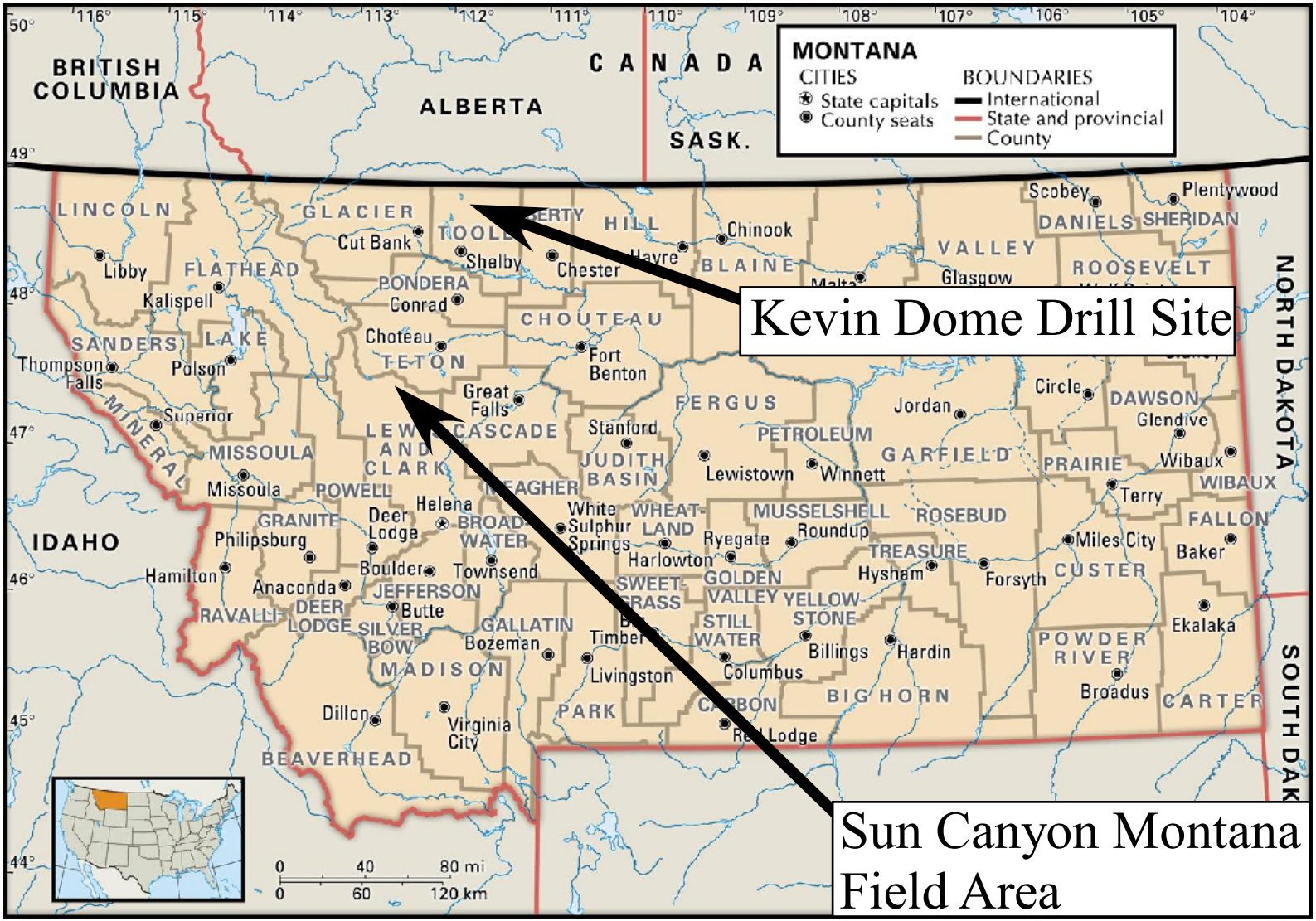

Figure 6.2. - Location of Sun Canyon field area and Kevin Dome

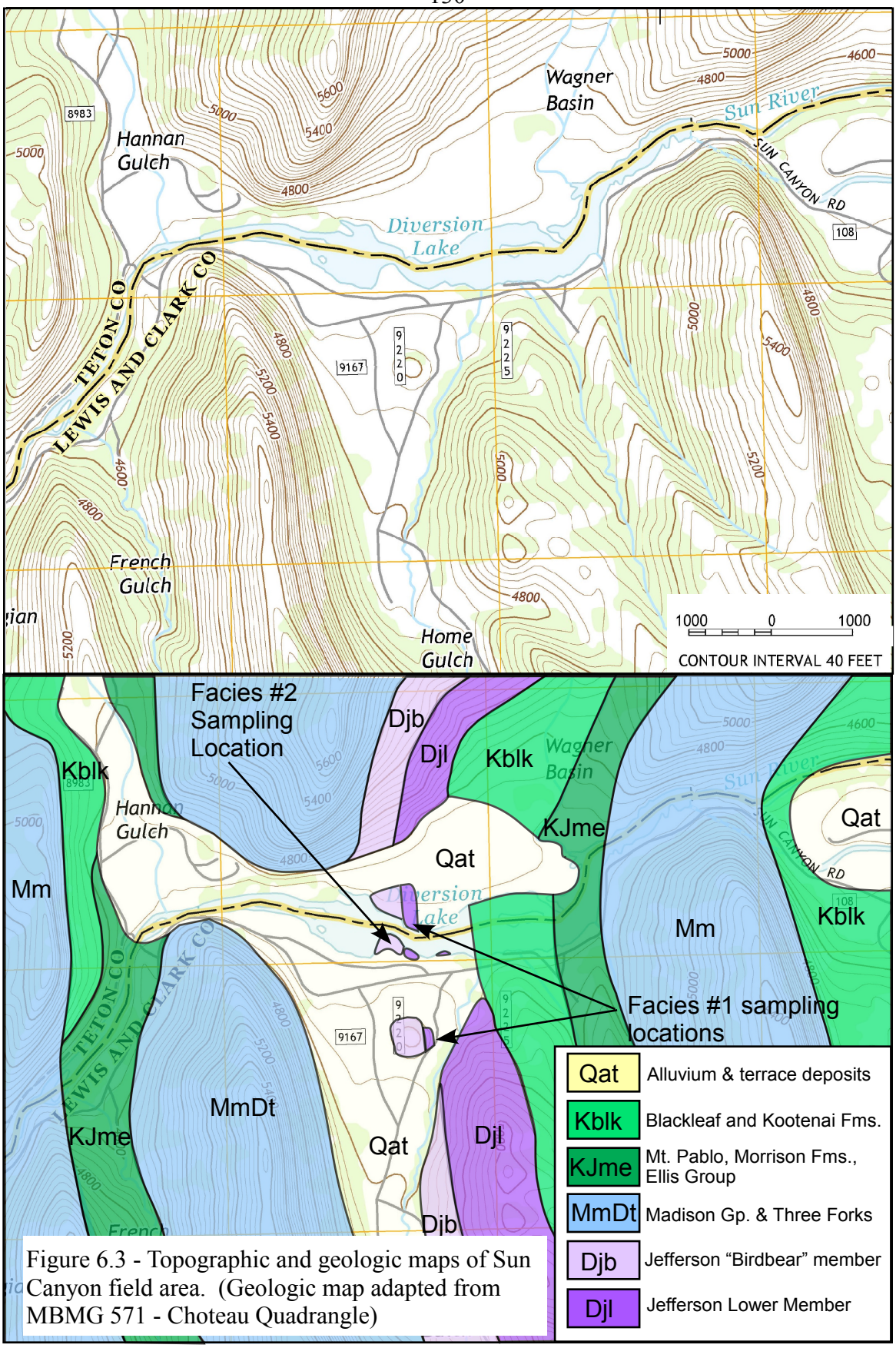

Figure 6.3 - Topographic and geologic maps of Sun Canyon field area. (Geologic map adapted from MBMG 571 - Choteau Quadrangle)

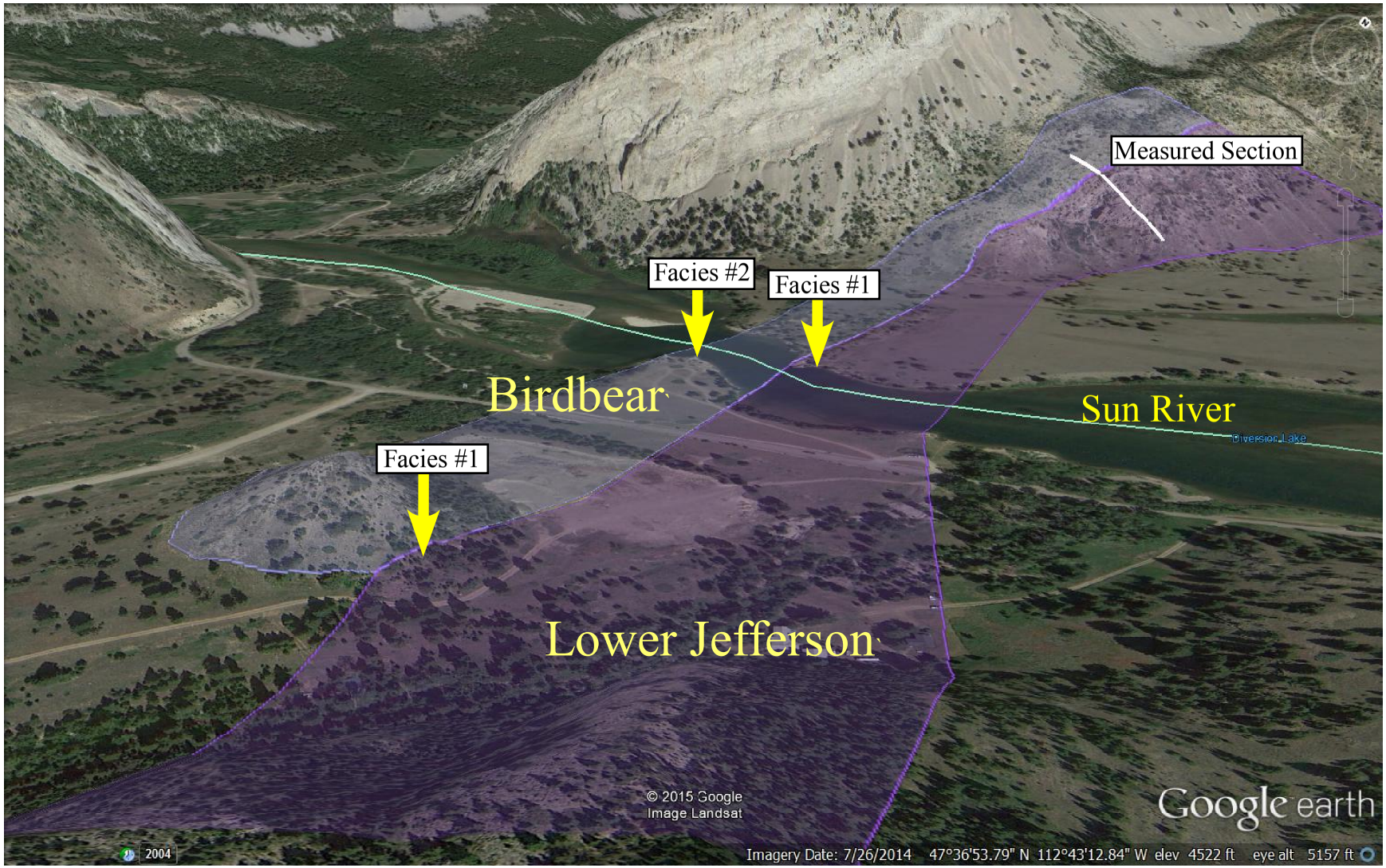

Fig. 6.4 - Home Gulch area with sampling locations and location of measured section labeled.

Mississippian	Madison Group	Castle Reef Dolomite		Dolomite, calcitic dolomite, magnesian calcite and thick bedded limestone. Light to medium gray in color with nodules, lenses, and lentils of chert.
		Allan Mountain Limestone		Dark gray limestone and dolomitic limestone. Thin bedded lower in section and more thickly bedded at very bottom. Chert lenses and nodules abundant.
				Unconformity
Devonian		Three Forks Formation		Intraformational breccia that in places is overlane by gray-ish brown limestone; locally upper part contains siltstone, carbonaceous shale, and green mudstone.
		Jefferson Formation	Birdbear Member	Light-grayish-brown dolomite, calcitic dolomite, argillaceous dolomite and limestone; thin bedded with thin pinch-and-swell type bedding on lower part. 150' to 235' thick.
			Lower Member	Dolomite with thin beds of limestone and calcitic dolomite in lower part; grayish-brown with some light gray beds; fetid odor; local intraformational breccia. 300-650' thick.

Fig. 6.5 - Stratigraphy of Sun Canyon area (from Mudge, 1972)

Mississippian	Madison Group	Mission Canyon		Similar to description of Madison Group in Sun Canyon, but having some beds of anhydrite.
		Lodgepole		
Devonian		Bakken		Black, carboniferous shale Unconformity
		Three Forks Formation		Similar to description of Three Forks Formation in Sun Canyon.
		Jefferson Formation	Potlatch Anhydrite	Thick layers of anhydrite with some thin beds of dolomite. Comprises the seal over reservoir zones in the Kevin Dome. Not present in Sun Canyon.
			"Nisku"	Dolomite, not well described from Kevin Dome, but potentially similar to Birdbear from Sun Canyon.
			"Duperow"	Equivalent of the Lower Jefferson. Composed of brown dolomite and calcite. Abundant fossil stromatoporoids in reef facies, which have been selectively dolomitized. Breccias occur in some localities.

Fig. 6.6 - Stratigraphy of Kevin-Dome Mississippian and Devonian strata (BSCSP).

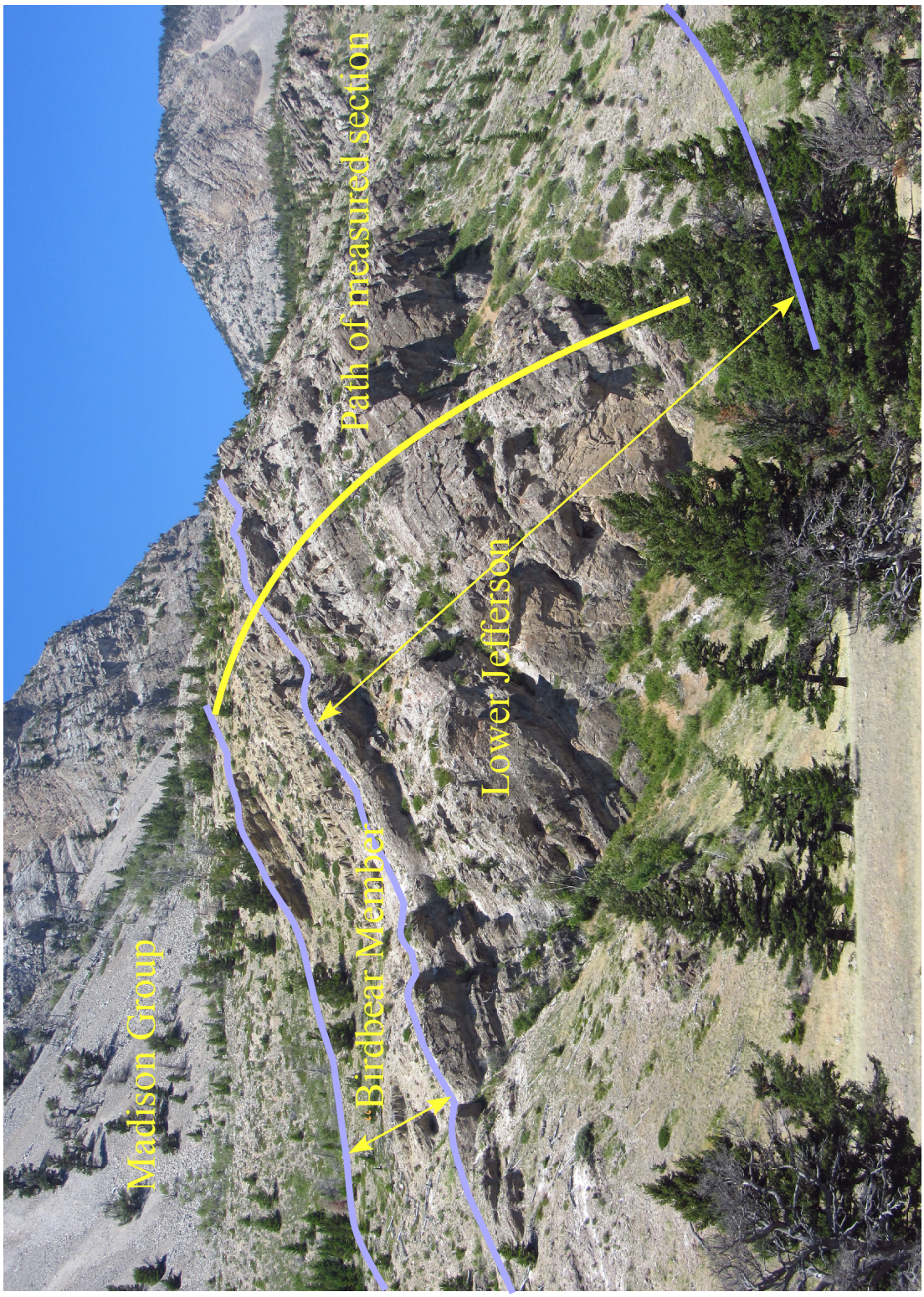

Fig. 6.7 - Jefferson outcrop on North Side of Diversion Lake with Birdbear and Lower members labeled.

Measured Section of Jefferson Formation, Sun Canyon, MT

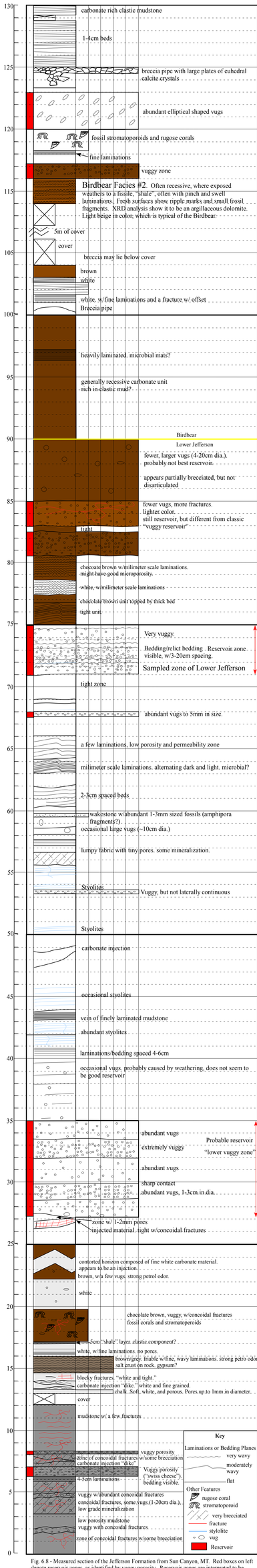

Fig. 6.8 - Measured section of the Jefferson Formation from Sun Canyon, MT. Red boxes on left denote reservoir zones, as identified by vuggy porosity. Reservoir zones are interpreted to be altered stromatoporoid boundstones.

Fig. 6.9 - Stromatoporoid boundstones showing the development of a vuggy texture at a Jefferson outcrop several miles away from Home Gulch. The hammer in the lower photo is the location being photographed by the man in the upper photo.

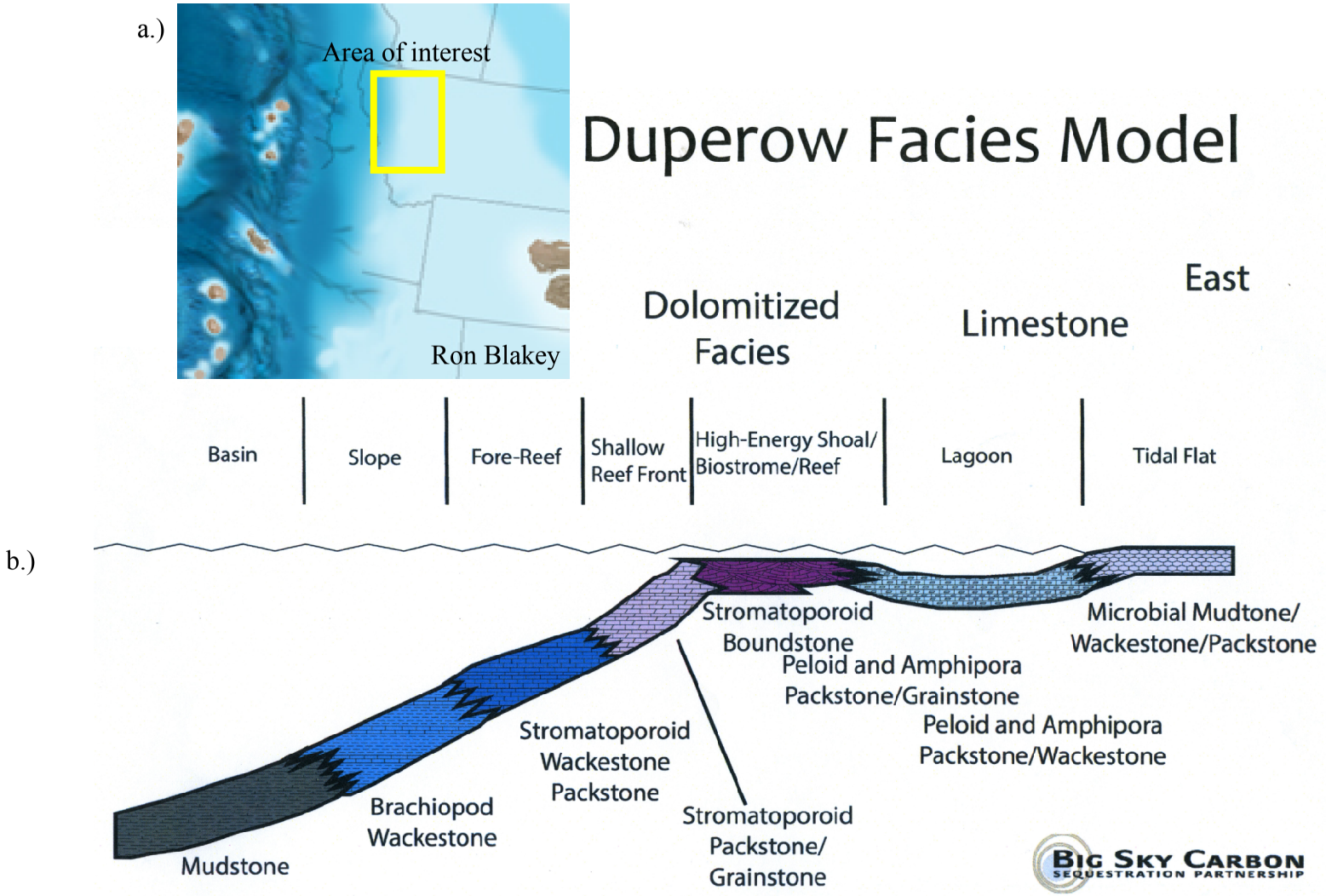

Fig. 6.10 - (a.)Paleo-depositional setting and (b.) associated facies and environments of the Jefferson/Duperow. (based on Bowen and Eby, 2014)

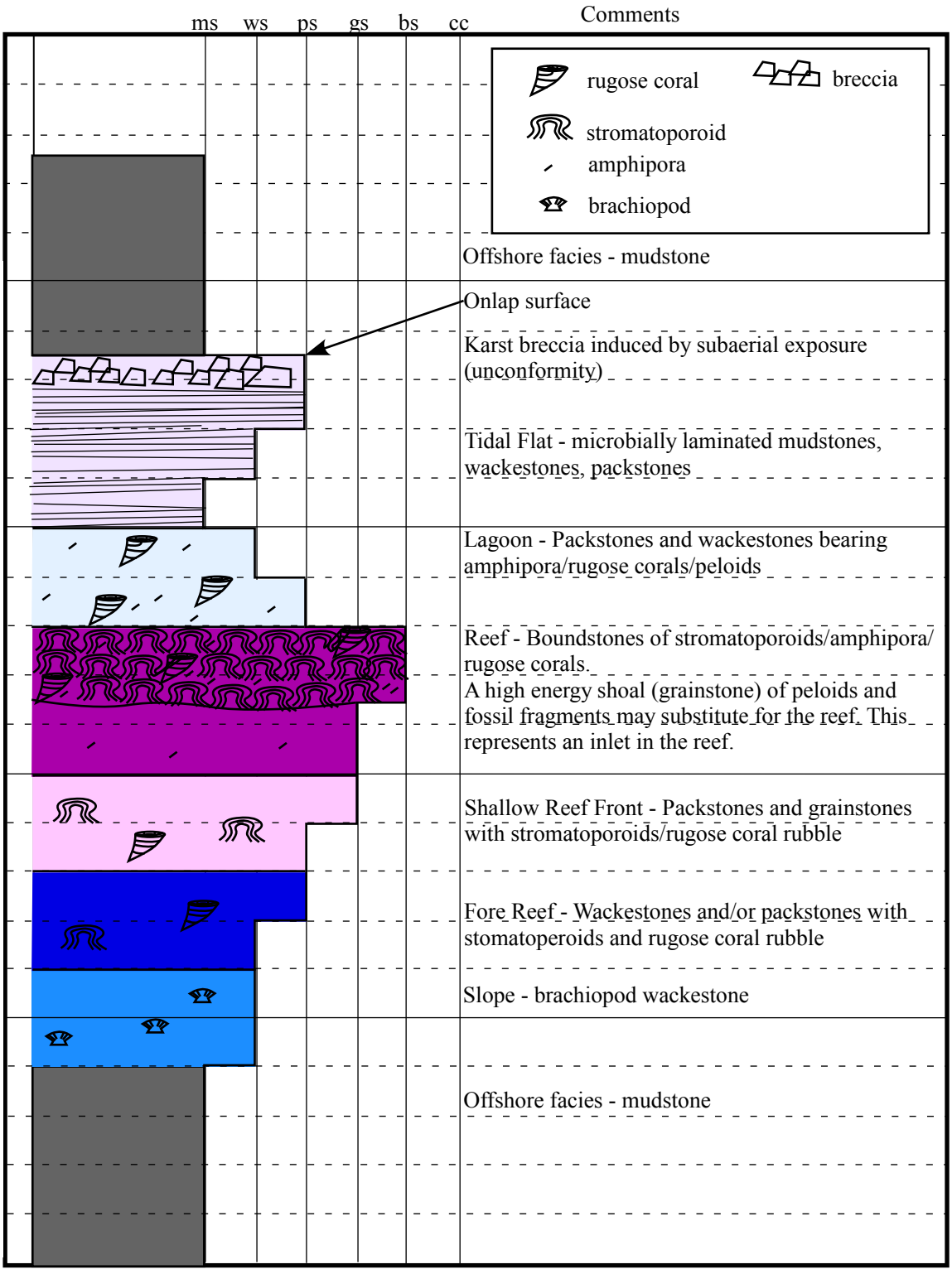

Fig. 6.11 - Idealized sedimentary cycle in the Jefferson. Adapted from BSCSP facies model (Fig. 6.10) and author's field observations.

Measured Section of Jefferson Formation, Sun Canyon, MT

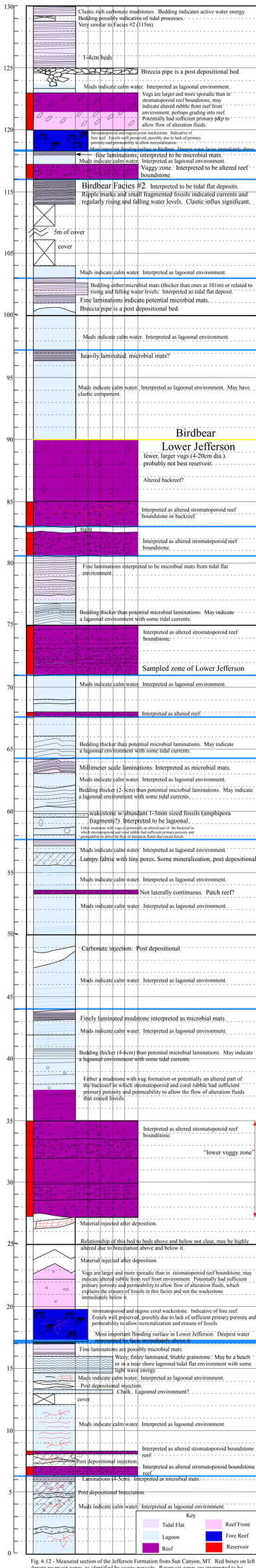

Fig. 6.12 - Measured section of the Jefferson Formation from Sun Canyon, MT. Red boxes on left denote reservoir zones, as identified by vuggy porosity. Reservoir zones are interpreted to be altered stromatoporoid boundstones.

Stratigraphy of the Jefferson Formation, Sun Canyon, MT

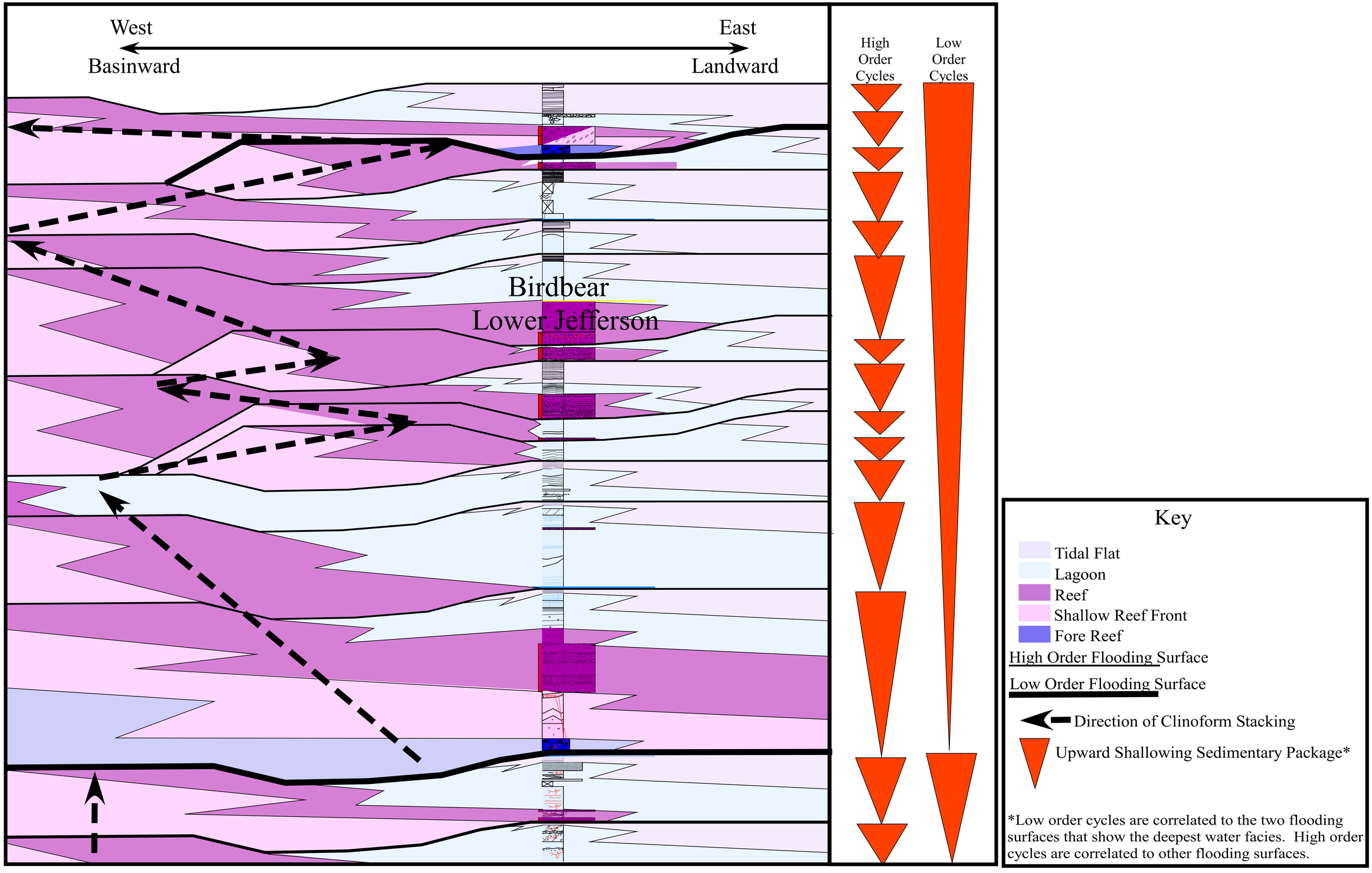

Fig. 6.13 - Stratigraphic interpretation of the Jefferson Formation at Sun Canyon, MT. The sedimentary packages were shown to be comprised of two low order cycles and fifteen higher order cycles. Overall the sediments were from fairly shallow waters that transition from reef to tidal flats. The deepest water facies were interpreted to be deposited in a fore reef setting.

Fig. 6.14 - Facies #1 from the Lower Jefferson being quarried in the field (above) and in the lab (below). Note vuggy texture and fractures.

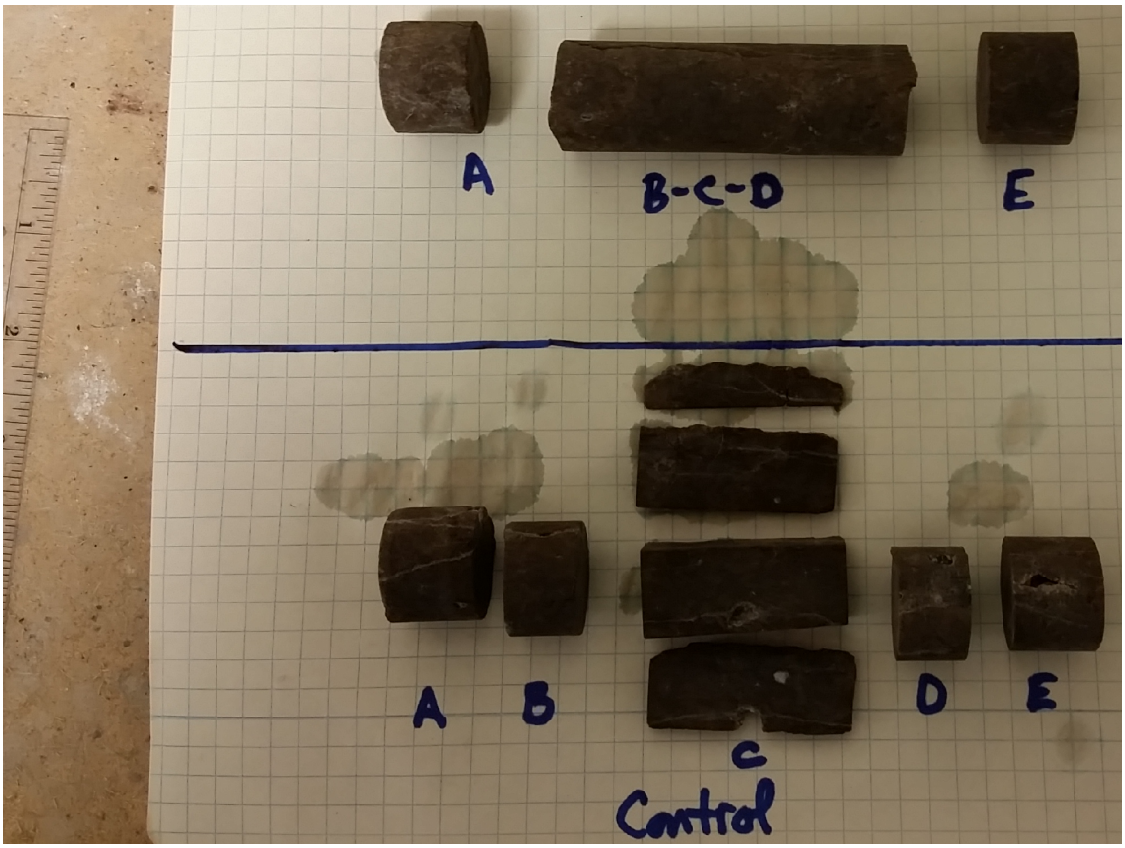

Fig. 6.15 - Cores cut from the Lower Jefferson reservoir block (Facies #1). The upper core was used for porosity and permeability testing, and was intended for use in a flow through experiment. The bottom core was used for a thin section, XRD, and XRF samples.

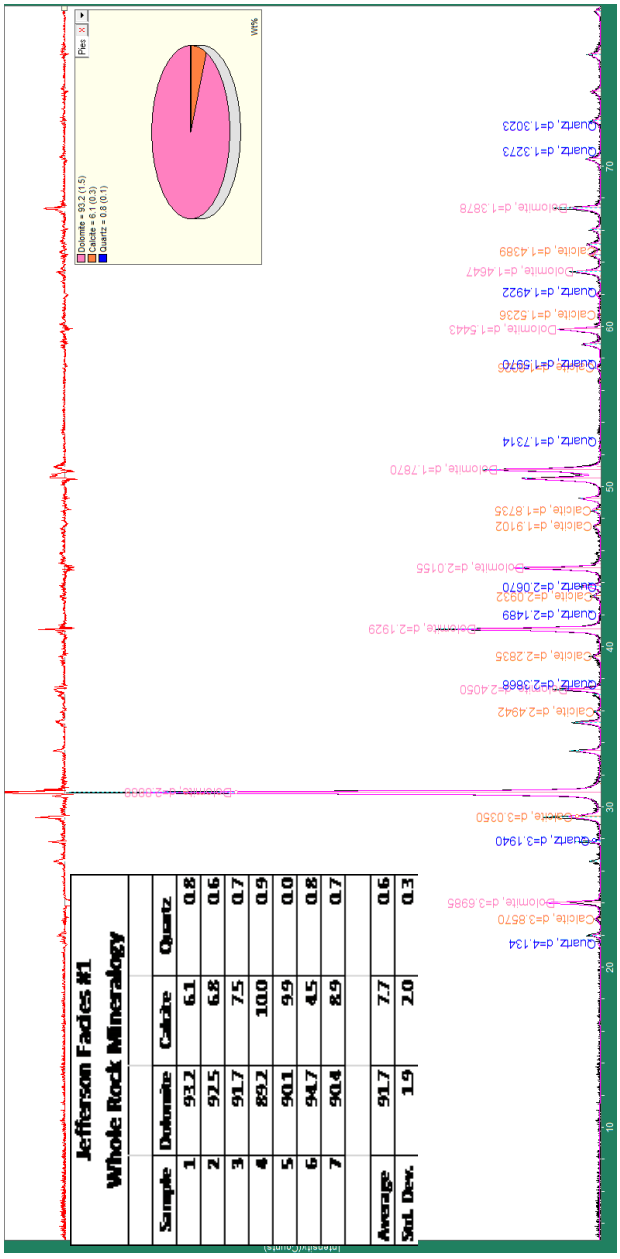

Fig. 6.16 – Example diffraction diagram for Jefferson Facies #1. The whole rock XRD quantification was done in the software package JADE and is based on analysis of 7 samples from the block.

Jefferson Facies #1 Whole Rock Elemental Composition (% Mass)

	Major Elements				Minor Elements													
Sample	**Mg**	**Mg Error**	**Ca**	**Ca Error**	**Si**	**Si Error**	**Al**	**Al Error**	**K**	**K Error**	**Fe**	**Fe Error**	**S**	**S Error**	**Sr**	**Sr Error**	**Cl**	**Cl Error**
Jefferson Ctrl. 1	8.023	1.142	29.218	0.178	0.911	0.052	0.266	0.109	0.101	0.015	0.043	0.005	0.112	0.011	0.004	0.001	0.054	0.005
Jefferson Ctrl. 2			29.173	0.175					0.11	0.015	0.043	0.005			0.005	0.001		
Jefferson Ctrl. 3	7.255	1.04	29.136	0.181	1.008	0.051	0.191	0.098	0.106	0.015	0.039	0.005	0.113	0.011	0.005	0.001	0.062	0.005
Jefferson Ctrl. 4	8.028	1.086	29.543	0.183	0.799	0.047	0.163	0.099	0.082	0.015	0.029	0.005	0.116	0.011	0.005	0.001	0.055	0.005
Jefferson Ctrl. 5	7.723	1.074	30.285	0.185	0.804	0.047	0.297	0.105	0.085	0.015	0.027	0.005	0.104	0.011	0.005	0.001	0.047	0.004
Jefferson Ctrl. 6	7.65	1.142	29.698	0.183	0.905	0.053	< LOD	0.156	0.095	0.015	0.032	0.005	0.115	0.012	0.005	0.001	0.055	0.005
Jefferson Ctrl. 7	8.156	1.048	28.476	0.181	0.76	0.045	0.239	0.098	0.082	0.014	0.034	0.005	0.105	0.01	0.004	0.001	0.053	0.004
Jefferson Ctrl. 8	8.46	1.099	29.676	0.184	0.763	0.046	0.179	0.1	0.076	0.015	0.032	0.005	0.12	0.011	0.005	0.001	0.058	0.005
jeff control 1b pre	8.618	1.075	28.685	0.179	0.745	0.045	0.221	0.099	0.067	0.014	0.029	0.005	0.117	0.011	0.004	0.001	0.066	0.005
jeff control 1b pre	9.308	1.188	29.097	0.181	0.836	0.05	< LOD	0.155	0.081	0.014	0.044	0.005	0.123	0.011	0.005	0.001	0.054	0.005
jeff control 1a pre	8.393	1.147	28.709	0.178	0.747	0.049	0.233	0.107	0.08	0.014	0.036	0.005	0.125	0.012	0.004	0.001	0.068	0.005
jeff control 2a pre	9.271	1.145	29.488	0.184	0.809	0.048	0.295	0.108	0.095	0.014	0.04	0.005	0.115	0.011	0.005	0.001	0.057	0.005
jeff control 2b pre	7.235	1.122	29.208	0.176	0.782	0.05	0.209	0.106	0.093	0.014	0.039	0.005	0.131	0.012	0.005	0.001	0.063	0.005
Average	8.177	0.679	29.261	0.487	0.822	0.080	0.229	0.021	0.089	0.012	0.036	0.006	0.116	0.008	0.005	0.000	0.058	0.006

Fig. 6.17 - Elemental composition of samples from Lower Jefferson reservoir (Facies #1). Data analysis by XRF.

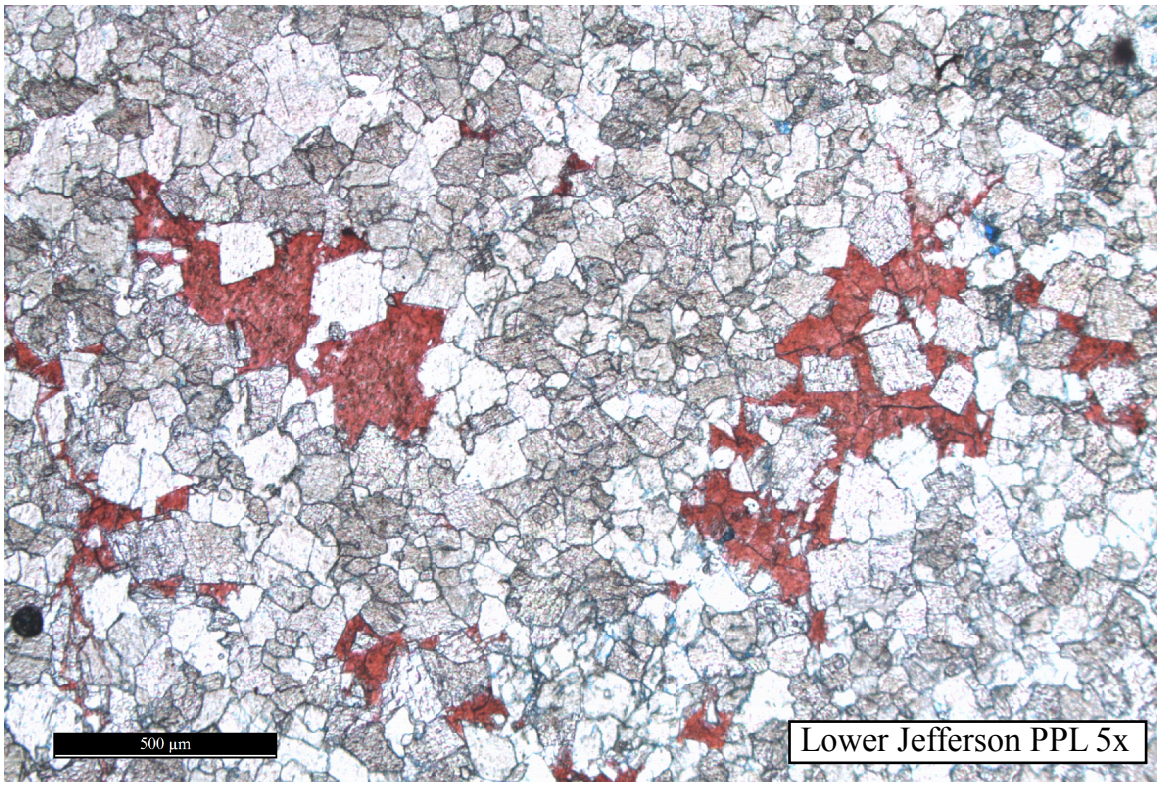

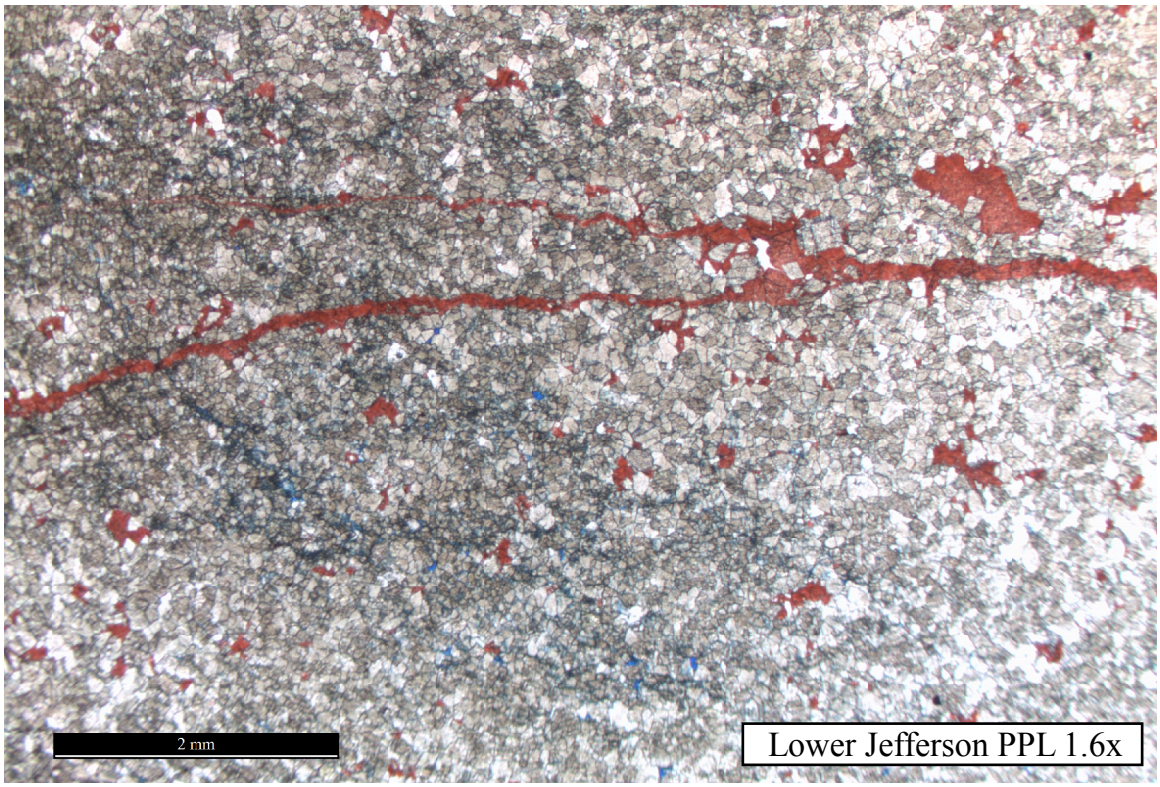

Fig. 6.18 - Jefferson reservoir zone (Facies #1) in plane polarized light (PPL). Slides are stained for calcite (red). Dolomite crystals are unstained. Blue is pores filled with epoxy. Note how calcite fills pores and fractures. Euhedral crystals, indicate recrystallization.

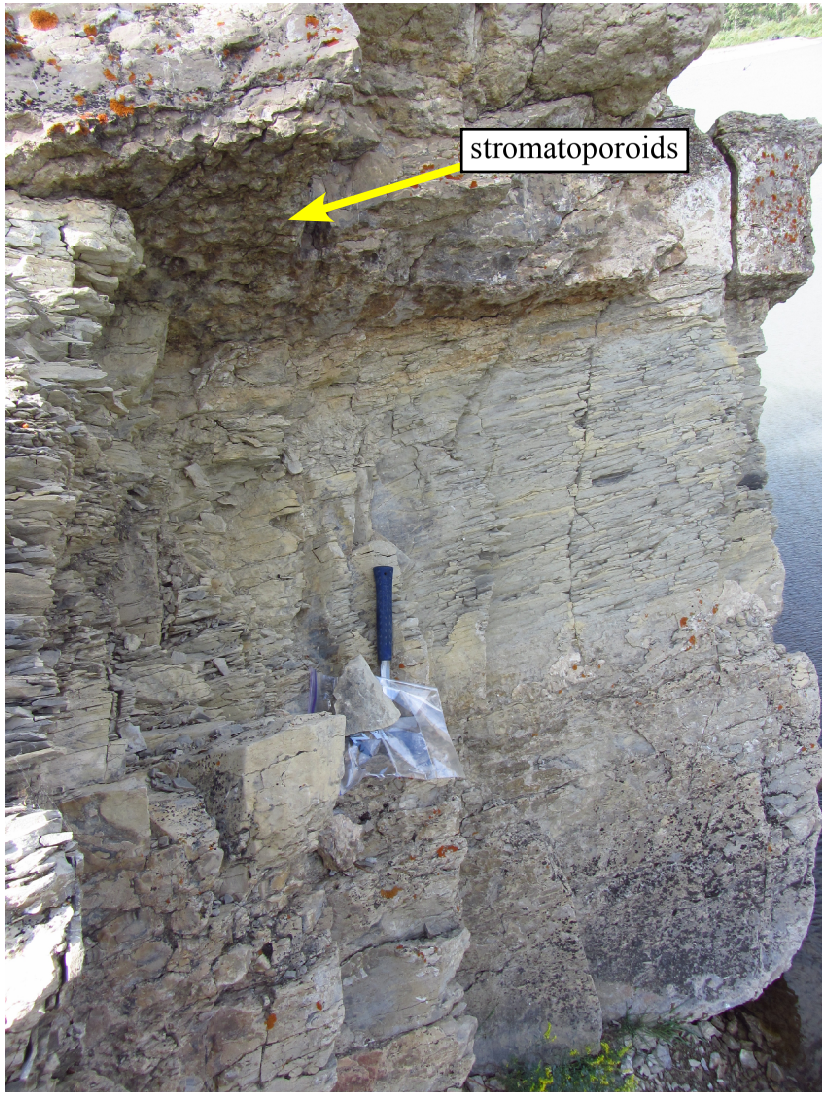

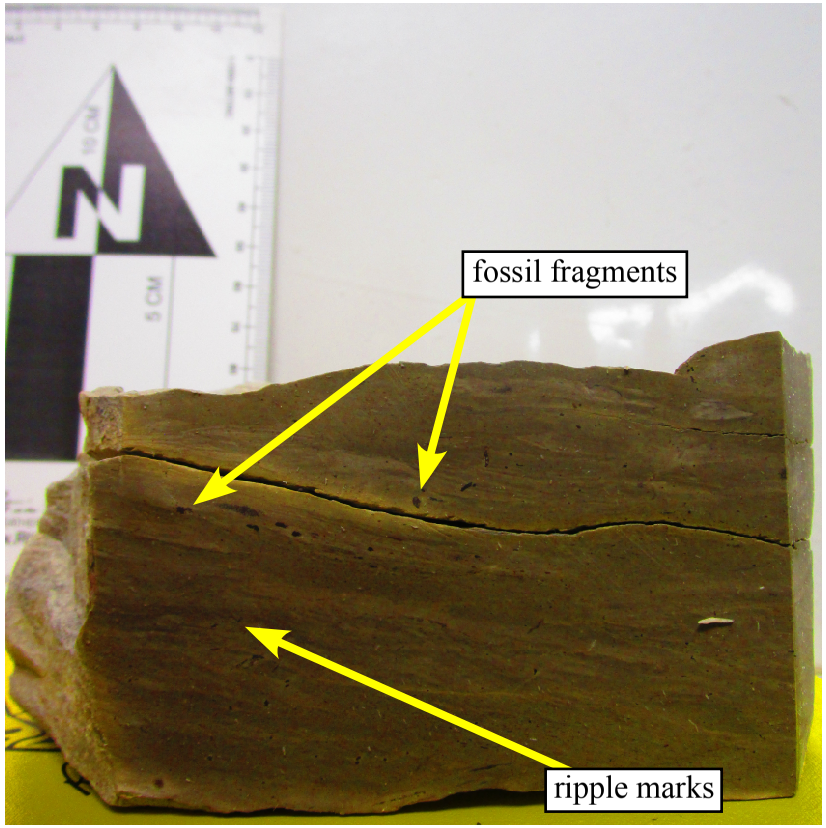

Fig. 6.19 - Facies #2 in outcrop (left, next to hammer) and polished (above). Note fissile nature and pinch and swell texture in outcrop. Also note stromatoporoids in overlying bed. Note ripple marks and fossil fragments in cut sample (above).

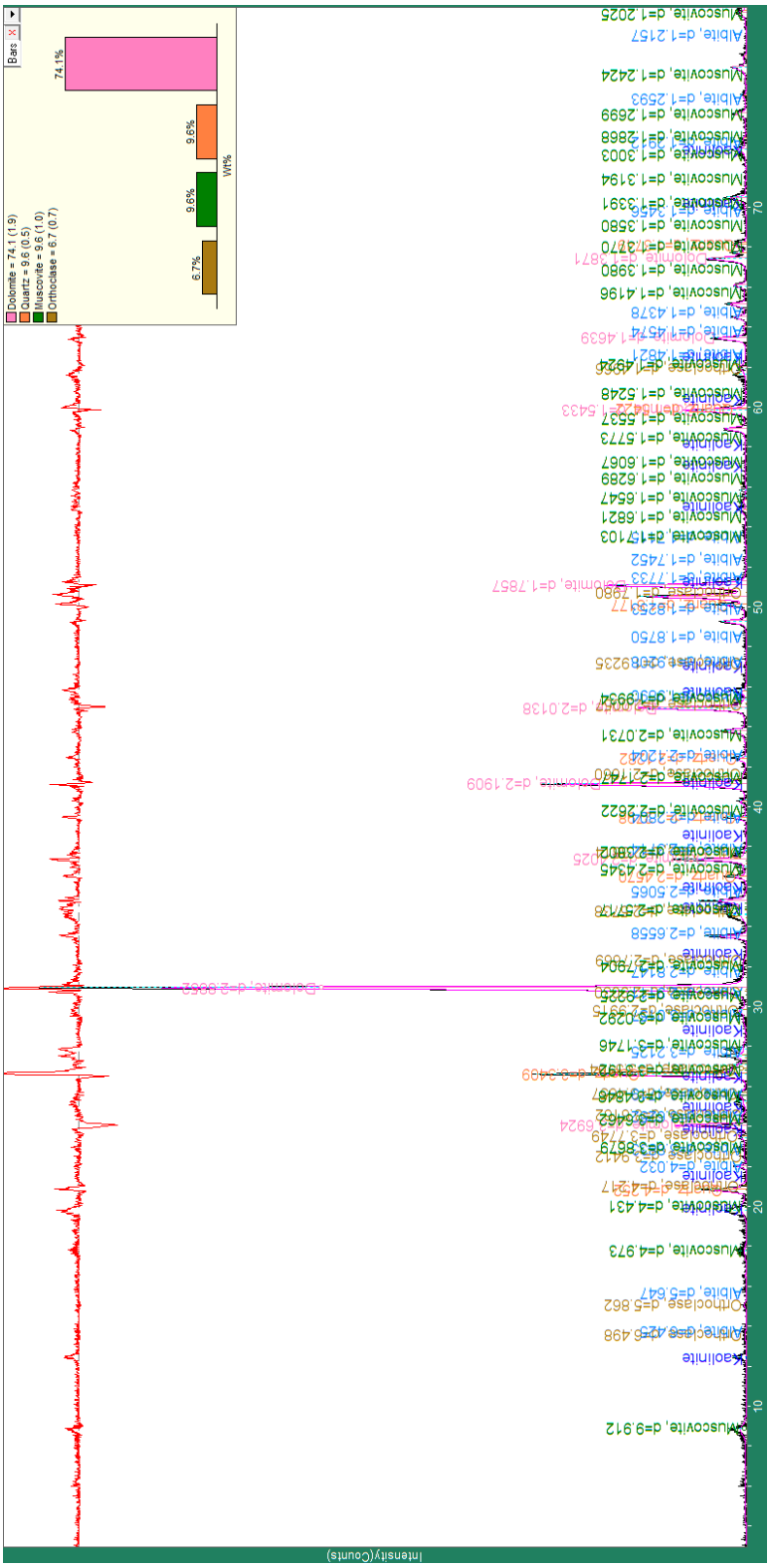

Fig. 6.20 – Diffraction pattern for Jefferson Facies #2 (argillaceous sample of Birdbear Member). Note diverse mineral composition that includes dolomite, quartz, muscovite, and orthoclase.

Jefferson Facies #2 Whole Rock Elemental Composition (% Mass)												
	Major Elements											
SAMPLE	Mg	Mg Error	Ca	Ca Error	Si	Si Error	Al	Al Error	K	K Error	Fe	Fe Error
Jefferson F2 Ctrl. Bulk	5.743	0.789	14.93	0.132	14.327	0.145	4.345	0.197	2.364	0.038	1.894	0.025
	Minor Elements											
	Ti	Ti Error	S	S Error	Zr	Zr Error	Ba	Ba Error	Sr	Sr Error	Rb	Rb Error
	0.243	0.009	0.042	0.009	0.006	0.001	0.015	0.004	0.004	0.001	0.004	0.001

Figure 6.21 - Elemental composition bulk sample of Facies #2 of the Jefferson Formation (Birdbear Member).

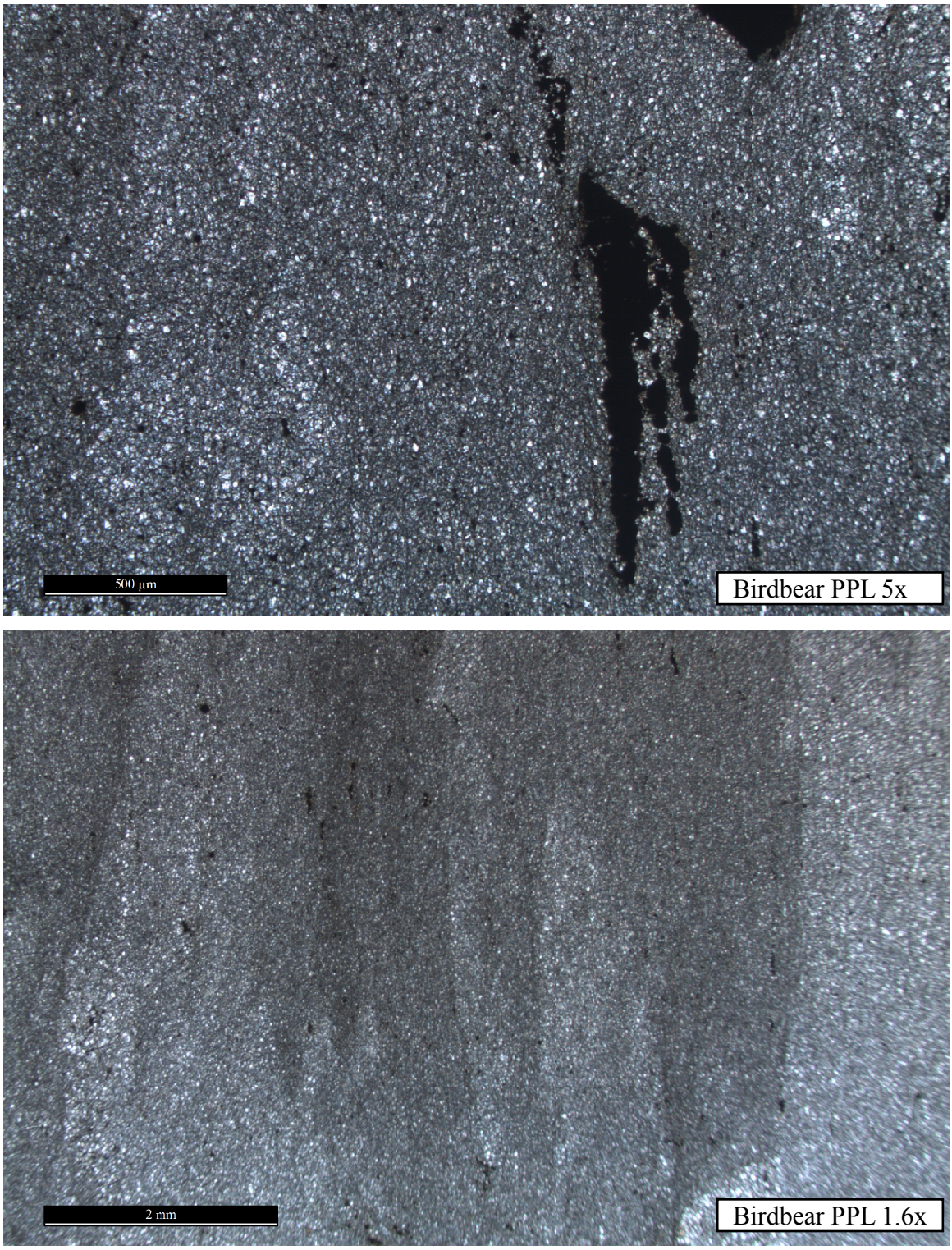

Figure 6.22 - Images of sample from the Birdbear (Facies #2). Note the dusky laminations in the bottom image, which are have large amounts of silicate minerals. The black substance filling pore space is bitumen. The visible crystals are predominantly dolomite.

CHAPTER 7 – CONCLUSIONS

Probably the most important contribution of this thesis is the research on the reactivity of iron oxides and pyrite with the brine-CO_2 system. Experiments studying the reactions of pyrite, magnetite, and hematite with CO_2-brine solutions are few. The evidence that minerals containing iron(II) can facilitate the dissolution of CO_2 into brine could have important implications for future CO_2 sequestration work.

The flow-through reactor is most useful for studying the general behavior of rock during a short time period. The aqueous chemical data generated from such experiments can be equivocal for interpreting mineral dissolution, especially if the rock being studied has a variety of minerals as the Berea sandstone does.

The main finding of the flow-through experiment on the Berea sandstone was that in a limited duration experiment, carbonate cement and iron bearing minerals are most reactive, although iron bearing minerals comprise only a small fraction of most sandstones and so probably do not contribute a great deal to their general reactivity. It had initially been thought that the reactions of phyllosilicates would have been important, or at least measurable during the flow-through experiments, but the batch experiments on muscovite showed that these minerals react slowly enough that their effects are negligible on the order of several days. In the context of longer time periods they could prove to have important effects on the properties of a reservoir, but further research would be required to determine this.

The Jefferson Formation is a likely next candidate for experiments with the flow through reactor and Parr vessels. Hopefully the stratigraphic and mineralogical study can aide future research.

REFERENCES CITED

Alcorn, Z. P., 2012, Lithostratigraphic Investigation of a Late Devonian Carbonate-Evaporite Sequence; the Duperow Formation, Willison Basin, North Dakota [Master of Science: University of North Dakota, 110 p.

Baily, P., 1957, Stabilization of Ferric Thiocyanate Color in Aqueous Solution: Analytical Chemistry, v. 29, no. 10, p. 1534-1536.

Blount, G. C., 1986, Stratigraphy, Depositional-Environments, and Diagenesis Related to Porosity Development and Destruction in Jefferson Formation, Northwestern Montana: Aapg Bulletin-American Association of Petroleum Geologists, v. 70, no. 8, p. 1032-1032.

BSCSP, 2015, Big Sky Carbon Sequestration Partnership; http://www.bigskyco2.org/.

Chopping, C., and Kaszuba, J. P., 2012, Supercritical carbon dioxide–brine–rock reactions in the Madison Limestone of Southwest Wyoming: An experimental investigation of a sulfur-rich natural carbon dioxide reservoir: Chemical Geology, v. 322–323, p. 223-236.

D.O.E., 2015, Carbon Capture and Storage Research; http://energy.gov/fe/science-innovation/carbon-capture-and-storage-research.

Dawson, G. K. W., Pearce, J. K., Biddle, D., and Golding, S. D., 2015, Experimental mineral dissolution in Berea Sandstone reacted with CO_2 or SO_2–CO_2 in NaCl brine under CO_2 sequestration conditions: Chemical Geology, online.

DePaolo, D., and Cole, D. R., 2013, Geochemistry of Geologic Carbon Sequestration: An Overview: Reviews in Mineralogy and Geochemistry, v. Geochemistry of Geologic CO_2 Sequestration, no. 77, p. 1-14.

DeWitt, W., 1951, Stratigraphy of the Berea sandstone and associated rocks in northeastern Ohio and northwestern Pennsylvania: Geological Society of America Bulletin, v. 62, no. 11, p. 1347-1369.

DeWitt, W. J., 1970, Age of the Bedford Shale, Berea Sandstone, and Sunbury Shale in the Appalachian and Michigan basins, Pennsylvania, Ohio, and Michigan: United States Geological Survey. Bulletin, 1294-G, p. 1-11.

Duan, Z., Sun, R., Chen, Z., and I-Ming, C., 2006, An improved model for the calculation of CO_2 solubility in aqueous solutions containing Na^+, K^+, Ca^{2+}, Mg^{2+}, Cl^-, and SO_4^{2-}: Marine Chemistry, v. 98, p. 131 – 139.

Eby, D. B. a. D., 2014, Big Sky Carbon Sequestration Partnership Annual Meeting, Jefferson Core Learning Session.

Finney, B., and Jacobs, M., 2010, Carbon Dioxide Phase Diagram, Volume 2015: http://commons.wikimedia.org/wiki/File:Carbon_dioxide_pressure-temperature_phase_diagram.svg.

Garcia, S., Rosenbauer, R. J., Palandri, J., and Maroto-Valer, M. M., 2012, Sequestration of non-pure carbon dioxide streams in iron oxyhydroxide-containing saline repositories: International Journal of Greenhouse Gas Control, v. 7, p. 89-97.

Garcia, S., Rosenbauer, R. J., Palandri, J., and Mercedes Maroto-Valer, M., 2011, Experimental and simulation studies of iron oxides for geochemical fixation of CO_2–SO_2 gas mixtures: Energy Procedia, v. 4, p. 5108-5113.

Gunde, A. C., Bera, B., and Mitra, S. K., 2010, Investigation of water and CO_2 (carbon dioxide) flooding using micro-CT (micro-computed tomography) images of Berea sandstone core using finite element simulations: Energy, v. 35, no. 12, p. 5209-5216.

Halevy, I., 2013, Production, preservation, and biological processing of mass-independent sulfur isotope fractionation in the Archean surface environment: Proceedings of the National Academy of Sciences of the United States of America, v. 110, no. 44, p. 17644-17649.

Hansen, L., 2009, Design and Experimental Testing of a High Pressure. High Temperature Flow-Though Rock Core Reactor Using Supercritical Carbon Dioxide [Master of Science: Montana State University, 70 p.

Hausner, D. B., Bhandari, N., Pierre-Louis, A.-M., Kubicki, J. D., and Strongin, D. R., 2009, Ferrihydrite reactivity toward carbon dioxide: Journal of Colloid and Interface Science, v. 337, no. 2, p. 492-500.

Kaldi, J. G., Gibson-Poole, C. M., and Payenberg, T. H. D., 2009, Geological input to selection and evaluation of CO_2 geosequestration sites: State of the Science: AAPG Studies in Geology, v. Carbon Dioxide Sequestration in Geological Media - State of the Science, no. 59, p. 5-16.

Kaszuba, J., Yardley, B., and Andreani, M., 2013, Experimental perspectives of mineral dissolution and precipitation due to carbon dioxide-water-rock interactions: Reviews in Mineralogy and Geochemistry, v. Geochemistry of Geologic CO_2 Sequestration, no. 77, p. 153-188.

Kaszuba, J. P., and Janecky, D. R., 2009, Geochemical Impacts of Sequestering Carbon Dioxide in Brine Formations: Carbon Sequestration and Its Role in the Global Carbon Cycle, no. Geophysical Monograph Series 183, p. 239-247.

Kim, Y., Wan, J., Kneafsey, J., T., and Tokunaga, T. K., 2012, Dewetting of Silica Surfaces upon Reactions with Supercritical CO2 and Brine: Pore-Scale Studies in Micromodels: Environmental Science & Technology, v. 46, no. 7, p. 4228–4235.

King, M. B., Mubarak, A., Kim, J. D., and Bott, T. R., 1992, The mutual solubilities of water with supercritical and liquid carbon dioxides: The Journal of Supercritical Fluids, v. 5, no. 4, p. 296-302.

Lammers, K., Murphy, R., Riendeau, A., Smirnov, A., Schoonen, M. A. A., and Strongin, D. R., 2011, CO2 Sequestration through Mineral Carbonation of Iron Oxyhydroxides: Environmental Science & Technology, v. 45, no. 24, p. 10422-10428.

Langmuir, D., 1997, Aqueous Environmental Geochemistry, Upper Saddle River, New Jersey, Prentice Hall, 600 p.

Mishra, A. K., and Ramaprabhu, S., 2011, Magnetite decorated graphite nanoplatelets as cost effective CO_2 adsorbent: Journal of Materials Chemistry, v. 21, no. 20, p. 7467-7471.

Mitchum, R. M., Jr., Vail, P. R., and Thompson, S. I., 1977, Seismic Stratigraphy and Global Changes of Sea Level: Part 2. The Depositional Sequence as a Basic Unit for Stratigraphic Analysis: Section 2. Application of Seismic Reflection Configuration to Stratigraphic Interpretation, AAPG Special Volumes.

Montes-Hernandez, G., and Pironon, J., 2009, Hematite and iron carbonate precipitation-coexistence at the iron–montmorillonite–salt solution–CO_2 interfaces under high gas pressure at 150°C: Applied Clay Science, v. 45, no. 4, p. 194-200.

Moore, D. M., and Reynolds, R. C. J., 1997, X-Ray Diffraction and the Identification and Analysis of Clay Minerals, New York, Oxford University Press.

Mudge, M. R., 1972, Structural Geology of the Sun River Canyon and Adjacent Areas, Northwestern Montana; U.S.G.S Professional Paper 663-B, *in* Survey, U. S. G., ed.: Washington, D.C., United States Government Printing Office.

Murphy, R., Lammers, K., Smirnov, A., Schoonen, M. A. A., and Strongin, D. R., 2010, Ferrihydrite phase transformation in the presence of aqueous sulfide and supercritical CO_2: Chemical Geology, v. 271, no. 1–2, p. 26-30.

Murphy, R., Lammers, K., Smirnov, A., Schoonen, M. A. A., and Strongin, D. R., 2011, Hematite reactivity with supercritical CO_2 and aqueous sulfide: Chemical Geology, v. 283, no. 3–4, p. 210-217.

Palandri, J. L., and Kharaka, Y. K., 2005, Ferric iron-bearing sediments as a mineral trap for CO_2 sequestration: Iron reduction using sulfur-bearing waste gas: Chemical Geology, v. 217, no. 3–4, p. 351-364.

Peng, S., Marone, F., and Dultz, S., 2014, Resolution effect in X-ray microcomputed tomography imaging and small pore's contribution to permeability for a Berea sandstone: Journal of Hydrology, v. 510, p. 403-411.

Pepper, J. F., DeWitt, W., Jr., and Demarest, D. F., 1954, Geology of the Bedford Shale and Berea Sandstone in the Appalachian Basin, Geological Survey Professional Paper 259: Washington, D.C.

Pierre-Louis, A.-M., 2014, Studies of the surface reactivity of metal oxyhydroxides and sulfides with relevance to environmental chemistry [3671943 Ph.D.]: Temple University, 272 p.

Robie, R. A., and Waldbaum, D.R., 1968, Thermodynamic Properties of Minerals and Related Substances at 298.15K and One Atmosphere Pressure and at Higher Temperatures: US Geologic Survey Bulletin 1259.

Romero, M. I., Gamage, P., Jiang, H., Chopping, C., and Thyne, G., 2013, Study of low-salinity waterflooding for single- and two-phase experiments in Berea sandstone cores: Journal of Petroleum Science and Engineering, v. 110, p. 149-154.

Shi, J.-Q., Xue, Z., and Durucan, S., 2011, Supercritical CO2 core flooding and imbibition in Berea sandstone — CT imaging and numerical simulation: Energy Procedia, v. 4, p. 5001-5008.

Sissmann, O., Brunet, F., Martinez, I., Guyot, F., Verlaguet, A., Pinquier, Y., and Daval, D., 2014, Enhanced Olivine Carbonation within a Basalt as Compared to Single-Phase Experiments: Reevaluating the Potential of CO_2 Mineral Sequestration: Environmental Science & Technology, v. 48, no. 10, p. 5512-5519.

Span, R., and Wagner, W., 1996, A new equation of state for carbon dioxide covering the fluid region from the triple-point temperature to 1100K at pressures up to 800 MPa: J. Phys. Chem. Ref. Data., v. 25, p. 1509-1596.

Van Waggoner, J. C., Mitchum, R. M., Campion, K. M., and Rahmanian, V. D., 1990, Siliciclastic Sequence Stratigraphy in Well Logs, Cores, and Outcrops: Concepts of High Resolution Correllation of Time and Facies: AAPG Methods in Exploration Series, v. 7., p. 1-71.

Viollier, E., Inglett, P. W., Hunter, K., Roychoudhury, A. N., and Van Cappellen, P., 2000, The ferrozine method revisited: Fe(II)/Fe(III) determination in natural waters: Applied Geochemistry, v. 15, no. 6, p. 785-790.

Vogt, S. J., Shaw, C. A., Maneval, J. E., Brox, T. I., Skidmore, M. L., Codd, S. L., and Seymour, J. D., 2014, Magnetic resonance measurements of flow-path enhancement during supercritical CO_2 injection in sandstone and limestone rock cores. : Journal of Petroleum Science and Engineering, v. 122, p. 507-514.

Winter, J. D., 2010, Principles of Igneous and Metamorphic Petrology, U.S.A., Prentice-Hall.

APPENDICES

APPENDIX A

REACTOR OPERATIONAL PROCEDURE

Reactor Operation

Installation of Sampling Manifold

The sample manifold must be re-assembled (if cylinders were removed for emptying) before being installed in the reactor. The manifold must then be cleaned, dried, and pressurized to 1,000psi with ultra-pure nitrogen. After cleaning, and pressurization with ultra-pure nitrogen, the manifold is hung from the two hooks attached to the incubator ceiling and attached to the manifold bypass via the two ¼" tube fittings. When the reactor has been activated and sampling is to begin, the valves are switched to direct flow away from the bypass and into one of the sampling chambers.

Operation of Data Logging Software

It is necessary to create a file for the experimental data, prior to activation of the data logging software. The data logger (Campbell CR1000) continuously downloads data at thirty second intervals to the computer. To create a file that only contains the data from the experimental timeframe of interest it is necessary to go to the data file (C:/CampbellSci/Loggernet) and change the file name. The old file can then be deleted if it contains no vital information. The data logger will automatically create a new file. When the experiment is completed, this file's name can then be changed to end data recording. The file can then be converted to Excel format and used for data analysis.

Reactor conditions are monitored during the experiment by "Real Time Monitoring Software." This software is activated by double clicking the "Loggernet" icon on the desktop. This brings up a small window. Connect the datalogger to the

computer by selecting “Main>Connect”. Select “Loggernet>RTMC Run-Time”” icon to begin real time monitoring.

Charging the CO_2 Pump

Charging the CO_2 pump (Pump C) is best when done at room temperature. This ensures that the maximum molar density of CO_2 fills the pump. The pump is charged from a cylinder of pressurized CO_2. Ultra-pure CO_2 is preferred but food grade can be used depending on the objective of the experiment. The line from the CO_2 tank to the pump should be flushed prior to filling the pump to ensure that no atmospheric gasses contaminate the experiment. This is done by opening the CO_2 tank and regulator to allow approximately 100psi of CO_2 to flow through the line for about one minute. The one way valve and open-close valve at the top of the CO_2 line are opened to allow flushing of the line. Then open the valve on the pump intake after closing the valve used to bleed the line. Refill Pump C with the controller. Open the CO_2 tank regulator to allow the full tank pressure to fill the syringe pump. Shut the valve on the Pump C intake. Set Pump C to constant pressure mode and set the pressure to the desired experimental pressure, but do not activate the pump yet.

Inserting and Flushing the Core

Prior to the experiment it is necessary to flush the core with ultra-pure nitrogen gas in order to remove atmospheric gasses from the core prior to the experiment. To do this hook the ultra-pure N_2 tank to the three way ball valve on the left side of the core holder. Open the other three way valve on the right hand side. Allow N_2 to flow through the core for 15 minutes at around 10 cubic feet per minute (CFM). When this is done

stop the gas flow and shut both valves before disconnecting the tank. A small amount of confining pressure around the core helps to prevent nitrogen leakage into the hydraulic fluid in the core holder. It is important to keep the core shut off from the rest of the reactor until everything is ready to introduce fluid to the core. There is a bypass tube around the core holder for this purpose.

Pressurizing the System

The pressure of the reactor system is controlled by the back pressure in the accumulator. In order to pressurize the system to this level, initiate flow from the syringe pumps. Pressure will rise until it reaches equilibrium with the back pressure. As fluid fills the accumulator the pressure in the reactor will steadily rise (more fluid in constant volume accumulator). During a typical experiment the rise in pressure is very slow due to the low flow rate. During calibration it will be faster. There are two ways to keep the pressure relatively constant in the system. The first is to periodically shut off flow into the reactor, empty the accumulator, and then restart flow. The second is to use a backpressure regulator or pressure release valve to vent nitrogen from the backpressure. For these experiments the former method was used (about every 12-24 hours) and there was little pressure perturbation. The downside to the second method is twofold: nitrogen is wasted, and pressure drops are sudden because the backpressure regulator only opens when accumulator pressure reaches around 100psi above the set point.

Calibrating the pH and Conductivity Sensors

The conductivity and pH sensors were calibrated before each experiment. Calibration is conducted at the planned operating pressure, but at room temperature.

Room temperature was found to produce a more linear calibration and heating pH 2 buffer solution to operational temperature is dangerous. The pH sensors are calibrated using both a zero point calibration and a two point calibration with pH 2.00 and 6.00 buffer solutions Catalog numbers SB107-20, SB96-20). The calibration process is described in the sensor manual. Typically 3-5 times the volume of the system (3x250mL) is flushed with the buffer prior to calibration to ensure that the sensors are in contact with pure buffer solution. A good way to know when the sensor is in contact with uncontaminated buffer solution is to watch the conductivity sensor. When it achieves an unchanging reading for several minutes it can be safely assumed that the system has been successfully flushed. It is recommended to use one pump for the pH 2.00 buffer and one for the pH 6.00 buffer. Flush the pumps with deionized water (from building system) before filling with buffer solution. Never flush the system with nano-pure (18MΩ) as it can damage the pH sensors (will pull the electrolyte out) and tubing (it can partially dissolve the inside of the tubing). A temperature correction may need to be made for the pH of the buffer solutions. These temperatures corrections are on the buffer container.

The conductivity sensor is calibrated using a standard solution available from Fisher; Catalog number (09-328-4). A solution that is close to the planned conductivity of the experimental brine is recommended. For the Berea this was the 6,600ppm solution (0.0001megaohm). As with the pH sensor calibration it is recommended that 3-5x the volume of the system be pumped through before calibrating the sensor. The effluent pH sensor can be used as a proxy to indicate when the sensor is exposed to pure,

uncontaminated standard solution. When the pH stabilizes for an extended period of time the sensor is ready for calibration.

Pressure Effects on pH and Conductivity

As buffer and standard solutions are pumped through the reactor the pressure will increase unless the accumulator is emptied. This can affect the readings, especially of the conductivity sensor. At higher pressures water is slightly compressible and so the solution in effect becomes more concentrated, registering a higher conductivity. This can be corrected during calibration by emptying the accumulator after each 500mL (a single pump's capacity) of fluid is pumped into it.

Emptying the Accumulator

The system is built with a 5 gallon (18.9L) diaphragm style accumulator supplied with nitrogen backpressure. The accumulator is emptied by shutting the incoming valve on the line from the reactor and then opening the accumulator drain valve. Do not open both valves at the same time or else the reactor will depressurize. Always open valves slowly to prevent rapid pressure changes and violent releases of accumulator fluids.

Starting the Brine Flow

Once the sensors have been calibrated it is time to charge the reactor with brine. The brine bag is hung on the shelf below the pumps and the ¼" NPT fitting at the end of the Teflon hose is attached to the inlet on the continuous flow system. The two brine pumps (A and B) are filled with approximately 30mL of brine and emptied. This cleans pumps of the remaining calibration fluid. This is repeated three times. Both brine pumps

are then filled to capacity, discharged, and refilled in order to purge the reactor of all remaining calibration fluid. The system is then ready for heating.

Heating the and Pressurizing the Core Holder

Pre-heating the incubator. The nitrogen pressure inside the core holder can be set so that the pressure increase due to heating can be accounted for using Gay-Lussac's Law:

$$\frac{P1}{T1} = \frac{P2}{T2}$$

For a desired confining pressure of 2500psi (17.2 MPa) at 100ºC this requires about 1975psi (13.6MPa) of pressure be added to the core holder at room temperature (22ºC). The core holder is also equipped with a pressure release regulator that can be set to provide a fail-safe in the event of unsafe pressure buildup in the core holder.

Pre-heating the syringe pumps and converting CO_2 to a supercritical fluid. The syringe pumps are pre-heated by circulating fluid through the jackets that enclose the cylinders. First, activate the Thermo-fisher constant temperature bath. Allow around 24 hours for heating. This is also a good time to pressurize the CO_2 to the desired operating pressure (it should match the influent pressure). To do this start Pump C in constant pressure mode and program to the desired pressure (this should match the system pressure as set by the accumulator). As the temperature rises the volume in the CO_2 pump will decrease as the CO_2 becomes a denser supercritical fluid. The stabilization of the volume indicates that the desired temperature has been reached.

Beginning the Experiment

When the system has been heated, the confining pressure is stable, and the supercritical CO_2 has reached constant volume, the experiment can begin. Brine flow is set to the desired flow rate and started (for the Berea experiments this was 0.5mL/min). The two three way valves that direct brine flow to the core are set to deliver brine flow away from the bypass and through the core. There may be a pressure drop when this is done, but to correct the pressure just increase the brine flow rate until pressure reaches operational pressure once again, then dial back the flow rate to the desired level. If a sample has a low permeability, the pressure may build up to unsafe levels (2,000psi) even at a low flow rate. In this case, the pumps can be switched to constant pressure mode and the flow rate can be monitored. The pressure in the system should always be kept at least 300-500psi lower than the confining pressure in the core holder, otherwise fluid will leak out of the sleeve and into the core holder's pressure vessel.

Starting Supercritical CO_2 Flow

Fluid should be allowed to flow through the core for at least 24 hours before CO_2 is added to the system in order to ensure that it is saturated (longer, as appropriate, when permeability is very low). At least one water sample should be taken at +12-24 hours to capture the brine chemistry between only brine and rock.

The goal of CO_2 injection should be to add enough so that the brine is saturated with respect to CO_2. The amount needed can be calculated using the equations from (Duan et al., 2006). Their laboratory website has a downloadable program that calculates CO_2 saturation when the pressure, temperature, and the concentrations of major ions

(Na^+, K^+, Ca^{2+}, Mg^{2+}, SO_4^{2-}, Cl^-) are input. Saturation is then calculated in molal units (moles CO_2/kg brine). Using the flow rate and CO_2 saturation in moles/kg brine the amount of CO_2 to inject per minute to achieve saturation can be calculated. To ensure saturation is reached, the calculated amount is increased by 10%-20%.

The CO_2 pump pressure is first set to match the influent pressure. The pump is then set to constant flow mode and the desired flow rate is input. The pump is then started and the open-close valve on the downstream side the CO_2 pump is opened. It usually takes around 12-24 hours for CO_2 to reach the influent pH sensor. pH should drop to around 3.5. If it does not reach this level, then saturation is probably not being achieved and the flow rate should be checked and increased if necessary. If increasing the flow rate does not solve the problem, then there may be an obstruction in the CO_2 valve assembly.

Running the Experiment

Experiments can be run for any desired period of time. Berea experiments were run for 72 hours. A brine only fluid sample was taken 12 hours after the experiment was started. Then CO_2 was injected and fluid samples were taken at twelve hour intervals. A 3in. long x 1in. dia. (7.62cm x 1.54cm) core porosity of 17% porosity has approximately 23mL of pore volume. At a flow rate of 0.5mL/min, ~94X the pore volume in fluid passed through the sample during the experiment. A control experiment was run with only brine + CO_2. Nickel plated steel spacers were placed into the core sleeve in place of a rock core. The control experiment evaluated the between brine, CO_2, and the reactor system.

Shutting Down the Reactor

After an experiment the system is shut down using the following procedure:

- Divert flow back to the core holder bypass
- Divert flow away from the sample manifold and into the manifold bypass
- Shut off CO_2 flow with the on-off valve on the downstream of the CO_2 pump and stop flow from the CO_2 pump (Pump C).
- Stop flow from brine pumps (A&B).
- Shut down the pre-heating system and incubator
- Re-name the data file on the computer to end data recording for the experiment
- Allow system to cool
- Purge brine and CO_2 from the reactor by flooding with 1000mL of pH 7 buffer solution
- Purge remaining brine from core sample by flowing ultra-pure N_2 through the sample as described in the pre-experimental procedure.
- Release the pressure from the core holder using the pressure release regulator
- Empty the accumulator
- De-pressurize the reactor by opening all three on-off valves at the stem used to empty the accumulator
- Pump an additional 100mL of pH 7 buffer solution through the system at ambient pressure and then close all valves.

- Bring the pressure of CO_2 in the syringe pump 900psi or less (below supercritical and liquid thresholds).
- Remove the core from the core holder and place in desiccator

APPENDIX B

ADDITIONAL REACTOR MODIFICATIONS

Additional Modifications to Flow-Through Reactor

1. Valve Replacement

Existing valves were rated to a maximum pressure of 2500psi (17.2MPa). While this pressure rating was within the operational limits of the system, this type of valve developed slow leaks after periods of use below 2,000psi (3.8MPa). The valves were replaced with ones with a rating of 3,000psi (20.7MPa) or higher.

2. Check Valves

One way check valves that prevent fluid backflow were installed at various points in the system to ensure that: 1) brine does not enter the CO_2 pump, 2) CO_2 does not flow backwards towards the brine pumps, and 3) that fluid from the accumulator does not flow backwards into the sample manifold, sensors, or core.

3. Nitrogen Confining Pressure for Core Holder

Hydraulic fluid was used to provide confining pressure in the core holder until the summer of 2014. It was a constant source of malfunction and leakage, so it was replaced with nitrogen gas as the confining fluid. This makes usage and core sleeve replacement easier. It also reduces the risk of overpressurization of the core holder during heating.

4. Monel Tubing and Fittings

After the first three experiments, corrosion proved to be a serious problem in parts of the system, particularly at the CO_2-brine junction and inside the sampling manifold. The corrosion of the CO_2-brine junction was so severe that CO_2 could no longer be delivered after running three 72 hour experiments. Rust flakes were observed in the brine

samples that came out of the sample cylinders. A rise in pH was noted between the influent and effluent pH sensors when CO_2 saturated brine was pumped through the system (but not when non-acidic fluids were pumped). This combined with the generation of hydrogen gas suggested that anaerobic steel corrosion was occurring inside the reactor tubing. After consulting with Swagelok about these problems it was decided to replace the tubing with a non-reactive material called Monel, or Alloy 400. It is composed of ~67% nickel with the balance being copper and traces of iron, manganese, carbon, and silicon. Replacement of the sample manifold would have been expensive and so it was given a nickel coating. The bulk of the reactor tubing, valves, and check valves, were replaced with monel fittings.

5. Removal of Redundant Temperature Sensors

Two temperature sensors were removed from the system because temperature was already being measured upstream and downstream of the core by the pH and conductivity sensors. The temperature sensors were placed at the fluid exit and return ports of the temperature bath.

6. Datalogger Programming Update

The datalogger programming was modified to monitor the additional pressure sensor and the operational parameters of the two additional syringe pumps (pressure, flow rate, and pump volume remaining). Functions no longer necessary were removed. The assistance of Tim Brox, who had initially designed and built the data logging system and its written programming was of great help in modifying that programming.

7. New Computer for Data Logger Software

A new desktop computer was installed to replace the older laptop upon which the data logging program was installed.

8. Replacement of pH and Conductivity Sensors

The two pH probes and the conductivity probe were replaced annually (last in fall 2014). Replacement is indicated by failure to calibrate or give accurate readings.

APPENDIX C

4-20mA OUTPUT SIGNAL REFERENCE

Syringe Pump 4-20mA Output Signal Reference

Channel 1:

Pin 1 – A Pump Flowrate

Pin 14 – A Pump Flowrate (Signal Return)

Channel 2:

Pin 2 – A Pump Pressure

Pin 15 – A Pump Pressure (Return)

Channel 3:

Pin 3 – A Pump Pressure

Pin 16 – A Pump Pressure (Return)

Channel 4:

Pin 4 – B Pump Flowrate

Pin 17 – B Pump Flowrate (Return)

Channel 5:

Pin 5 – B Pump Pressure

Pin 18 – B Pump Pressure (Return)

Channel 6:

Pin 6 – B Pump Volume Remaining

Pin 19 – B Pump Volume Remaining (Return)

Channel 7:

Pin 7 – C Pump Flowrate

Pin 20 – C Pump Flowrate (Return)

Channel 8:

Pin 8 – C Pump Pressure

Pin 21 – C Pump Pressure (Return)

Channel 9:

Pin 9 – C Pump Volume Remaining

Pin 22 – C Pump Volume Remaining (Return)

Channel 10:

Pin 10 – Undefined

Pin 23 - Undefined

Channel 10:

Pin 11 – Undefined

Pin 24 - Undefined

Channel 12:

Pin 12 – Undefined

Pin 25 - Undefined

APPENDIX D

BRINE DEOXYGENATION EXPERIMENTS

Introduction

Two experiments were conducted to determine the amount of time required to remove all dissolved oxygen from brine by bubbling with N_2. Deoxygenated brine was used in these experiments in order to simulate the anoxic to sub-oxic conditions of a deep saline aquifer. Sub-oxic is defined as 0.03 – 0.96 ppm dissolved oxygen (DO). Anoxic is defined as <0.03ppm DO (Langmuir, 1997). Two tests were conducted to determine how quickly brine could be de-oxygenated by bubbling it with ultra-pure nitrogen gas (99.99% purity). 18 mega-Ohm water was used in place of brine for ease of conducting the experiment. The high total dissolved solids (TDS) present in brine results in a lower maximum dissolved oxygen saturation level than in pure water due to the salting out effect (Langmuir, 1997). Therefore, brine should be more easily de-oxygenated than pure water.

Equipment

- 6 liters DI water
- 10L Nalgene carboy with air lock
- Mettler Toledo GoPro Dissolved Oxygen Meter (lower detection limit 0.01ppm).
- Ultra-pure nitrogen (99.99% purity)
- Regulator
- Bubbling stone

Procedure

Six liters of water was placed into the 10L carboy. The nitrogen line with bubbling stone was placed to the bottom of the carboy along with the probe of the dissolved oxygen meter. Parafilm was stretched over the opening to the carboy with a small opening left for the gas line, DO probe, and gas exit. An initial DO measurement was taken and then gas was bubbled through the water at the desired flow rate and a DO measurement was taken every ten minutes. Two test runs were conducted, one with 10 cubic feet per minute (CFM) of N_2, and one at 20 CFM.

Results

Dissolved oxygen levels can be driven below the detection limit of 0.01 ppm in 40 minutes at 20 cfm and in 50 minutes at 10 cfm (Fig. D1).

Conclusions

Bubbling for one hour at 10 cfm is sufficient to bring the brine to a DO level below the instrumental detection limit of 0.01ppm DO. This is within the threshold of anoxia as defined by Langmuir, 1997. Bubbling at 10 cfm is more efficient that 20 cfm.

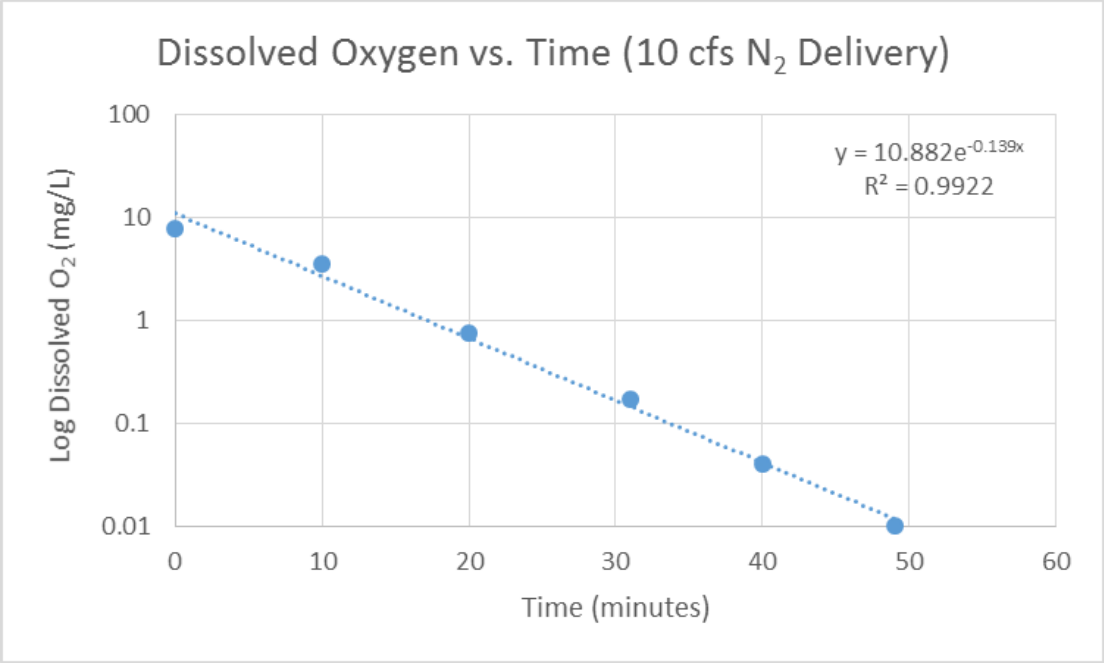

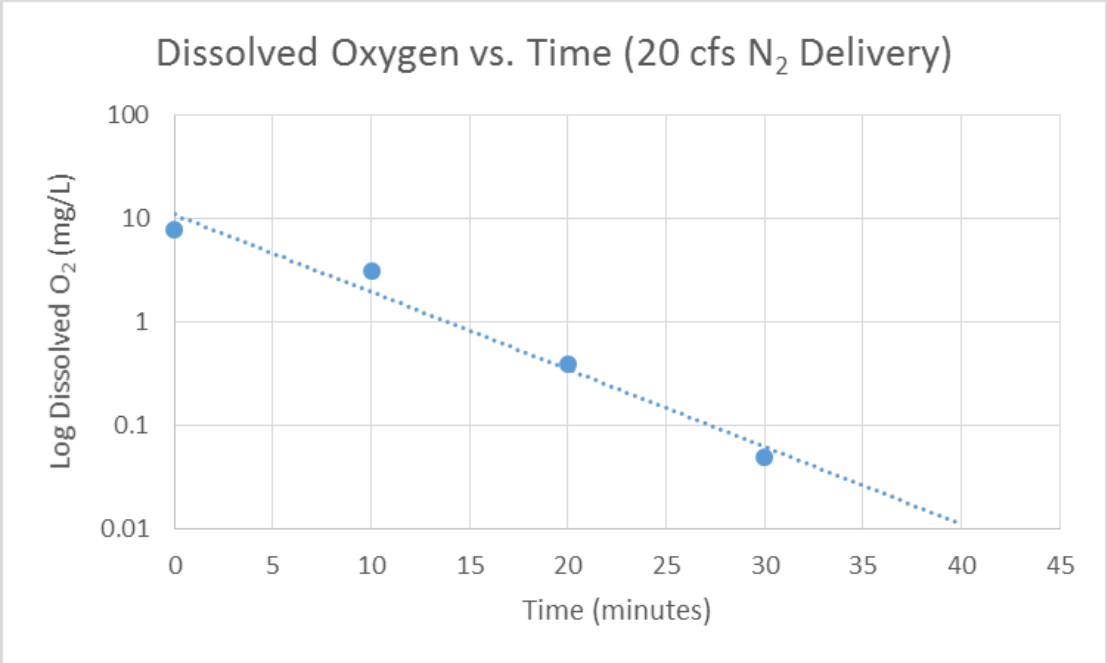

Fig. D1 – (above) Time to drive DO below detection limit at 10cfs vs. 20cfs.

APPENDIX E

BRINE DEOXYGENATION PROCEDURE

Deoxygenation Procedure

To ensure that experimental DO levels were representative of the subsurface environment (<0.96ppm, Langmuir, 1997), brine was de-oxygenated by bubbling with ultra-pure N_2 in a 10L carboy (Fig. E1) and then sealed inside a gas-impermeable media bag (Fig. E2). A procedure was designed to de-oxygenate the brine in an hour (Appendix D).

- Atmospheric gas is purged from the media bag by attaching it to the carboy spout securely (using the ¼" hose). The hose with a ¼" NPT fitting is attached to the N_2 tank. The carboy spout is opened so that the N_2 can vent into the carboy and out the airlock at the top. Enough N_2 is circulated through the bag and carboy to displace the volume of the media bag and carboy three times (75 liters/20 gallons).
- The carboy spout is then closed and the two clips are used to close off the two hoses that go into and out of the media bag. The ¼" NPT fitting is removed from the N_2 tank.
- The brine is added to the carboy and the airlock lid is re-attached. The airlock has two vents. One has a hose descends to the bottom of the carboy with a bubbling stone on it. To the top of this vent is attached a hose that goes to the N_2 tank. The fitting has a hose that vents the spent N_2 to the window (in order to prevent displacement of oxygen from the room).
- Nitrogen is bubbled through the brine at 20 cubic feet per minute (CFM) for one hour. A hose is attached to the exit vent of the airlock

- When the bubbling is finished, the spout that vents the N_2 is removed from the airlock to seal the carboy.
- The spout is then opened, as are the two clips on the media bag and the brine is drained into the bag.
- Occasional bursts of N_2 need to be pumped into the carboy to push the brine out.
- When the brine is drained into the media bag, the two hoses on the back are shut with the clips and the bag is detached form the carboy.
- When ready, the bag is attached to the reactor with the ¼" NPT fitting.

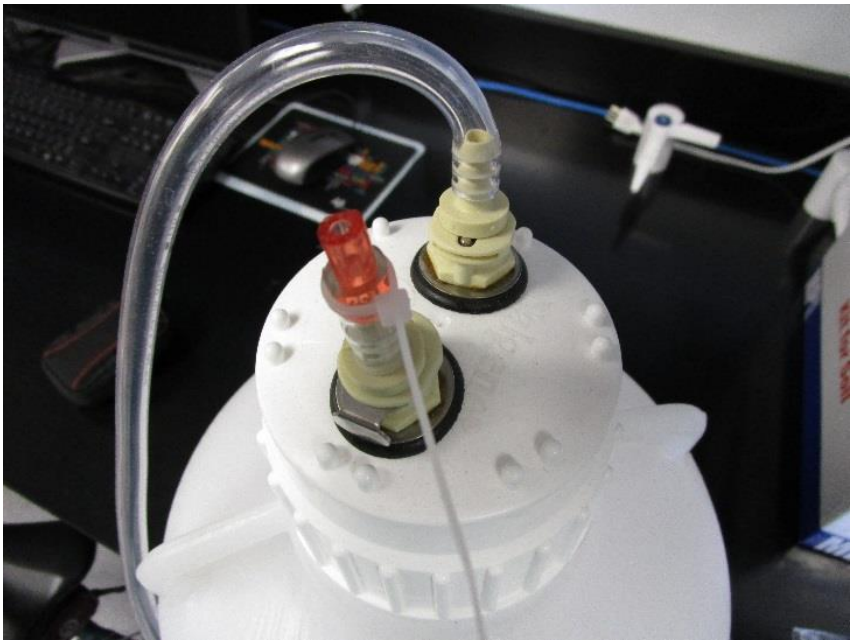

Fig. E1 - Carboy with airlock and spout

Fig. E2 - Gas-impermeable media bag

APPENDIX F

GAS AND BRINE SAMPLE RETRIEVAL PROCEDURE

Gas Sample Retrieval

After the sample manifold has cooled to room temperature, the gas and water samples are extracted from the cylinders. The cylinders are detached at the Vacuum Coupling O-Ring (VCO) fittings (Fig. 2.4) (they seal flat to the valves, so they are more easily removed without bending the rest of the manifold). Make sure to leave the valves at both ends firmly attached to the cylinder to prevent sample from being lost. The six sample cylinders can also be removed during an experiment and cooled outside the incubator. To retrieve the gas and liquid contents easily, mount each cylinder vertically to a laboratory burette stand (Fig. F1).

Gas samples from the sample cylinders are captured in a gas bag using the system depicted below (F1). It is also effective for sampling headspace gas in Parr vessels. The bag is mounted to the bag evacuation system, which is attached to the top of the sample cylinder. Its valve is opened and it is filled with ultra-pure nitrogen and then vacuum pumped out. This is repeated three times to remove all atmospheric gas. The sample cylinder is then gently opened and the gas is allowed to vent into the bag. The bag's valve is closed and the sample is put aside for analysis.

Brine Sample Retrieval

After the gas has been vented the brine is drained into a 60mL syringe (Fig. F2.a). A Whatman Swinlok 25mm reusable filter holder containing a GE Whatman 0.2micron cellulose acetate filter is then attached to the syringe and the fluid is pushed through the filter and captured in another syringe (Fig. F.2.b). Effort is taken to minimize exposure

to the atmosphere, particularly via splashing that can oxygenate the brine. Once in the second syringe the sample can either be placed into Vaccutainers (Fig. F.2.c) or diluted and or acidified for later analysis.

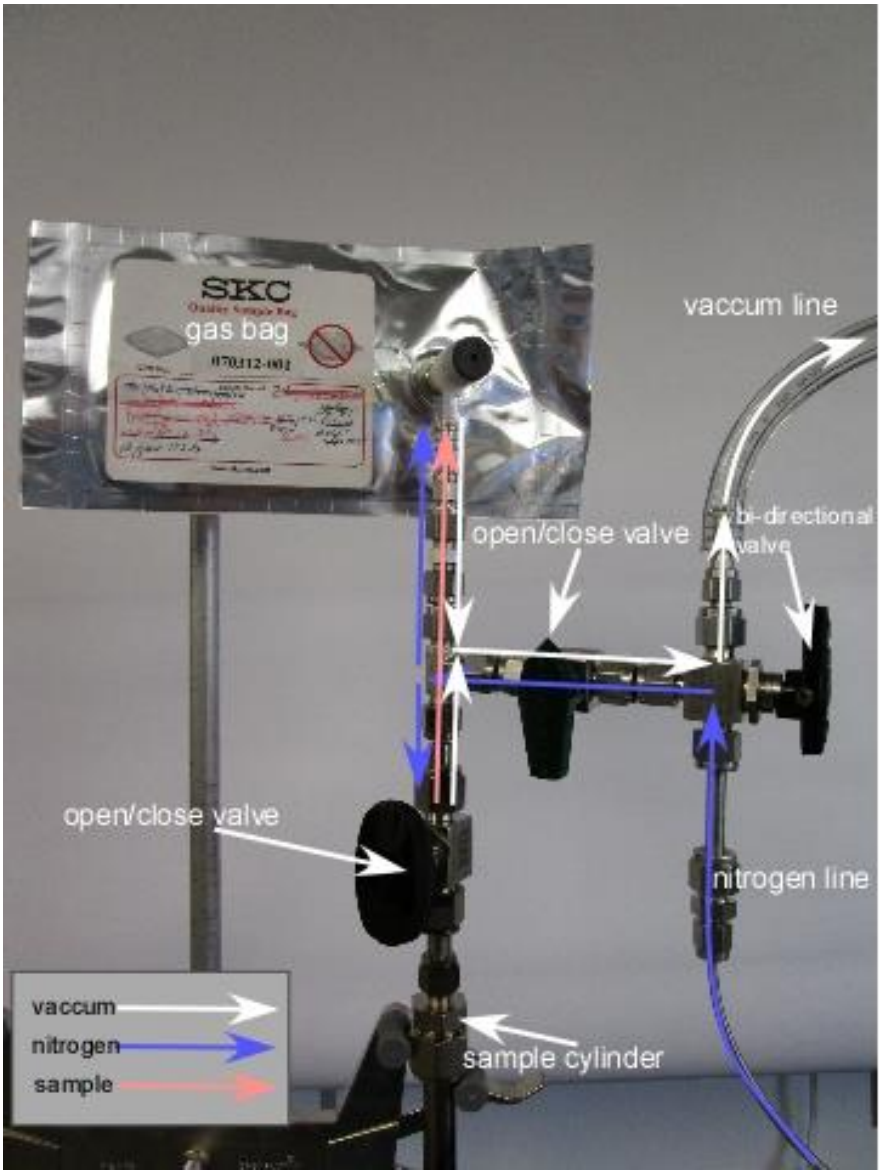

Fig. F.1. – Gas sample capture apparatus

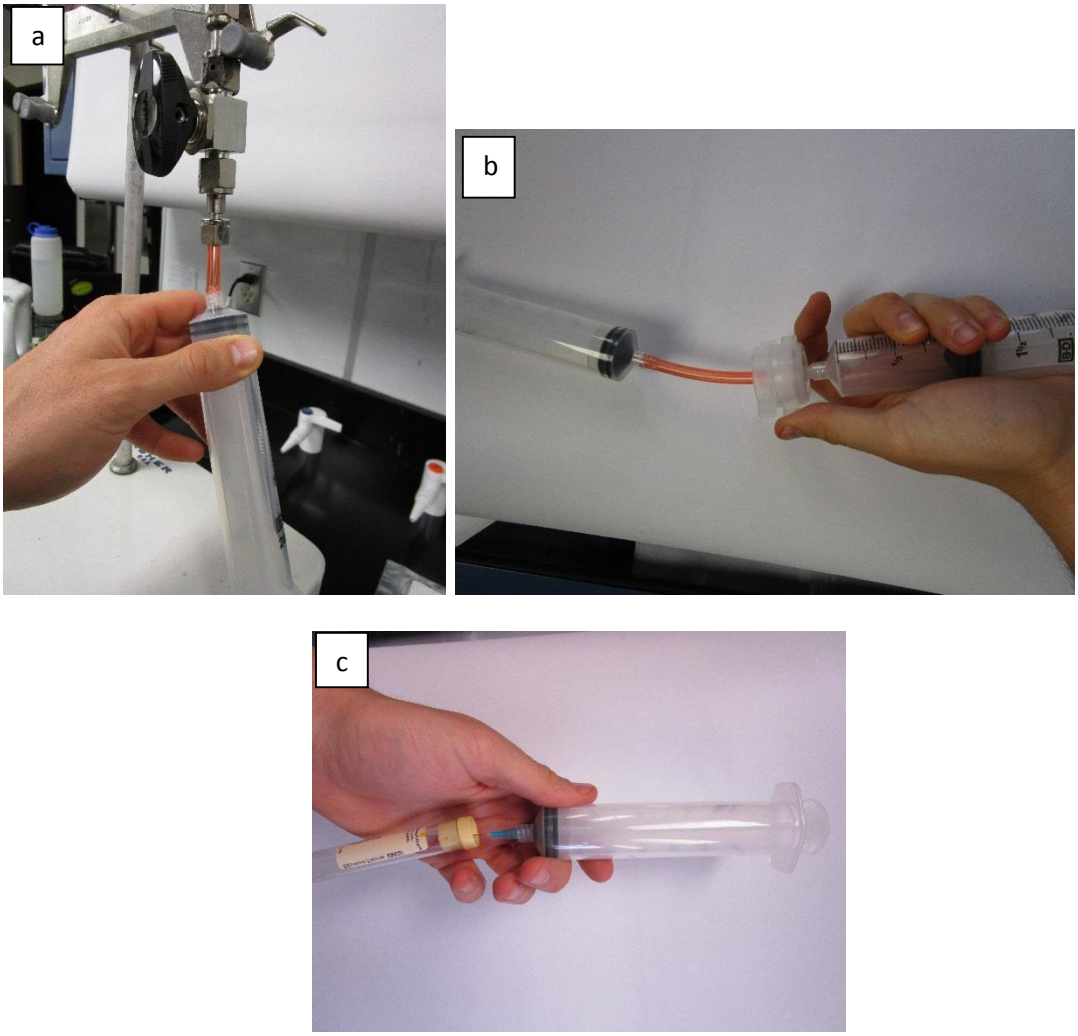

Fig. F.2 - Steps for extracting brine samples from cylinders.

APPENDIX G

SAMPLE MANIFOLD CLEANING PROCEDURE

Sample Manifold Cleaning Procedure

1.) Re-assemble and pressure test following previous experiment
2.) Once confirmed to be pressure tight, flush with deionized water for ~1minute per cylinder
3.) Flush with 0.001M HCl (pH 3) for around ~2 min per cylinder
4.) Flush with deionized water for ~2 minutes per cylinder
5.) Flush with ultra-dry air (with all cylinders open) for ~20 minutes or until no more moisture drains out of manifold
6.) Flush with Ultra-pure N_2 for around 1 minute per cylinder and then ~10 minute with all cylinders open
7.) Pressurize to 1000psi with Ultra-pure N_2 and seal all valves
8.) Connect to reactor

APPENDIX H

PERMEABILITY MEASUREMENT PROCEDURE

Introduction

The flow through reactor can be used to measure permeability using Darcy's Law.

$$k = v\,\mu\frac{\Delta x}{\Delta P}$$

Where:

k = permeability (m^2)
v = Darcy velocity (this is the volumetric flow in m^3 divided by the area of the core in m^2 rate) (m/s)
μ = dynamic viscosity (Pa*s)
Δx = length of flow path (length of core) (m)
ΔP = differential pressure (Pa)

Materials

1. 6L 0.25% NaCl brine
2. Core plug

Procedure

1. Measure core length and diameter. Calculate cross sectional area.
2. Make 6L 0.25% NaCl brine.
3. Place core in core holder and connect tubing. Preferably, the core should be saturated in brine already.
4. Set confining pressure in core holder to 2000-2500 psi with N_2 cylinder.
5. Fill dual pumps with brine.

6. Flood plumbing with brine using constant flow rate setting at 100mL/min. When plumbing is flooded with brine turn off pumps and turn valves to direct brine flow through core.
7. Set pumps to "Constant Pressure" mode. This allows the differential pressure to be controlled during the experiment. The differential pressure should be maximized in order to minimize any errors associated with the pressure sensors. This also maximizes the flow rate and therefore minimizes errors associated with measuring the flow rate. The downstream pressure is controlled by the pressure in the accumulator. Setting to "Constant Pressure" allows the operator to control the upstream pressure.
    a. The confining pressure should always be at least 300-400psi greater than the maximum flow pressure through the system in order to prevent the core sleeve from being compromised. If the confining pressure is 2500, then the constant pressure set at the pump should be no more than 2100-2200psi. If the confining pressure is 2000psi, then the pressure set at the pump should be no more than 1700psi.
8. Pump 500mL of brine through core.
9. Set up a spreadsheet in order to calculate the permeability (Table H.1)
10. Graphing the permeability will result in a plot such as Fig. H.1.
11. Take an average of the permeability and calculate the standard deviation. This is the permeability and associated uncertainty. If there is a large trend up or down then the flow rate had not stabilized and the associated data should not be counted

as part of the average. If necessary run more brine through the core until pressure stabilization is reached.

Sample		Core Diameter (mm)	Core Diameter (m)	Core Radius	Core Area (m^2)	Volumetric Flow Rate (mL/min)	Volumetric Flow Rate (m^3/s)	Fluid flow velocity (m/s)	dynamic viscosity (μ) poise	dynamic viscosity (μ) Pa*s	Core length Δx (mm)	Core length Δx (m)	ΔP (psi)	ΔP (Pa)		Permeability (m^2)	Permeability (millidarcies)
Jefferson 1	1	25.01	0.02501	0.012505	0.0004913	1.424	2.373E-08	4.83105E-05	0.0091	0.00091	78.46	0.07846	338	2330428		1.48012E-15	1.50
	2	25.01	0.02501	0.012505	0.0004913	1.468	2.447E-08	4.98032E-05	0.0091	0.00091	78.46	0.07846	336	2316638		1.53493E-15	1.56
	3	25.01	0.02501	0.012505	0.0004913	1.381	2.302E-08	4.68517E-05	0.0091	0.00091	78.46	0.07846	337	2323533		1.43968E-15	1.46
	4	25.01	0.02501	0.012505	0.0004913	1.381	2.302E-08	4.68517E-05	0.0091	0.00091	78.46	0.07846	337	2323533		1.43968E-15	1.46
	5	25.01	0.02501	0.012505	0.0004913	1.424	2.373E-08	4.83105E-05	0.0091	0.00091	78.46	0.07846	337	2323533		1.48451E-15	1.50
	6	25.01	0.02501	0.012505	0.0004913	1.272	2.12E-08	4.31538E-05	0.0091	0.00091	78.46	0.07846	338	2330428		1.32213E-15	1.34

Table H.1 – Table of values to calculate permeability

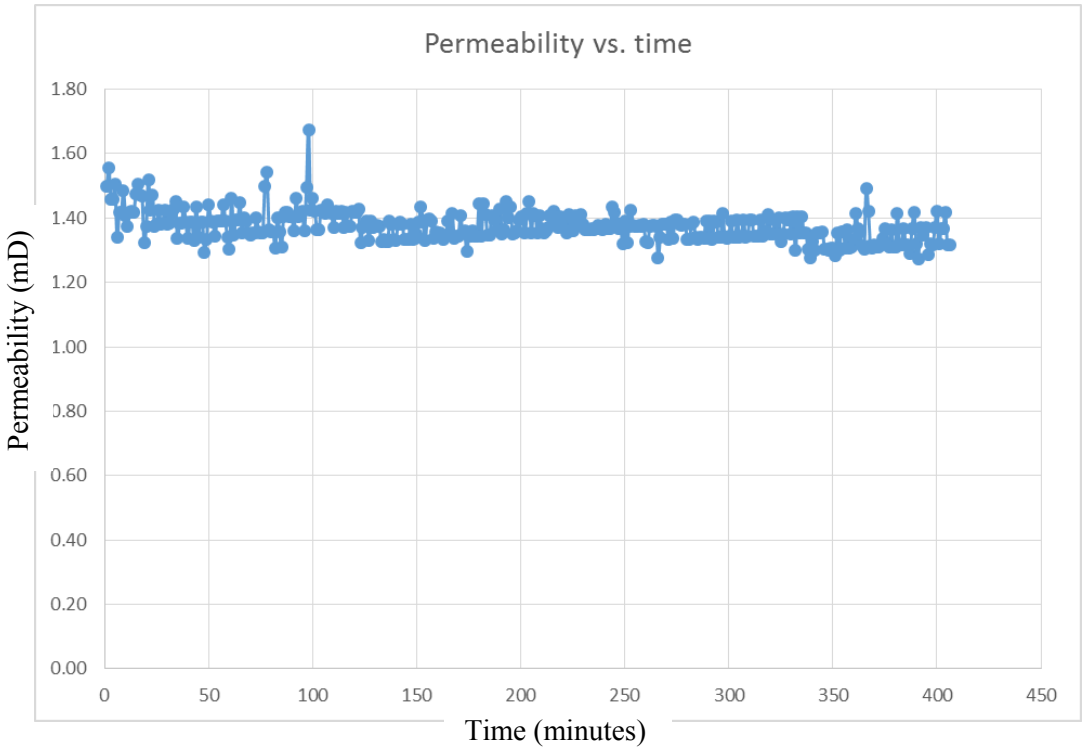

Fig. H.1 – Plot of permeability (mD) vs. time (minutes). Note the relatively constant value for permeability.

APPENDIX I

PARR REACTOR VESSEL DEOXYGENATION PROCEDURE

Parr Vessel Deoxygenation Procedure

1.) Attach vessel to modified gas bag capture apparatus (Fig. F1). Do this by removing gas bag and placing cap on the fitting where it was. Attach the gas line from the Parr vessel to the fitting where the sample cylinder was attached in F1.

2.) Fill Parr vessel with ~1,000psi of ultra-pure N_2 and allow to sit for 5 minutes.

3.) Switch to vacuum for 5 minutes.

4.) Repeat N_2 pressurization-vacuum 3x, ending with vacuum.

5.) Fill with ultra-pure CO_2. Make sure to purge line from CO_2 tank of atmospheric gas before attaching to Parr vessel.

APPENDIX J

WATER CHEMISTRY DATA

	Sample ID	Unreacted brine	Control	Muscovite #1	Muscovite #2	Pyrite #1	Pyrite #2	Magnetite	Substituted Hematite	Iron(II) chloride
Na^+	mg/l	323.7	340.8	379.7	388.1	402.2	400.2	405.5	529.7	298.8
K^+	mg/l	0	21.88	5.4	14.4	9.2	5.33	17.43	3.44	8.43
Ca^{2+}	mg/l	539.5	226.5	331.8	83.53	349.2	274.4	881.2	616.1	
Mg^{2+}	mg/l	865.2	649.2	715.1	662.1	700.8	709.8	652.4	777	
Fe^{2+}	mg/l	0	4.7	0.1	8	44	17.2	8.8	17.5	21491.1
Fe^{3+}	mg/l	0	0.3	1.4	0.7	1.2	0	0	1	0
Cl^-	mg/l	2598	1551	1740	1745	1777	1765	1921	2369	44308.3
SO_4^{2-}	mg/l	1823	1941	2018	1621	2053	2184	1350	1555	
NO_3^-	mg/l	0	93.4	141.2	5.8	174	3.8	96.6	61.4	57.2
NO_2^-	mg/l	0	2.9	0	0	0	0	27.3	25.7	
NH_4^+	mg/l	0	21.11	0	0.7	0	1.6	74.9	0	10.48
F^-	mg/l	0	2.1	0	2.8	0	2.5	0	0	
Br^-	mg/l	0	0	0	2.9	0	3.1	0	0	0
HPO_4^{2-}	mg/l	0	21.3	0	0	0	0	0	38.4	
$SiO_{2(aq)}$	mg/l	0	0	0	39.1	0	11.3	0	110.5	0
HCO_3^-	mg/l	28.7		1425	0	2500	0	2800	2500	
pH		7.5	5.1	5.5	6	5.5	5.5	6.5	6.2	1.5
Charge imbalance	eq/kg	4.94E-04	-0.004752	6.16E-05	-0.006882	8.01E-04	-0.005144	3.38E-04	7.09E-04	-0.4121
Charge imbalance error	%	0.27%	-3.61%	0.04%	-5.29%	0.49%	-3.55%	0.18%	0.37%	-25.14%
Dissolved solids	mg/kg	6055	4804	6328	4507	7313	5297	7856	6861	63491.4
Eh (Fe^{3+}/Fe^{2+})	V		0.4154	0.5437	0.5413	0.3839			0.34	
Eh (NO_3^-/NO_2^-)	V							0.4463	0.471	
Eh (NO_3^-/NH_4^+)	V									0.7716

Table J.1 – Water chemistry data for batch experiments. Ca^{2+}, Mg^{2+}, and SO_4^{2-} were not analyzed because high iron levels affected the shape of the peaks on the IC, making the results unreliable.

	Sample ID	unreacted brine	#1	#2	#3	#4	#5	#6
Time elapsed	**hr**	**0**	**12**	**24**	**36**	**48**	**60**	**72**
Na^+	**mg/l**	334.8	367.1	350.6	352.3	346.1	344.6	342.6
K^+	**mg/l**	0	801	750	772.3	59	435	84
Ca^{2+}	**mg/l**	242.8	253.4	287.1	317	325.7	296.5	304.8
Mg^{++}	**mg/l**	568.6	518.3	591.7	654.7	679.4	651	637.1
Cl^-	**mg/l**	1487	2429	2455	2292	1584	1964	1593
SO_4^{2-}	**mg/l**	1854	1711	1850	1827	1878	1841	1866
HCO_3^-	**mg/l**	28.7						
pH		7.5	4.9	4.5	4.6	4.2	4.6	4.1
Fe^{2+}	**mg/l**	0.0	2.3	1.1	5.4	9.9	11.1	4.9
Fe^{3+}	**mg/l**	0	0.2	0.3	0.1	0	0.1	1.8
Charge imbalance	**eq/kg**	-0.007421	-0.01209	-0.01006	0.002283	0.00371	0.001176	0.001243
Charge imbalance error		-6.10%	-7.28%	-5.87%	1.33%	2.71%	0.77%	0.93%
Dissolved solids	**mg/kg**	4449	5989	6189	6125	4810	5460	4764
Eh (Fe^{3+} /Fe^{2+})	**V**		0.626	0.6549	0.587		0.5676	0.6618

Table J.2 – Water chemistry data for Control flow-through experiment.

	Sample ID	Unreacted brine	#2	#3	#4	#5	#6
Time elapsed	**hr**	**0**	**24**	**36**	**48**	**60**	**72**
Na^+	**mg/l**	1058	937.2	1038	1070	952.7	1909
K^+	**mg/l**	0	40.26	23.67	15.46	47.93	28.03
Ca^{2+}	**mg/l**	260.1	1080	276.1	274.9	253.4	730.6
Mg^{2+}	**mg/l**	1469	1080	1339	1385	1161	3385
HCO_3^-	**mg/l**						
Cl^-	**mg/l**	4435	3542	3988	3988	3299	12296
SO_4^{2-}	**mg/l**	1546	873.8	989.3	1173	844.8	2730
pH		6.5	5.5	5.5	4.5	4.9	5
Charge imbalance	**eq/kg**	0.02222	0.0654	0.03605	0.03715	0.0396	-0.00479
Charge imbalance error	**%**	7.60%	24.36%	13.32%	13.49%	16.85%	-0.70%
Dissolved solids	**mg/kg**	8624	7434	7531	7779	6456	20616.5

Table J.3 – Water chemistry data for oxygenated brine Berea flow-through experiment (BER 8/29/2013).

	Sample ID	Unreacted brine	#1	#2	#3	#4	#5	#6
Time elapsed	**hr**	**0**	**12**	**24**	**36**	**48**	**60**	**72**
Na^+	**mg/l**	444	418	889		493	576	474
K^+	**mg/l**	0	8.4	5.8	5	4.3	1.9	4
Ca^{2+}	**mg/l**	681	483	1141		637	720	682
Mg^{++}	**mg/l**	364	357	952		518	697	392
Cl^-	**mg/l**	1574	2158	3904		2507	1941	1597
SO_4^{2-}	**mg/l**	921	1229	1903		1182	929	916
HCO_3^-	**mg/l**	28.7						
pH		7.5	5.9	5	4.8	4.9	4.9	5.5
Fe^{2+}	**mg/l**	0		23.75	13	11.5	17.5	7.5
Fe^{3+}	**mg/l**	0				6	9	
Charge imbalance	**eq/kg**	0.01922	-0.01458	0.0252		0.001178	0.0451	0.02316
Charge imbalance error		15.10%	-10.71%	9.18%		0.71%	26.55%	17.63%
Dissolved solids	**mg/kg**	4012	4653	8818		5362	4896	4072
Eh (Fe^{3+} /Fe^{2+})	**V**					0.5285	0.5271	

Table J.4 - Water chemistry data for de-oxygenated brine Berea flow-through experiment (BER10/5/2013). Most of Sample #3 was lost during collection and could not be analyzed.

	Sample ID	Unreacted brine	11-5.1	11-5.2	11-5.3	11-5.4	11-5.5	11-5.6
Time elapsed	**hr**	**0**	**12**	**24**	**36**	**48**	**60**	**72**
Na^+	**mg/l**	497	502	532	566	563	536	384
K^+	**mg/l**	0	10.1	139.6	7.6	11.7	9.7	8
Ca^{2+}	**mg/l**	587	665	593	614	601	771	870
Mg^{++}	**mg/l**	319	384	291	412	413	429	463
Cl^-	**mg/l**	1279	1588	1481	1618	1600	1587	
SO_4^{2-}	**mg/l**	788	972	861	978	957	958	
HCO_3^-	**mg/l**	28.7						
pH		7.5	6	5.5	5.4	5.6	5.4	5.2
Fe^{2+}	**mg/l**	0	170	42.5	56.67	782.3	85.01	53.78
Fe^{3+}	**mg/l**	0	0	42.5		170.1	70.84	7.076
Charge imbalance	**eq/kg**	0.02423	0.02785	0.02274	0.02536	0.054	0.03681	0.1005
Charge imbalance error		21.29%	20.39%	18.21%	18.57%	33.46%	25.52%	100%
Dissolved solids	**mg/kg**	3498	4289	4008	4251	5191	4488	1789
Eh (Fe^{3+} /Fe^{2+})	**V**			0.4715		0.421	0.4798	0.4518

Table J.4 - Water chemistry data for de-oxygenated brine + $NaSO_3$ Berea flow-through experiment (BER 11/5/2013).